

Ministry of Education and Science of the Russian Federation  
Saint Petersburg National Research University of Information  
Technologies, Mechanics, and Optics

***NANOSYSTEMS:***  
***PHYSICS, CHEMISTRY, MATHEMATICS***

**2013, volume 4(5)**

**Наносистемы: физика, химия, математика**

**2013, том 4, № 5**



# NANOSYSTEMS:

**PHYSICS, CHEMISTRY, MATHEMATICS**

## ADVISORY BOARD MEMBERS

**Chairman:** V.N. Vasiliev (*St. Petersburg, Russia*),  
V.M. Ievlev (*Voronezh*), P.S. Kop'ev (*St. Petersburg, Russia*),  
V.N. Parmon (*Novosibirsk*), A.I. Rusanov (*St. Petersburg, Russia*).

## EDITORIAL BOARD

**Editor-in-Chief:** N.F. Morozov (*St. Petersburg, Russia*)  
**Deputy Editor-in-Chief:** I.Yu. Popov (*St. Petersburg, Russia*)

### Section Co-Editors:

Physics – V.M. Uzdin (*St. Petersburg, Russia*),  
Chemistry, material science – V.V. Gusarov (*St. Petersburg, Russia*),  
Mechanics – A.K. Belyaev (*St. Petersburg, Russia*),  
Mathematics – I.Yu. Popov (*St. Petersburg, Russia*).

### Editorial Board Members:

V.M. Adamyan (*Odessa, Ukraine*); O.V. Al'myasheva (*St. Petersburg, Russia*); S. Bechta (*Stockholm, Sweden*); V.G. Bepalov (*St. Petersburg, Russia*); A. Chatterjee (*Hyderabad, India*); S.A. Chivilikhin (*St. Petersburg, Russia*); A.V. Chizhov (*Dubna, Russia*); P.P. Fedorov (*Moscow, Russia*); E.A. Gudilin (*Moscow, Russia*); D.A. Indeitsev (*St. Petersburg, Russia*); A.L. Ivanovskii (*Ekaterinburg, Russia*); H. Jónsson (*Reykjavik, Iceland*); A.A. Kiselev (*Madison, USA*); Yu.S. Kivshar (*Canberra, Australia*); S.A. Kozlov (*St. Petersburg, Russia*); Yu.B. Kudasov (*Sarov, Russia*); S.E. Kul'kova (*Tomsk, Russia*); P.A. Kurasov (*Stockholm, Sweden*); A.V. Lukashin (*Moscow, Russia*); V.A. Margulis (*Saransk, Russia*); I.V. Melikhov (*Moscow, Russia*); G.P. Miroshnichenko (*St. Petersburg, Russia*); H. Neidhardt (*Berlin, Germany*); K. Pankrashkin (*Orsay, France*); B.S. Pavlov (*Auckland, New Zealand*); A.V. Ragulya (*Kiev, Ukraine*); V. Rajendran (*Tamil Nadu, India*); V.P. Romanov (*St. Petersburg, Russia*); V.Ya. Rudyak (*Novosibirsk, Russia*); V.M. Talanov (*Novocherkassk, Russia*); A.Ya. Vul' (*St. Petersburg, Russia*).

### Editors:

I.V. Blinova; A.I. Popov; M.A. Skryabin; A.I. Trifanov; E.S. Trifanova (*St. Petersburg, Russia*),  
R. Simoneaux (*USA*).

**Address:** University ITMO, Kronverkskiy pr., 49, St. Petersburg 197101, Russia.

**Phone:** +7(812)232-67-65, **Journal site:** <http://nanojournal.ifmo.ru/>,

**E-mail:** [popov1955@gmail.com](mailto:popov1955@gmail.com)

## AIM AND SCOPE

The scope of the journal includes all areas of nano-sciences. Papers devoted to basic problems of physics, chemistry, material science and mathematics inspired by nanosystems investigations are welcomed. Both theoretical and experimental works concerning the properties and behavior of nanosystems, problems of its creation and application, mathematical methods of nanosystem studies are considered.

The journal publishes scientific reviews (up to 30 journal pages), research papers (up to 15 pages) and letters (up to 5 pages). All manuscripts are peer-reviewed. Authors are informed about the referee opinion and the Editorial decision.

# Content

## PHYSICS

- E.M. Aryslanova, A.V. Alfimov, S.A. Chivilikhin  
**Model of porous aluminum oxide growth in the initial stage of anodization** 585
- S.A. Chivilikhin, A.S. Amosov, I.F. Melikhov  
**Response of a stratified viscous half-space to a perturbation of the free surface** 592
- T.P. Dyachkova, A.V. Melezhyk, S.Yu. Gorsky, I.V. Anosova, A.G. Tkachev  
**Some aspects of functionalization and modification of carbon nanomaterials** 605
- V.E. Egorushkin, N.V. Melnikova, N.G. Bobenko, A.N. Ponomarev  
**Low-temperature thermopower in disordered carbon nanotubes** 622
- V.P. Pashchenko  
**Surface acoustic wave ferroelectric phononic crystal tunable by electric field** 630
- A.I. Trifanov, G.P. Miroshnichenko  
**Reduced conditional dynamic of quantum system under indirect quantum measurement** 635
- D.S. Yasyrkina, S.V. Kuznetsov, A.V. Ryabova, D.V. Pominova, V.V. Voronov, R.P. Ermakov, P.P. Fedorov  
**Dependence of quantum yield of up-conversion luminescence on the composition of fluorite-type solid solution  $\text{NaY}_{1-x-y}\text{Yb}_x\text{Er}_y\text{F}_4$**  648
- O.A. Zolotov, V.E. Zalizniak  
**Accurate energy conservation in molecular dynamics simulation** 657

## CHEMISTRY AND MATERIAL SCIENCE

- Ashok kumar Gupta, Gautam kumar sah  
**Miscibility studies of PC/PMMA blends in Tetrahydrofuran by Viscometry, FTIR and SEM analysis** 670
- M.A. Jafarov, E.F. Nasirov  
**Nanoscale structures based on the  $\text{Zn}_{1-x}\text{Cd}_x\text{S}$**  680

S.A. Lermontov, A.N. Malkova, L.L. Yurkova, A.Ye. Baranchikov, V.K. Ivanov <b>Sulfated nano-ceria as a catalyst of hex-1-ene oligomerization</b>	<b>690</b>
N.A. Lomanova, V.V. Gusarov <b>Influence of synthesis temperature on BiFeO<sub>3</sub> nanoparticles formation</b>	<b>696</b>
V.V.Postnov, A.Ya.Scaletckaya, O.A.Krokhina, V.A.Keskinov, N.A.Charykov, K.N. Semenov <b>Sorption and liquid chromatographic separation of light fullerenes C<sub>60</sub> and C<sub>70</sub> with multiwall carbon nanotubes</b>	<b>706</b>
Nazme Moushumy, Kamal Alameh, V. Rajendran, Yong Tak Lee <b>Correction to the paper “Silver-Nanoparticle-Based Etch Mask Control for Subwavelength Structure Development”</b>	<b>716</b>
<b>Information for authors</b>	<b>718</b>

# MODEL OF POROUS ALUMINUM OXIDE GROWTH IN THE INITIAL STAGE OF ANODIZATION

E. M. Aryslanova, A. V. Alfimov, S. A. Chivilikhin

St. Petersburg National Research University of Information Technologies,  
Mechanics and Optics, 49 Kronverkskiy, St. Petersburg, 197101, Russia

elizabeth.aryslanova@gmail.com

**PACS 81.05.Xj, 81.15.Pq, 82.45.Aa, 81.07.Gf, 61.46.Km**

Currently, due to the development of nanotechnology and metamaterials, it has become important to obtain regular self-organized structures, with different parameters. Porous anodic alumina films are self-organizing structures, which can be represented in a hexagonal packing of cylindrical pores normal to the plane of the aluminum film and used as a template for synthesis of various nanocomposites. The diameter of pores and the distance between them can vary (pore diameter — from 2 to 350 nm, the distance between the pores — from 5 to 50 nm), using different electrolytes, voltage and anodizing time. Currently, there are various models that describe the growth of a porous film of aluminum oxide, but none take into account the influence of aluminum layers and electrolyte on the rate of aluminum oxide growth, as well as the effect of surface diffusion. In present work we consider those effects.

**Keywords:** porous aluminum oxide, anodizing, anodized aluminum oxide.

## 1. Introduction

Currently the scope of anodic aluminum oxide (AAO) use has expanded beyond corrosion, electrical protection and thermal protection to the development of a template for the synthesis of various nanocomposites. Some examples are: the synthesis of nanotubes via the matrix method [1–4]: where in 50–60 nm thick films, with an ordered system of nanopores (diameter of 40–100 nm) are used for synthesizing oriented carbon nanotubes using pyrolysis of dichloromethane ( $\text{CH}_2\text{Cl}_2$ ) under an inert atmosphere of argon at 500 °C, the synthesis of which varies from 6 minutes to 4 hours [5]; the ability to control parameters of the porous structure of  $\text{Al}_2\text{O}_3$  can be used as filters, carriers for catalysts [1–4]; films with high regularity of the porous structure are increasingly used for creating nanoscale structures in electronic, magnetic, and photonic devices [6]; with sorption of silver ions in the matrix of porous alumina, followed by chemical deposition nanocomposites are synthesized with biochemical activity properties [7].

AAO films consist of a so-called honeycomb structure. This system has a dense hexagonal packing, which is oriented in a perpendicular manner to the substrate surface. In the center of each  $\text{Al}_2\text{O}_3$  cell, nanoscale pores formed. The bottom surface of the pores is separated from the aluminum substrate by a thin barrier layer. The cells are separated by a so-called honey “Skeleton” [8–13].

The chemical composition of these regions varies and is dependent upon the anodization conditions. The inner part of the cell may include electrolyte anions, where the “skeleton” is made of pure hydrated alumina [11]. The diameter and the distance between them can vary (pore diameter — from 2 to 350 nm, the distance between the pores — from 5 to 50 nm), using different electrolytes, voltage and anodizing times [2, 7].

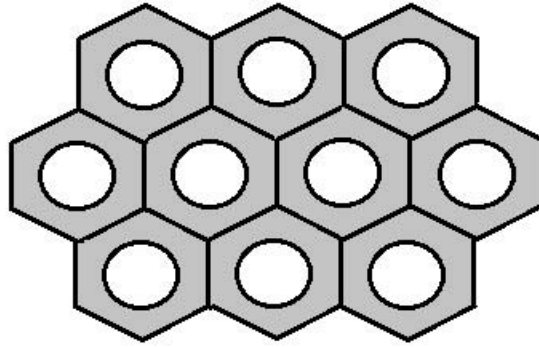


FIG. 1. Hexagonal packing of the porous AAO

## 2. Anodization technique

On the surface of the aluminum, a non-conductive oxide film is formed that is fairly uniform in its coverage of the aluminum surface (Fig. 2). An electrochemical field is concentrated on surface irregularities of the oxide film and preferentially dissolves the oxide in places where the inhomogeneity is higher. Thus, in areas of inhomogeneity on the surface, pore-growth occurs, increasing with higher temperatures, and with electrical field amplification. Initially, a competition is occurring between adjacent pores, which, after some time, leads to a stabilization of the process and to orderly pore growth [10].

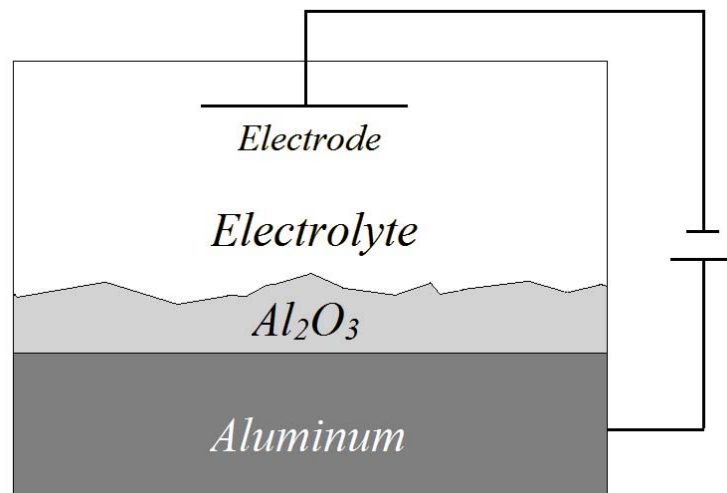


FIG. 2. The process of formation of the porous alumina

In the anodizing process, aqueous solutions of acids moderately dissolve Al<sub>2</sub>O<sub>3</sub>. The process is carried out in a vessel with an electrolyte, which houses the anode (aluminum) and a cathode (inert conductive material), which are respectively connected to the positive and negative outputs of the power supply (Fig. 2). Thus, the film is formed on the metal, the top layer of which is a micro-porous metal oxide partially hydrated, under which is the bottom layer — anhydrous microscopically thin film of vitreous oxide, featuring a considerable hardness [1–4].

### 3. Modeling

We considered the motion of the interfaces between the electrolyte- $\text{Al}_2\text{O}_3$  (dissolution), and between  $\text{Al}_2\text{O}_3$ -aluminum (oxidation), as well as the dynamics of moving boundaries and the change of small perturbations of these boundaries. Each area under Laplace's equation is solved for the potential of the electric field. The growth process of the porous alumina is described by the theory of small perturbations. In zero approximation boundaries are considered flat and the speed of their movements is proportional to the current density at these boundaries. In the first approximation, small perturbations of the interface are considered, which lead to small changes in the potential and the current on these boundaries. The evolution of small perturbations of the interface is defined as a disturbance of the current density at the borders, and the process of surface diffusion.

#### 3.1. The evolution of perturbations of the film boundaries of $\text{Al}_2\text{O}_3$ -layer model (Figure 3):

Fig. 3 shows the geometry of the area under consideration. Here  $h_1$  and  $h_2$  are small perturbations of the Al- $\text{Al}_2\text{O}_3$  and  $\text{Al}_2\text{O}_3$ -electrolyte boundaries, respectively.

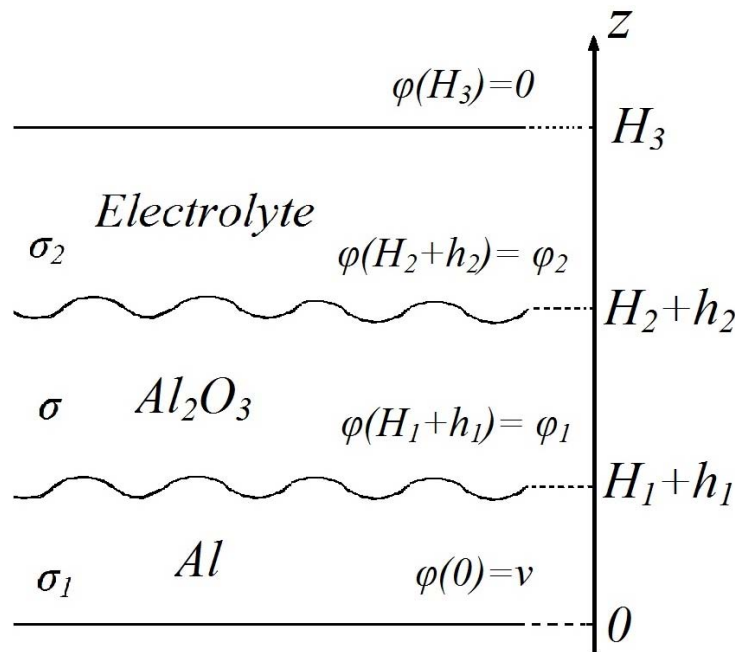


FIG. 3. Inhomogeneous film with rough boundaries

We present the results of potentials perturbation calculations in each layer [14–16]:  
 In the aluminum layer:

$$\hat{\phi}_{\vec{k}} = \left( \hat{\phi}_1 + \frac{v}{\sigma_1 \vartheta} h_{1\vec{k}} \right) \frac{sh(kz)}{sh(kH_1)}.$$

In the electrolyte layer:

$$\hat{\phi}_{\vec{k}} = \left( \hat{\phi}_2 + \frac{v}{\sigma_2 \vartheta} h_{2\vec{k}} \right) \frac{sh(k(z - H_3))}{sh(k(H_2 - H_3))}.$$

In the aluminum oxide layer:

$$\hat{\phi}_{\vec{k}} = \frac{1}{sh(kH)} \left( \left( \hat{\phi}_{2\vec{k}} + \frac{v}{\sigma\vartheta} h_{2\vec{k}} \right) sh(k(z - H_1)) - \left( \hat{\phi}_{1\vec{k}} + \frac{v}{\sigma\vartheta} h_{1\vec{k}} \right) sh(k(z - H_2)) \right),$$

where  $\hat{\phi}_{\vec{k}}$  — the Fourier transform of the potential disturbance to the coordinates  $x, y$ :

$$\hat{\phi}_{\vec{k}} = \int_{-\infty}^{\infty} e^{-ik_y y} \int_{-\infty}^{\infty} \hat{\phi} e^{-ik_x x} dx dy, k^2 = k_x^2 + k_y^2, \phi = \phi_{(z)}^0 + \hat{\phi}, \phi_{(z)}^0 — stationary potential$$

for the homogeneous problem,  $\hat{\phi}$  — potential oscillations,  $\phi_1$  — electrostatic potential of the aluminum layer on Al-Al<sub>2</sub>O<sub>3</sub> interface,  $\phi_2$  — electrostatic potential of the aluminum layer on electrolyte-Al<sub>2</sub>O<sub>3</sub> interface,  $\sigma_1$  — conductivity of the aluminum,  $\sigma$  — conductivity of aluminum-oxide,  $\sigma_2$  — conductivity of the electrolyte,  $\vartheta = \left( \frac{H}{\sigma} + \frac{H_1}{\sigma_1} + \frac{H_3 - H_2}{\sigma_2} \right)$ ,  $v$  — anodization voltage,  $H$  — thickness of aluminum oxide,  $H_1 + h_1$  — thickness of the aluminum layer,  $H_3 - (H_2 + h_2)$  — thickness of the electrolyte layer,  $h_{1\vec{k}} = \int_{-\infty}^{\infty} e^{-i(k_y y)} \int_{-\infty}^{\infty} e^{-i(k_x x)} h_1 dx dy$ ,

$$h_{2\vec{k}} = \int_{-\infty}^{\infty} e^{-i(k_y y)} \int_{-\infty}^{\infty} e^{-i(k_x x)} h_2 dx dy.$$

Using conditions of continuity of the current density at both interfaces, we obtain the system of equations relating the potential disturbance on the interfaces:

$$\begin{cases} (-\sigma_2 sh(kH) - \sigma ch(kH)) \hat{\phi}_{2\vec{k}} + \sigma \hat{\phi}_{1\vec{k}} = \beta e^{kH} - \alpha \\ -\sigma \hat{\phi}_{2\vec{k}} + (\sigma_1 sh(kH) + \sigma ch(kH)) \hat{\phi}_{1\vec{k}} = \beta - \alpha e^{kH} \end{cases} \quad (1)$$

where  $\alpha = \frac{v}{\vartheta} h_{1\vec{k}}, \beta = \frac{v}{\vartheta} h_{2\vec{k}}$ .

We consider the solutions of the system (1) for different values  $kH$ :

I. For  $kH \ll 1$ ,

$$\begin{cases} \hat{\phi}_{1\vec{k}} = 0 \\ \hat{\phi}_{2\vec{k}} = \frac{(\alpha - \beta)\sigma_1}{\sigma_1 \sigma_2 kH + \sigma_1 \sigma + \sigma_2 \sigma} \end{cases} .$$

II. For  $kH \gg 1$ ,

$$\begin{cases} \hat{\phi}_{1\vec{k}} = 0 \\ \hat{\phi}_{2\vec{k}} = \frac{2}{\sigma_2} \left( \frac{\alpha}{e^{kH}} - \beta \right) \end{cases} .$$

### 3.2. Calculation of the evolution of alumina boundaries perturbations, without consideration of surface diffusion

The rate of change of small perturbations of the Al-Al<sub>2</sub>O<sub>3</sub> and Al<sub>2</sub>O<sub>3</sub>-electrolyte boundaries without the influence of surface diffusion is proportional to the perturbation of the current density at these interfaces  $\frac{dh}{dt} = a\sigma \frac{\partial \phi}{\partial z}$ .

For Al-Al<sub>2</sub>O<sub>3</sub> interface:

$$\frac{\partial \hat{\phi}_{\vec{k}}}{\partial z} = k \left( \hat{\phi}_1 + \frac{v}{\sigma_1 \vartheta} h_{1\vec{k}} \right) \frac{ch(kz)}{sh(kH_1)}.$$

Then:

$$\frac{dh_{1\vec{k}}}{dt} = \left( \frac{a_1 v k}{\vartheta} h_{1\vec{k}} \right) cth(kH_1), \quad h_{1\vec{k}}(t) = h_{1\vec{k}}(0) \cdot e^{\frac{a_1 k v \cdot cth(kH_1)}{\vartheta} t}. \quad (2)$$

For the Al<sub>2</sub>O<sub>3</sub>-electrolyte interface:

$$\frac{\partial \hat{\phi}_{\vec{k}}}{\partial z} = k \left( \hat{\phi}_2 + \frac{v}{\sigma_2 \vartheta} h_{2\vec{k}} \right) cth(kH) \quad (3)$$

We consider two cases:

I. When  $kH \ll 1$ ,

Since the conductivity of the electrolyte and alumina is small compared with aluminum, we obtain from (3):

$$h_{2\vec{k}} = h_{1\vec{k}}(0) \cdot e^{\frac{a_1 kv}{\vartheta} t} + \left( h_{2\vec{k}}(0) - h_{1\vec{k}}(0) \right) e^{-\frac{a_2 kv}{\vartheta} t} \quad (4)$$

II. When  $kH \gg 1$ ,

$$h_{2\vec{k}} = \frac{2h_{1\vec{k}}(0) a_2 e^{\frac{a_1 kv}{\vartheta} t}}{(a_1 + a_2) e^{kH}} + \left( h_{2\vec{k}}(0) - \frac{2h_{1\vec{k}}(0) a_2}{(a_1 + a_2) e^{kH}} \right) e^{-\frac{a_2 kv}{\vartheta} t}. \quad (5)$$

From (4-5), we see that in this approximation, the perturbation on the  $\text{Al}_2\text{O}_3$ -electrolyte interface increases indefinitely with time.

### 3.3. Calculation of the evolution of alumina boundaries perturbations, with consideration of surface diffusion

The rate of change of small perturbations of the Al- $\text{Al}_2\text{O}_3$  and  $\text{Al}_2\text{O}_3$ -electrolyte boundaries with the influence of surface diffusion is described by the relation  $\frac{\partial h}{\partial t} = V + D\Delta^2 h$ , where  $D$  — is the surface diffusion coefficient.

For the Al- $\text{Al}_2\text{O}_3$  interface:

$$V_1 = \left( \frac{a_1 v}{\vartheta} h_{1\vec{k}} \right),$$

$$\frac{dh_{1\vec{k}}}{dt} = h_{1\vec{k}} \left( \frac{a_1 v k}{\vartheta} - D_1 k^4 \right), h_{1\vec{k}} = h_{1\vec{k}}(0) e^{\left( \frac{a_1 v k}{\vartheta} - D_1 k^4 \right) t}. \quad (6)$$

From (6), we get the value of spectral parameter corresponding to the limit of stability for the Al- $\text{Al}_2\text{O}_3$  interface:

$$k_1 = \left( \frac{a_1 v}{\vartheta D_1} \right)^{1/3}. \quad (7)$$

All perturbations of this interface with  $k < k_1$  are unstable. Perturbations of the upper boundary in this spectral interval are the source of pore formation. We will estimate of distance between centers of aluminum oxide pores as  $2\pi/k_1$ .

For the  $\text{Al}_2\text{O}_3$ -electrolyte interface:

For  $kH \ll 1$ ,

$$V_2 = \frac{v k a_2}{\vartheta H} \left( h_{1\vec{k}}(0) \cdot e^{\frac{a_1 kv \cdot \text{cth}(kH_1)}{\vartheta} t} - h_{2\vec{k}} \right). \quad (8)$$

For  $kH \gg 1$ ,

$$V_2 = \sigma_2 k a_2 \left( \frac{2}{\sigma_2} \left( \frac{\alpha}{e^{kH}} - \beta \right) + \frac{v}{\sigma_2 \vartheta} h_{2\vec{k}} \right). \quad (9)$$

Then, as in (7-8), we obtain the expression, taking into account the surface diffusion:

For  $kH \ll 1$ ,

$$h_{2\vec{k}} = h_{1\vec{k}}(0) \cdot e^{\left( \frac{a_1 kv}{\vartheta} - D_2 k^4 \right) \cdot t}. \quad (10)$$

For  $kH \gg 1$ ,

$$h_{2\vec{k}} = \frac{2h_{1\vec{k}}(0) a_2 e^{\left( \frac{a_1 kv}{\vartheta} - D_2 k^4 \right) \cdot t}}{(a_1 + a_2) e^{kH}}. \quad (11)$$

From (10–11), we get the value of spectral parameter corresponding to the limit of stability for the  $\text{Al}_2\text{O}_3$ -electrolyte interface:

$$k_2 = \left( \frac{a_1 v}{\vartheta D_2} \right)^{1/3}. \quad (12)$$

All perturbations of this interface with wavelength  $k < k_2$  are unstable. The evolution of perturbations in this spectral interval determines the imperfection of the porous structure. This should be considered when preparing the aluminum plate used in this process.

#### 4. Conclusion

As a result of the developed model, we obtained the minimum distance  $2\pi \left( \frac{\vartheta D_1}{a_1 v} \right)^{1/3}$  between centers of aluminum oxide pores in the beginning of anodizing process. The irregularities of the porous structure contains in the spectral interval  $k_2 < \left( \frac{a_1 v}{\vartheta D_2} \right)^{1/3}$ .

#### References

- [1] D.I. Petukhov, K.S. Napol'skii, A.A. Eliseev. Permeability of anodic alumina membranes with branched channels. *Nanotechnology*, **23**(33), P. 1–6 (2012).
- [2] D.I. Petukhov, K.S. Napol'skii, M.V. Berekchiyan, A.G. Lebedev, A.A. Eliseev. Comparative Study of Structure and Permeability of Porous Oxide Films on Aluminum Obtained by Single- and Two-Step Anodization. *ACS applied materials & interfaces*, **5**, P. 7819–7824 (2013).
- [3] K.S. Napol'skii., I. V. Roslyakov, A.A. Eliseev, D.V. Byelov, A.V. Petukhov, N.A. Grigoryeva, W.G. Bouwman, A.V. Lukashin, A.P. Chumakov, S.V. Grigoriev. The Kinetics and Mechanism of Long-Range Pore Ordering in Anodic Films on Aluminum. *Journal of Physical Chemistry C*, **115**(48), P. 23726–23731 (2012).
- [4] D.I. Petukhov, A.A. Yeliseyev, D.A. Buldakt, R.S. Napol'skiy, A.V. Lukashin, Yu.D. Tret'yakov, Yu.D. Yampol'skiy. Anodic aluminum oxide: membranes with controlled gas permeability. *Membranes*, **3**(43), P. 16–22 (2009).
- [5] V.Yu. Koda, M.M. Nishchenko, G.P. Prikhod'ko, S.Ya. Brichka. Electronic and mechanical properties of carbon nanotubes produced by the matrix method. *Proceeding of conference ICHMS'2005*, P. 455–457.
- [6] V.M. Parkun, I.A. Vrublevskiy, Ye.P. Ignashev, M.V. Parkun Investigation of porous alumina volume growth. *Doklady BGUIR*, **1**(2), P. 66–72 (2003).
- [7] Ye.V. Zolotukhina, B.A. Spiridonov, V.I. Fedyanin, Ye.V. Grudneva. Disinfection of water by the use of nanocomposites based on porous aluminum oxide and silver compounds. *Sorbtsionnyye i khromatograficheskiye protsessy*, **10**(1), P. 78–85 (2010).
- [8] A.I. Chukavin, R.G. Valeev, A.N. Beltukov. The synthesis of germanium nanostructures in porous anodic alumina matrix. *Bulletin of Udmurt University. Physics. Chemistry*, **2**, P. 3–7 (2011).
- [9] G. Patermarakis The origin of nucleation and development of porous nanostructure of anodic alumina films. *Journal of Electroanalytical Chemistry*, **635**, P. 39–50 (2009).
- [10] I.V. Roslyakov, K.S. Napol'skiy, A.A. Yeliseyev, A.V. Lukashin, D.Yu. Chernyshov, S.V. Grigor'yev Synthesis of magnetic nanoparticles with controlled anisotropy of functional properties in the matrix of porous alumina. *Nanotechnologies in Russia*, **4**(3–4), P. 82–86 (2009).
- [11] L. Datas, Le Coz F., L. Arurault. Chemical analysis of a single basic cell of porous anodic aluminium oxide templates. *Mat. Char*, **61**, P. 283–288 (2010).
- [12] G.R. Singh, A.A. Golovin, I.S. Aranson. Formation of self-organized nanoscale porous structures in anodic aluminum oxide. *Physical review B*, **73**, P. 205422, 1–12 (2006).
- [13] A.V. Atrashchenko, A.A. Krasilin, I.S. Kuchuk, Ye.M. Aryslanova, S.A. Chivilikhin, P.A. Belov. Electrochemical methods of synthesis of hyperbolic metamaterials. *Nanosystems: Physics, chemistry, mathematics*, **3**(1), P. 31–51 (2012).
- [14] E.M. Aryslanova, A.V. Alfimov, S.A. Chivilikhin. Modelling the initial stage of porous alumina growth during anodization. *Proceedings of SPIE. Nanotechnology*, P. 8766, 1–16 (2013).

- [15] E.M. Ayslanova, A.V. Alfimov, S.A. Chivilikhin, I.Yu. Popov, V.V. Gusarov. Modeling the process of aluminum anodization. Book of abstracts of “International Summer School “Advanced Problems in Mechanics”, St. Petersburg, Russia , July 1 – 6, 2013, P. 30–31.

# RESPONSE OF A STRATIFIED VISCOUS HALF-SPACE TO A PERTURBATION OF THE FREE SURFACE

<sup>1</sup>S. A. Chivilikhin, <sup>2</sup>A. S. Amosov, <sup>1</sup>I. F. Melikhov

<sup>1</sup> St. Petersburg National Research University of Information Technologies,  
Mechanics and Optics, St. Petersburg, Russia

<sup>2</sup> Corning Incorporated, Corning, USA

chivilikhin@gmail.com, amosovas@corning.com, ivan.melikhov@gmail.com

## PACS PACS 47.15.G-

The flow of a highly viscous liquid in a half-space due to the deformation of the free surface is investigated. The viscosity of the layer adjoining to the free surface is different from the viscosity of the remaining half-space. In the framework of small perturbation theory, the relationship between the deformation of the free surface and the deformation of the layer/half-space interface is obtained. It was demonstrated that the volume and geometrical center of the perturbation on the interface and on the free surface are the same. The dependence of the perturbation's amplitude and width on layer thickness was investigated. The results of numerical and analytical calculations are close, even for moderate free surface perturbations.

**Keywords:** quasisteady-state Stokes approximation, free surface, linear approximation, evolution of perturbation.

## 1. Introduction

In this paper, we consider an infinite viscous half-space covered by a fluid layer with a different viscosity. Using a Fourier transform-based approach, we calculated the deformation of the layer/half-space interface due to the perturbation of the free surface.

A Newtonian viscous incompressible fluid was considered. Viscosities of the layer and the half-space may not necessarily be the same, but they are assumed to be constant within each domain. We considered the localized perturbation of the fluid near the free surface, assuming it decays to zero infinitely far from the origin. Two formulations were developed: i) 2D axisymmetric to describe flow perturbation caused by a small particle (fig. 1-a) and ii) 2D planar to represent perturbation due to a long groove (fig. 1-b). In both cases, the shape of the initial perturbation of the free-surface is described by a smooth analytical function.

In section 2, we analytically derive the relation between the shape and amplitude of the free surface perturbation and the corresponding deformation of the layer/half-space interface.

In section 3, the analytical solution is compared to the numerical solution obtained with COMSOL Multiphysics finite element package.

## 2. Analytical model

The analytical model was developed under the following assumptions:

- Planar or axisymmetric viscous flow
- The fluid dynamics can be described by the Stokes equations ( [6], [1], [7], [3], [4], [9], [2])
- Perturbation amplitude is small compared to the layer thickness ( [5], [8], [10], [11])

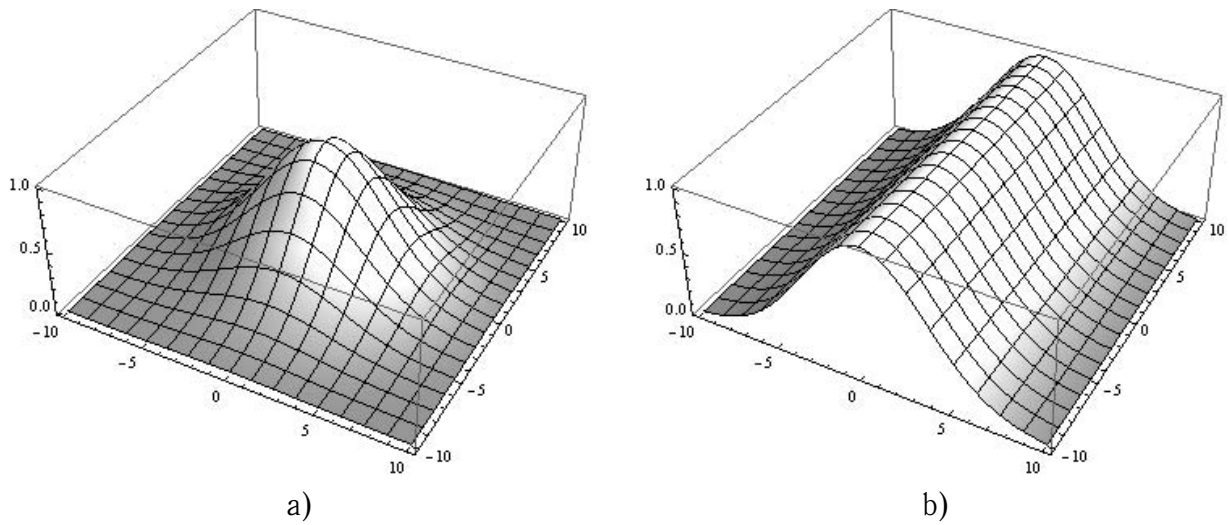


Fig. 1. Perturbation geometry: a) axisymmetric b) planar

- Fluid viscosity is constant within each domain (layer and half-space)

**2.1. The problem statement**

In the analytical model, a fluid layer of the thickness  $H$  covering an infinite half-space is considered. The layer has viscosity  $\mu$  and the half-space has viscosity  $\mu_1$ . Consider the Cartesian coordinate system as shown on the figure 2 below. The axes  $x_1$  and  $x_2$  form a non-deformed planar boundary and the axis  $z$  is oriented through thickness having origin on the free surface of the layer.

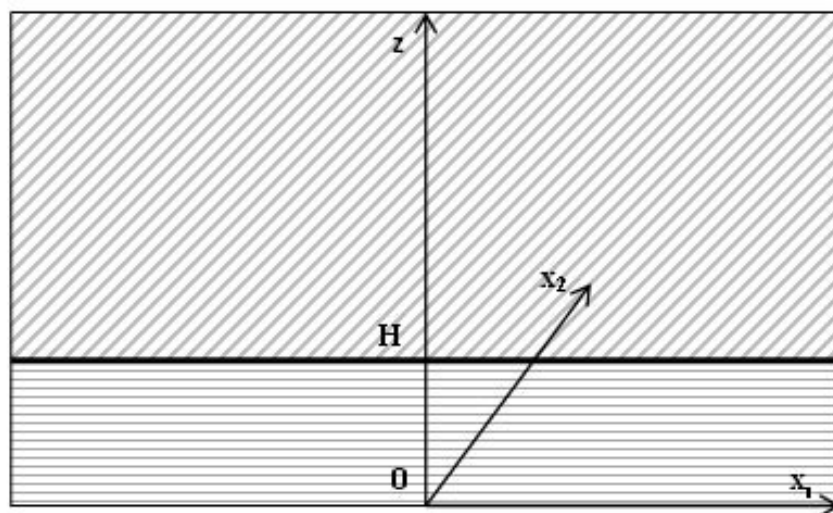


Fig. 2. Coordinate system used in the analysis

The Stokes equations for the surface layer take the form:

$$\begin{aligned}\partial_{zz}^2 V_z + \partial_{\beta\beta}^2 V_z &= \frac{1}{\mu} \partial_z P \\ \partial_{zz}^2 V_\alpha + \partial_{\beta\beta}^2 V_\alpha &= \frac{1}{\mu} \partial_\alpha P \\ \partial_z V_z + \partial_\beta V_\beta &= 0,\end{aligned}\tag{1}$$

where  $V_\alpha$ ,  $V_z$  are the velocity components,  $P$  is the pressure,  $\mu$  is the viscosity of the fluid in the layer. The summation over the repeated indexes is assumed. From (1), it can be seen that pressure is a harmonic function:

$$\partial_{zz}^2 P + \partial_{\beta\beta}^2 P = 0.\tag{2}$$

Zero tangential stress and a given normal velocity are assumed on the external free boundary. Corresponding boundary conditions are:

$$V_z|_{z=0} = V_{z0}, \quad \mu(\partial_\alpha V_z + \partial_z V_\alpha)|_{z=0} = 0.\tag{3}$$

Similarly to (1), the Stokes equations for the half-space domain become:

$$\begin{aligned}\partial_{zz}^2 V_z + \partial_{\beta\beta}^2 V_z &= \frac{1}{\mu_1} \partial_z P \\ \partial_{zz}^2 V_\alpha + \partial_{\beta\beta}^2 V_\alpha &= \frac{1}{\mu_1} \partial_\alpha P \\ \partial_z V_z + \partial_\beta V_\beta &= 0 \\ \partial_{zz}^2 P + \partial_{\beta\beta}^2 P &= 0.\end{aligned}\tag{4}$$

Zero perturbation infinitely far from the free surface is required:

$$\begin{pmatrix} V_z \\ V_\alpha \\ P \end{pmatrix} \Big|_{z \rightarrow \infty} = 0.\tag{5}$$

The velocity field must be continuous through the interface:

$$V_z|_{z=H-0} = V_z|_{z=H+0}, \quad V_\alpha|_{z=H-0} = V_\alpha|_{z=H+0}.\tag{6}$$

Also, both the normal and tangential stresses must be continuous:

$$\begin{aligned}(-P + 2\mu\partial_z V_z)|_{z=H-0} &= (-P + 2\mu_1\partial_z V_z)|_{z=H+0}, \\ \mu(\partial_\alpha V_z + \partial_z V_\alpha)|_{z=H-0} &= \mu_1(\partial_\alpha V_z + \partial_z V_\alpha)|_{z=H+0}.\end{aligned}\tag{7}$$

The equations of the evolution of the free boundary and the interface are the following:

$$\partial_t h_0 = V_z|_{z=0}, \quad \partial_t h = V_z|_{z=H},\tag{8}$$

where  $h_0(x_1, x_2, t)$  and  $h(x_1, x_2, t)$  are the  $z$ -displacements of the free boundary and interface respectively.

## 2.2. Calculation of the perturbation decay

Applying the Fourier transform, defined as (9) over the  $x_1$  and  $x_2$  coordinates to the equations (1)-(8):

$$f_{\mathbf{k}} = \int f(\mathbf{x}) e^{-i\mathbf{k}\mathbf{x}} d^2x\tag{9}$$

one can get the following equations:

$$\begin{aligned} \partial_{zz}^2 V_{z\mathbf{k}} - k^2 V_{z\mathbf{k}} &= \frac{1}{\mu} \partial_z P_{\mathbf{k}} \\ \partial_{zz}^2 V_{\alpha\mathbf{k}} - k^2 V_{\alpha\mathbf{k}} &= \frac{ik_\alpha}{\mu} P_{\mathbf{k}} \quad 0 < z < H, \end{aligned} \quad (10)$$

$$\begin{aligned} \partial_z V_{z\mathbf{k}} + ik_\beta V_{\beta\mathbf{k}} &= 0 \\ \partial_{zz}^2 P_{\mathbf{k}} - k^2 P_{\mathbf{k}} &= 0 \end{aligned}$$

$$V_{z\mathbf{k}}|_{z=0} = V_{z_0\mathbf{k}}, \quad \mu(ik_\alpha V_{z\mathbf{k}} + \partial_z V_{\alpha\mathbf{k}})|_{z=0} = 0, \quad (11)$$

$$\partial_{zz}^2 V_{z\mathbf{k}} - k^2 V_{z\mathbf{k}} = \frac{1}{\mu_1} \partial_z P_{\mathbf{k}}$$

$$\partial_{zz}^2 V_{\alpha\mathbf{k}} - k^2 V_{\alpha\mathbf{k}} = \frac{ik_\alpha}{\mu_1} P_{\mathbf{k}} \quad z > H, \quad (12)$$

$$\begin{aligned} \partial_z V_{z\mathbf{k}} + ik_\beta V_{\beta\mathbf{k}} &= 0 \\ \partial_{zz}^2 P_{\mathbf{k}} - k^2 P_{\mathbf{k}} &= 0 \end{aligned}$$

$$\begin{pmatrix} V_{z\mathbf{k}} \\ V_{\alpha\mathbf{k}} \\ P_{\mathbf{k}} \end{pmatrix} \Big|_{z \rightarrow \infty} = 0, \quad (13)$$

$$V_{z\mathbf{k}}|_{z=H-0} = V_{z\mathbf{k}}|_{z=H+0}, \quad V_{\alpha\mathbf{k}}|_{z=H-0} = V_{\alpha\mathbf{k}}|_{z=H+0}, \quad (14)$$

$$(-P_{\mathbf{k}} + 2\mu\partial_z V_{z\mathbf{k}})|_{z=H-0} = (-P_{\mathbf{k}} + 2\mu_1\partial_z V_{z\mathbf{k}})|_{z=H+0} \quad (15)$$

$$\mu(ik_\alpha V_{z\mathbf{k}} + \partial_z V_{\alpha\mathbf{k}})|_{z=H-0} = \mu_1(ik_\alpha V_{z\mathbf{k}} + \partial_z V_{\alpha\mathbf{k}})|_{z=H+0}.$$

$$\partial_t h_{0\mathbf{k}} = V_{z\mathbf{k}}|_{z=0}, \quad \partial_t h_{\mathbf{k}} = V_{z\mathbf{k}}|_{z=H}. \quad (16)$$

It is convenient to separate the longitudinal  $V_{\mathbf{k}}^{\parallel}$  and transversal  $V_{\mathbf{k}}^{\perp}$  components of the velocity  $V_{\alpha\mathbf{k}}$  in Fourier space:

$$V_{\alpha\mathbf{k}} = \frac{k_\alpha}{k} V_{\alpha\mathbf{k}}^{\parallel} + V_{\alpha\mathbf{k}}^{\perp}, \quad V_{\alpha\mathbf{k}}^{\parallel} = \frac{k_\beta}{k} V_{\beta\mathbf{k}}, \quad V_{\alpha\mathbf{k}}^{\perp} = \left( \delta_{\alpha\beta} - \frac{k_\alpha k_\beta}{k^2} \right) V_{\beta\mathbf{k}}.$$

The equations (10)-(16) can be rewritten in terms of  $V_{\mathbf{k}}^{\parallel}$  and  $V_{\mathbf{k}}^{\perp}$ :

$$\begin{aligned} \partial_{zz}^2 V_{z\mathbf{k}} - k^2 V_{z\mathbf{k}} &= \frac{1}{\mu} \partial_z P_{\mathbf{k}} \\ \partial_{zz}^2 V_{\mathbf{k}}^{\parallel} - k^2 V_{\mathbf{k}}^{\parallel} &= \frac{ik}{\mu} P_{\mathbf{k}} \\ \partial_{zz}^2 V_{\alpha\mathbf{k}}^{\perp} - k^2 V_{\alpha\mathbf{k}}^{\perp} &= 0 \end{aligned} \quad 0 < z < H, \quad (17)$$

$$\partial_z V_{z\mathbf{k}} + ik V_{\beta\mathbf{k}}^{\parallel} = 0$$

$$\partial_{zz}^2 P_{\mathbf{k}} - k^2 P_{\mathbf{k}} = 0$$

$$V_{z\mathbf{k}}|_{z=0} = V_{z_0\mathbf{k}}, \quad \mu(ik V_{z\mathbf{k}} + \partial_z V_{\mathbf{k}}^{\parallel})|_{z=0} = 0, \quad (18)$$

$$(-P_{\mathbf{k}} + 2\mu\partial_z V_{z\mathbf{k}})|_{z=H-0} = f_{zH\mathbf{k}}$$

$$\mu(ik V_{z\mathbf{k}} + \partial_z V_{\mathbf{k}}^{\parallel})|_{z=H-0} = f_{H\mathbf{k}}^{\parallel} \quad (19)$$

$$\mu\partial_z V_{\alpha\mathbf{k}}^{\perp}|_{z=H-0} = f_{\alpha H\mathbf{k}}^{\perp},$$

$$\partial_t h_{0\mathbf{k}} = V_{z\mathbf{k}}|_{z=0}, \quad \partial_t h_{\mathbf{k}} = V_{z\mathbf{k}}|_{z=H}, \quad (20)$$

$$\begin{aligned}
\partial_{zz}^2 V_{z\mathbf{k}} - k^2 V_{z\mathbf{k}} &= \frac{1}{\mu_1} \partial_z P_{\mathbf{k}} \\
\partial_{zz}^2 V_{\mathbf{k}}^{\parallel} - k^2 V_{\mathbf{k}}^{\parallel} &= \frac{ik}{\mu_1} P_{\mathbf{k}} \\
\partial_{zz}^2 V_{\alpha\mathbf{k}}^{\perp} - k^2 V_{\alpha\mathbf{k}}^{\perp} &= 0 \\
\partial_z V_{z\mathbf{k}} + ik V_{\mathbf{k}}^{\parallel} &= 0 \\
\partial_{zz}^2 P_{\mathbf{k}} - k^2 P_{\mathbf{k}} &= 0
\end{aligned} \quad 0 < z < H, \tag{21}$$

$$\begin{aligned}
(-P_{\mathbf{k}} + 2\mu_1 \partial_z V_{z\mathbf{k}})|_{z=H+0} &= f_{zH\mathbf{k}} \\
\mu_1 (ik V_{z\mathbf{k}} + \partial_z V_{\mathbf{k}}^{\parallel})|_{z=H+0} &= f_{H\mathbf{k}}^{\parallel}
\end{aligned} \tag{22}$$

$$\begin{aligned}
\mu_1 \partial_z V_{\alpha\mathbf{k}}^{\perp}|_{z=H+0} &= f_{\alpha H\mathbf{k}}^{\perp} \\
\left( \begin{array}{c} V_{z\mathbf{k}} \\ V_{\mathbf{k}}^{\parallel} \\ V_{\alpha\mathbf{k}}^{\perp} \\ P_{\mathbf{k}} \end{array} \right) \Big|_{z \rightarrow \infty} &= 0.
\end{aligned} \tag{23}$$

From the continuation equation (the third one in (17) and (21)) one can obtain:

$$V_{\mathbf{k}}^{\parallel} = \frac{i}{k} \partial_z V_{z\mathbf{k}}. \tag{24}$$

Taking into account the equation for  $V_{z\mathbf{k}}$ , we get the following boundary conditions for the tangential stress:

$$\begin{aligned}
(2\mu k^2 V_{z\mathbf{k}} + \partial_z P_{\mathbf{k}})|_{z=0} &= 0, \\
(2\mu k^2 V_{z\mathbf{k}} + \partial_z P_{\mathbf{k}})|_{z=H-0} &= (2\mu_1 k^2 V_{z\mathbf{k}} + \partial_z P_{\mathbf{k}})|_{z=H+0}.
\end{aligned} \tag{25}$$

The requirement of normal stress continuity on the interface becomes:

$$(-P_{\mathbf{k}} + 2\mu \partial_z V_{z\mathbf{k}})|_{z=H-0} = (-P_{\mathbf{k}} + 2\mu_1 \partial_z V_{z\mathbf{k}})|_{z=H+0}. \tag{26}$$

The equations of the evolution of the free boundary and the interface (20) involve only the  $V_{z\mathbf{k}}$  term. To obtain it in the layer and half-space domains, we write out the equations and boundary conditions using (17), (21), (23), (25) and (26):

$$\partial_{zz}^2 V_{z\mathbf{k}} - k^2 V_{z\mathbf{k}} = \frac{1}{\mu} \partial_z P_{\mathbf{k}} \quad \partial_{zz}^2 P_{\mathbf{k}} - k^2 P_{\mathbf{k}} = 0 \quad 0 < z < H, \tag{27}$$

$$\partial_{zz}^2 V_{z\mathbf{k}} - k^2 V_{z\mathbf{k}} = \frac{1}{\mu_1} \partial_z P_{\mathbf{k}} \quad \partial_{zz}^2 P_{\mathbf{k}} - k^2 P_{\mathbf{k}} = 0 \quad z > H, \tag{28}$$

$$V_{z\mathbf{k}}|_{z=0} = V_{z_0\mathbf{k}}, \quad (2\mu ik^2 V_{z\mathbf{k}} + \partial_z P_{\mathbf{k}})|_{z=0} = 0, \tag{29}$$

$$V_{z\mathbf{k}}|_{z=H-0} = V_{z\mathbf{k}}|_{z=H+0}, \quad \partial_z V_{z\mathbf{k}}|_{z=H-0} = \partial_z V_{z\mathbf{k}}|_{z=H+0}, \tag{30}$$

$$(-P_{\mathbf{k}} + 2\mu \partial_z V_{z\mathbf{k}})|_{z=H-0} = (-P_{\mathbf{k}} + 2\mu_1 \partial_z V_{z\mathbf{k}})|_{z=H+0}, \tag{31}$$

$$(2\mu k^2 V_{z\mathbf{k}} + \partial_z P_{\mathbf{k}})|_{z=H-0} = (2\mu_1 k^2 V_{z\mathbf{k}} + \partial_z P_{\mathbf{k}})|_{z=H+0}, \tag{32}$$

$$\left( \begin{array}{c} V_{z\mathbf{k}} \\ P_{\mathbf{k}} \end{array} \right) \Big|_{z \rightarrow \infty} = 0. \tag{33}$$

First, consider the half-space domain  $z > H$ . To simplify the system, we assume  $V_{z\mathbf{k}}$  to be represented in the form:

$$V_{z\mathbf{k}} = \tilde{V}_{z\mathbf{k}} + \frac{z-H}{2\mu_1} P_{\mathbf{k}}. \tag{34}$$

In that case:

$$\partial_{zz}^2 \tilde{V}_{z\mathbf{k}} - k^2 \tilde{V}_{z\mathbf{k}} = 0 \quad \partial_{zz}^2 P_{\mathbf{k}} - k^2 P_{\mathbf{k}} = 0 \quad z > H, \quad (35)$$

$$\tilde{V}_{z\mathbf{k}} = V_{zH\mathbf{k}} e^{-k(z-H)}, \quad P_{\mathbf{k}} = P_{H\mathbf{k}}^+ e^{-k(z-H)},$$

$$V_{z\mathbf{k}} = \left( V_{zH\mathbf{k}} + \frac{z-H}{2\mu_1} P_{H\mathbf{k}}^+ \right) e^{-k(z-H)}. \quad (36)$$

In the layer domain  $0 < z < H$ , we assume the velocity  $V_{z\mathbf{k}}$  is represented as:

$$V_{z\mathbf{k}} = \tilde{V}_{z\mathbf{k}} + \frac{z-H}{2\mu} P_{\mathbf{k}}. \quad (37)$$

Therefore,

$$\partial_{zz}^2 \tilde{V}_{z\mathbf{k}} - k^2 \tilde{V}_{z\mathbf{k}} = 0 \quad \partial_{zz}^2 P_{\mathbf{k}} - k^2 P_{\mathbf{k}} = 0 \quad 0 < z < H. \quad (38)$$

The solution of these equations is:

$$P_{\mathbf{k}} = P_{H\mathbf{k}}^- \frac{\sinh(kz)}{\sinh(kH)} + P_{0\mathbf{k}} \frac{\sinh(k(H-z))}{\sinh(kH)}, \quad (39)$$

$$V_{z\mathbf{k}} = \left( V_{zH\mathbf{k}} + \frac{z-H}{2\mu} P_{H\mathbf{k}}^- \right) \frac{\sinh(kz)}{\sinh(kH)} + \left( V_{z0\mathbf{k}} + \frac{z}{2\mu} P_{H\mathbf{k}}^- \right) \frac{\sinh(k(H-z))}{\sinh(kH)}.$$

Using (36), (39) and the corresponding boundary conditions, the equations connecting  $V_{zH\mathbf{k}}$ ,  $V_{z0\mathbf{k}}$ ,  $P_{0\mathbf{k}}$ ,  $P_{H\mathbf{k}}^-$ ,  $P_{H\mathbf{k}}^+$  may be summarized as:

$$\begin{aligned} (\mu \cosh(kH) + \mu_1 \sinh(kH)) V_{zH\mathbf{k}} - \mu V_{z0\mathbf{k}} &= \frac{H}{2} P_{0\mathbf{k}} \\ 2(\mu - \mu_1) k \sinh(kH) V_{zH\mathbf{k}} + \cosh(kH) P_{H\mathbf{k}}^- + \sinh(kH) P_{H\mathbf{k}}^+ &= P_{0\mathbf{k}} \\ k e^{-kH} V_{zH\mathbf{k}} - k \left( V_{z0\mathbf{k}} + \frac{H}{2\mu} \right) P_{0\mathbf{k}} + \frac{1}{2\mu} \sinh(kH) P_{H\mathbf{k}}^- &= \frac{1}{2\mu_1} \sinh(kH) P_{H\mathbf{k}}^+ \\ 2\mu k \sinh(kH) V_{z0\mathbf{k}} + P_{H\mathbf{k}}^- - \cosh(kH) P_{0\mathbf{k}} &= 0. \end{aligned} \quad (40)$$

This system of equations allows one to find the relation between the  $V_{zH\mathbf{k}}$  and  $V_{z0\mathbf{k}}$ :

$$V_{zH\mathbf{k}} = \gamma V_{z0\mathbf{k}} \quad (41)$$

or

$$h_{\mathbf{k}} = \gamma h_{0\mathbf{k}}. \quad (42)$$

The attenuation coefficient  $\gamma$  is the ratio of the amplitudes of the displacement of the interface to the displacement of the external free boundary:

$$\gamma = \frac{kH(\sinh(kH) + m \cosh(kH)) + \cosh(kH) + m \sinh(kH)}{kH \left( m - \frac{1}{m} \right) + (\cosh(kH) + m \sinh(kH)) \left( \cosh(kH) + \frac{1}{m} \sinh(kH) \right)}, \quad (43)$$

here  $H$  is the layer thickness,  $k$  is the length of the Fourier coordinate vector,  $m = \mu/\mu_1$ ,  $\mu$  is the layer fluid viscosity,  $\mu_1$  is the half-space fluid viscosity. Applying the inverse Fourier transform to (41) and integrating the result over time, the interface deformation can be obtained:

$$h(x, y) = \frac{1}{(2\pi)^2} \iint_{-\infty}^{+\infty} \left[ \gamma \left( \sqrt{k_x^2 + k_y^2} \right) h_{0\mathbf{k}}(k_x, k_y) e^{i(k_x x + k_y y)} \right] dk_x dk_y \quad (44)$$

With a given deformation shape  $h_0$ , one can evaluate the normalized interface deformation amplitude using the explicit expressions:

$$\delta = \frac{1}{(2\pi)^2 A_0} \iint_{-\infty}^{+\infty} \left[ \gamma \left( \sqrt{k_x^2 + k_y^2} \right) \iint_{-\infty}^{+\infty} h_0(x, y) e^{-i(k_x x + k_y y)} dx dy \right] dk_x dk_y$$

in the axisymmetric case, and:

$$\delta = \frac{1}{2\pi A_0} \int_{-\infty}^{+\infty} \left[ \gamma(|k|) \int_{-\infty}^{+\infty} h_0(x) e^{-ikx} dx \right] dk$$

in the planar case.

### 2.3. Subsequent analytical results

Using the approach described above, a number of conclusions correlating the parameters of the free-surface perturbation and interface deformation can be made.

(1) Asserting  $k = 0$  in (41) and applying  $\gamma|_{k=0} = 1$ , one can get:

$$\int V_{zH} d^2x = \int V_{z0} d^2x \quad (45)$$

or

$$\int \partial_t h_0 d^2x = \int \partial_t h d^2x. \quad (46)$$

Integrating (46) over the time and asserting zero initial deformations of the free surface and interface, one can obtain the equality of the interface deformation volume and the free surface deformation volume:

$$\int h_0 d^2x = \int h d^2x = V. \quad (47)$$

(2) Differentiate (42) by  $k_\alpha$  and apply  $k = 0$ . Taking into account:

$$\left. \frac{\partial \gamma}{\partial k_\alpha} \right|_{k=0} = 0, \quad \left. \frac{\partial h_{\mathbf{k}}}{\partial k_\alpha} \right|_{k=0} = -i \int x_\alpha h(\mathbf{x}) d^2x, \quad \left. \frac{\partial h_{0\mathbf{k}}}{\partial k_\alpha} \right|_{k=0} = -i \int x_\alpha h_0(\mathbf{x}) d^2x$$

one can obtain:

$$\int x_\alpha h(\mathbf{x}) d^2x = \int x_\alpha h_0(\mathbf{x}) d^2x$$

or

$$\langle x_\alpha \rangle = \langle x_\alpha \rangle_0, \quad (48)$$

where:

$$\langle x_\alpha \rangle = \frac{1}{V} \int x_\alpha h(\mathbf{x}) d^2x, \quad \langle x_\alpha \rangle_0 = \frac{1}{V} \int x_\alpha h_0(\mathbf{x}) d^2x$$

are the coordinates of the geometrical centers of the interface and free surface respectively.

(3) Differentiate (42) by  $k_\alpha$  and  $k_\beta$  and apply  $k = 0$ . Taking into account

$$\left. \frac{\partial^2 \gamma}{\partial k_\alpha \partial k_\beta} \right|_{k=0} = -H^2 \delta_{\alpha\beta}, \quad \left. \frac{\partial^2 h_{\mathbf{k}}}{\partial k_\alpha \partial k_\beta} \right|_{k=0} = - \int x_\alpha x_\beta h(\mathbf{x}) d^2x,$$

$$\left. \frac{\partial^2 h_{0\mathbf{k}}}{\partial k_\alpha \partial k_\beta} \right|_{k=0} = - \int x_\alpha x_\beta h_0(\mathbf{x}) d^2x$$

one can obtain the following:

$$\int x_\alpha x_\beta h(\mathbf{x}) d^2x = \int x_\alpha x_\beta h_0(\mathbf{x}) d^2x + V H^2 \delta_{\alpha\beta}$$

or

$$\langle x_\alpha x_\beta h \rangle = \langle x_\alpha x_\beta h \rangle_0 + H^2 \delta_{\alpha\beta}, \quad (49)$$

where

$$\langle x_\alpha x_\beta h \rangle = \frac{1}{V} \int x_\alpha x_\beta h(\mathbf{x}) d^2x, \quad \langle x_\alpha x_\beta h \rangle_0 = \int x_\alpha x_\beta h_0(\mathbf{x}) d^2x.$$

Asserting  $\alpha = \beta = 1$  leads to relation of the mean-square width of the deformations on the interface and free surface:

$$\langle x_1^2 \rangle = \langle x_1^2 \rangle_0 + H^2 \quad \langle x_2^2 \rangle = \langle x_2^2 \rangle_0 + H^2 \quad (50)$$

Consider the squared cross sectional dimensions  $R^2 = x_1^2 + x_2^2$ . Using (50) one can get the following expression for the dimensional change of the perturbation:

$$\langle R^2 \rangle = \langle R^2 \rangle_0 + 2H^2. \quad (51)$$

(4) Integrate (42) over the two-dimensional  $\mathbf{k}$ -space:

$$\int h_{\mathbf{k}} d^2k = \int \gamma(k) h_{0\mathbf{k}} d^2k.$$

Taking into account  $\int h_{\mathbf{k}} d^2k = (2\pi)^2 h|_{\mathbf{x}=0}$ , the next relation can be obtained:

$$h|_{\mathbf{x}=0} = \frac{1}{(2\pi)^2} \int \gamma(k) h_{0\mathbf{k}} d^2k. \quad (52)$$

Consider a free space deformation of the small cross sectional dimensions comparing to the layer thickness  $H$ . In this case, the Fourier image of such deformation is localized in a domain of bigger scale than  $H^{-1}$ . On the other hand,  $\gamma(k)$  attenuates rapidly with  $k \gg H^{-1}$ . Therefore, (52) can be represented as:

$$h|_{\mathbf{x}=0} = \frac{1}{(2\pi)^2} \int \gamma(k) [h_{0\mathbf{k}}]_{k=0} d^2k = \frac{V}{(2\pi)^2} \int \gamma(k) d^2k. \quad (53)$$

Since  $k$  and  $H$  enters in  $\gamma(k)$  as product  $kH$ , (53) can be rewritten in the form:

$$h|_{\mathbf{x}=0} = \frac{V}{H^2} \phi(m), \quad (54)$$

where

$$\phi(m) = \frac{1}{(2\pi)^2} \int \gamma\left(\frac{\xi}{H}\right) d^2\xi, \quad m = \frac{\mu}{\mu_1}. \quad (55)$$

(5) Using the expressions  $\gamma|_{k=0} = 1$ ,  $\frac{\partial \gamma}{\partial k_\alpha}|_{k=0} = 0$ ,  $\frac{\partial^2 \gamma}{\partial k_\alpha \partial k_\beta}|_{k=0} = -H^2 \delta_{\alpha\beta}$  obtained above we can expand  $\gamma$  in Taylor series:

$$\gamma = 1 - \frac{1}{2} k^2 H^2 + \dots$$

Equation (42) can be expressed in the form:

$$h_{\mathbf{k}} = \left(1 - \frac{1}{2} k^2 H^2 + \dots\right) h_{0\mathbf{k}}. \quad (56)$$

Applying the inverse Fourier transform to (56) and truncating the series after the second term one can obtain:

$$h(\mathbf{x}) = \left(1 + \frac{1}{2} H^2 \Delta\right) h_0(\mathbf{x}), \quad (57)$$

where  $\Delta = \partial_1^2 + \partial_2^2$  is the Laplace operator by the plane coordinates. Formula (57) is valid when the perturbation width is much larger than the layer thickness  $H$ .

As an example of (57), consider the deformation of the free surface described by  $h_0(\mathbf{x}) = A \exp(-\alpha_1 x_1^2 - \alpha_2 x_2^2)$ ,  $\alpha_1 H^2 \ll 1$ ,  $\alpha_2 H^2 \ll 1$ . In this case, the interface deformation becomes:

$$h(\mathbf{x}) = (1 + H^2[\alpha_1(2\alpha_1 x_1^2 - 1) + \alpha_2(2\alpha_2 x_2^2 - 1)]) A \exp(-\alpha_1 x_1^2 - \alpha_2 x_2^2).$$

It can be shown that the interface deformation amplitude is smaller than the one for the free surface:

$$h|_{\mathbf{x}=0} = [1 - H^2(\alpha_1^2 + \alpha_2^2)] h_0|_{\mathbf{x}=0}.$$

On the other hand, with  $|x_1| > \frac{1}{\sqrt{2\alpha_1}}$  and  $|x_2| > \frac{1}{\sqrt{2\alpha_2}}$ , the interface deformation is larger than the one for the free surface.

### 3. Numerical model

To obtain a numerical solution, COMSOL Multiphysics was used. Two-dimensional planar and axisymmetric models were implemented. These models have only minor differences in their setups. Both use *Laminar Flow* and *Moving Mesh* interfaces.

A domain of layer and half-space is described by two rectangles with different *Fluid Properties*. *Symmetry* boundary conditions on the side faces are set (*Axial Symmetry* and *Symmetry* in axisymmetric case). The slip boundary condition is applied along other boundaries.

The deformation of the bottom boundary is prescribed by an analytical expression which is linear with respect to time (*Prescribed Mesh Displacements* is used). The side faces are free for vertical deformation and locked for horizontal. Displacement of the interface is described by *Prescribed Mesh Velocity*: velocity of the mesh is equal to the local fluid velocity.

Since we model incompressible flow in a small finite domain, we have to keep the volume to satisfy mass conservation. In the case of the two-dimensional problem, it can be said that we have to keep the area of the domain. There are three ways to solve this problem. The first one is to choose deformation function which satisfies the conditions described above. For example, it can be a sinusoidal function. The second option is to add negative deformation far enough from the area of interest. Since the phenomenon under study is local, its effect should be negligible. The third option is to allow the top border deformation, i.e. assume the free boundary condition on the top border. Again, since the perturbation is local, the effect of the free boundary shouldn't be significant.

The parameters of the model are layer thickness, layer/half-space viscosity ratio and the boundary deformation shape. The primary result of the model is the shape of the interface after the deformation.

*Parametric Sweep* was used to compute the model for different layer thicknesses and viscosities. The half-space thickness was kept constant at 15 m. The layer thickness was varied from 0.5 m to 2 m in 0.1 m increments. Viscosity ratios of 0.1, 1 and 10 were considered. The free surface perturbation was described by functions  $h_0(x) = \frac{A_0}{2} \cos\left(\frac{2\pi x}{\lambda_0}\right)$  (only for planar case) and  $h_0(x) = A_0 e^{-\frac{x^2}{\lambda_0^2}}$ .

*Linearity with respect to perturbation amplitude* The analytical model asserts that for small perturbations, the normalized interface deformation doesn't depend on the surface defect amplitude. Numerical computation shows that this is correct, even for quite large amplitudes compared to the layer thickness (fig. 4).

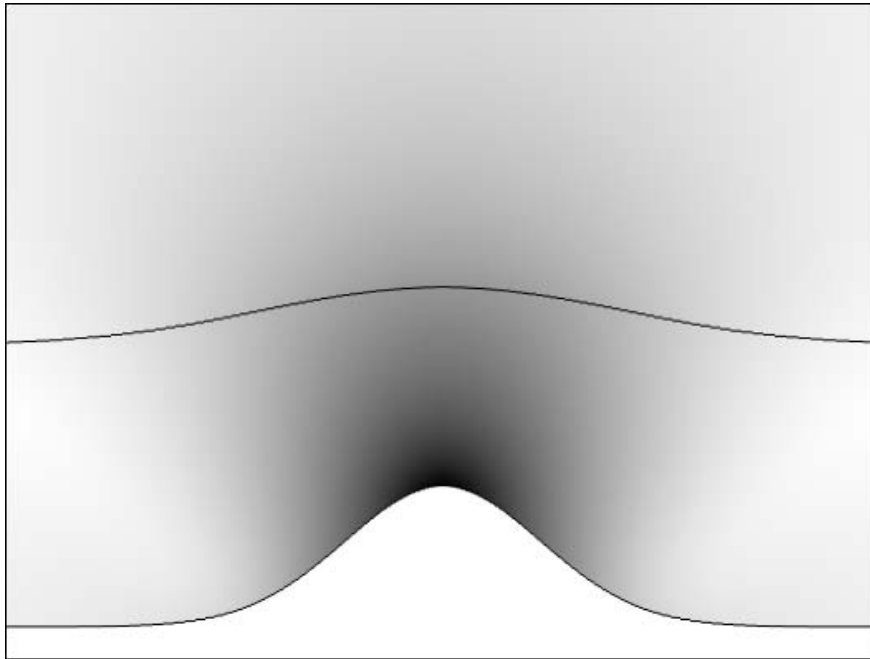


Fig. 3. Velocity magnitude and the deformations of the free surface and the interface

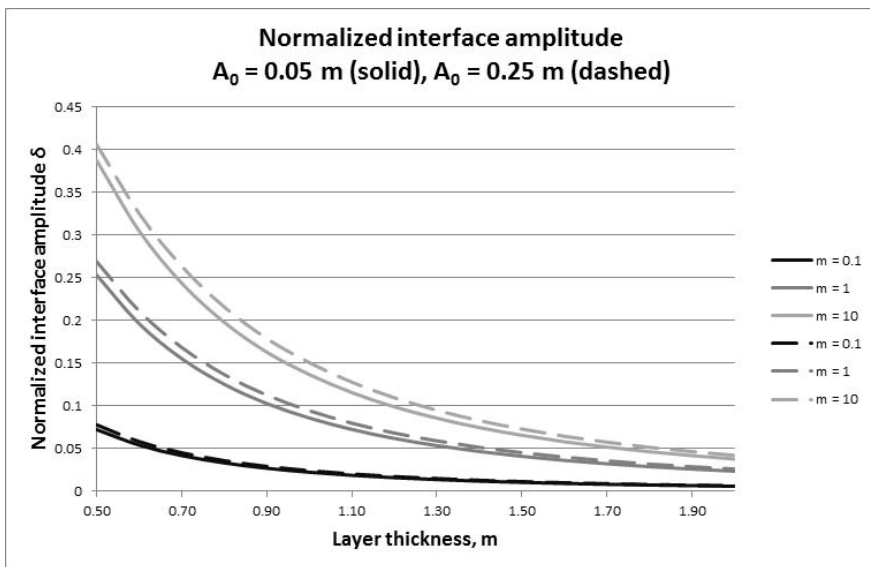


Fig. 4. Normalized interface deformation due to different amplitudes of the free surface perturbation (axisymmetric model)

### 3.1. Result comparison

A number of numerical experiments were made for different parameters of the free surface perturbation, layer thickness and viscosity ratio. As a result, the dependences of the interface perturbation amplitude on the layer thickness was obtained. First, consider planar harmonic free surface perturbation described by  $h_0(x) = \frac{A_0}{2} \cos\left(\frac{2\pi x}{\lambda_0}\right)$ . Since the Fourier transform of this function is:

$$h_0 k = \frac{A_0}{2} \pi [\delta(k - 2\pi/\lambda_0) + \delta(k + 2\pi/\lambda_0)],$$

it's easy to find analytical expression for the interface displacement  $h(x)$ :

$$h(x) = h_0(x)\gamma \left( \frac{2\pi H}{\lambda_0} \right).$$

Comparison with the numerical results gave very good agreement (fig.5). On all figures below, dashed lines correspond to the analytical approach and dots correspond to the numerical solution.

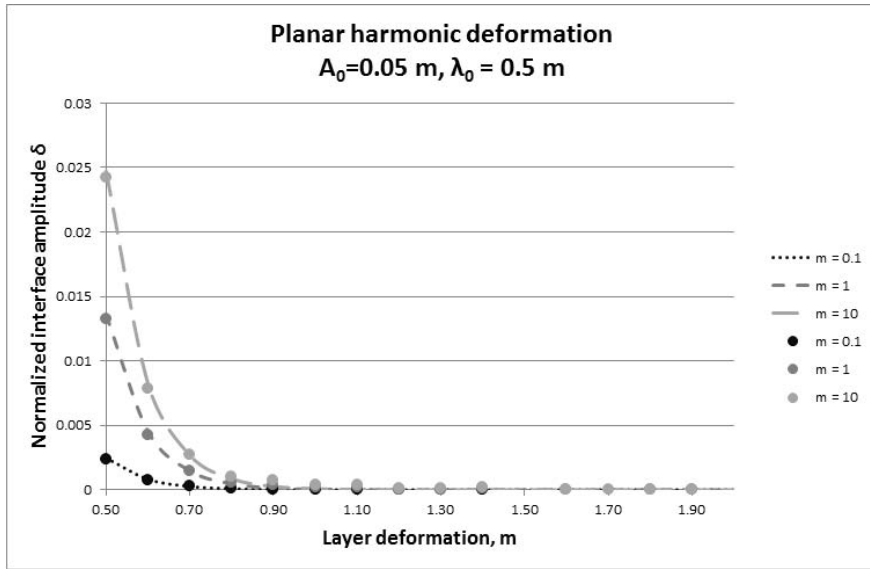


Fig. 5. Interface perturbation due to harmonic deformation of the free surface (planar case)

In the case of Gaussian deformation  $h_0(x) = A_0 e^{-\frac{x^2}{\lambda_0}}$ , the analytical approach remains accurate even for large deformation amplitudes  $A_0$  (figures 6–7).

**4. Conclusion**

Numerical and analytical models were developed to analyze the propagation of the free surface perturbation in the layered viscous half-space. Analytical formulas for perturbation amplitude and width on the interface between the half-space and the layer were obtained. The results may be summarized as follows:

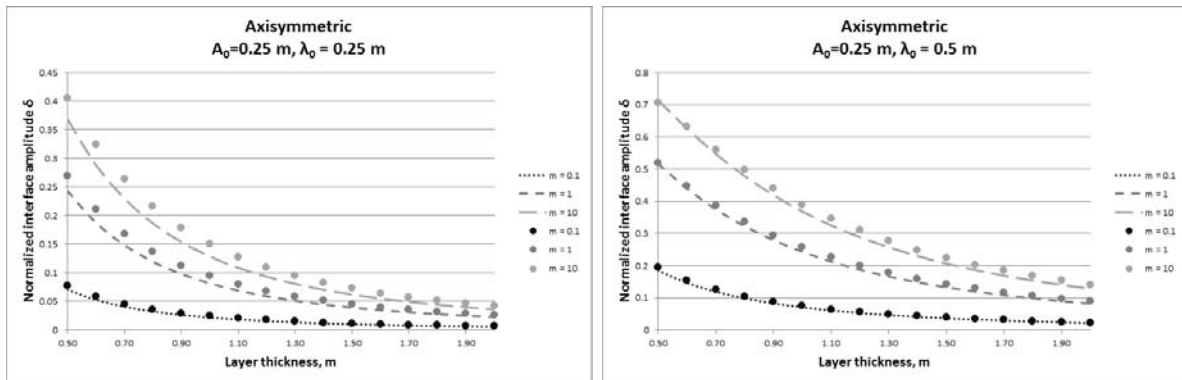


Fig. 6. Interface perturbation due to Gaussian deformation of the free surface (axisymmetric case)

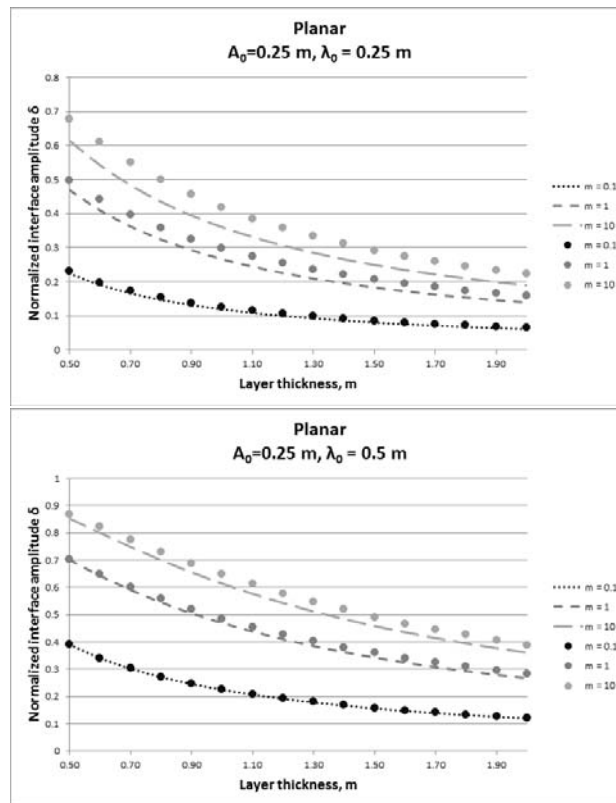


Fig. 7. Interface perturbation due to Gaussian deformation of the free surface (planar case)

- Perturbation of the interface between the layer and the remaining half-space decreases rapidly with the layer thickness increase
- Propagation depends on the ratio of the viscosities: higher viscosity of the half-space fluid helps to reduce perturbation on the interface
- Propagation depth increases with the wavelength of the initial perturbation on the free surface
- For the same wavelength, a smaller amplitude of the the initial perturbation causes a smaller deformation of the interface. Normalized perturbation remains almost the same.

## References

- [1] Happel S. J. and Brenner H. *Low Reynolds Number Hydrodynamics*. Upper Saddle River: Prentice-Hall, 553 p. (1965).
- [2] Chivilikhin S. and Amosov A. Planar Stokes flows with free boundary. In book "Hydrodynamics - Advanced Topics". Book edited by: Dr. Harry Edmar Schulz, Andre Luiz. P. 77–92. Intech (2011).
- [3] Hopper R. W. Stokes flow of a cylinder and half-space driven by capillarity. *J. Fluid. Mech.*, **243**, P. 171–181 (1992).
- [4] De Voeght F. and Joos P. Damping of a disturbance of a liquid surface. *Journal of Colloid and Interface Science*, **98**(1), P. 20–32 (1984).
- [5] Mullins W. W. Flattening of a nearly planar solid surface due to capillarity. *J. Appl. Phys.*, **30**(77), P. 77–83 (1959).
- [6] Lamb H. *Hydrodynamics*. Cambridge University press, Cambridge, 768 p. (1993).
- [7] Levich V. G. *Physicochemical hydrodynamics*. Longman, Harlow, 700 p. (1962).

- [8] Zatsopin A. G., Kostyanoi A. G., and Shapiro G. I. Slow spreading of a viscous liquid over a horizontal surface. *Dokl. Akad. Nauk SSSR*, **265**(1), P. 193–198 (1982).
- [9] Jeong J. T., Moffatt H. K. Free-surface cusps associated with flow at low Reynolds number. *J. Fluid Mech.*, **241**, P. 1–22 (1992).
- [10] Chivilikhin S. A. Relaxation of small perturbations of highviscous liquids planar surface. *Nanosystems: Physics, chemistry, mathematics*, **3**(4), P.54–66 (2012).
- [11] Chivilikhin S. A. Relaxation of a small local perturbation of the surface of a viscous fluid in the Stokes approximation. *Mekhanika Zhidkosti i Gaza*, **3**, P. 133–137 (1985).

# SOME ASPECTS OF FUNCTIONALIZATION AND MODIFICATION OF CARBON NANOMATERIALS

T. P. Dyachkova, A. V. Melezhyk, S. Yu. Gorsky, I. V. Anosova, A. G. Tkachev

Tambov State Technical University, Tambov, Russia

nanotam@yandex.ru

**PACS 61.48.De, 72.80.Tm**

Some regularities of covalent functionalization of multi-walled carbon nanotubes (MWCNTs) with oxygen-containing moieties were investigated. The materials obtained were studied by electron microscopy, thermogravimetry, FT-IR and Raman spectroscopy. The dependence of the degree of MWCNTs functionalization on the process conditions was studied. The advantages of the gas phase to liquid phase oxidation of MWCNTs were shown. The effects of pristine and functionalized MWCNTs on the properties of composites with polysulfone were investigated. Both pristine and functionalized MWCNTs were modified with polyaniline. The effects of the method and the degree of pre-functionalization of the MWCNTs on the oxidative polymerization of aniline and the properties of the materials obtained were elucidated.

**Keywords:** multiwalled carbon nanotubes, functionalization, modification, oxidation, composites, polyaniline.

## 1. Introduction

Carbon nanotubes (CNTs), due to their unique properties, are finding increasing application in various branches of engineering and technology. They are suggested for use as components of polymer composites [1], electrode materials [2], sorbents [3], modifying additives in building materials [4], etc. However, the surface of carbon nanotubes is originally inert and solvophobic, thus favoring their agglomeration in various matrices and preventing their uniform dispersion. As a result, the practical effect of the application of CNTs, especially in composites, is lower than expected. A possible solution to this problem is to modify the surface of carbon nanotubes by covalent or non-covalent functionalization. Numerous methods for attaching different functional groups to the surface of CNTs have been described and the best effect of the use of composites with functionalized carbon nanomaterials was proved [5].

Thus, the presence of amine [6] and carboxyl [7] functional groups on the surface of CNTs facilitates their embedding into a polysulfone matrix [8]. Often, to achieve the best effect, pre-oxidized CNTs were subjected to a secondary functionalization. For example, the oxidized CNTs were reacted with 5-isocyanato-isophthaloylchloride in order to attach different groups ( $-\text{OOC}-$ ,  $-\text{CONH}-$ , etc.) [9]. With use of these CNTs, a composite microporous material with polysulfone matrix was obtained which was suitable for the production of ultrafiltration membranes. The treatment of carboxylated nanotubes with octadecylamine was shown to improve the thermal stability, strength and sorption properties of the CNTs/polysulfone composite membranes [8]. According to some literature data, preliminary attachment of  $-\text{COOH}$  groups to CNTs promotes the oxidative polymerization of aniline on the CNTs surface. This fact can be explained by the chemisorption of aniline monomer and soluble oligomers by carboxyl groups on the surface of CNTs. The interaction of aniline with oxidized nanotubes was thought to occur not only due to  $\pi$ -electron interaction of CNTs with aniline molecules, but also because of emergence of hydrogen bonds between the  $-\text{NH}_2-$  and  $-\text{COOH}$  groups [10, 11]. The works

TABLE 1. General characteristics of CNTs used in this work

Parameter\CNTs	“Taunit”	“Taunit-M”	“Taunit-MD”
External diameter, nm	20÷70	30÷80	8÷15
Internal diameter, nm	5÷10	10÷20	4÷8
Length, $\mu m$	2 and more	20 and more	2 and more
Contents of mineral impurities, wt. % (after acid purification)	$\leq 5$ ( $\leq 1$ )	$\leq 5$ ( $\leq 1$ )	$\leq 5$ ( $\leq 1$ )
Bulk density, $g/cm^3$	0,4÷0,6	0,03÷0,05	0,03÷0,05
Specific surface area, $m^2/g$	120÷130	180÷200	300÷320

cited above did not analyze the influence of the method used and the degree of functionalization of the CNTs.

Most methods of CNTs functionalization described in literature are very expensive and can be performed only at a laboratory scale because they require the use of large amounts of expensive reagents. The growing application of carbon nanomaterials to different technologies necessitates the development of methods for obtaining functionalized carbon nanomaterials in large quantities at acceptable costs. In this regard, it is necessary to study the standard conditions for CNTs functionalization processes and the effect of reaction conditions on the properties of the resulting materials with a view to further increasing the scale of synthesis.

## 2. Materials and methods

“Taunit”, “Taunit-M” and “Taunit-MD” CNTs produced by “NanotechCenter” (Tambov, Russia) were used in this work. Their geometric parameters and some physical properties are shown in Table 1, while SEM images are shown in Fig. 1.

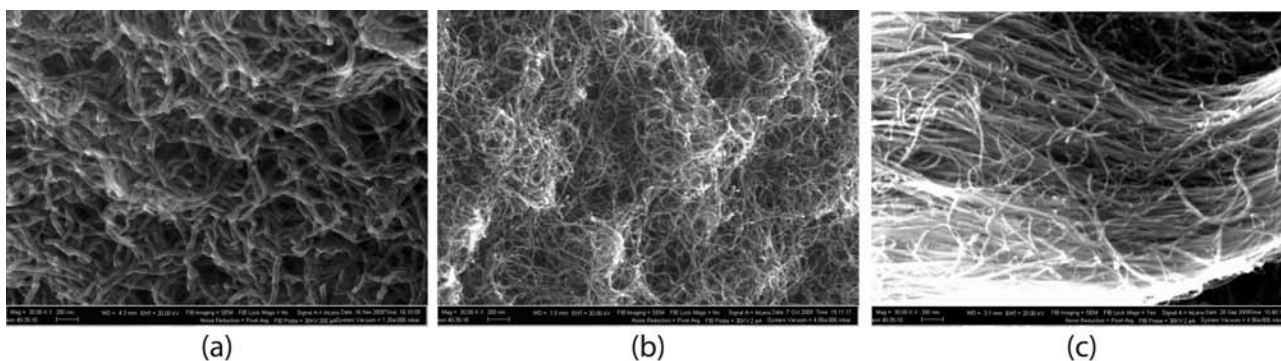


FIG. 1. SEM images of CNTs used: a – “Taunit”, b – “Taunit-M”, c – “Taunit-MD”

The functionalization of CNTs surfaces with oxygen-containing groups was carried out by several methods: 1) by treatment with concentrated nitric acid, 2) oxidation by potassium permanganate in acidic medium, 3) oxidation by nitric acid vapor.

Surface functional groups were identified by IR spectroscopy. The amount of COOH groups (mmol) per unit weight of CNTs was determined titrimetrically according to known methods [12].

In order to obtain Raman spectra, the CNTs samples were placed on a Raman amorphous polycrystalline  $Al_2O_3$  substrate, and Raman spectra were recorded with use of an Integra Spectra spectrometer, NT MDT (wavelength of laser excitation 473 nm). SEM images of carbon

nanotubes and their composites with polyaniline were obtained using a two beam scanning electron microscopic complex Neon 40, Carl Zeiss.

Modification of carbon nanotubes with polyaniline was performed during oxidative polymerization of aniline under the action of ammonium persulfate  $(\text{NH}_4)_2\text{S}_2\text{O}_8$  in an acidic solution in the presence of CNTs. The weight content (%) of polyaniline in the nanocomposites obtained was calculated as the difference between the mass of dry composite and the starting CNTs, referred to as the weight of the nanocomposite.

TG and DTG plots of the samples were recorded by a simultaneous thermal analysis device STA 449 F3 Jupiter (Netzsch). During measurement, the sample chamber was purged with air at a rate of 30 ml/min, the thermobalance chamber – with inert gas (argon) at a rate of 10 ml/min. The temperature program included holding at 30 °C for 10 minutes, heating from 30 to 900 °C at a rate of 10 °C/min and cooling the samples to room temperature at a rate of 15 °C/min.

To determine the electrical resistivity samples of the materials were placed in a glass tube and compressed using two metal pistons at a pressure of 10 MPa. The measured electrical resistance of materials was recalculated to the specific resistivity ( $\rho$ , Ohm-cm). The relative error of measurement did not exceed 10%.

Capacitance of the obtained materials was determined by using a three-electrode cell in which a sample of the polyaniline-modified CNTs (0.05 g) was deposited on glassy carbon disk which served as the working electrode. The auxiliary electrode was made from an expanded graphite foil. Saturated silver chloride electrode was used as a reference electrode. Measurements were performed in a galvanostatic mode at a current of 2–10 mA, the potential swept from -0.5 to 0.5, and from -0.3 to 0.3 V. An aqueous solution of 0.5 M  $\text{Na}_2\text{SO}_4$  was used as electrolyte.

Polysulfone Ultrason 6020 (“BASF”) in the form of films with thickness of 20 and 150 microns was used as the polymer matrix. The volume resistivity of this dielectric is  $> 1.0 \cdot 10^{16}$  Ohm-cm. Composite films were obtained from the dispersion of CNTs in a 20% solution of polysulfone in dimethylacetamide (DMA), which was then subjected to ultrasonic treatment in an IL-10 (2 kW, 22 KHz, 20 min). The film thickness was determined by a “Constant K5” device for measurement of geometrical parameters, and electrical resistance – by a teraohmmeter “E6-13A.” The concentration of carbon nanotubes in the polymer was 2 wt.%.

Images of the composite films were obtained by using metallographic inverted microscope Axiovert 40 MAT (Carl Zeiss) in reflected light using the contrast method by bright field.

### **3. Results and discussion**

#### **3.1. The study of CNTs oxidation processes**

Treatment of CNTs with potassium permanganate, according to the literature, gives rise to oxygen-containing functional groups (hydroxyl, carboxyl) on the CNT surface [13–16]. These oxidation processes proceed quickly. A typical IR spectrum of “Taunit-M” CNTs oxidized with potassium permanganate is characterized by the presence of a number of absorption bands. Peaks at 2928 and 2852  $\text{cm}^{-1}$  are caused by asymmetric and symmetric C–H vibrations of alkyl group [17] which are a residue of hydrocarbon molecules used for growing the CNTs in the CVD process. The band at 3423  $\text{cm}^{-1}$  can be attributed to vibrations of O–H bonds in hydroxyl and carboxyl groups formed upon the oxidation of the nanotubes. According to [18], the absorption peaks at 1562 and 1637  $\text{cm}^{-1}$  can be attributed to  $>\text{C}=\text{O}$  groups. Therefore, IR

spectra prove the presence of oxygen-containing functional groups on the surface of “Taunit M” CNTs treated with potassium permanganate in acidic medium.

IR-spectra of the initial CNTs and those oxidized with nitric acid in liquid and gas phase (Fig. 2) are characterized by the presence of absorption bands corresponding to C–H ( $2920$ ,  $2850$ , and  $1460\text{ cm}^{-1}$ ),  $>\text{C}=\text{C}<$  ( $1630\text{ cm}^{-1}$ ), and O–H ( $3450\text{ cm}^{-1}$ ) bonds. The absorption band corresponding to the C=O bond vibration in the carboxyl ( $1740\text{ cm}^{-1}$ ) in the IR spectrum of the boiling nitric acid-oxidized CNTs, has a very low intensity. This peak was more pronounced for the material oxidized with nitric acid vapor. Thus, the IR-spectroscopy data indirectly indicated that treatment of the CNTs with nitric acid vapor resulted in much more deep oxidation and thus, the appearance more carboxyl groups than obtained with boiling in concentrated nitric acid.

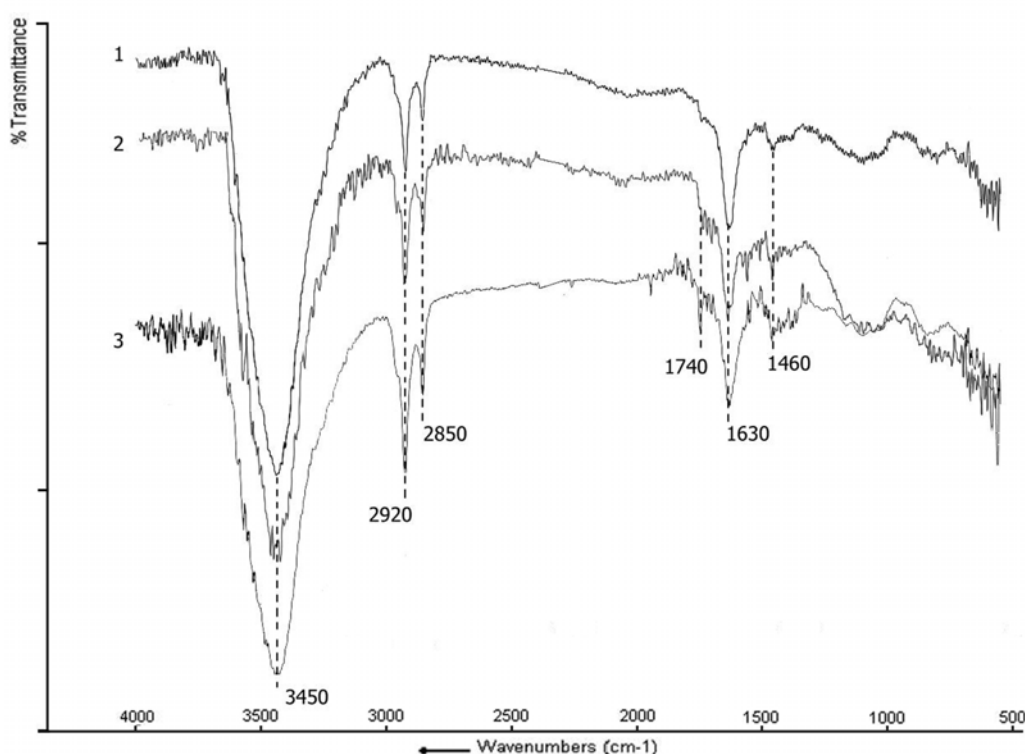


FIG. 2. IR-spectra: 1 – initial CNTs “Taunit-MD”; 2 – the CNTs oxidized by boiling in concentrated nitric acid; 3 – the CNTs oxidized in vapor of nitric acid

According to the TG data obtained, the initial “Taunit M” CNTs are stable to thermal oxidation in air up to  $440\text{ }^{\circ}\text{C}$ . At  $495\text{ }^{\circ}\text{C}$ , a 10% loss of the sample mass occurs, and the most intensive thermal oxidation of the material occurs at temperatures above  $515\text{ }^{\circ}\text{C}$  (plot 1 in Fig. 3). The character of TG and DSC curves for CNTs samples oxidized with potassium permanganate at a rate of 0.2 and 1.0 g  $\text{KMnO}_4$  per 1 g of CNTs does not differ from the analogous plots for non-functionalized material. However, increasing the mass ratio of  $(\text{KMnO}_4)/(\text{CNTs})$  leads to an increase in the degree of functionalization, however, the thermal stability of the material, as well as the heat effect of the thermal oxidation, decreases (plots 2 and 3 in Fig. 3). Loss of sample mass for oxidized CNTs begins at a temperature of  $150\text{ }^{\circ}\text{C}$ . According to [19], in similar TG conditions, loss of surface functional groups on CNTs occurs at temperatures up to  $400\text{ }^{\circ}\text{C}$ , and at higher temperatures, the thermal oxidation of CNTs themselves proceeds. Thus, the low temperature mass loss of CNTs treated with potassium permanganate proves the presence of

functional groups on their surface and accordingly, the degree of functionalization was increased with a higher  $(\text{KMnO}_4)/(\text{CNTs})$  mass ratio.

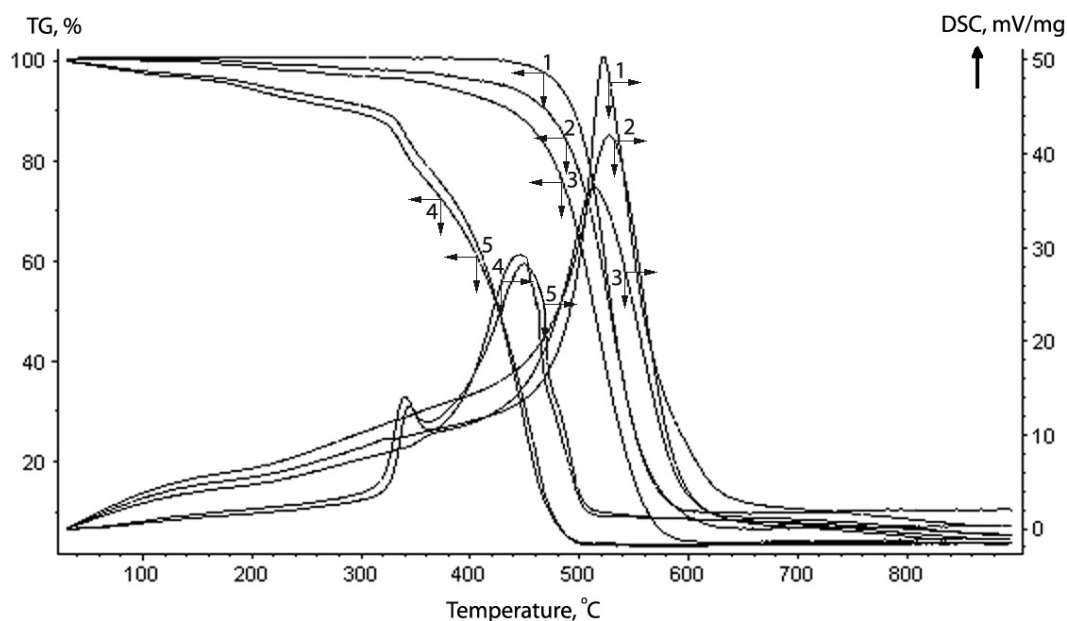


FIG. 3. TG and DSC plots (in air) for original (1) and oxidized with potassium permanganate CNTs “Taunit-M” at the mass ratio  $(\text{KMnO}_4)/(\text{CNTs})$  equal to 0.2 (2), 1.0 (3), 3.0 (4), and 4.0 (5)

TG and DSC plots for material obtained after treatment with  $\text{KMnO}_4$ , at levels equal to 3 and 4 g per 1 g of CNTs have different character (plots 4 and 5 in Fig. 3). At least 3 sections of marked weight reduction were observed on the TG curve. The first, in the temperature range near 150 °C, is associated with removal of adsorbed water. Obviously, these materials have increased hydrophilicity, and thus, require longer drying times. The second section, from 150 to 320 °C, according to the literature [20] corresponds to the decarboxylation of functionalized CNTs. The weight loss of materials in the temperature range from 320 to 400 °C can be explained by the cleavage of hydroxyl groups [21]. DSC plots of these materials have two distinct maxima corresponding to the cleavage of carboxyl functional groups and the carbon thermal oxidation.

Carbon nanotubes oxidized with liquid or gas phase nitric acid have different thermal stabilities (Fig. 4). The original CNTs are most resistant to high temperatures in an oxidizing atmosphere, while those treated with nitric acid vapor are the least stable. The nature of TG plots for functionalized materials is significantly different from the TG plot for starting CNTs. The peaks in the DSC plots for the original and concentrated nitric acid-oxidized “Taunita-MD” CNTs were observed at 615–620 °C. On a similar plot for the “Taunita-MD” CNTs treated with  $\text{HNO}_3$  vapor, there is an ill-defined extremum at 350 °C and a more pronounced one at 520 °C. Each of these corresponds to characteristic areas on the TG plot.

According to titrimetric data, increasing the potassium permanganate amount taken for CNTs oxidation results in a smooth increase in the degree of functionalization for “Taunita-M” CNTs with carboxyl groups ( $D_f$ ) (Fig. 5). Based on the data obtained, it is possible to synthesize carboxylated CNTs with a given degree of functionalization by varying amount of oxidant used. The advantage of this CNTs functionalization method over the more frequently used acidic treatment is the shortness of reaction times. The  $\text{KMnO}_4$ -mediated oxidation of CNTs at 50–60°C is typically complete in 20–30 minutes, whereas in refluxing concentrated

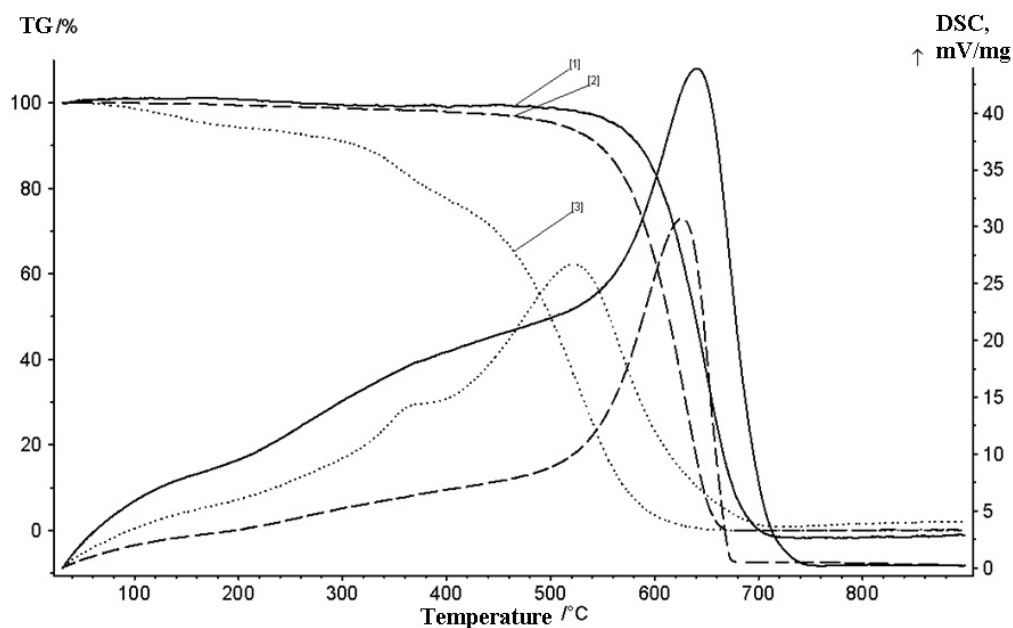


FIG. 4. TGA and DSC plots: 1 – original CNTs “Taunit-MD”; 2 – CNTs “Taunit-MD” oxidized by refluxing in concentrated nitric acid; 3 – CNTs “Taunit-MD” oxidized in  $\text{HNO}_3$  vapor

nitric acid, to achieve a CNTs functionalization of 0.6 mmol/g requires about 10 h. At smaller loadings of potassium permanganate per unit mass of CNTs (up to 1.2 g/g) about 20–30% of the oxidizer is spent for useful oxidation of the CNTs surface. At higher loadings of potassium permanganate (2 g per 1 g of CNTs and more), more than 95% of the  $\text{KMnO}_4$  was consumed in unwanted side reactions (oxidation of CNTs to  $\text{CO}_2$ , decomposition of  $\text{KMnO}_4$ ). Therefore, the use of  $\text{KMnO}_4$  for CNTs oxidation is justified only for the preparation of materials with a low degree of COOH functionalization.

The amount of COOH groups on the surfaces of “Taunit”, “Taunit-M” and “Taunit-MD” CNTs oxidized in the gas phase, is higher compared to those performed with boiling nitric acid at the same duration (Fig. 6). With an increase in the treatment time, the difference in the degree of CNTs carboxylation between the liquid- and gas-phase processes becomes even more pronounced.

With extended treatment of “Taunit” and “Taunit-MD” CNTs in refluxing nitric acid, the degree of carboxyl group functionalization tends to approach some limiting value. The average external diameters of the “Taunit-MD” and “Taunit” CNTs are similar, but these nanomaterials differ in the structure of their graphene layers. “Taunit-MD” consists of cylindrical carbon nanotubes whose graphene layers are highly ordered. At the same time, surface defects, consisting of protruding carbon atoms in the  $\text{sp}^3$ -hybridization state, are the most reactive sites for functionalization. Therefore, from the materials in question “Taunit-MD” CNTs have the lowest degree of carboxylation upon treatment with oxidizing agents. The concentration of COOH groups on the surface of oxidized “Taunit” CNTs is higher because its graphene layers have a conical shape. The carbon atoms in the  $\text{sp}^3$ -hybridization state, which are located at the edges of the conical graphene layers, are much more susceptible to oxidation than the  $\text{sp}^2$ -hybridized carbon atoms on the surface of the cylindrical nanotubes.

The degree of functionalization for “Taunit-M”, is somewhat higher than that of “Taunit” and “Taunit-MD” at the same duration of treatment. “Taunit-M” consists of cylindrical

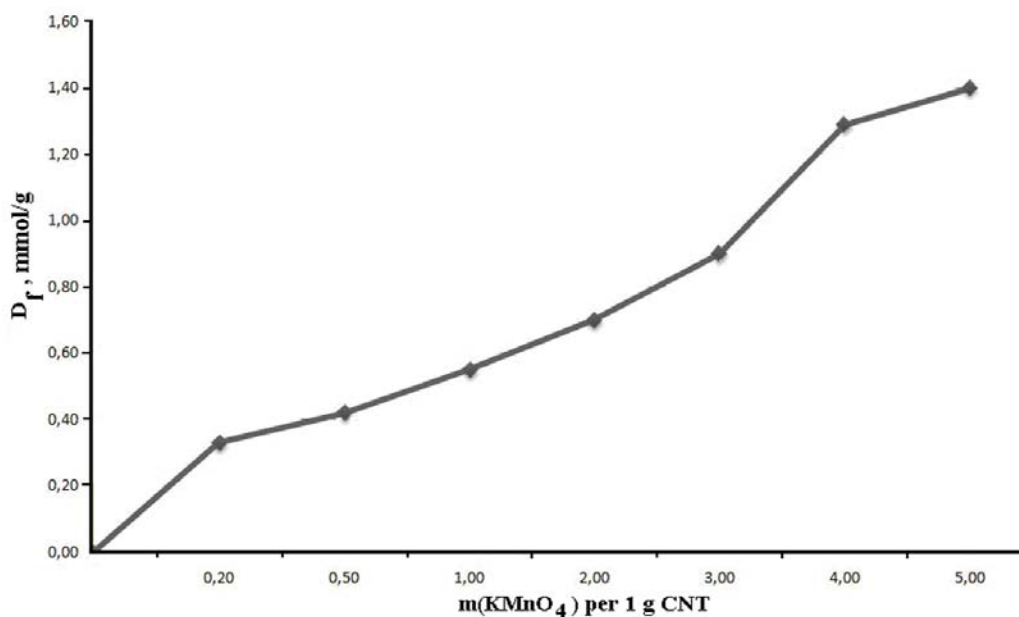


FIG. 5. The influence of  $\text{KMnO}_4$  charge (per 1 g of CNTs) on the degree of functionalization ( $D_f$ ) of CNTs “Taunit-M” with carboxyl groups

nanotubes like “Taunit-MD”, but the diameter of “Taunit-M” is several times less, and thus, its specific surface area is higher. At the same ratio of carboxyl groups to the total carbon atoms of the outer layer of the CNTs, the degree of functionalization of “Taunit M” CNTs, expressed in mmol per 1 g of the material is higher compared to “Taunit-MD” CNTs, because the latter has a greater number of carbon atom layers. Oxidation predominantly affects the outer layer, while the inner layers remain intact. After saturation of the outer carbon layer with carboxyl groups, its destruction begins, whereupon the oxidation and degradation of the following subsurface layers occurs. A higher degree of carboxylation of “Taunit M” in comparison with “Taunit” is explained as a result of its smaller number of carbon atom layers and higher specific surface area.

“Taunit-M” CNTs also shows changes in the character and degree of functionalization with increased reaction time in boiling nitric acid. During the first five hours, a dramatic increase in the concentration of carboxyl groups occurs. In the next five hours, the degree of carboxylation increases insignificantly, but, after having reached a certain value, begins to increase over the next 10 hours, showing no tendency to reach a limiting value. Perhaps this is due to the fact that the original “Taunit-M” CNTs are more defective and have a smaller diameter than “Taunit-MD” CNTs. Then, the combustion of surface layers leads to a considerable reduction in the CNTs diameter, and the fraction of surface atoms increases, as well as the maximum concentration of functional groups.

In gas-phase oxidation process “Taunit-M” CNTs showed the greatest degree of functionalization at equal treatment times. The concentration of surface groups for this material grows with treatment time and does not show any limit. Obviously, again, the rapid oxidation of the surface layer occurs, and then it begins to decay and the underlying layers become available for oxidation. The destruction of the “Taunit-M” CNTs under nitric acid vapor oxidation is proved by the decrease in the mass of material for long reaction times. Consequently, in the case of “Taunit-M” CNTs, only the short-term processing in nitric acid vapor is acceptable, which, nevertheless, still allows a high degree of functionalization.

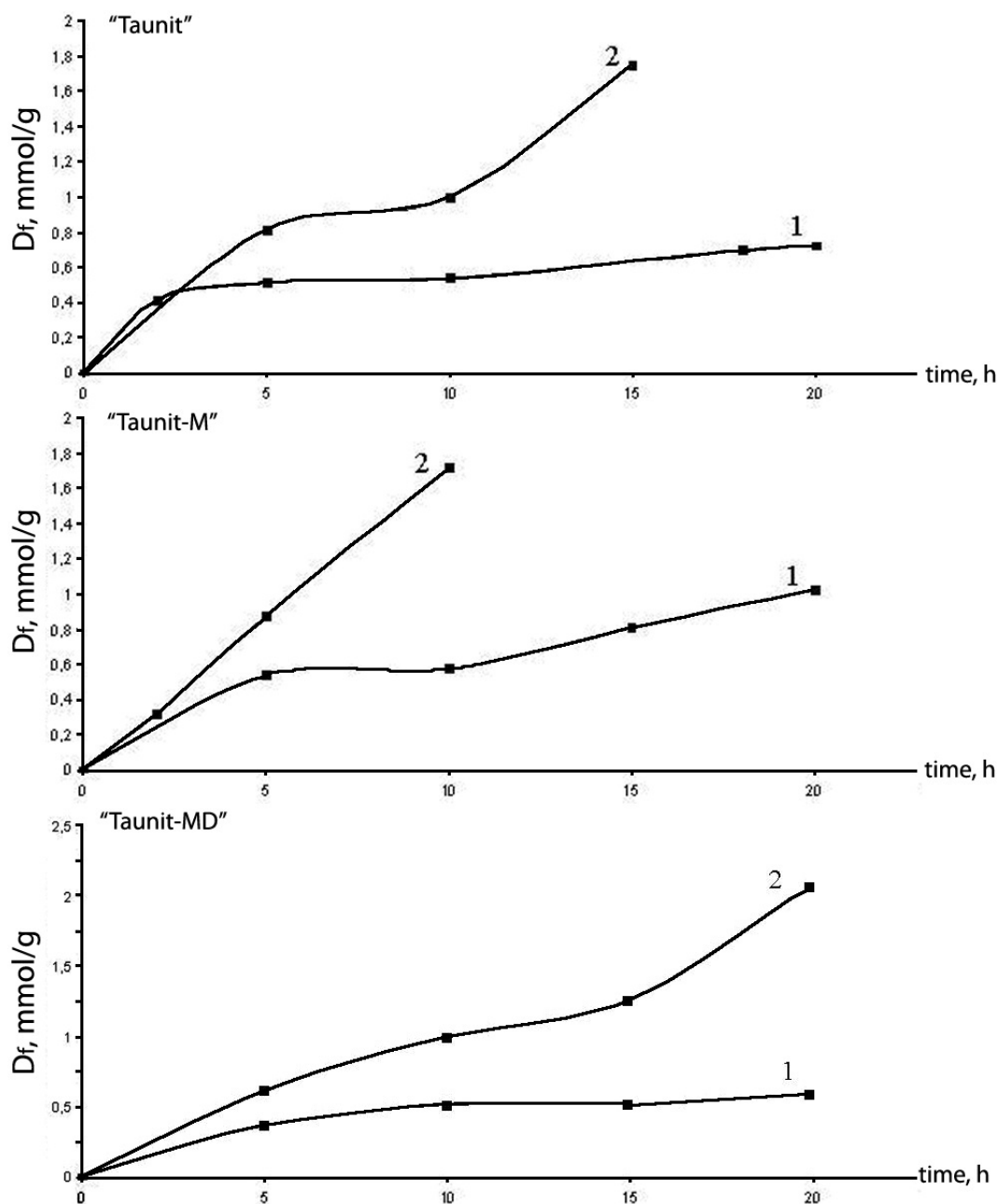


FIG. 6. Changes of the degree of functionalization ( $D_f$ ) of CNTs "Taunit-MD", "Taunit-M", and "Taunit" with carboxyl groups in time during liquid phase (1) and gas phase (2) oxidation with nitric acid

The degree of carboxylation of "Taunit-MD" when using  $\text{HNO}_3$  vapor progresses more slowly with treatment time. Three areas can easily be distinguished in the corresponding plot: rapid increase of the surface group concentration (up to 10 hours), deceleration of the process (10–15 hours), and subsequent renewal of reaction (after 15 hours). Similar sequences were observed for the nitric acid vapor-oxidation of "Taunit" CNTs: rapid carboxylation was observed up to 5 hours, at 5 to 10 hours—a slowing down of the process, and after 10 hours - again a sharp rise in the oxidation. The characteristics shown by the "Taunit" and "Taunit-MD" plots probably appear due to the greater resistance of the CNTs surface layers to destruction. The stunting in the time dependence of the degree of functionalization is most likely caused by

saturation of the surface layer with functional groups, and the subsequent increase in reaction is due to its destruction. As follows from the data obtained, among the CNTs studied, the surface of “Taunit-MD” is the most resistant to gas-phase oxidative degradation.

We can suggest several reasons for higher efficiency of gas-phase oxidation of CNTs compared to liquid-phase. First, in the liquid phase process, the attachment of carboxyl groups occurs only at the points of initial defects on the CNTs surface. It is also likely that a higher degree of functionalization in the gas phase can be achieved due to the higher temperature, because the liquid-phase  $\text{HNO}_3$  oxidation of CNTs proceeds at 90–110 °C, while the gas-phase oxidation occurs at 140 °C. Finally, it is impossible to completely remove catalyst residues, particularly transition metals, from CNTs obtained by the CVD technique. When boiling in liquid nitric acid, transition metals are transformed into soluble nitrates, which are in solution in low concentration. However, in the gas phase process, the transition metals or their compounds remain on the surface or inside of the nanotubes. In the nitric acid vapor method, metals and metal oxides can be converted into nitrates, which at the process temperatures immediately decompose to form non-volatile metal oxides or basic nitrates. It is even possible to establish a dynamic equilibrium “transition metal nitrate  $\rightleftharpoons$  basic nitrate  $\rightleftharpoons$  metal oxide“. Due to these processes, the transition metal compounds can migrate to the surface of the nanotubes. At the same time, it is known that transition metal compounds can catalyze oxidation reactions. Consequently, due to the presence of the transition metal compounds in the surface layer, and the migration of these compounds to the surface of CNTs, the attachment of carboxyl groups can occur not only in the points of initial defects of carbon layers.

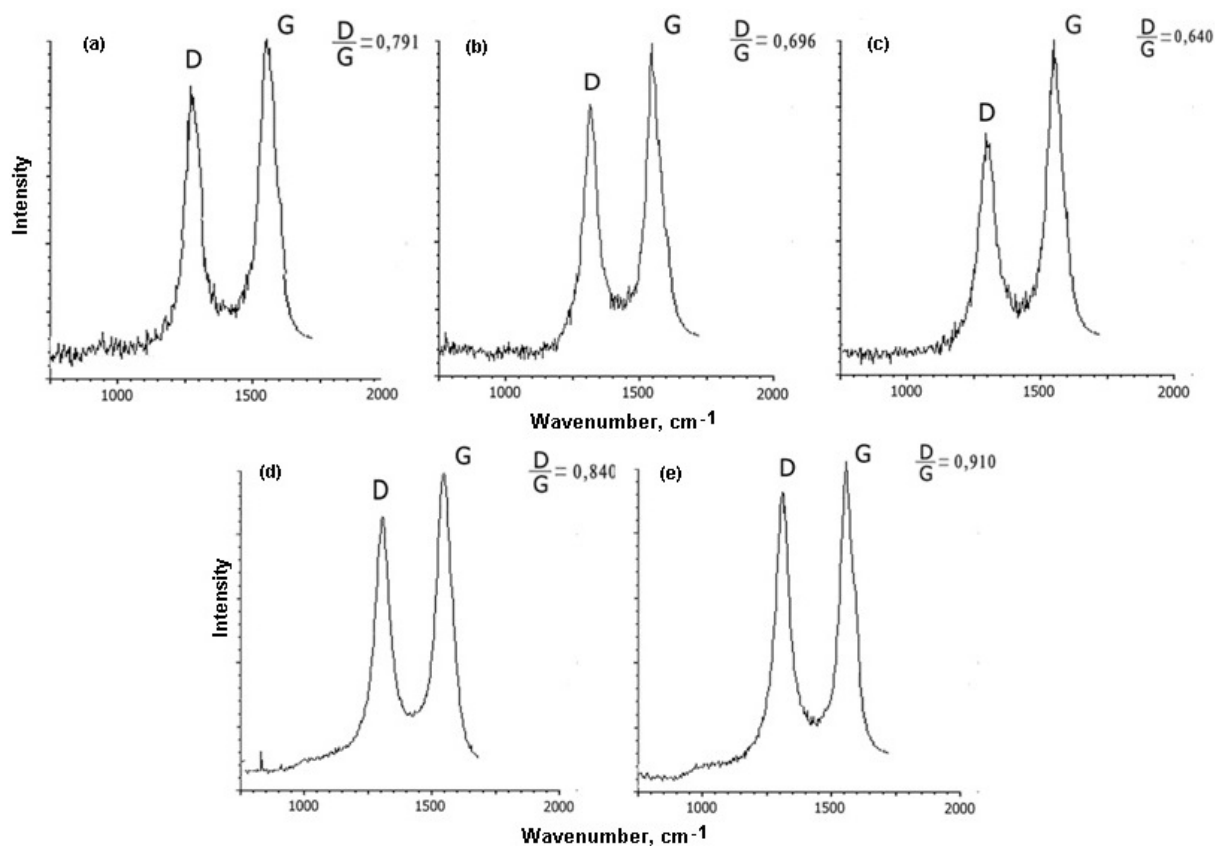


FIG. 7. Raman spectra of initial (a) and oxidized by potassium permanganate CNTs “Taunit-M” at the mass ratio  $(\text{KMnO}_4)/(\text{CNTs})$  equal to 0.2 (b), 1.0 (c), 3.0 (d), and 4.0 (e)

TABLE 2. Estimation of the structure defects of carbon nanotubes according to Raman spectra

Substance	Initial “Taunit-M”	“Taunit-M” after boiling in HNO <sub>3</sub>	“Taunit-M” after gas-phase functionalization	Initial “Taunit-MD”	“Taunit-MD” after boiling in HNO <sub>3</sub>	“Taunit-MD” after gas-phase functionalization
D/G ratio	0.791	0.899	0.732-0.771	0.451	0.670	0.595-0.750

For the structural characteristics of the original and functionalized CNTs, Raman spectroscopy [22] can be applied, in which there are two characteristic modes: G (1500–1600 cm<sup>-1</sup>), due to the in-plane vibrations of carbon atoms in the graphene layer, and D (1250–1450 cm<sup>-1</sup>), caused by the disturbance of the symmetry of an ideal graphene layer. Therefore, the ratio of D/G intensities can be used to characterize the degree of order in the surface structure of a multi-walled CNTs. The oxidative treatment of CNTs influences the value of the D/G ratio in two opposing ways. First, there is the removal of low ordered carbon structures, which should reduce the degree of disorder as determined by Raman spectra [23]. Conversely, intensive oxidation of the CNTs surfaces generates new defects that act as functional groups, and this increases D/G ratio [24]. According to the data obtained (Fig. 4), potassium permanganate oxidation initially leads to a decrease, and then an increase in the D/G index. This demonstrates the predominant influence of the first factor at low loading of the oxidant per unit mass of CNTs (up to 1 g/g). In this case, the number of defects which arise due to the appearance of oxygen-containing groups on the surface is compensated for by the removal of amorphous carbon. When the loading of potassium permanganate and degree of COOH functionalization are higher, the second of the mentioned factors begins to predominate.

Comparison of the structural defects of initial, liquid- and vapor-phase nitric acid-functionalized CNTs according to Raman spectra shows that in the case of “Taunit-M” CNTs, boiling in nitric acid substantially destroys the structure of the surface layers (Table 2). When carrying out the oxidation process in gas phase by various oxidizing agents, the D/G ratio is reduced, which may indicate the removal of amorphous carbon in this case. Functionalization of “Taunit-MD” CNTs with carboxyl groups promotes the emergence of additional defects on the surface of the nanotubes, however, in some cases, gas phase reactions can be milder.

Thus, oxidation of the “Taunit-M” and “Taunit-MD” materials in nitric acid vapor is more efficient in terms of degree of functionalization. At the optimum duration of the gas-phase oxidation process, the structure of graphene layers of nanotubes is also preserved much better compared to boiling in HNO<sub>3</sub>. Additionally, consumption of the oxidizing agent per unit weight of the product is reduced, which lessens the required neutralization of acidic by-products. Based on these studies, it can be concluded that the gas-phase technology is suitable for scaling to pilot plant scale and thus, industrial production of functionalized CNTs.

It should also be noted that a significant part of the individual nanotubes in as-synthesized “Taunit-MD” materials are in the form of parallel-packed nanotube bundles. Treatment of “Taunit-MD” CNTs with oxidizing agent vapors preserves the original arrangement of individual tubes in the bundles, whereas the liquid-phase process results in destruction of the bundles and entanglement of the nanotubes.

Oxygen-containing functional groups are responsible for the electrostatic and chemical interactions of CNTs with polar polymer matrices, which favors the uniform distribution of CNTs in a polymer matrix. However, too high a degree of functionalization causes a large

amount of surface defects in the graphene layers. In this regard, for introduction into polymers, it is necessary to choose oxidized CNTs with an optimal degree of functionalization.

### 3.2. Modification of nanotubes with polyaniline

Considering the promising applications of polyaniline (PANI)/CNTs nanocomposites as electrode materials in electrochemical cells, adsorbents and other areas, we investigated the process of oxidative aniline polymerization in the presence of CNTs. Analysis of the temperature profiles of oxidative aniline polymerization in the presence and in the absence of CNTs indicates the exothermic nature of the processes (Fig. 8). An initial decrease in the temperature plots is caused by the endothermic dissolution of ammonium persulfate in water. This is followed by an induction period, during which the temperature remains almost unchanged. In the presence of CNTs, this period is reduced from 8 to 1–2 minutes. This is followed by a sharp rise in the temperature. In the presence of non-functionalized CNTs the temperature at the maximum point on the temperature plot is almost the same as in the normal synthesis of polyaniline without the addition of CNTs. However, this maximum is reached in a shorter time. Judging by the pictures, the rate of oxidative aniline polymerization on the surface of functionalized and initial CNTs is about the same. However, the presence of  $-\text{COOH}$  groups on the surface of CNTs contributes to some additional processes accompanied by a slight evolution of heat, as evidenced by the higher values of temperature at extrema points on the plots in Fig. 8.

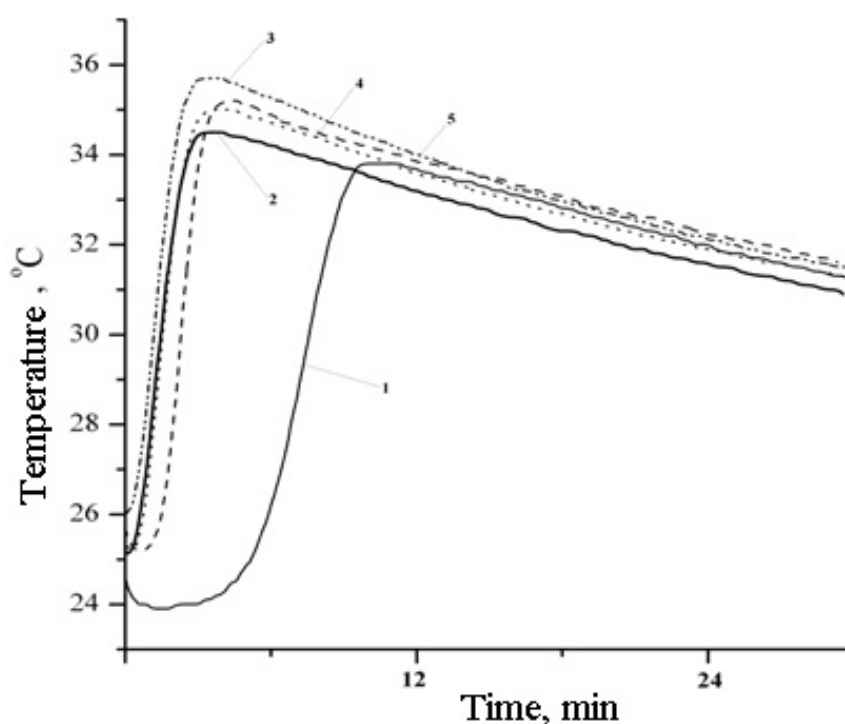
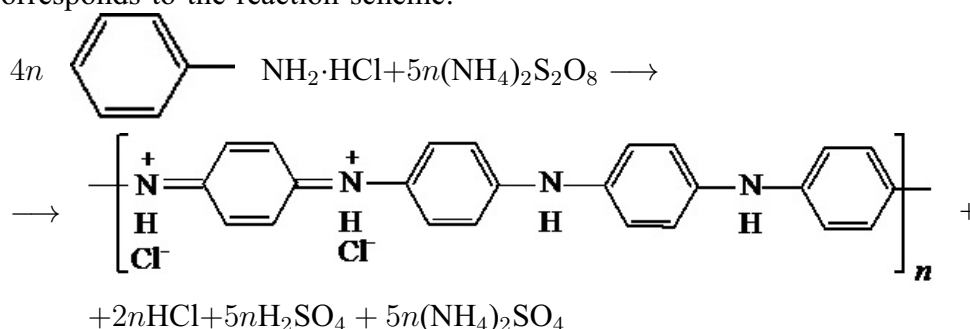


FIG. 8. Temperature profiles of aniline oxidative polymerization without CNTs (1), in presence of non-functionalized CNTs (2), and pre-oxidized CNTs “Taunit-M” with degree of functionalization with carboxyl groups equal to 0.18 (3), 0.65 (4), and 1.25 mmol/g (5)

The acidity of the reaction medium increases during the oxidative polymerization (Fig. 9), which corresponds to the reaction scheme:



When CNTs were introduced into the reaction medium, the minimum pH value was achieved in a shorter time (Fig. 9). Increasing the degree of CNTs pre-functionalization with COOH groups somewhat decreases the velocity of reaching minimal pH, while the actual pH values in the presence of functionalized CNTs are somewhat higher than in the presence of the starting CNTs.

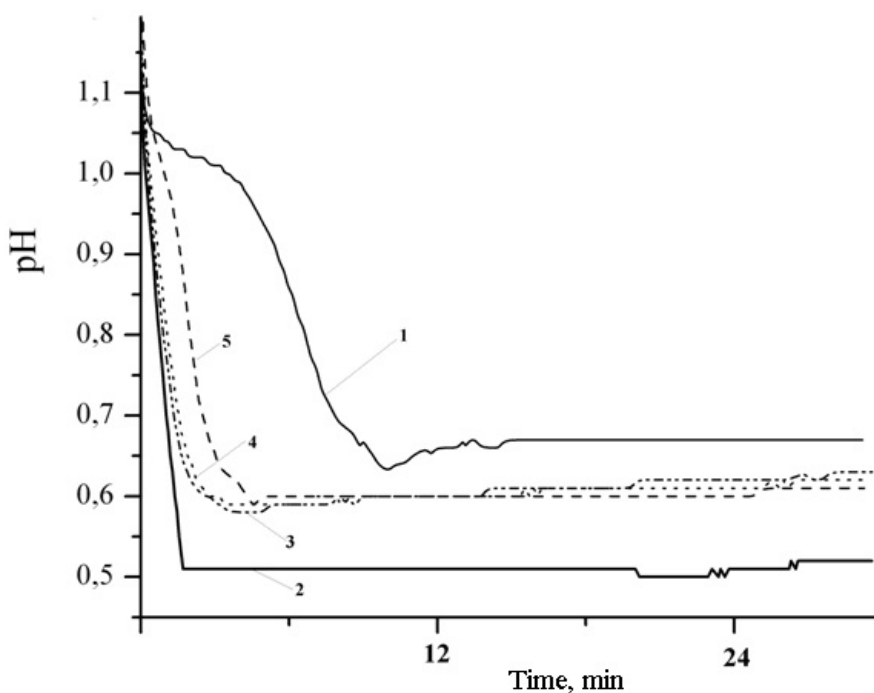


FIG. 9. Change of pH during the oxidative polymerization of aniline without CNTs (1), in presence of non-functionalized CNTs (2), and in presence of pre-oxidized CNTs “Taunit-M” with degree of functionalization with carboxyl groups equal to 0.18 (3), 0.65 (4), and 1.25 mmol/g (5)

As was indicated in [25], pre-functionalization of CNTs with carboxyl groups increases the yield of polyaniline when the process is carried out at 0–2 °C and the oxidant is supplied gradually. However, when implementing the oxidative polymerization process at 20–25 °C and adding all the required amount of oxidant at the beginning, the degree of CNTs carboxylation does not affect the yield of the desired reaction product.

Pre-functionalization of carbon nanotubes by carboxyl groups affects the electrical properties of the PANI/CNTs composites in an ambiguous way. The minimum electrical resistance

TABLE 3. Electrical properties of PANI/CNTs composites (80 wt.% PANI)

Material	PANI/“Taunit-M”				PANI/“Taunit-MD”			
$D_f$ , mmol/g	0	0.3	0.5	1.3	0	0.4	0.5	1.1
Specific electrical resistance, Ohm·cm	5.8	2.5	4.1	2.9	2.4	1.3	2.5	2.3
Specific electrical capacity, F/g	162	190	171	164	–	140	188	168

was observed at low values for the degree of COOH functionalization of CNTs (Table 3). The low degree pre-functionalization of CNTs with –COOH groups improves the capacitance properties of the composites (Table 3). Materials based on CNTs with a low degree of functionalization (0.33 mmol of COOH groups/g), modified with PANI, show the best capacitive properties. However, other PANI/CNTs composites are also characterized by consistently high capacitance values.

Analysis of SEM-images (Fig. 10) shows that the modification of the original non-functionalized nanotubes with polyaniline resulted in a material with nonuniform distribution of PANI on the surface of CNTs. In fact, on some nanotubes, the polyaniline coating was practically absent. In the case of boiling nitric acid-oxidized CNTs, a more uniform layer of polyaniline was formed on the CNTs surface. The best quality and uniformity of the polyaniline coating was observed on the surface of CNTs oxidized with nitric acid vapor.

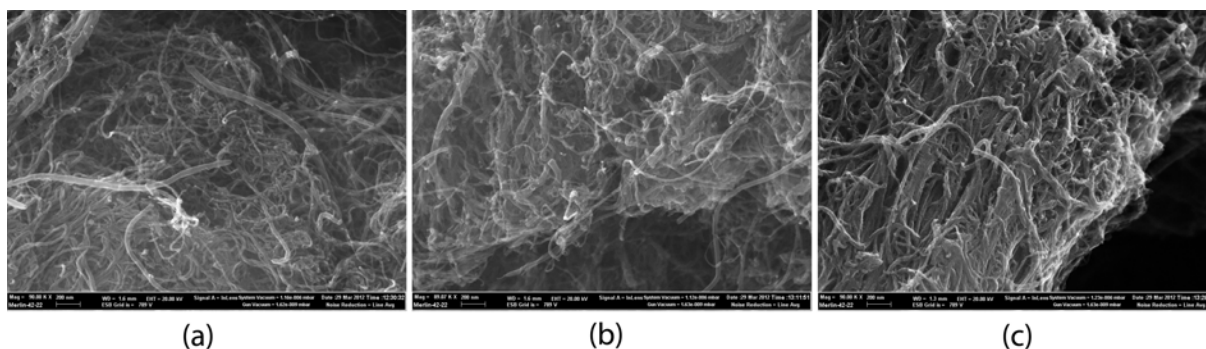


FIG. 10. SEM images of carbon nanotubes “Taunit-MD” modified with PANI: non-functionalized CNTs (a); oxidized by boiling in concentrated nitric acid (b); oxidized in HNO<sub>3</sub> vapor (c)

### 3.3. Investigation of the CNT/polysulfone composites

According to optical microscopy, unmodified polysulfone contains few pores of various sizes (Fig. 11a). Introduction of non-functionalized “Taunit-M” CNTs significantly increased the porosity of the polymer (Fig. 11b), and the pore sizes became significantly different. Visually, large agglomerates of CNTs were observed. When pre-oxidized CNTs with low degrees of COOH functionalization ( $D_f = 0.33$  mmol/g, Fig. 11c) were introduced into a polysulfone matrix, the pores in the composite film became much smaller and uniform in size. CNTs agglomerates were visible as black spots of different shapes, but their sizes were much smaller than in the case of polysulfone containing non-functionalized CNTs.

“Taunit-M” CNTs with higher degrees of COOH functionalization ( $D_f = 0.9$  mmol/g) were distributed in the matrix more uniformly than low-functionalization CNTs. The color of films became darker, pores in them were practically non-existent (Fig. 11d). CNTs agglomerates became more uniform in size and were uniformly distributed in the bulk of polymer. This can be

explained by increasing the lyophilic properties of CNTs with increasing concentration of surface carboxylic groups and increasing their interaction with polar solvent, and possibly with dissolved polysulfone. When forming films from solution, the structure of the CNTs agglomerates formed is retained in CNTs containing films.

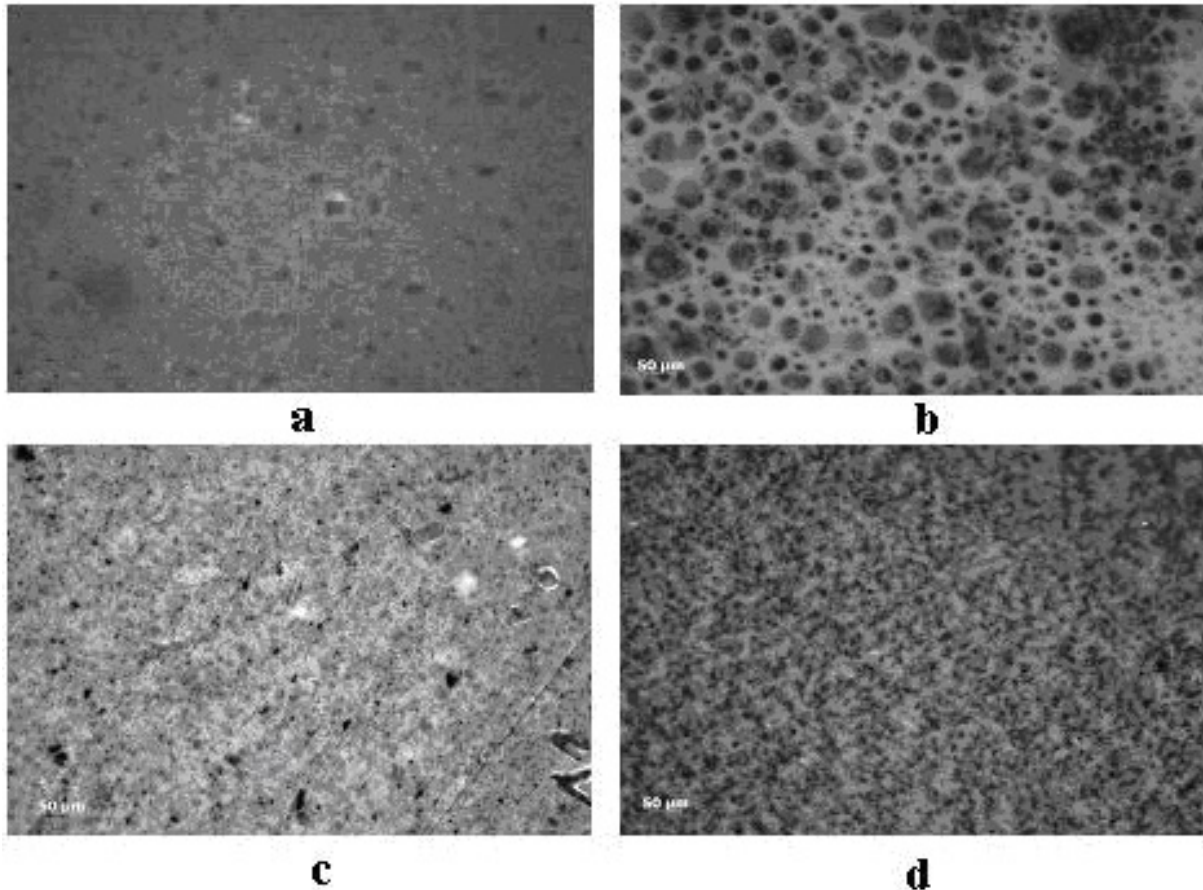


FIG. 11. Optical microscope images of polysulfone films (Ultrason 6020 “BASF”): (a) polysulfone film without CNTs; (b) filled with raw (non-oxidized) CNTs “Taunit-M”; (c, d) filled with oxidized carbon nanotubes “Taunit-M”,  $D_f = 0.33$  (c) and 0.90 (d) mmol/g

Fig. 12 shows the data on the surface conductivity of polysulfone films filled with raw and oxidized “Taunit-M” CNTs, obtained using conditions of the present study.

As seen in Fig. 12, the electrical resistance ( $R$ ) of the films of varying thickness filled with oxidized nanotubes was higher than that of the films filled with initial (non-oxidized) CNTs. It appears from plots 1 and 2 that the electrical resistance of composite films increased with an increased degree of CNTs functionalization. Accordingly, the change of  $R$  in the range of  $D_f$  from 0.3 to 0.9 mmol/g is negligible. Increasing the carboxyl group content above 0.9 mmol/g leads to a sharp rise in the resistance, in spite of the higher degree of dispersion and more uniform CNTs distribution in the polymer matrix.

The restructuring of the nanocomposite to greater uniformity and higher degree of CNTs dispersion, as observed in Figure 11, should result in a decrease of the percolation threshold, and consequently, a decrease in the electrical resistance. Since it does not, it can be concluded that the electrical conductivity of the composite films is also affected by the nature of CNTs. However, in some studies [26,27], it was observed that the electrical conductivity of CNTs

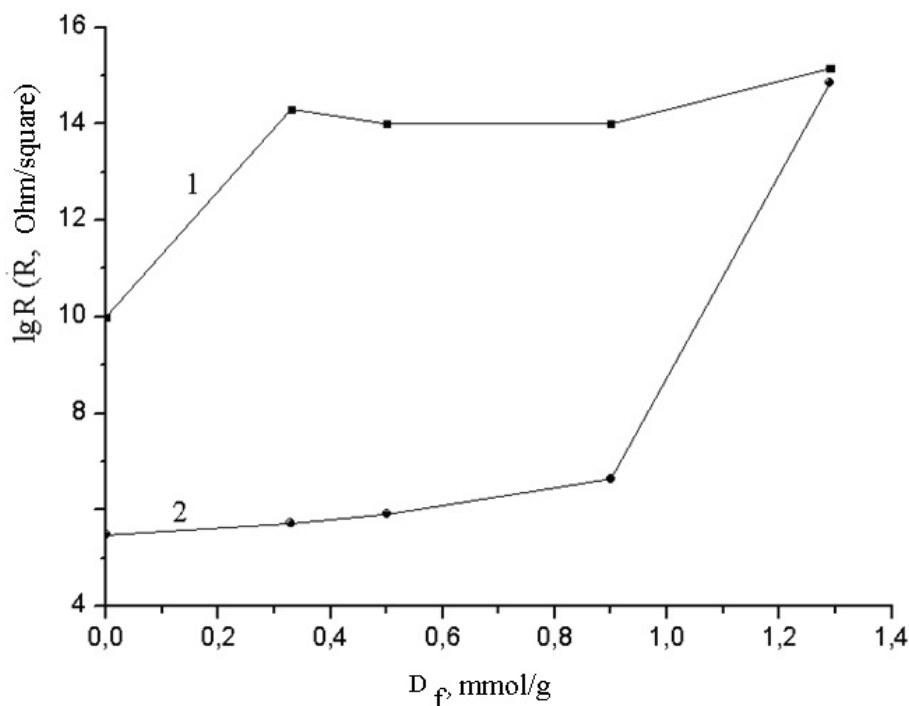


FIG. 12. Dependence of surface electrical resistance of the polysulfone films (Ultrason 6020 “Basf”) on the degree of functionalization of CNTs “Taunit-M” with carboxyl group ( $D_f$ ) at film thickness 20 microns (1) and 150 microns (2). Mass content of CNTs in the composite was 2%

increased with their oxidative treatment. Increasing the degree of disorder of CNTs surface layers, as determined by D/G ratio in Raman spectra, was shown to reduce the conductive properties of CNTs [28]. However, in this case, the surface defects considered were not caused by oxygenated functional groups. Therefore, the decrease in electrical conductivity for CNTs/polysulfone composite films with increased degree of COOH functionalization on the CNTs is despite the anticipated increase of conductivity of the CNTs themselves.

It can be assumed that increasing the degree of CNTs functionalization results in a strengthening of their interaction with polysulfone, but reduces interaction of CNTs with each other. So, fragments of percolation network become isolated from each other by layers of a non-conductive polymer. Consequently, for obtaining composite materials with maximal conductivity one should take CNTs with low degrees of COOH functionalization or non-oxidized CNTs.

#### 4. Conclusions

1. The laws of the liquid-phase and gas phase oxidation of carbon nanotubes were studied. The possibility of obtaining materials with a given degree of functionalization with oxygen-containing groups was shown. The influence of the degree of functionalization on the surface defects of the CNTs was studied. Gas-phase oxidation methods were more efficient and can be amenable to scaling for pilot plant production.
2. The laws of oxidative aniline polymerization on the surface of pristine and pre-functionalized CNTs were investigated. It was shown that the presence functional groups on the surface of the CNT changed the rate and thermal effects of the processes.
3. The effect of the method and the degree of pre-functionalization of the CNTs on the properties of composite materials was shown. The necessity of choosing an optimal

method and degree of pre-functionalization of CNTs for composite materials with superior properties was proven.

## Acknowledgments

This work has been supported by RFBR (grant 12-03-97555-r\_center\_a)

## References

- [1] Z. Spitalsky, D. Tasis, K. Papagelis, C. Galiotis. Carbon nanotube - polymer composites: Chemistry, processing, mechanical and electrical properties. *Progress in Polymer Science*, **35** (3), P. 357–401 (2010).
- [2] Y. Zhang, H. Feng, et al. Progress of electrochemical capacitor electrode materials: A review. *International journal of hydrogen energy*, **34** (11), P. 4889–4899 (2009).
- [3] X. Ren, C. Chen, M. Nagatsu, X. Wang. Carbon nanotubes as adsorbents in environmental pollution management: A review. *Chemical Engineering Journal*, **170** (2-3), P. 395–410 (2011).
- [4] L. Raki, J. Beaudoin, et al. Cement and Concrete Nanoscience and Nanotechnology. *Materials*, **3**, P. 918–942 (2010).
- [5] N.G. Sahoo, S. Rana, et al. Polymer nanocomposites based on functionalized carbon nanotubes. *Progress in Polymer Science*, **35** (7), P. 837–867 (2010).
- [6] C. Trisca-Rusu, A.C. Nechifor, et al. Pylsulfone-functionalized multiwalled carbon nanotubes composite membranes for potential sensing applications. *Semiconductor Conference, CAS 2009* (2009).
- [7] V. Vatanpour, S.S. Madaeni, et al. Fabrication and characterization of novel antifouling nanofiltration membrane prepared from oxidized multiwalled carbon nanotube/polyethersulfone nanocomposite. *Journal of Membrane Science*, **375** (1-2), P. 284–294 (2010).
- [8] S. Qiu, L. Wu, et al. Preparation and properties of functionalized carbon nanotube/PSF blend ultrafiltration membranes. *Journal of Membrane Science*, **342** (1-2), P. 165–172 (2009).
- [9] S. Kim, L. Chen, J.K. Johnson, E. Marand. Polysulfone and functionalized carbon nanotube mixed matrix membranes for gas separation: Theory and experiment. *Journal of Membrane Science*, **294** (1-2), P. 147–158 (2007).
- [10] T.-M. Wu, Y.-W. Lin, C.-S. Liao. Preparation and characterization of polyaniline/multi-walled carbon nanotube composites. *Carbon*, **43** (4), P. 734–740 (2005).
- [11] T.-M. Wu, Y.-W. Lin. Doped polyaniline/multi-walled carbon nanotube composites: Preparation, characterization and properties. *Polymer*, **47** (10), P. 3576–3582 (2006).
- [12] H.P. Boehm. Surface oxides on carbon and their analysis: a critical assessment. *Carbon*, **40** (2), P. 145–149 (2002).
- [13] L. Zhang, Q. Ni, Y. Fu, T. Natsuki. One-step preparation of water-soluble single-walled carbon nanotubes. *Applied Surface Science*, **255** (15), P. 7095–7099 (2009).
- [14] K. Hernadi, A. Siska, et al. Reactivity of different kinds of carbon during oxidative purification of catalytically prepared carbon nanotubes. *Solid State Ionics*, **141-142**, P. 203–209 (2001).
- [15] D. Dutta, R. Dubey, et al. Preparation of spongy microspheres consisting of functionalized multiwalled carbon nanotubes. *New Carbon Materials*, **26** (2), P. 98–102 (2011).
- [16] V. Datsyuk, M. Kalyva, et al. Chemical oxidation of multiwalled carbon nanotubes. *Carbon*, **46** (6), P. 833–840 (2008).
- [17] A.A.M. Daifullah, B.S. Girgis. Impact of surface characteristics of activated carbon on adsorption of BTEX. *Colloids and Surfaces A: Physicochem. Eng. Aspects*, **214** (1-3), P. 181–193 (2003).
- [18] W.M. Davis, C.L. Erickson, C.T. Johnston. Quantitative Fourier Transform Infrared Spectroscopic Investigation of Humic Substance Functional Group Composition, *Chemosphere*, **38** (12), P. 2913–2928 (1999).
- [19] Y.-P. Sun, K. Fu, Y. Lin, W. Huang. Functionalized Carbon Nanotubes: Properties and Applications. *Acc. Chem. Res.*, **35** (12), P. 1096–1104 (2002).
- [20] M. Tang, H. Dou, K. Sun. One-step synthesis of dextran based stable nanoparticles assisted by self-assembly. *Polymer*, **47** (2), P. 728–734 (2006).
- [21] S. Grandi, A. Magistis, et al. Synthesis and characterisation of SiO<sub>2</sub>-PEG hybrid materials. *J. Noncryst. Sol.*, **352** (3), P. 273–280 (2006).
- [22] A.M. Keszler, L. Nemes, S.R. Ahmad, X. Fang. Characterisation of carbon nanotube materials by Raman spectroscopy and microscopy - A case study of multiwalled and singlewalled samples. *Journal of Optoelectronics and Advanced Materials*, **6** (4), P. 1269–1274 (2004).

- [23] S. Osswald, M. Havel, Y. Gogotsi. Monitoring oxidation of multiwalled carbon nanotubes by Raman spectroscopy. *Journal of Raman Spectroscopy*, **38** (6), P. 728–736 (2007).
- [24] S. Irle, A. Mews, F. Morokuma. Theoretical Study of Structure and Raman Spectra for Models of Carbon Nanotubes in Their Pristine and Oxidized Forms. *J. Phys. Chem. A*, **106** (49), P. 11973–11980 (2002).
- [25] A.V. Melezhik, T.P. Dyachkova, E.Yu. Filatova, A.G. Tkachev. *Carbon nanotubes and their composites with polyaniline: prospects of application*. Electronics and nanotechnology, Kyiv, 2010.
- [26] C.H. Lau, R. Cervini, et al. The effect of functionalization on structure and electrical conductivity of multi-walled carbon nanotubes. *J. Nanopart. Res.*, **10** (1), P. 77–88 (2008).
- [27] S. Agrawal, M. Raghuvver, H. Li, G. Ramanath. Defectinduced electrical conductivity increase in individual multiwalled carbon nanotubes. *Appl. Phys. Lett.*, **90**, P. 193104–193103 (2007).
- [28] P. Singjai, S. Changsarn, S. Thongtem. Electrical resistivity of bulk multi-walled carbon nanotubes synthesized by an infusion chemical vapor deposition method. *Materials science and Engineering :A*, **443** (1-2), P. 42–46 (2007).

# LOW-TEMPERATURE THERMOPOWER IN DISORDERED CARBON NANOTUBES

V. E. Egorushkin<sup>1</sup>, N. V. Melnikova<sup>2</sup>, N. G. Bobenko<sup>1</sup>, A. N. Ponomarev<sup>1</sup>

<sup>1</sup> Institute of Strength Physics and Material Science, Siberian Branch of the Russian Academy of Sciences, Tomsk, Russia

<sup>2</sup> V.D. Kuznetsov Siberian Physical Technical Institute of Tomsk State University, Tomsk, Russia

phdmelnikova@gmail.com

## PACS 61.48.De

Low-temperature thermopower in disordered carbon nanotubes was calculated while taking into account multiple elastic electron scattering on impurities and short-range structural inhomogeneities. A possible explanation is presented for the low-temperature behavior of thermopower which depends on defect structure, impurities and chirality.

**Keywords:** Carbon nanotube, thermopower, structural disordered, low-temperature.

## 1. Introduction

Thermopower  $S$  in multi-walled carbon nanotubes (CNTs) and bundles of single-walled CNTs is found to be high (much higher than in metals) and characterized by nonlinear temperature dependence at low temperatures. In disordered, unannealed CNTs, thermopower is positive and the curve  $S(T)$  has a maximum or a bend at  $T \sim 30\text{--}100$  K. However, after degassing or high-temperature annealing of CNTs, the thermopower changes sign and  $S(T)$  weakly deviates from linear dependence without any minimum or bend [1–11].

In [1], the large value of thermopower is explained by the proximity of chemical potential to the boundary of electronic band. The change of thermopower sign is connected with the location of chemical potential relative to the center area of electronic band in CNTs. However, other researchers have postulated that the peculiarities of band structure in CNTs cannot be the only reason for the low-temperature behavior of thermopower. In bundles of single-walled carbon nanotubes (SWNTs), the electron-hole symmetry is broken and charge transfer between single-walled nanotubes takes place. This may become another reason for the considered low-temperature features in thermopower.

Previously, the thermopower of multi-walled CNTs (MWNTs) mats synthesized using spark plasma sintering technique has been investigated [3]. The authors explained the singularities in low-temperature thermopower by electron-phonon interaction. In [4], the contributions to thermopower from the electron transport in a clean tube and impurity scattering have been considered. The authors believe that the contribution of the impurity scattering resulted in a deviation from linear dependence of  $S(T)$ , and note that the nitrogen saturation of the same tube resulted in a change of sign of the thermopower.

The non-linear  $S(T)$  has been described by competing contributions from phonon drag and diffusive electron transport, the former dominating at very low temperatures and the latter predominating at high  $T$  [5].

The thermopower in bundles of multi-walled CNTs about 20 nm in diameter has been investigated in the framework of the two-band model [6]. However, at  $T < 30$  K, the results

of calculations in [6] were not in agreement with the experimental data and thus, the authors assumed that the effect of weak localization may be a reason for the divergence between their theoretical and experimental data.

The low-temperature thermopower in the long bundles of multi-walled CNTs (length  $\sim 1$  mm and diameter  $\sim 30$  nm), has been investigated and the following expression has been proposed:  $S(T) \sim T \log T$  at  $T < 20$  K [7]. The authors presume that the deviation of  $S(T)$  from linear dependence was caused by the repulsive interaction between electrons in a disordered local environment. The change of thermopower sign and the type of its temperature dependence were shown to be determined by the chirality angle and the ratio of the overlap integrals for electron transport along the cylindrical axis of the helix and the base spiral of CNTs [8,9].

There is a number of studies of low-temperature thermopower in nanotubes, where the role of other factors such as annealing temperature, nanotube chirality or diameter, was considered [6,10,11]. For example, in [10], the influence of annealing temperature on electron transport properties in long multi-walled CNTs with 10–12 nm diameter was investigated. The electrical resistivity and heat conductivity were found to increase when temperature rises. At the same time, the thermopower decreased and may even change sign from positive to negative. The latter may be associated with decreased oxygenation after annealing. There are also data on the value of low-temperature thermopower in CNTs which decreases with the increased nanotube diameter, and the deviation from linearity becomes more pronounced [2,4,6].

Thus, we may conclude that the origin of low-temperature thermopower peculiarities in CNTs is not understood and still attracts the attention of investigators. The following features in the behavior of thermoelectric power in disordered carbon nanotubes may be emphasized:

- The value of thermopower in CNTs is on the order of 5–50  $\mu\text{V/K}$ , which is much larger than in metals.
- In disordered (gas saturated) and unannealed CNTs, the thermopower is always positive, while it is always negative in clean (degassed) nanotubes.
- The positive thermopower increases nonlinearly with increasing temperature (at  $T < 100$  K) and the curve  $S(T)$  has a maximum or bend at  $T \sim 30$ –100 K. The negative thermopower decreases nonlinearly with increasing temperature (at  $T < 100$  K) but the curve  $S(T)$  has no minimum or bend.
- Saturation of the CNTs with nitrogen or oxygen changes the sign of thermopower, and the subsequent degassing of nanotubes by annealing at high temperatures again leads to a change in the sign of the thermopower.
- Changing the concentration of the impurities, the structural defects or the diameter of the nanotube, which is directly proportional to the chirality of the CNT, leads to the deviation of temperature dependence from linearity, which may be pronounced to different degrees.

The significant influence of the factors mentioned above (chirality or diameter of nanotubes, concentration of impurities and defect structure) on the low-temperature behavior of thermopower requires further study. Previously, we showed that at low temperatures, the electrical properties of SWNTs and MWNTs bundles, including thermopower, display similar properties to metallic alloys with short-range order and amorphous metals [12]. That is why we proposed to use the approach developed to describe the low-temperature anomalies of the electrical properties in amorphous metals for the investigation of disordered CNTs [13,14]. Using the Green functions (GF) method, we calculated the electron relaxation time [15] and found a single-electron and a multiple-electron contribution to thermopower [12] which took into account the multiple elastic electron scattering by defects, the interference of inelastic

electron-electron interactions and the elastic scattering by defects. The expression obtained for thermopower gave good qualitative agreement with experimental data and explained behaviors of thermopower in the ‘dirty’ metallic nanotubes.

However, in [12] we did not take into account the chirality of the nanotubes. In [16] we could develop and supplement our theory by considering the electronic spectrum of CNTs in its dependence on the chirality. This allowed us to calculate the contribution to thermopower for the disordered (20,20) CNTs and gave a possible explanation for the changing sign of the thermoelectric power, the emergence of a bend or a maximum in  $S(T)$  depending on chirality of nanotube, the concentration of defects and type of short-range ordering in the structure of nanotubes. When taking into account the electronic spectrum, which depends on nanotube chirality, we were able to calculate the contribution to electronic density of states (DOS), and obtain the conditions for electrical conductivity under which the nanotubes behave as metal or as semiconductor [17, 18].

In the present work, we would like to analyze the low-temperature behavior of thermopower for bundles of single-walled CNTs and individual multi-walled CNTs with chiralities (10,10) and (16,16). The second aim of this paper is to investigate the derivative of thermopower and to find conditions when  $S(T)$  has a maximum or bend. Finally, we hope here to understand how annealing influences the structure of CNTs and why the thermopower becomes negative.

## 2. Thermopower: results and discussion

In [16] we have obtained the expression for thermopower of the disordered carbon nanotubes. However, in calculating  $S(T)$ , we neglected a summand which is not important at low temperatures ( $T < 50$  K) but, as we found later, plays a role in the formation of the maximum in  $S(T)$  at higher temperatures ( $T > 50$  K). So, the more exact expression for thermopower is the following:

$$S(T) = -\frac{\pi^2 k^2 T}{3e} \left[ \left( \frac{\pi a \gamma_0}{\sqrt{3} C_h} - 2\pi k T \right)^{-1} - \left\{ 2\pi k T \left( 1 + \frac{1}{BT^{1/2}} \right) \right\}^{-1} \right], \quad (1)$$

where  $k$  is the Boltzmann constant, the chirality  $C_h = a\sqrt{n^2 + mn + m^2}$  is related to the diameter of nanotube  $d$  as follows:  $C_h/\pi = d$ ,  $(n, m)$  are the indexes of chirality. Then  $a$  is the lattice constant and  $\gamma_0$  is the transfer integral between the first neighbor  $p_z$  orbitals. Finally  $B = \frac{2\sqrt{2}\pi(1-c)m^{3/2}k^{1/2}}{\nu_0 N} \sum_i \alpha_i$ , where  $\alpha_i$  are the short-range order coefficients ( $\alpha_0 = 1$ ) [19],  $N$  is the number of atoms inside the structure inhomogeneity of the short-range order type,  $m$  is mass of electron and  $\nu_0 = \frac{p_0}{\pi^2 \sqrt{3} a \gamma_0} \sqrt{p_0^2 - \left(\frac{2}{3d}\right)^2}$  is the density of states at the Fermi level and  $p_0$  is the Fermi momentum for an ideal CNT.

The first term in (1) is connected with the contribution from DOS and the second term is connected with the contribution from the electron relaxation time. These contributions have different signs; one of them increases while the other one decreases when temperature rises. That is why in the  $S(T)$  curve there is a maximum which takes place when the velocities of change of these contributions are equal.

The contributions to thermopower, calculated using the formula (1) for the (10,10) CNT, are represented in Fig. 1. The full  $S(T)$  is the sum of the contribution from electron scattering on structural defects of CNTs (S1) and the linear contribution to thermopower of ideal CNTs

(S2). As is seen in Fig. 1, the deviation from linearity of  $S(T)$  may be due to the electron scattering on the short-range ordered domain structure of the nanotube. The dependences obtained here were confirmed by the experimental data [4].

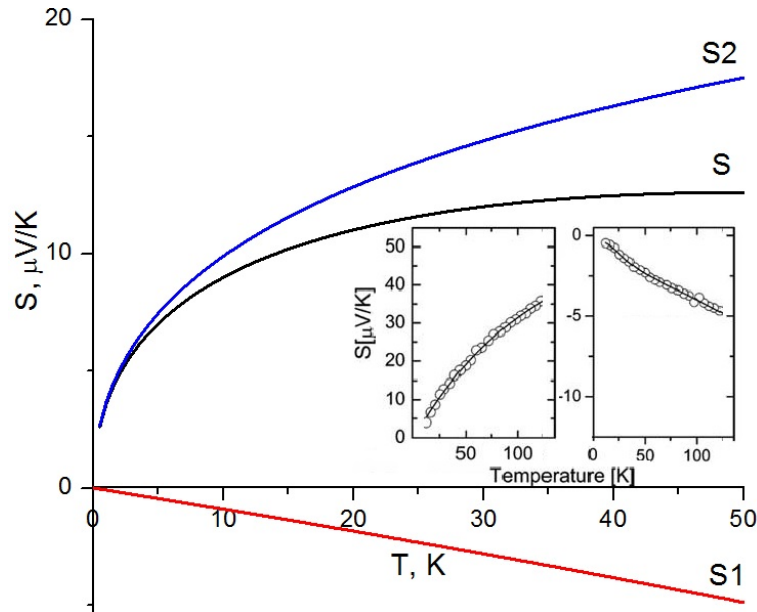


FIG. 1. Contribution to thermopower of a 'metallic' CNT calculated for the tube chirality (10,10) and  $\sum_i \alpha_i \approx 0.1$ . n insert [4]: (a) thermopower of pure MWNT mat; (b) thermopower of N-doped MWNT mat

Thermoelectric power  $S(T)$  calculated for the (10,10) CNT for the different values of short-range order parameters and concentration of impurities, is shown in Fig. 2. As mentioned above, the sum of parameters of short-range order is determined by the different types of structural defects of the CNT and may be positive or negative, depending on what coordination sphere (the first or the second one) will be occupied by atoms of the impurity or defects. From our data, the thermopower is positive when the defects are located mainly in the first coordination sphere and thermopower becomes negative at  $\sum_i \alpha_i \leq 0.1$  when most defects are pushed out of the first coordination sphere.

In particular, this takes place in the case of annealed and degassed nanotubes [1,2]. In reality, annealing resulted in decrease in the concentration of impurities, structural defects and sorbed gas; the higher annealing temperature, the lower concentration of defects (of all types as impurities as structural inhomogeneities of short-range order) and thus, lower thermopower.

Finally in the fully-degassed samples, thermopower becomes negative [10]. However, when we distinguished the calculated contributions to thermopower depending on concentration of impurities and short-range order parameters we found that the tendency of  $S(T)$  to decrease takes place only for decreasing short-range order parameter. As for the concentration of the impurities, then the opposite effect occurs:  $S(T)$  is higher for CNTs with the lower concentration of impurities. However, the change in the thermopower value does not exceed 5%. This would seem to indicate that annealing regulates the short-range ordered structure of CNTs more strongly than the concentration of impurities.

It is interesting that the same effect is found in nitrogen-doped multiwalled carbon nanotubes [4], although boron doping results in a positive thermopower of MCNT. We can

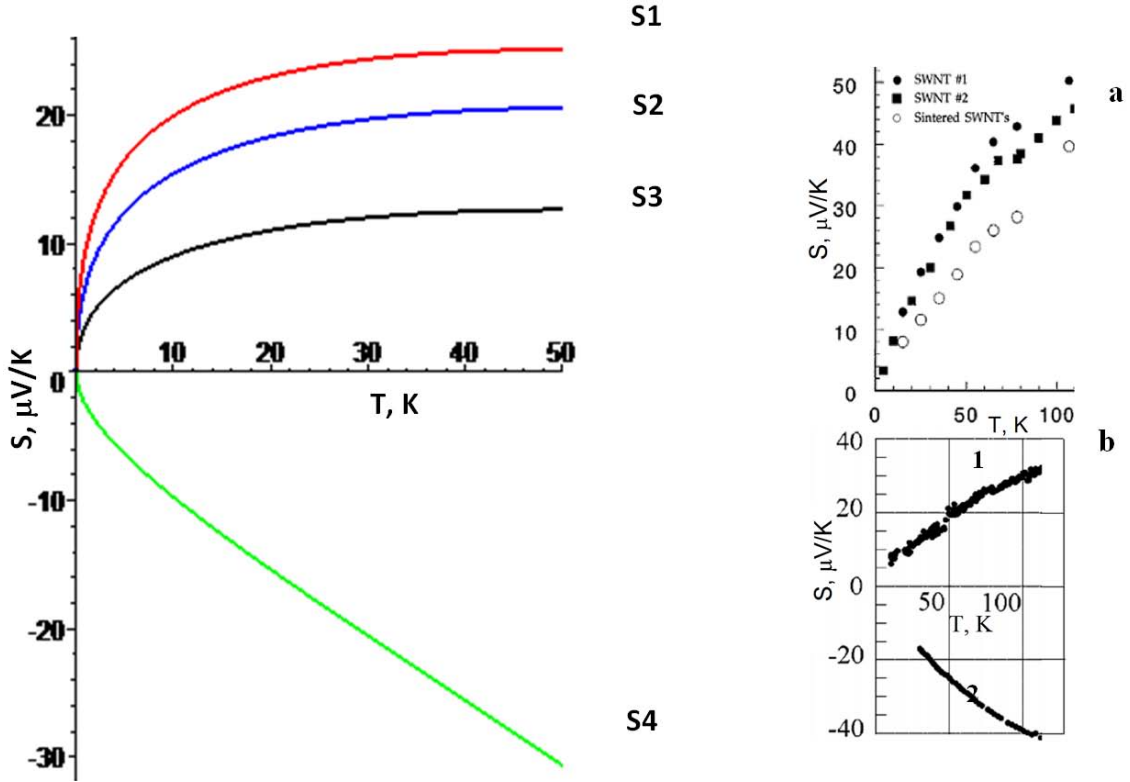


FIG. 2. Temperature dependence of thermopower of the CNT (10,10), calculated for different values  $S(T)$  of short-range order:  $\sum_i \alpha_i = 0.3$  (S1),  $\sum_i \alpha_i = 0.2$  (S2),  $\sum_i \alpha_i = 0.1$  (S3) and  $\sum_i \alpha_i = -0.1$  (S4). On insert the experimental data: (a) temperature dependence of thermopower of bundles of SWNTs: the samples 1 and 2 are not annealed and the sintered SWNT is annealed at 1000 ° [2] and (b) the temperature dependence of thermopower of the oxygenated CNT (curve 1) and deoxygenated one (curve 2) [1]

explain this phenomenon by occupation of the first and second coordination spheres by nitrogen and boron, respectively .

Equation (1) may be rewritten in a way which may be more convenient for the interpretation of the experimental data:

$$S(T) = -\frac{\pi k}{6e} [(\gamma_h + B^2) T + \gamma_h^2 T^2 - BT^{1/2}], \quad (2)$$

where  $\gamma_h = \frac{\sqrt{3}C_h k}{a\gamma_0}$ .

Analyzing (2), we found that when thermopower is negative, the derivative does not have real (physical) roots. Hence, there are no any bending points in the negative  $S(T)$ . This result is in good agreement with the experimental data [10] – the negative thermopower never has a maximum or minimum in its temperature dependence!

In the case of positive thermopower, which takes place at  $\sum_i \alpha_i > 0$ , the derivative  $\frac{\partial S(t)}{\partial T}$  has two real roots, one of which is in the range of low temperatures ( $T < 100$  K) and the other one is in the high-temperature region (above 5000–6000 K). Since we studied

only the low-temperature behavior of thermopower, we found out that the second derivative of thermopower in the low-temperature thermopower was negative. So the positive  $S(T)$  has a maximum. This fact is also consistent with the experimental data [3] presented in the insert (a) in Fig. 3.

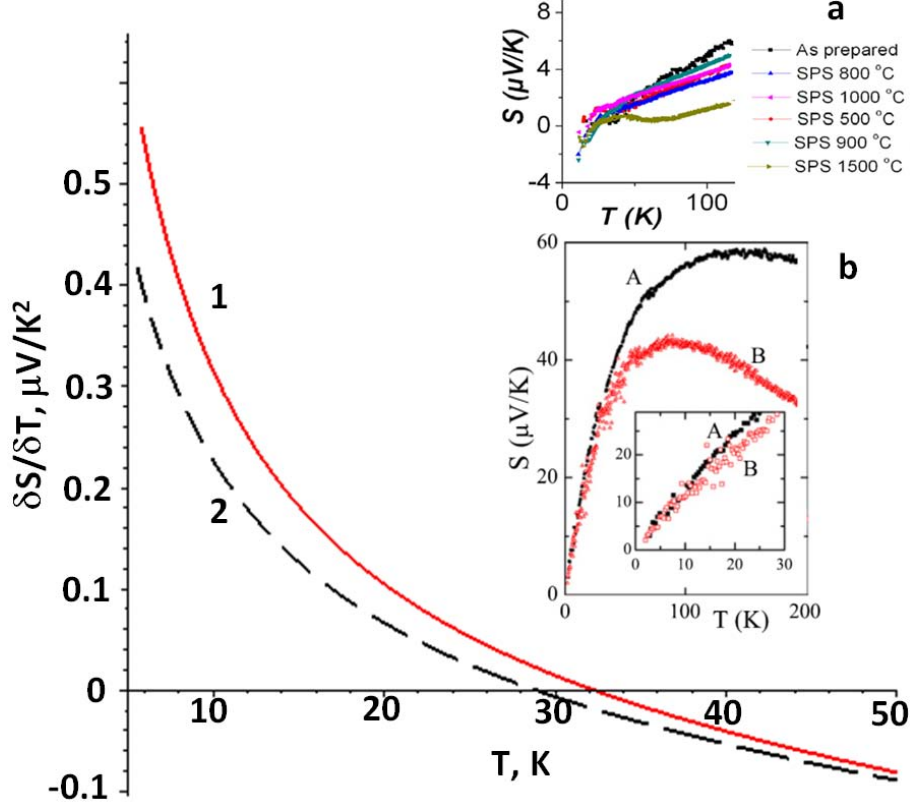


FIG. 3.  $\frac{\partial S(T)}{\partial T}$  in metallic (16,16) CNT for  $\Sigma\alpha = 0.15$  (curve 1) and  $\Sigma\alpha = 0.1$  (curve 2). Inserts: (a) temperature dependence of thermopower in MCNTs synthesized at different temperatures [3]; (b) temperature dependence of thermopower in unannealed (A) and annealed (B) boundless of SWNTs [11]

Insert (b) shows the temperature dependence of thermopower for unannealed (A) and annealed (B) boundless of SWNTs [11]. Indeed, from this insert, one may see that the annealed sample has a lower  $T_{max}$  than the unannealed one.

Now, let us analyze the temperature dependencies of thermopower (1) as a function of the short-range order coefficients. We shall consider the CNTs with the following parameters: chiral indices equal to (10,10), temperature varies from 0.1 to 80 K,  $\nu_0 \approx 0.1$  eV [13] and  $U_0 = 0.05$  eV; sum of short-range order parameters  $\sum_i \alpha_i$  is varied from  $-0.5$  to  $0.5$ . The latter corresponds to the different types of short-range order: when the short-range order parameter is negative, the defects are located in the second coordination sphere, and when positive, the defects are in the first sphere [19].

The temperature of the maximum in  $S(T)$  differs for different CNTs and depends upon the chirality and short-range order parameters, as shown in Table 1.

From Table 1, one may see that the value of the temperature at maximum  $T_{max}$  decreases dramatically when the index of chirality increases at the fixed  $\sum_i \alpha_i$  and  $T_{max}$  increases more

TABLE 1. Temperature of maximum in  $S(T)$ , in Kelvin, depending on parameter of short-range order (the first line of the table) and index of chirality (the first column of the table)  $n$  (here we assume  $c = 0, 1$ )

$n \backslash \sum_i \alpha_i$	0.05	0.1	0.15	0.2	0.25
6	70	87	88	85.6	82.1
8	48.3	63.7	66.4	65.4	63.4
10	35.8	49.8	52.9	52.8	51.6
12	27.9	40.5	43.8	44.1	43.5
14	22.4	33.8	37.2	37.9	37.6
16	18.5	28.9	32.2	33	33

slowly when  $\sum_i \alpha_i$  rises at the fixed  $n$ . This means that the negative “structure” contribution defined by chirality, increases more quickly than the contribution determined by the short-range ordering.

### 3. Conclusion

In the present paper we have described the low-temperature peculiarities of thermopower in disordered carbon nanotubes in the framework of the short-range ordered structure model and thus explained the influence of different factors (chirality or diameter of nanotubes, concentration of impurities and structural defects, annealing temperature) on the low-temperature behavior of thermopower, taking into account only multiple elastic electron scattering on structure defects (without electron-electron correlations) and concluded the following:

- The non-linear temperature dependence of thermopower is due to electron scattering on structural defects of CNTs. In an ideal CNT the dependence  $S(T)$  is linear.
- A decrease in the short-range order parameters results in a smaller slope of the  $S(T)$  curve and even in a changed thermopower sign. These results agree with the experimental data [2, 5, 10, 11].
- Position of the bend or maximum with a subsequent change in the slope of the  $S(T)$  curve to the temperature axis is determined by the chirality of and the types of structural defects present in the CNTs .

### Acknowledgments

This work was supported by grants of the Russian Fund of Fundamental Investigations ((No. 12-02-16048, No. 12-02-16063) and the Russian Ministry of Education and Science (No. 2012-1.4-12-000-1011-005).

**References**

- [1] K. Bradley, S.-H. Jhi, et al. Is the Intrinsic Thermoelectric Power of Carbon Nanotubes Positive? *Phys. Rev. Lett.*, **85**, P. 4361–4364 (2000).
- [2] J. Hone, I. Ellwood, et al. Thermoelectric Power of Single-Walled Carbon Nanotubes. *Phys. Rev. Lett.*, **80**, P. 1042–1045 (1998).
- [3] K. Yang, J. He, et al. Tuning electrical and thermal connectivity in multiwalled carbon nanotube buckypaper. *J. Phys.: Condens. Matter*, **22**, P. 334215–1334215-6 (2010).
- [4] Y.-M. Choi, D.-S. Lee, et al. Nonlinear Behaviour in the Thermopower of Doped Carbon Nanotubes Due to Strong. Localized States. *Nano Lett.*, **3**, P. 839–842 (2003).
- [5] I. Ovsienko, L. Matzui, V. Pundyk. Thermopower of Nanocarbon Materials with Different Structure and Phase Composition. *J. Mat. Sci. Res.*, **1** (3), P. 19–24 (2012).
- [6] T. Mingliang, L. Fanqing, C. Lin, M. Zhiqiang. Thermoelectric power behaviour in carbon nanotubule bundles from 4.2 to 300 K. *Phys. Rev. B*, **58**, P. 1166–1168 (1998).
- [7] N. Kang, L. Lu, et al. Observation of a logarithmic temperature dependence of thermoelectric power in multiwall carbon nanotubes. *Phys. Rev. B*, **67**, P. 033404 (2003).
- [8] S.Y. Mensah, F.K. Allotey, N.G. Mensah, G. Nkrumah. Differential thermopower of a CNT chiral carbon nanotube. *J. Phys.: Cond. Matter*, **13**, P. 5653–5662 (2001).
- [9] G.Ya. Slepyan, S.A. Maksimenko, et al. Electronic and electromagnetic properties of nanotubes. *Phys. Rev. B*, **57**, P. 9485–9497 (1998).
- [10] R. Jin, Z.X. Zhou, et al. The effect of annealing on the electrical and thermal transport properties of macroscopic bundles of long multi-wall carbon nanotubes. *Physica B*, **388**, P. 326–330 (2007).
- [11] W.J. Kong, L. Lu, et al. Thermoelectric power of a single-walled carbon nanotubes strand. *J. Phys: Cond. Matter*, **17**, P. 1923–1928 (2005).
- [12] V.E. Egorushkin, N.V. Mel'nikova, A.N. Ponomarev. The role of structural inhomogeneities in the temperature behavior of the thermopower in metallized nanotubes with impurities. *Russian Physics Journal*, **52**, P. 252–264 (2009).
- [13] V.E. Egorushkin, N.V. Melnikova. Low-temperature anomalous properties of amorphous metals and alloys. *J. Phys. F: Metal Physics*, **17**, P. 1379–1389 (1987).
- [14] V.E. Egorushkin, N.V. Melnikova. Calculation of the temperature dependence of the thermopower in amorphous metals. *J. Phys. F: Metal Physics*, **17**, P. 2389–2394 (1987).
- [15] V. Egorushkin, N. Melnikova, A. Ponomarev, A. Reshetnyak. Anomalous thermal conductivity in multiwalled carbon nanotubes with impurities and short-range order. *J. Phys. Conf. Ser.*, **248**, P. 012005 (2010).
- [16] N.V. Mel'nikova, V.E. Egorushkin, N.G. Bobenko, A.N. Ponomarev. The density of states and thermopower in disordered carbon nanotubes. *Russian Physics Journal*, **55** (11), P. 1266–1277 (2013).
- [17] V. Egorushkin, N. Mel'nikova, A. Ponomarev, N. Bobenko. Low-Temperature Peculiarities of Electron Transport Properties of Carbon Nanotubes. *J. Mat. Sci. Eng.*, **1**, P. 161–167 (2011).
- [18] V. Egorushkin, N. Melnikova, N. Bobenko, A. Ponomarev. Electronic and Transport Properties of Carbon Nanotubes with Impurities and Structure Disorder. *Phys. Sci. Appl.*, **2**, P. 224–232 (2012).
- [19] V.I. Iveronova, A.A. Katsnelson. *Short-range Order in Solid Solutions*. Nauka, Moscow, 1977, 256 p.

# SURFACE ACOUSTIC WAVE FERROELECTRIC PHONONIC CRYSTAL TUNABLE BY ELECTRIC FIELD

V. P. Pashchenko<sup>1,2</sup>

<sup>1</sup>Saint Petersburg State Polytechnical University, Saint Petersburg, Russia

<sup>2</sup>Avangard JSC, Saint Petersburg, Russia

v.paschenko@gmail.com

**PACS 81.05.Xj, 78.67.Pt**

Theoretical investigation results of the periodic domain structures induced by an electric field in barium strontium titanate ( $\text{Ba}_x\text{Sr}_{1-x}\text{TiO}_3$ ) ferroelectric thin film are presented. A novel type of tunable phononic crystal based on an electric field-induced piezoelectric effect in a thin ferroelectric film is proposed. Surface acoustic wave propagation equations for the substrate under electric field-induced periodic domains are derived. Finite element simulation revealed the possibility of applying the ferroelectric phononic crystal as an electrically tunable surface acoustic wave filter.

**Keywords:** tunable phononic crystal, induced piezoeffect, surface acoustic wave (SAW), periodic domains, ferroelectric film.

## 1. Introduction

Periodic domain structures in piezoelectric and ferroelectric materials have attracted much interest from researchers. There are various acousto-optics and laser devices based on periodic domains [1]. Periodic domain structures are mainly created in strong piezoelectrics, such as iron-doped ( $\text{Fe}_{2+}$  and  $\text{Fe}_{3+}$ ) lithium niobate and lithium tantalate. A direct electric field ( $E \sim 10^7$  V/m) applied to piezoelectric crystals leads to sufficiently stable periodic domain formation. The periodic domain's polarization is in alignment with the electric field's orientation [2].

Tunable SAW filters based on phononic crystals with periodic domains have been reported previously [3]. Major disadvantages of these phononic crystals are the laser-induced tunability and the required use of a high voltage source. In this paper we propose a novel type of surface acoustic wave phononic crystal based on an electric field-induced piezoelectric effect in the ferroelectric [4–7]. Tuning of the proposed phononic crystal is achieved by applying voltage ranging from 1 to 5 V.

## 2. Theory

The proposed tunable phononic crystal is shown schematically in Fig 1. The phononic crystal consists of a substrate with a deposited ferroelectric film and a series of interdigital transducers (IDT) atop the ferroelectric film. Phononic crystals have a SAW delay line design. Input and Output IDTs must excite and receive the SAW in a wide band, therefore their topology must be like chirped IDTs with a linear variation of the finger pitch. The conventional topologies of Input IDT and Output IDT are depicted in Fig. 1 for simplicity. Alternative electric signal are applied to the Input IDT and excite the surface acoustic wave. The output signal is received from Output IDT. DC control voltage is applied to the IDT

located between the Input IDT and Output IDT, namely the Bias IDT. The bias IDT has a conventional topology.

The ferroelectric film thickness is approximately 0.5 to 1  $\mu\text{m}$ . Due to such values of the film thickness, we can obtain a high electric field in ferroelectric film in areas according to Bias IDT location. So, if the applied bias is 1 V and the ferroelectric film thickness is 0.5  $\mu\text{m}$ , we obtain an electric field value of  $2 \cdot 10^6$  V/m.

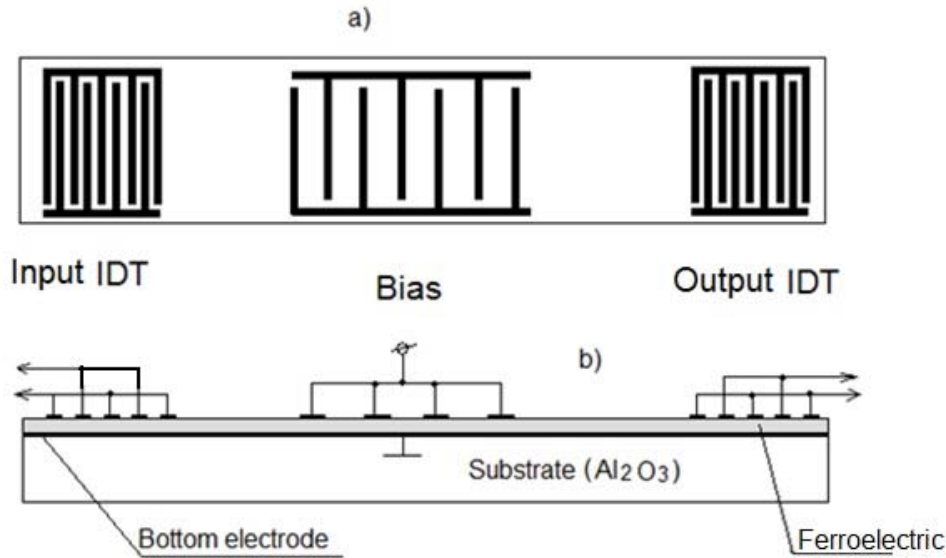


FIG. 1. Electric field tunable phononic crystal. a) Top view. b) Side view

The ferroelectric in the paraelectric phase is well known to have no spontaneous polarization. A DC electric field applied to a ferroelectric in the paraelectric phase causes piezoelectric phenomena in the film. This effect is used in tunable bulk acoustic wave resonators [4–5]. The applied DC electric field exerts an influence on the elastic and piezoelectric moduli of the ferroelectric film. The relations between the electric field and material properties were obtained in [6]:

$$\tilde{h}_{ijm}(E_i) = h_{ijm} - 2G_{ijmn}\varepsilon_0\varepsilon_{ij}(E_i)E_i, \quad (1)$$

$$\tilde{C}_{ijmn}(E_i) = C_{ijmn} + M_{ijklmn}(\varepsilon_0\varepsilon_{ij}(E_i)E_i)^2, \quad (2)$$

where  $h_{ijm}$  — piezoelectric tensor in absence of electric field (caused by defects in film),  $G_{ijmn}$  — electrostriction tensor,  $E_i$  — electric field components ( $i = 1, 2, 3$ ),  $C_{ijmn}$  — stiffness tensor,  $M_{ijklmn}$  — nonlinear electrostriction tensor,  $\varepsilon_0 \approx 8,8542 \cdot 10^{-12}$  F/m,  $\varepsilon_{ij}$  — permittivity tensor.

When an electric voltage is applied to the Bias IDT, piezoelectric domains are formed under the electrodes with piezoelectric module  $\tilde{h}$  and stiffness module  $\tilde{C}$ . Between the biasing electrodes, where the electric field is zero, piezoelectric domains are formed with piezoelectric module  $h$  and stiffness module  $C$ . Thereby, we have a material with periodic piezoelectric and elastic properties along the substrate length. The domain period is defined by the Biasing IDT period. Consequently, SAW propagate on the ferroelectric film and interact with the periodic domains. Frequency band gaps occur due to the periodic domains in such structures. Varying the Bias IDT period or the applied voltage's magnitude allows the possibility of tuning the phononic crystal band gap. This can be implemented for a tunable SAW filter based on this phononic crystal.

Let's consider the equations which describe acoustic wave propagation in anisotropic piezoelectric media [7]:

$$\begin{cases} C_{ijmn} \frac{\partial^2 U_m}{\partial x_j \partial x_n} + e_{mij} \frac{\partial^2 \phi}{\partial x_j \partial x_m} = \rho \frac{\partial^2 U_i}{\partial t^2}, \\ e_{ijm} \frac{\partial^2 U_j}{\partial x_i \partial x_m} - \varepsilon_{ij} \frac{\partial^2 \phi}{\partial x_i \partial x_j} = 0, \end{cases} \quad (3)$$

where  $U$  — mechanical displacement,  $\rho$  — ferroelectric material mass density,  $\phi$  — electric potential,  $e$  — piezoelectric tensor which coupled with the tensor  $h$  accordingly with [5]:

$$e_{ijm} = \varepsilon_0(\varepsilon_{ij} - 1)h_{ijm}. \quad (4)$$

Substituting (1) and (2) into (3), taking into account (4) and that the electric field is a function of the spatial coordinates, we obtain the system of equations which describe elastic wave propagation in a phononic crystal:

$$\begin{cases} (C_{ijmn} + M_{ijklmn} (\varepsilon_0 \varepsilon_{ij} (E_i(x, y, z)) E_i(x, y, z))^2) \frac{\partial^2 U_m}{\partial x_j \partial x_n} + \\ + \varepsilon_0(\varepsilon_{ij} - 1) (h_{mij} - 2G_{ijmn} \varepsilon_0 \varepsilon_{ij} (E_i(x, y, z)) E_i(x, y, z)) \frac{\partial^2 \phi}{\partial x_j \partial x_m} = \rho \frac{\partial^2 U_i}{\partial t^2}, \\ \varepsilon_0(\varepsilon_{ij} - 1) (h_{ijm} - 2G_{ijmn} \varepsilon_0 \varepsilon_{ij} (E_i(x, y, z)) E_i(x, y, z)) \frac{\partial^2 U_j}{\partial x_i \partial x_m} - \varepsilon_{ij} \frac{\partial^2 \phi}{\partial x_i \partial x_j} = 0. \end{cases} \quad (5)$$

## 2.1. Numerical simulation results

We have performed 2D numerical simulations using COMSOL software.

The problem was divided into two steps. In the first step, an electric field distribution has been found by solving the electrostatic problem. In the second step, the piezoelectric problem was solved using the electric field distribution stored in the previous step. The material constants for BaTiO<sub>3</sub> were taken from [4–6].

Input IDT excited the SAW from 490 to 520 MHz bandwidth. The bias IDT has a center frequency of 500 MHz, which is defined by  $fc = V/(2p)$ , where  $V$  and  $p$  are SAW velocity in the structure and the IDT period respectively. The bias IDT electrode's width is chosen as  $p/2$ . The period  $p$  is equal to the SAW wavelength. Thus,  $p/2$  satisfies the Bragg condition and  $fc$  is the forbidden frequency. The number of electrodes in the Bias IDT is 40.

COMSOL simulation results of the electric field distribution are depicted in Fig. 2. We can see from Fig. 2 that there are edge effects on the electrodes and electric field distribution is not homogenous. These effects can be taken into account due to numerical simulation only.

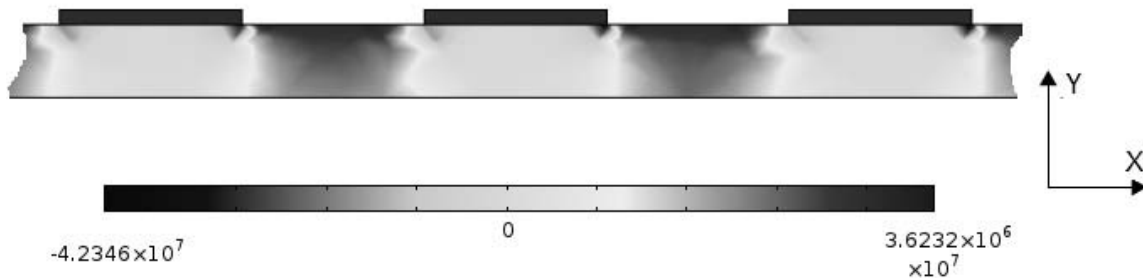


FIG. 2. Electric field (Y component) distribution in phononic crystal. Bias 5 Volts

The phononic crystal transmission coefficient as a function of frequency is shown in Fig. 3. The phononic crystal stopband is approximately 7 MHz. Dispersion curves and the

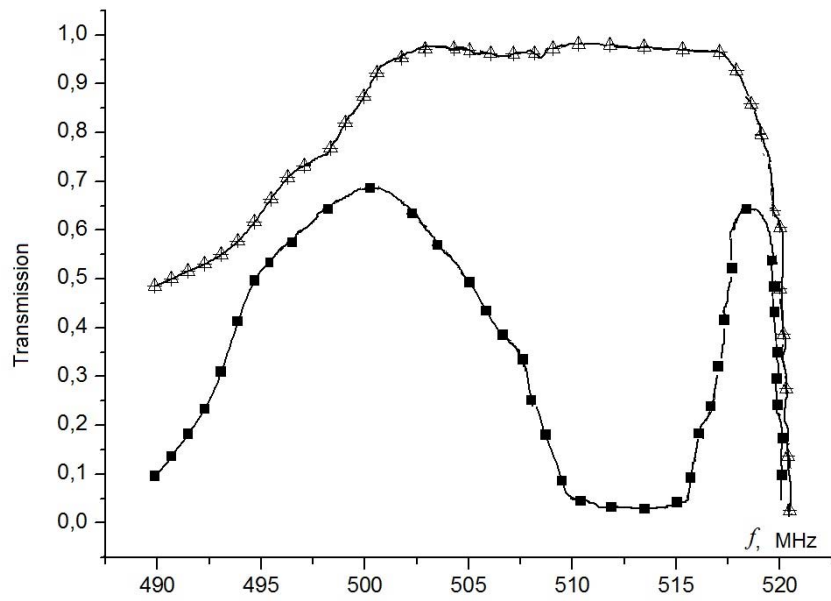


FIG. 3. SAW transmission versus frequency in phononic crystal.

▲ — Electric field off (Bias 0 V)  
 ■ — Electric field on (Bias 5 V)

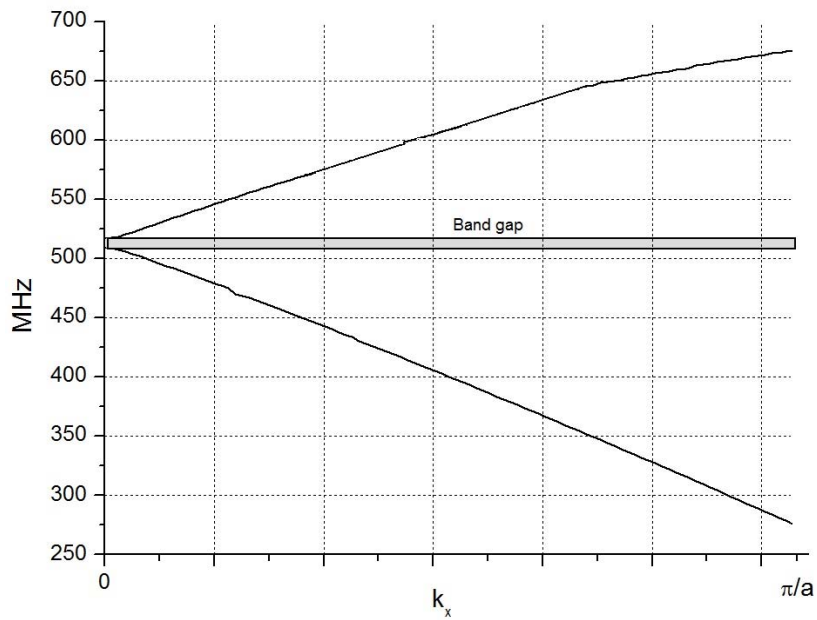


FIG. 4. Dispersion curves for SAW

band gap for two SAW modes at the first Brillouin zone are depicted in Fig. 4. Bulk acoustic wave modes are not taken into account.

### 3. Conclusion

Finite-element modeling in COMSOL software revealed the presence of a phononic band gap for surface acoustic waves in a structure consisting of electrically-induced periodic ferroelectric domains. This effect can be used in tunable surface acoustic wave filters. The influence of electric field and the number of electrodes on the band gap will be investigated further.

### References

- [1] Shi-Ning Zhu, Yong-Yuan Zhu, Yan-Qing Lu and Nai-Ben Ming. Engineering Ferroelectric Superlattice Materials and Applications. Proceedings of the 2000 12-th IEEE International Symposium, V. 1, P. 313–315.
- [2] A. V. Golenishchev-Kutuzov, V. A. Golenishchev-Kutuzov, R. I. Kalimullin. Induced domains and periodic domain structures in electrically and magnetically ordered materials. *UFN*, **170**(7), P. 697–712 (2000).
- [3] A. V. Golenishchev-Kutuzov, V. A. Golenishchev-Kutuzov, R. I. Kalimullin, A. A. Potapov. *Technical Physics Letters*, **38**(9), P. 825–827 (September 2012).
- [4] Pavel Turalchuk, Irina Vendik, Orest Vendik, John Berge. Electrically Tunable Bulk Acoustic Filters with Induced Piezoelectric Effect in BSTO Film. Proceedings of the 38-th European Microwave Conference. October 2008, Amsterdam: IEEE, P. 274–277 (2008).
- [5] John Berge and Spartak Gevorgian. Tunable Bulk Acoustic Wave Resonators Based on  $\text{Ba}_{0.25}\text{Sr}_{0.75}\text{TiO}_3$  Thin Films and a  $\text{HfO}_2/\text{SiO}_2$  Bragg Reflector. *IEEE Transactions on Ultrasonics, Ferroelectrics, and Frequency Control*, **58**, P. 2768–2771.
- [6] Andreas Noeth, Tomoaki Yamada, Alexander K. Tagantsev, Nava Setter. Electrical tuning of dc bias induced acoustic resonances in paraelectric thin films. *Journal of Applied Physics*, **104**, P. 094102-1–094102-10 (2008).
- [7] Daniel Royer, Eugene Dieulesain. *Elastic Waves in Solids Free and Guided Propagation*, V. 1. Springer, 216 pp. (2000).

# REDUCED CONDITIONAL DYNAMIC OF QUANTUM SYSTEM UNDER INDIRECT QUANTUM MEASUREMENT

A. I. Trifanov, G. P. Miroschnichenko

Saint Petersburg National Research University of Information Technologies, Mechanics and Optics, 197101, 49 Kronverksky, Saint Petersburg, Russia

alextrifanov@gmail.com, gpmirosh@gmail.com

**PACS 42.50.Ar, 42.50.Lc, 42.50.Pq**

In this report, we study the reduced conditional dynamics of a quantum system in the case of indirect quantum measurement. The detector's microscopic part (pointer) interacts with the measured system (target) and the environment, which results in a nonunitary interaction between target and pointer. The quantum state evolution conditioned by the measurement result is under investigation. Particularly, we are interested in explicit analytical expressions for the conditional evolution superoperators and basic information characteristics of this measurement process, which is applied to the cavity mode photodetection problem.

**Keywords:** indirect quantum measurements, conditional evolution, photodetection problem, rotating wave approximation, quantum entropy.

## 1. Introduction

An interaction between a quantum system and the environment is one of the fundamental problems in Quantum Physics. In light of quantum communication and computation [1, 2] development, the evolution of monitored quantum systems becomes very important, though the guidelines are difficult at present. Particularly, quantum measurement [3], decoherentization and superselection [4] problems, which are significant, are closely related to the theory of open quantum system dynamics [5].

There are several approaches, which deal with quantum system evolution in the presence of the environment, e.g. the optical master equation [6], the model of quantum Brownian motion [7] and their generalizations for the cases of non Markovian dynamics [8]. In this context, different measurement models were proposed: indirect measurements, weak measurements, nondemolition measurements, etc. [3]. From a formal point of view, one can assign at least three formulations which reflect the detector's role in the quantum measurement process [9, 10]: the model of projection measurement based on the von Neumann postulate [11]; the language of "effects" and "operations" [12] and formalism based on the Feynman path integral [13, 14].

The technique of direct projective measurement is the first proposed and the simplest way to estimate the state of a quantum system. Unfortunately, during this process, we often have to cancel the system of interest. The idea of indirect measurement is to organize an interaction between the measured system and the detector's microscopic part (pointer) followed by pointer state detection. This gives a wide opportunity for quantum state preparation, unsharp and weak measurements, realization of quantum logical operations [15, 16], quantum state [17] and quantum process [18, 19] tomography.

Formally, the indirect measurement process may be described by parameterization  $(\rho_P, U_\tau, \{\Pi_x\})$  of the initial projective measurement. Here,  $\rho_P$  is initial pointer state,  $U_\tau$  is unitary operator and  $\{\Pi_x\}$  - set of projector valued measures. This may be completed by the

canonical Naimark extension [20]. This technique was successfully applied in [21] to describe the Stern-Gerlach experiment with unsharp measurement. Another way is to start from an arbitrarily suitable pointer and comparatively simple interaction and construct Positive Operator Valued Measures (POVM) corresponding to this kind of generalized detection. This method was used for the description of indirect measurement on trapped ions [22], obtaining quantum control and quantum gate realization in the QED cavity [16].

In fact, the efficiency of a measurement device is usually not exactly equal to identity [23] (not to speak of the photodetection and particularly IR region, where this quantity is quite different than unity). One can define at least two factors which are participating in this process. The first one is a classical and quantum stochastic process, which governs the behavior of the measurement apparatus. This factor may be taken into account by introducing the corresponding phenomenological probability distributions for detection events and errors [24].

The second one is a nonunitary interaction between the measured system and the microscopic part of detector (pointer), which may take place due to the interaction with the environment. This process may change detection statistics significantly. To consider it, one should construct the parameterization scheme using nonunitary evolution. Namely, instead of triple  $(\rho_P, U_\tau, \{\Pi_x\})$ , one should use  $(\rho_P, U_\tau, \{\Pi_x\})$ , where  $U_\tau = \exp(-iL\tau)$  and  $L$  is the evolution generator.

Here, we examine the situation of nonunitary evolution considering the intracavity interaction between two level atom and cavity quantum mode during the process of indirect electromagnetic field measurement. We model the process, when two level atom passes through the cavity and “collects” information about the state of quantum mode. Just after the interaction, the atomic state is determined in a selective detector, which gives one of two possible alternatives: atom is found in its ground state  $|g\rangle_A$  or in an excited state  $|e\rangle_A$ . From these results, the state of cavity quantum mode may be calculated.

The structure of this paper is organized as follows: *in section 2* we give a brief review about the conception of quantum measurement process. *Section 3* consists of the description for the model problem of intracavity quantum mode photodetection and presents the master equation in superoperator form. *In section 4* the system of differential equations for conditional superoperators is obtained and solved in two extreme cases: strong and weak relaxation limits. The basic information characteristics are presented *in section 5*. Here we show them as a function of interaction time and discuss the basic results. *Section 6* concludes the paper.

## 2. Parametrization of the Quantum Measurement Process

The goal of this section is to briefly give a review about the conception of the quantum measurement process. We will start from the ordinary case of projection measurement and define the set of projection valued measures. Then, the concept of indirect measurement will be presented and the corresponding generalization of detectors measures (POVM) will be described. At the end of this section we will introduce a parametrization scheme for indirect measurement followed by interaction between the pointer and the environment.

### 2.1. Von Neumann Measurement

For complete specification of the measurement apparatus, a full set of projector valued measures  $\{\Pi_x\}$  should be known. Let  $B_S$  be the outcome space of this device, then for every detection result  $r \in B_S$  the probability distribution:

$$p_r = \text{Tr}_S(\rho_S \cdot \Pi_r), \quad (1)$$

may be obtained. Here,  $\rho_S$  is the quantum state of a measured system and  $Tr_S$  is the trace over its state space  $H_S$ . The completeness condition gives us:

$$\sum_r \Pi_r = I_S, \tag{2}$$

where  $I_S$  is the operator identity.

Following the von Neumann postulate, we can determine the state of the system just after the detection process with certain outcome  $r$ :

$$\rho_S \rightarrow \rho_S^r = \frac{\Pi_r \rho_S \Pi_r}{Tr[\rho_S \cdot \Pi_r]} = \frac{\Lambda_r \rho_S}{Tr[\Lambda_r \rho_S]}. \tag{3}$$

Here,  $\Lambda_r$  is state transformer. It should be emphasized that there is an ambiguity in the definition of transformers  $\Lambda_r$ , which reflects the fact that different detectors may have identical measurement statistics. So, we have to mention the equivalence class of measurement devices.

### 2.2. Indirect Measurement. Unitary Evolution

Now, we can assume that the projection measurement described above is used for state detection of some auxiliary system (pointer), which had interacted with our system just before the measurement. Let us denote the state space of ancilla by  $H_A$  and the outcome space of ancilla state detector by  $B_A$ . The triplet of parameters  $(\rho_P, U_\tau, \{\Pi_x\}_A)$  describes the change of the system state in the presence of detector which outcome is ignored:

$$\rho_S \rightarrow \tilde{\rho}_S = Tr_A [U_\tau (\rho_S \otimes \rho_P) U_\tau^\dagger]. \tag{4}$$

Here,  $Tr_A$  is a trace operation in  $H_A$ .

Additional information, obtained by using the measurement result  $r \in B_A$  of pointer state, allows one to determine the conditional state of monitored system. Let  $\Pi_r = |\varphi_r\rangle\langle\varphi_r|$ ,  $|\varphi_r\rangle \in H_A$ , then the following mapping describes the conditional evolution of quantum system:

$$\rho_S \rightarrow \rho_S^r = \langle\varphi_r| [U_\tau (\rho_S \otimes \rho_P) U_\tau^\dagger] |\varphi_r\rangle = \Xi_r \rho_S. \tag{5}$$

Due to the first Kraus representation theorem, the action of transformer  $\Xi_r$  on arbitrary state  $\rho_S$  may be written as follows:

$$\Xi_r \rho_S = \sum_j M_j^r \rho_S M_j^{r\dagger}, \tag{6}$$

where  $M_j^r$  is bounded (Kraus) operators. If  $\rho_P = |in\rangle\langle in|$ , we can write for them:

$$M_j^r = a(j|r) \langle\varphi_j| U_\tau |in\rangle, \tag{7}$$

where  $a(j|r)$  is the amplitude of conditional probability to find pointer in state  $\varphi_j$  if detection result  $\varphi_r$  is obtained (for an imperfect measurement apparatus).

There is a direct but nontrivial way to calculate the Kraus operators in the case of unitary evolution between system and pointer. Let  $H_{int}$  be their interaction Hamiltonian. Substituting the evolution operator decomposition:

$$U(t) = \sum_{i,r \in B_A} |\varphi_i\rangle\langle\varphi_r| M_{i,r}(t), \tag{8}$$

into the Schrödinger equation:

$$i \frac{d}{dt} U(t) = H_{int} U(t), \quad U(0) = I, \quad (9)$$

we can obtain the following system of differential equations, which determine the time evolution of Kraus operators  $M_{i,r}(t)$  (index  $i$  corresponds to the initial atomic state whereas  $r$  corresponds to detected state):

$$i \frac{d}{dt} M_{i,r}(t) = \sum_{k \in B_A} \langle \varphi_i | H_{int} | \varphi_k \rangle \cdot M_{k,r}(t).$$

Its complexity depends on the algebra structure which obey the operators  $\langle \varphi_i | H_{int} | \varphi_r \rangle$ . For some cases, we can find exact analytical solution for them, but in general, it is quite a nontrivial problem.

### 2.3. Indirect Measurement. Nonunitary Evolution

Interaction between the pointer and the environment leads to a nonunitary common reduced evolution of both target and pointer. To take it into account, the triplet  $(\rho_P, U_\tau, \{\Pi_x\})$  is introduced. For convenience, in future discussion, the superoperator representation for density matrix is used:

$$\rho_P = |in\rangle\langle in| = |in\rangle. \quad (10)$$

In the following, we will assume that a secular approximation is established. Namely, the typical time scale of the intrinsic evolution of the pointer is large compared to the time over which it's state varies appreciably due to interaction with the environment. Under this approximation, description of the measurement process formally is the same as in the previous subsection. Namely, secular approximation allows the following decomposition of superoperator  $U_\tau$ :

$$U_\tau = \sum_{i,r \in B} |\varphi_i\rangle\langle\langle \varphi_r | \mathfrak{M}_{i,r}(\tau), \quad (11)$$

where we write  $\mathfrak{M}_{i,r}$  instead of  $M_{i,r}$  underlining that  $\mathfrak{M}_{i,r}$  is superoperator (transformer) and  $\mathfrak{M}_{i,r} = \Xi_r$  for initial conditions, indexed by  $i \in B_A$ . Substitution of equation (11) into the master equation for the diagonal density matrix (rotating wave approximation):

$$i \dot{\rho}^d(t) = L \rho^d(t)$$

gives the following system of differential equations for superoperators  $\mathfrak{M}_{s,r}$ :

$$i \dot{\mathfrak{M}}_{i,r}(t) = \sum_{k \in B_A} \langle\langle \varphi_i | L | \varphi_k \rangle\rangle \mathfrak{M}_{k,r}(t). \quad (12)$$

For every fixed  $i$  we obtain the closed system for  $\mathfrak{M}_{i,r}$ . In the next section, this formalism will be applied to the indirect photodetection problem.

### 3. Master Equation

Here, we will apply the indirect measurement model, followed by nonunitary interaction, to the problem of intracavity mode photodetection. The master equation in this case has the Lindblad form:

$$i\dot{\rho} = L\rho = [H_{int}, \rho] + iD_A\rho, \quad (13)$$

where  $H_{int}$  is the Jaynes-Cummings Hamiltonian:

$$H_{int} = \Omega\sigma_+a \exp(i\Delta t) + m\Omega^*\sigma_-a^\dagger \exp(-i\Delta t), \quad (14)$$

$D_A$  is the atomic ‘‘dissipater’’

$$D_A\rho = \gamma_{ge}/2(2\sigma_-\rho\sigma_+ - \sigma_+\sigma_-\rho - \rho\sigma_+\sigma_-) + \gamma_{eg}/2(c.c.), \quad (15)$$

and the following notations are used:  $\Omega$  is a coupling between atom and mode,  $\sigma_+ = |e\rangle\langle g|$  and  $\sigma_- = |g\rangle\langle e|$  are atomic operators,  $a$  is an annihilation operator of cavity mode,  $\Delta$  is detuning,  $\gamma_{ge}$  and  $\gamma_{eg}$  are atomic population relaxation rates. Also it is more convenient to write the dissipater in superoperator form:

$$(D_A\rho)_{j,k} = \begin{cases} -\rho_{jk}\Gamma_{jk}, & \Gamma_{jk} = \Gamma_{kj} = \Gamma, \quad j \neq k; \\ \sum_{q \in \{g,e\}} (\gamma_{qk}\rho_{qq} - \gamma_{kq}\rho_{kk}), & j = k, \end{cases} \quad (16)$$

where we introduce nonzero phase relaxation rate  $\Gamma$ .

Let  $B_A = \{g, e\}$  be a set of results of atomic state detection. Here, we will assume the ideal (projective) measurement of pointer state. Using density operator decomposition:

$$\rho_{AF}(t) = \sum_{\mu, \nu \in B_A} |\mu\rangle\langle \nu| \otimes \rho_{\mu\nu}(t), \quad (17)$$

in (13), one can obtain a system of differential equations for matrix elements of the density operator  $\rho_{AF}$  in atomic basis:

$$\begin{aligned} \dot{\rho}_{gg} &= -i(\Omega^*a^\dagger\rho_{eg}e^{-i\Delta t} - \Omega\rho_{ge}ae^{i\Delta t}) + \gamma_{eg}\rho_{ee} - \gamma_{ge}\rho_{gg}, \\ \dot{\rho}_{ge} &= -i(\Omega^*a^\dagger\rho_{ee}e^{-i\Delta t} - \Omega^*\rho_{gg}a^\dagger e^{-i\Delta t}) - \Gamma_{ge}\rho_{ge}, \\ \dot{\rho}_{eg} &= -i(\Omega a\rho_{gg}e^{i\Delta t} - \Omega\rho_{ee}ae^{i\Delta t}) - \Gamma_{eg}\rho_{eg}, \\ \dot{\rho}_{ee} &= -i(\Omega a\rho_{ge}e^{i\Delta t} - \Omega^*\rho_{eg}a^\dagger e^{-i\Delta t}) + \gamma_{ge}\rho_{gg} - \gamma_{eg}\rho_{ee}. \end{aligned} \quad (18)$$

The transformation  $\rho_{ge} = \tilde{\rho}_{ge}e^{-i\Delta t}$ ,  $\rho_{eg} = \tilde{\rho}_{eg}e^{i\Delta t}$  (in the following, the tilde will be dropped) and secular approximation (rotating wave approximation)  $\Gamma \gg \Omega$  ( $\dot{\rho}_{ge} = \dot{\rho}_{eg} = 0$ ), gives the following closed system of differential equations for diagonal elements  $\rho_{gg}(t)$  and  $\rho_{ee}(t)$  of density matrix:

$$\begin{aligned} \dot{\rho}_{gg} &= \kappa\Gamma(2a^\dagger\rho_{ee}a - \rho_{gg}a^\dagger a - a^\dagger a\rho_{gg}) - i\kappa\Delta[a^\dagger a, \rho_{gg}] + \gamma_{eg}\rho_{ee} - \gamma_{ge}\rho_{gg}, \\ \dot{\rho}_{ee} &= \kappa\Gamma(2a\rho_{ee}a^\dagger - \rho_{gg}aa^\dagger - aa^\dagger\rho_{gg}) - i\kappa\Delta[a^\dagger a, \rho_{ee}] + \gamma_{ge}\rho_{gg} - \gamma_{eg}\rho_{ee}. \end{aligned} \quad (19)$$

which may be written as:

$$\dot{\rho}^d(t) = L'\rho^d(t), \quad (20)$$

where  $\rho^d(t) = \text{diag}\{\rho_{gg}(t), \rho_{ee}(t)\}$  and  $\kappa = |\Omega|^2 / (\Gamma^2 + \Delta^2)$ .

To obtain the analytical expression for  $L'$  in superoperator form, let us introduce the following superoperators, which act on the density matrix of cavity field:

$$K_0\rho_F = \frac{1}{2}(a^\dagger a\rho_F + \rho_F a a^\dagger), \quad K_+\rho_F = a^\dagger\rho_F a, \quad K_-\rho_F = a\rho_F a^\dagger, \quad N\rho_F = [a^\dagger a, \rho_F], \quad (21)$$

and obey the commutation relations of  $SU(1, 1)$  algebra:

$$\begin{aligned} [K_-, K_+] &= 2K_0, & [K_0, K_+] &= K_+, & [K_0, K_-] &= -K_-, \\ [K_0, N] &= [K_+, N] = [K_-, N] &= 0. \end{aligned} \quad (22)$$

Also, for the following, it is convenient to introduce atomic superoperators  $\theta_{jk}$ :

$$\theta_{jk}\rho = |j\rangle\rangle\langle\langle k| \rho = |j\rangle\langle k| \rho |k\rangle\langle j|. \quad (23)$$

With these notations, we can write evolution equation in Lowville form (20) with

$$L' = L_0 + L_r, \quad (24)$$

where

$$\begin{aligned} L_0 &= -\kappa\Gamma \left[ K_0(\theta_{gg} + \theta_{ee}) + \frac{1}{2}(\theta_{ee} - \theta_{gg}) - K_+\theta_{ge} - K_-\theta_{eg} \right] - i\kappa\Delta N(\theta_{gg} - \theta_{ee}), \\ L_r &= \sum_{j,k} \gamma_{jk}(\theta_{kj} - \theta_{jj}). \end{aligned} \quad (25)$$

#### 4. Superoperators of Conditional Evolution

To solve Eq. (20) with the evolution generator taken from (25), we will use evolution superoperator decomposition (11) in the following form:

$$\rho(t) = \mathfrak{A}(t)\rho(0) = \sum_{i,j \in B_A} \mathfrak{M}_{ij}(t) \otimes |\varphi_i\rangle\rangle\langle\langle \varphi_j| \rho(0). \quad (26)$$

Substituting the first part of this equality into (20) gives the differential equation for superoperator  $\mathfrak{A}(t)$ :

$$\dot{\mathfrak{A}}(t) = (L_0 + L_r)\mathfrak{A}(t), \quad \mathfrak{A}(0) = \mathfrak{S}. \quad (27)$$

Here,  $\mathfrak{S}$  is the identical superoperator. Then, using the second part of equality (26) in (27), we can write two separate systems of differential equations. One of these determines superoperators  $\mathfrak{M}_{gg}$  and  $\mathfrak{M}_{eg}$ , which describe the conditional evolution when atom was prepared in its ground state  $|g\rangle$  and detected in states  $|g\rangle$  and  $|e\rangle$  correspondingly. Other superoperators  $\mathfrak{M}_{eg}$  and  $\mathfrak{M}_{ee}$  describe the measurement process with an atom prepared in the excited state  $|e\rangle$ . We will solve only the first of these systems, because the method for solving the second one is identical. For the first one, we can write (dependence of  $t$  is dropped):

$$\begin{cases} \dot{\mathfrak{M}}_{gg} = -(\alpha K_0 + \beta + \gamma_{ge})\mathfrak{M}_{gg} + (\alpha K_+ + \gamma_{eg})\mathfrak{M}_{eg}, \\ \dot{\mathfrak{M}}_{eg} = (\alpha K_- + \gamma_{ge})\mathfrak{M}_{gg} - (\alpha K_0 - \beta + \gamma_{eg})\mathfrak{M}_{eg}. \end{cases} \quad (28)$$

Here,  $\alpha = \kappa\Gamma$  and  $\beta = \kappa(i\Delta N - \Gamma/2)$ . This system may also be represented in a more symmetrical way with substitution:

$$\begin{aligned}\mathfrak{M}_{gg} &= \exp[-(\alpha K_0 + \beta + \gamma_{ge})] \mathfrak{M}'_{gg}, \\ \mathfrak{M}_{eg} &= \exp[-(\alpha K_0 - \beta + \gamma_{eg})] \mathfrak{M}'_{eg},\end{aligned}\quad (29)$$

in use. In this case it may be written as follows:

$$\begin{cases} \dot{\mathfrak{M}}'_{gg} = (e^{\alpha t} K_+ + \gamma_{eg}) e^{(2\beta + \gamma_{ge} - \gamma_{eg})t} \mathfrak{M}'_{eg}, \\ \dot{\mathfrak{M}}'_{eg} = (e^{-\alpha t} K_- + \gamma_{ge}) e^{-(2\beta + \gamma_{ge} - \gamma_{eg})t} \mathfrak{M}'_{gg}. \end{cases}\quad (30)$$

It is a nontrivial problem to get the exact analytical solutions for systems (28) or (30). Here, we use two extreme cases of strong and weak relaxation to obtain approximate expressions for the superoperators  $\mathfrak{M}_{gg}$  and  $\mathfrak{M}_{eg}$  from perturbation theory up to the first order:

$$\begin{aligned}\mathfrak{M}_{gg} &= \mathfrak{M}_{gg}^{(0)} + \mathfrak{M}_{gg}^{(1)}, \\ \mathfrak{M}_{eg} &= \mathfrak{M}_{eg}^{(0)} + \mathfrak{M}_{eg}^{(1)},\end{aligned}\quad (31)$$

leaving the exact analytical solutions for subsequent research.

#### 4.1. Perturbation Theory. Strong Relaxation

In the secular approximation which we used to obtain (28), we assumed that  $|\Omega| \ll \Gamma$ , which leads to  $\kappa \ll 1$ . Let us assume now that  $\gamma_{ge} < \kappa\Gamma \approx \kappa\Delta \ll \gamma_{eg}$ , which means that the low temperature approximation is used. It gives the following system for the zero order approximation:

$$\begin{cases} \dot{\mathfrak{M}}_{gg}^{(0)} = \gamma_{eg} \mathfrak{M}_{eg}^{(0)}, \\ \dot{\mathfrak{M}}_{eg}^{(0)} = -\gamma_{eg} \mathfrak{M}_{eg}^{(0)}. \end{cases}\quad (32)$$

It has a simple analytical solution:

$$\mathfrak{M}_{gg}^{(0)} = \mathfrak{S}, \mathfrak{M}_{eg}^{(0)} = 0, \quad (33)$$

for the first order, the system has the form:

$$\begin{cases} \dot{\mathfrak{M}}_{gg}^{(1)} = \gamma_{eg} \mathfrak{M}_{eg}^{(1)} - (\alpha K_0 + \beta + \gamma_{ge}), \\ \dot{\mathfrak{M}}_{eg}^{(1)} = -\gamma_{eg} \mathfrak{M}_{eg}^{(1)} + (\alpha K_- + \gamma_{ge}), \end{cases}\quad (34)$$

and solution:

$$\begin{aligned}\mathfrak{M}_{gg}^{(1)}(t) &= (\alpha K_- + \gamma_{ge}) (e^{-\gamma_{eg}t} - 1) / \gamma_{eg} - [\alpha(K_0 - K_-) + \beta] t, \\ \mathfrak{M}_{eg}^{(1)}(t) &= (\alpha K_- + \gamma_{ge}) (1 - e^{-\gamma_{eg}t}) / \gamma_{eg}.\end{aligned}\quad (35)$$

#### 4.2. Perturbation Theory. Weak Relaxation

Here we examine another extreme case, assuming that  $\gamma_{ge} < \gamma_{eg} \ll \kappa\Gamma \approx \kappa\Delta$ , so that in the zero order of perturbation theory, we get the following system:

$$\begin{cases} \dot{\mathfrak{M}}_{gg}^{(0)} = -(\alpha K_0 + \beta) \mathfrak{M}_{gg}^{(0)} + \alpha K_+ \mathfrak{M}_{eg}^{(0)}, \\ \dot{\mathfrak{M}}_{eg}^{(0)} = \alpha K_- \mathfrak{M}_{gg}^{(0)} - (\alpha K_0 - \beta) \mathfrak{M}_{eg}^{(0)}. \end{cases}\quad (36)$$

From straightforward calculations, one can obtain:

$$\ddot{\mathfrak{M}}_{eg}^{(0)} + \alpha(2K_0 + 1) \dot{\mathfrak{M}}_{eg}^{(0)} + (\alpha^2 C - \beta(\alpha + \beta)) \mathfrak{M}_{eg}^{(0)} = 0, \quad (37)$$

where  $C = K_0^2 - K_0 - K_+K_-$  is the Casimir operator. Notice, that all coefficients in (37) are commute, so we can solve it as an ordinary second order differential equation. The characteristic roots are:

$$\mu_{1,2} = \frac{1}{2} \left( \pm\sqrt{D} - \alpha (2K_0 + 1) \right), \tag{38}$$

where  $D = 2\alpha^2 (K_+K_- + K_-K_+) + (\alpha + 2\beta)^2 + 4\alpha^2 K_0$ , and the solution may be written as:

$$\mathfrak{M}_{eg}^{(0)}(t) = \alpha (e^{\mu_1 t} - e^{\mu_2 t}) \left( \sqrt{D} \right)^{-1} K_-. \tag{39}$$

To obtain expression for  $\mathfrak{M}_{gg}(t)$ , we use the following substitution:

$$\mathfrak{M}'_{gg}^{(0)} = \alpha K_+ e^{(\alpha-a)t} \mathfrak{M}_{eg}^{(0)},$$

which leads to

$$\mathfrak{M}_{gg}^{(0)} = e^{-(\alpha K_0 + \beta)t} \left\{ 1 + \alpha^2 K_+ \left[ \lambda_1^{-1} (e^{\lambda_1 t} - 1) + \lambda_2^{-1} (e^{\lambda_2 t} - 1) \right] \sqrt{D^{-1}} K_- \right\},$$

where  $\lambda_{1,2} = \mu_{1,2} + \alpha - a = \frac{\alpha \pm \sqrt{D}}{2} + \beta$ .

In the first order of perturbation theory, we get the following system:

$$\begin{cases} \mathfrak{M}'_{gg}^{(1)} = -(\alpha K_0 + \beta) \mathfrak{M}_{gg}^{(1)} + \alpha K_+ \mathfrak{M}_{eg}^{(1)} + \gamma_{eg} \mathfrak{M}_{eg}^{(0)}, \\ \mathfrak{M}'_{eg}^{(1)} = \alpha K_- \mathfrak{M}_{gg}^{(1)} - (\alpha K_0 - \beta) \mathfrak{M}_{eg}^{(1)} - \gamma_{eg} \mathfrak{M}_{eg}^{(0)}. \end{cases} \tag{40}$$

Repeating the same procedure as in the zero order solution and using method of variation of parameters, one can obtain the following first order solution:

$$\begin{aligned} \mathfrak{M}_{eg}^{(1)}(t) = \gamma_{eg} D^{-1} \{ (\lambda_1 + \lambda_2) \mathfrak{M}_{eg}^{(0)}(t) - \alpha t (\lambda_1 e^{\mu_1 t} - \lambda_2 e^{\mu_2 t}) K_- \} \\ + \gamma_{eg} \int_0^t \mathfrak{M}_{eg}^{(0)}(t - \tau) \mathfrak{M}_{eg}^{(0)}(\tau) d\tau, \end{aligned} \tag{41}$$

$$\begin{aligned} \mathfrak{M}_{gg}^{(1)}(t) = \alpha^2 \gamma_{eg} K_+ D^{-3/2} [(\lambda_1 + \lambda_2) (e^{\mu_1 t} / \lambda_1 - e^{\mu_2 t} / \lambda_2) \\ + (\lambda_1 + \lambda_2) (\mu_1 - \mu_2) e^{-(\alpha K_0 + \alpha + \beta)t} / \lambda_1 \lambda_2 - (\mu_1 - \mu_2) (e^{\mu_1 t} + e^{\mu_2 t}) t] K_- \\ + \alpha \gamma_{eg} K_+ \int_0^t \int_0^\tau e^{-(\alpha K_0 + \alpha + \beta)(t - \tau)} \mathfrak{M}_{eg}^{(0)}(\tau - \theta) \mathfrak{M}_{eg}^{(0)}(\theta) d\theta d\tau. \end{aligned} \tag{42}$$

### 5. Information Characteristics of Photodetection Process

Here, the basic information characteristics of the photodetection process will be investigated in the bounds of the model discussed above. The following quantities are of most interest: probability of certain detection result  $r \in \{g, e\}$ :

$$P_r(t) = Tr_F [\mathfrak{M}_{rg}(t) \rho_F], \tag{43}$$

information gain  $I_r = -\Delta H$  as a measure of entropy change resulting from photodetection:

$$\Delta H = \rho_F^r \log \rho_F^r - \rho_F \log \rho_F \tag{44}$$

and fidelity:

$$F_r = \sqrt{\sqrt{\rho_F} \rho_F^r \sqrt{\rho_F}}, \quad (45)$$

which characterizes the state change caused by the measurement process.

These quantities are shown on Fig.1 – Fig.4 as functions of time interaction  $\tau$  for different dimensions of cavity mode state space. Fig. 1 and Fig. 2 show the results obtained from the strong relaxation approximation, while Fig 3 and Fig 4 show these dependences for the case of weak relaxation limit. For each approximation, two initial states are tested: completely mixed state  $\rho_F = 1/d$  and Fock state  $\rho_F = |n\rangle\langle n|$ . Here,  $d$  is the dimension of the cavity mode state space and  $n \leq d$  is the number of photons in cavity mode (cases  $d = 2, 4, 6$  and  $n = 1, 3, 5$  are depicted). We investigate the case of conditional reduced density matrix evolution, which corresponds to the detection result,  $r = g$ . The top rows of the graphs in each figure represent information characteristics in different approximations, while the bottom rows in Fig.1 and Fig. 2 show the field density matrix elements in certain moment ( $\Omega\tau = 0, 10, 50$ ) in the case  $d = 4$  (or  $n = 3$ ).

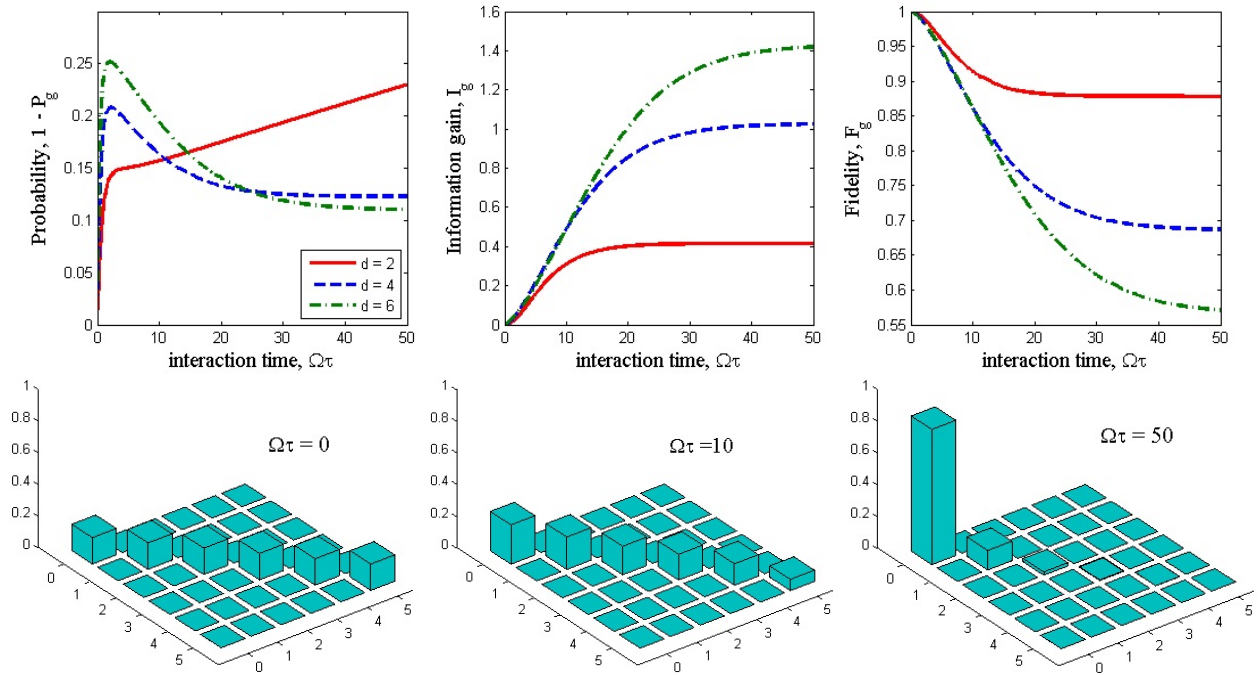


FIG. 1. Ground state detection: probability, information gain and fidelity as a functions of interaction time for mixed state  $\rho_F = 1/d$  (top); density matrix elements ( $d = 4$ ) at the moments  $\Omega\tau = 0, 10, 50$  (bottom). Strong relaxation approximation.

The first graph in each of the top rows shows the probability  $1 - P_g = P_e$  to detect atom in its non-ground state. In strong relaxation, the limit (Fig. 1 and Fig. 2) curves corresponding to interaction with several photons (blue dotted and green chain lines) tend to approach a constant nonzero value due to the nonzero atomic spontaneous excitation. In the case of interaction with only one photon in the cavity mode (red solid line) the probability to detect an atom in its excited state increases with time because of the comparatively weak atom-field interaction. For the weak relaxation limit, all curves tends to some constant value.

The second graph in each of top rows shows the information gain as a function of time. The behavior of this dependence for the cases of initially mixed (Fig. 1 and Fig. 3) and

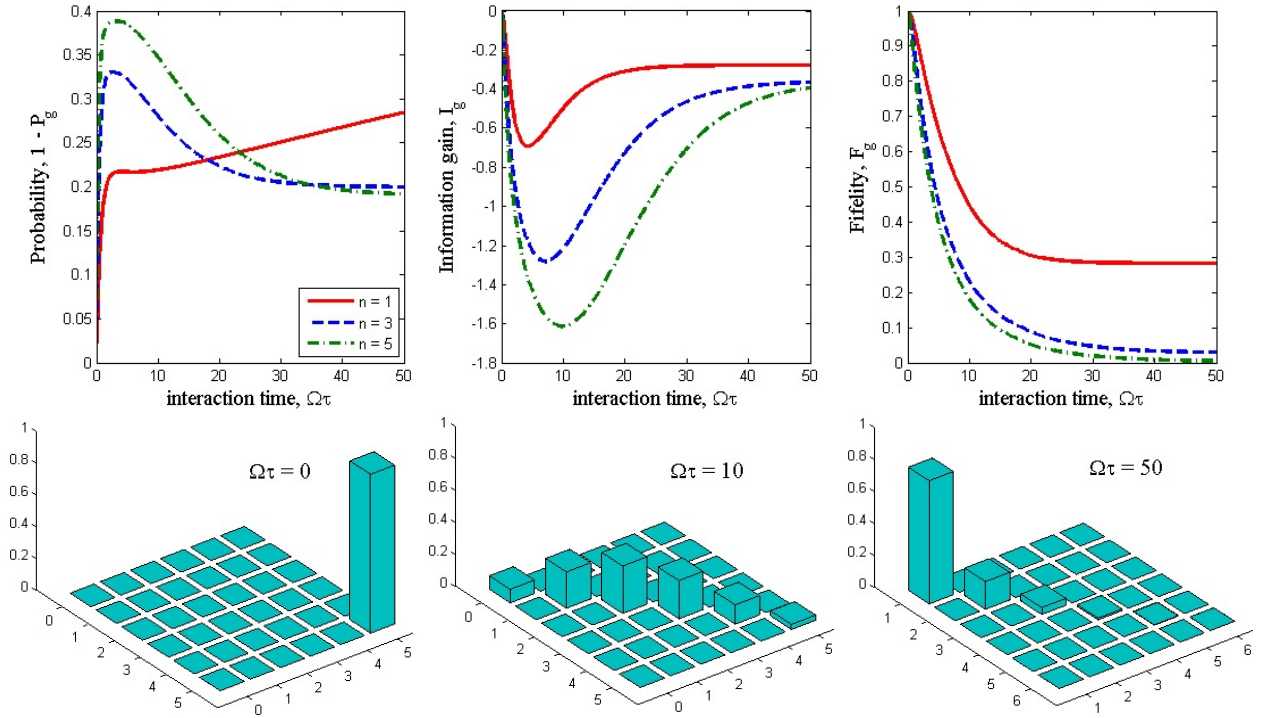


FIG. 2. Ground state detection: probability, information gain and fidelity as a functions of interaction time: for Fock state  $\rho_F = |n\rangle\langle n|$  (top); density matrix elements ( $n = 3$ ) at the moments  $\Omega\tau = 0, 10, 50$  (bottom). Strong relaxation approximation.

Fock states (Fig. 2 and Fig. 4) are completely different. For the initial mixed state in strong relaxation limit, all curves increase monotonically because this state has maximum entropy and tend to some constant value, which corresponds to the final vacuum state (with zero entropy). For the mode prepared in the Fock state and in the same limit, initial entropy is zero and rises due to common evolution with the atom. Finally, all curves tend to the vacuum value, which surely has zero entropy, but due to the nonzero spontaneous atomic excitation, the resulting state has a constant non-vanishing value of entropy. These dependences for the weak relaxation limit may be explained in the same way.

Finally, the third graph in each of the top rows shows the detection fidelity as a function of time. It is interesting to investigate the stationary limit of these dependences in strong relaxation approximation. In this approximation, all curves decay monotonically, which corresponds to an irreversible state change. For the field prepared in the completely mixed state, the stationary value is nonzero for all cases because the mixed state and the final vacuum state are nonorthogonal. For the case of Fock state initially prepared, the curves tends to approach zero with the increased photon numbers. This may be explained by the orthogonality of the initial and final states. But, due to spontaneous excitation, the probability to detect an atom in its excited state is nonzero and superoperators of conditional evolution transform the density matrix to its final state, which is not orthogonal to its initial state. That is why all curves tend to approach small but nonzero value.

In the weak relaxation limit for the considered interaction times, stationary limits are not obtained. In this approximation (see bottom rows in Fig.3 and Fig.4), we compare the numerical

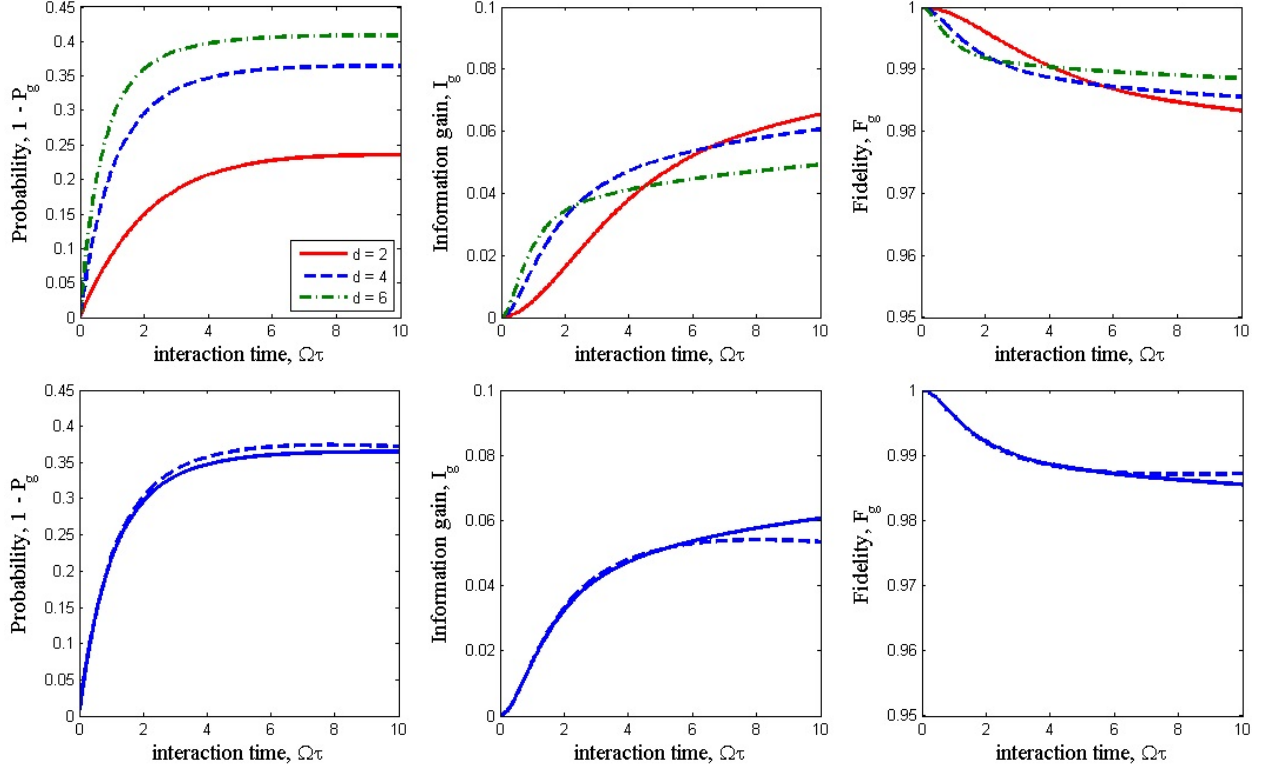


FIG. 3. Ground state detection: probability, information gain and fidelity as a functions of interaction time: for mixed state  $\rho_F = 1/d$  (top); numerical simulations (solid line) and analytical solution (dashed line) for the case  $d = 4$ . Weak relaxation approximation.

simulation and the analytical solution (42) results for the case  $d = 4$  ( $n = 3$ ). Here, we used the quadrature method to calculate the integral in (42).

For numerical modeling, the following values of parameters are used (in unit  $\gamma_{eg} = 1$ ):  $\gamma_{ge} = 0.1$ ,  $\gamma_{eg} = 1$ ,  $\Gamma = 2$ ,  $\Delta = 0.5$  and  $\Omega = 0.7$  (for strong relaxation limit);  $\gamma_{ge} = 0$ ,  $\gamma_{eg} = 0.01$ ,  $\Gamma = 2$ ,  $\Delta = 0.5$  and  $\Omega = 0.7$  (for weak relaxation limit).

## 6. Conclusion

The parametrization of the measurement process in the presence of a nonunitary evolution was investigated. Interaction between the pointer and the environment was discussed and applied to the quantum photodetection problem. Basic characteristics of measurement process as a function of interaction time for two approximations were obtained. Properties of superoperators corresponded to different measurement results may be used for finding special regimes of detection: measurement without state or entropy change from one side and detection with best information gain from another. The generalization of previous description beyond secular approximation (quantum Brownian motion) will be considered in the future. It is attractive to obtain detector superoperators from evolution generator, though it requires deep analysis of their algebraic properties.

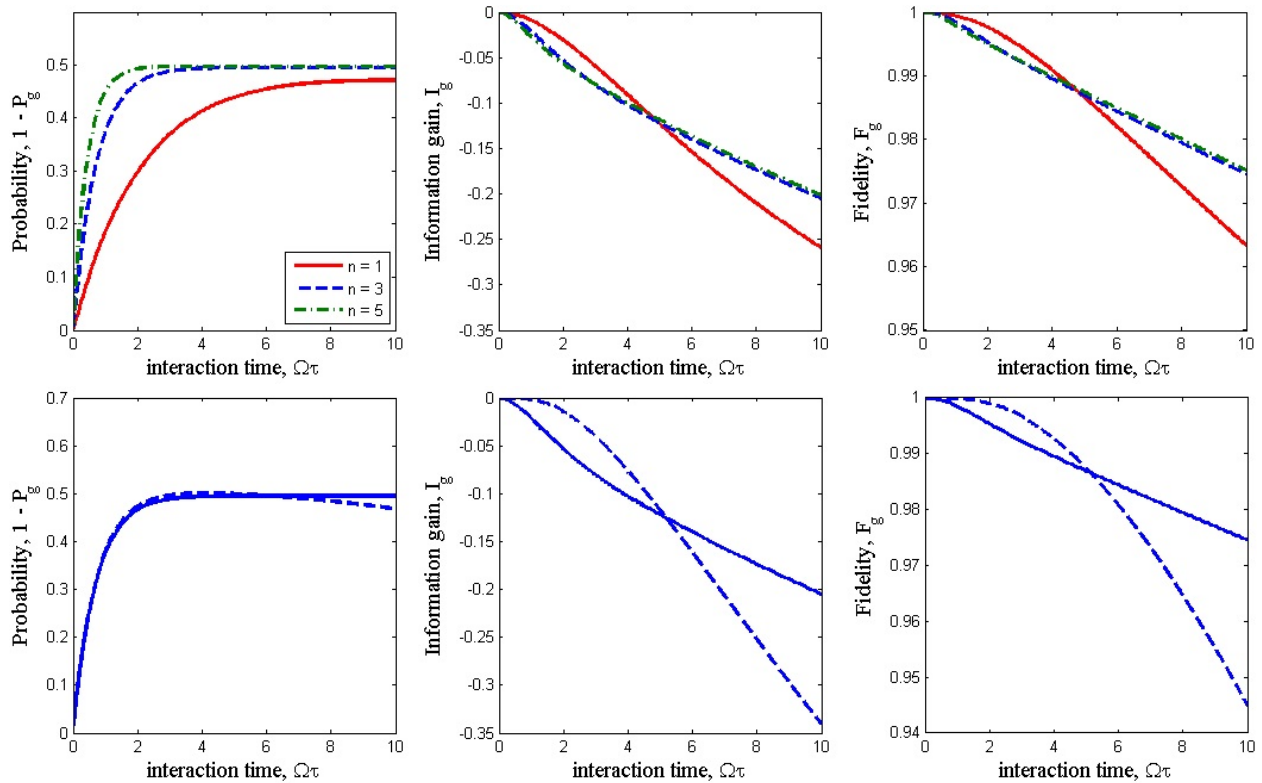


FIG. 4. Ground state detection: probability, information gain and fidelity as functions of interaction time: for mixed state for Fock state  $\rho_F = |n\rangle\langle n|$  (top); numerical simulations (solid line) and analytical solution (dashed line) for the case  $n = 3$ . Weak relaxation approximation.

## Acknowledgements

The study was supported by the Ministry of education and science of Russian Federation, project No. 14.B37.21.0371 and President of Russian Federation grant for young Russian scientists MK –1493.2013.1.

## References

- [1] M.A. Nielsen, I.L. Chuang. *Quantum Computation and Quantum Information*, Cambridge University Press, Cambridge, 2001.
- [2] C.A. Perez-Delgado, P. Kok. Quantum computers: Definition and implementations. *Phys. Rev. A*, **83** (1), P. 012303(15) (2011).
- [3] V.B. Braginsky, F.Ya. Khalili. *Quantum Measurement*, Cambridge University Press, Cambridge, 1992.
- [4] W.H. Zurek. Decoherence, einselection, and the quantum origins of the classical. *Rev. Mod. Phys.*, **75** (3), P. 715(61) (2003).
- [5] H.-P. Breuer, F. Petruccione. *The theory of open quantum systems*, Oxford University Press Inc., New York, 2002.
- [6] H. Carmichael. *An open system approach to quantum optics*, Springer-Verlag Berlin Heidelberg New York, 1991.
- [7] H. Grabert, P. Schramm, G.-L. Ingold. Quantum Brownian motion: The functional integral approach. *Phys. Rep.*, **168**, P. 115–207 (1988).
- [8] T. Mančal, V. May. Non-Markovian relaxation in an open quantum system. *EPJ B*, **18** (4), P. 633–643 (2000).
- [9] C.M. Caves. Quantum mechanics of measurements distributed in time. II Connections among formulations. *Phys. Rev. D*, **35** (6), P. 1815–1830 (1987).

- [10] C.M. Caves. Quantum mechanics of measurements distributed in time. A path-integral formulation. *Phys. Rev. D*, **33** (6), P. 1643–1665 (1986).
- [11] J. von Neumann. *Mathematical foundations of quantum mechanics*. Trans. by R.T. Beyer. Princeton: Unive. Press, 1955.
- [12] K. Kraus. *States, Effects and Operations. Fundamental notions of quantum theory*, Springer-Verlag Berlin Heldeiberg, 1983.
- [13] R.P. Feinman. Space-time approach to non-relativistic quantum mechanics. *Rev. Mod. Phys.*, **20** (2), P. 367–387 (1948).
- [14] M.B. Mensky. *Continuous quantum measurements and path integrals*, IOP Publishing Ltd., London, 1993.
- [15] Jun-Tao Chang, M. Suhail Zubairy. Three-qubit phase gate based on cavity quantum electrodynamics. *Phys. Rev. A*, **77** (1), P. 012329(8) (2008).
- [16] G.P. Miroshnichenko, A.I. Trifanov. Conditional phase shift for quantum CCNOT operation. *Quantum Inf. Process.*, **12** (3), P. 1417–1428, 2013.
- [17] A. Shukla, K.R.K. Rao, T.S. Mahesh. Ancilla-assisted quantum state tomography in multiqubit registers. *Phys. Rev. A*, **87** (6), P. 062317 (8) (2013).
- [18] A. Bendersky, F. Pastawski, J.P. Paz. Selective and Efficient Estimation of Parameters for Quantum Process Tomography. *Phys. Rev. Lett.*, **100**, P. 190403(4) (2008).
- [19] Seth T. Merkel et al. Self-consistent quantum process tomography. *Phys. Rev. A*, **87** (6), P. 062119(9) (2013).
- [20] M.A. Naimark. About second-kind self-adjoint extensions of symmetrical operator. *Izv. Akad. Nauk USSR, Ser. Mat.*, **4**, P. 53–104 (in russian) (1940).
- [21] C. Sparaciari, M.G.A. Paris. Canonical Naimark extension for generalized measurements involving sets of Pauli quantum observables chosen at random. *Phys. Rev. A*, **87** (1), P. 012106(7) (2013).
- [22] Sujit K. Choudhary, T. Konrad, H. Uys. Implementation schemes for unsharp measurements with trapped ions. *Phys. Rev. A*, **87** (1), P. 012131(8) (2013).
- [23] A.V. Dodonov, S.S. Mizrahi, V.V. Dodonov. Inclusion of nonidealities in the continuous photodetection model. *Phys. Rev. A*, **75** (1), P. 013806 (8) (2007).
- [24] G.P. Miroshnichenko, A.I. Trifanov. The photodetection process under the conditions of an imperfect measurement device. *EPJ D*, DOI: 10.1140/epjd/e2013-30739-8 (2013).

# DEPENDENCE OF QUANTUM YIELD OF UP-CONVERSION LUMINESCENCE ON THE COMPOSITION OF FLUORITE-TYPE SOLID SOLUTION $\text{NaY}_{1-x-y}\text{Yb}_x\text{Er}_y\text{F}_4$

D. S. Yasyrkina, S. V. Kuznetsov, A. V. Ryabova, D. V. Pominova,  
V. V. Voronov, R. P. Ermakov, P. P. Fedorov

A. M. Prokhorov General Physics Institute, Russian Academy of Sciences,  
38 Vavilov Street, Moscow, 119991, Russia

ppfedorov@yandex.ru

**PACS 78.20-e**

A study of the properties of polycrystalline fluorite-type  $\text{NaY}_{1-x-y}\text{Yb}_x\text{Er}_y\text{F}_4$  solid solutions demonstrated that  $\text{NaY}_{0.87}\text{Yb}_{0.10}\text{Er}_{0.03}\text{F}_4$  and  $\text{NaY}_{0.885}\text{Yb}_{0.1}\text{Er}_{0.015}\text{F}_4$  samples produced up-conversion luminescence with 3.35% and 3.62% quantum yields, which were higher than quantum yields of the other  $\text{NaY}_{1-x-y}\text{Yb}_x\text{Er}_y\text{F}_4$  samples.  $\text{NaY}_{1-x-y}\text{Yb}_x\text{Er}_y\text{F}_4$  specimens were prepared by co-precipitation from aqueous solutions by drop-wise addition of rare earth nitrate solutions to aqueous sodium fluoride.

**Keywords:** fluorides, nanopowders, sodium, yttrium, up-conversion luminescence, quantum yield.

## 1. Introduction

At the present time, scientists are actively looking for materials that can efficiently transform infrared light to visible light by up-conversion for photodynamic cancer therapy (PDT) [1-3]. In order to satisfy the PDT strict requirements, these materials must have a high photochemical activity (i.e., they must effectively produce reactive oxygen species when excited); their particle size should be ca. 30–80 nm; their excitation should occur at the maximal transparency of human tissue; they should possess a specificity toward target tissues and low toxicity. Among the various substances that are used for photodynamic therapy (oxides, fluorides, CdSe-based quantum dots, etc.), Yb- and/or Er-doped  $\text{NaYF}_4$  matrices maintain a special place, because of their unusually high up-conversion quantum yields [4-6].

Properties of these matrices stem from the features intrinsic to  $\text{NaYF}_4$ . According to the phase diagram of NaF-YF<sub>3</sub> [7] (Fig. 1),  $\text{NaYF}_4$  exists in the form of two phases: a high-temperature non-stoichiometric cubic phase with fluorite structure (phase *F*) and a low-temperature hexagonal phase with Gagarinite-type structure (cubic phase *F* may be prepared in metastable state by low temperature synthesis [1]).

Researchers believe that the most promising up-converter matrix is the low-temperature hexagonal  $\text{NaYF}_4$  phase, due to its high quantum yield values. This phase can be synthesized by various methods [1], but all of them require special conditions. We have shown [9] that it was possible to prepare hexagonal  $\text{NaYF}_4$  at room temperature by co-precipitation from aqueous solutions in the presence of some structure-forming substances like polyethyleneimine (PEI), but the obtained products frequently were not thermally stable and were not suitable for fluorescence studies. Literature description of the aforementioned

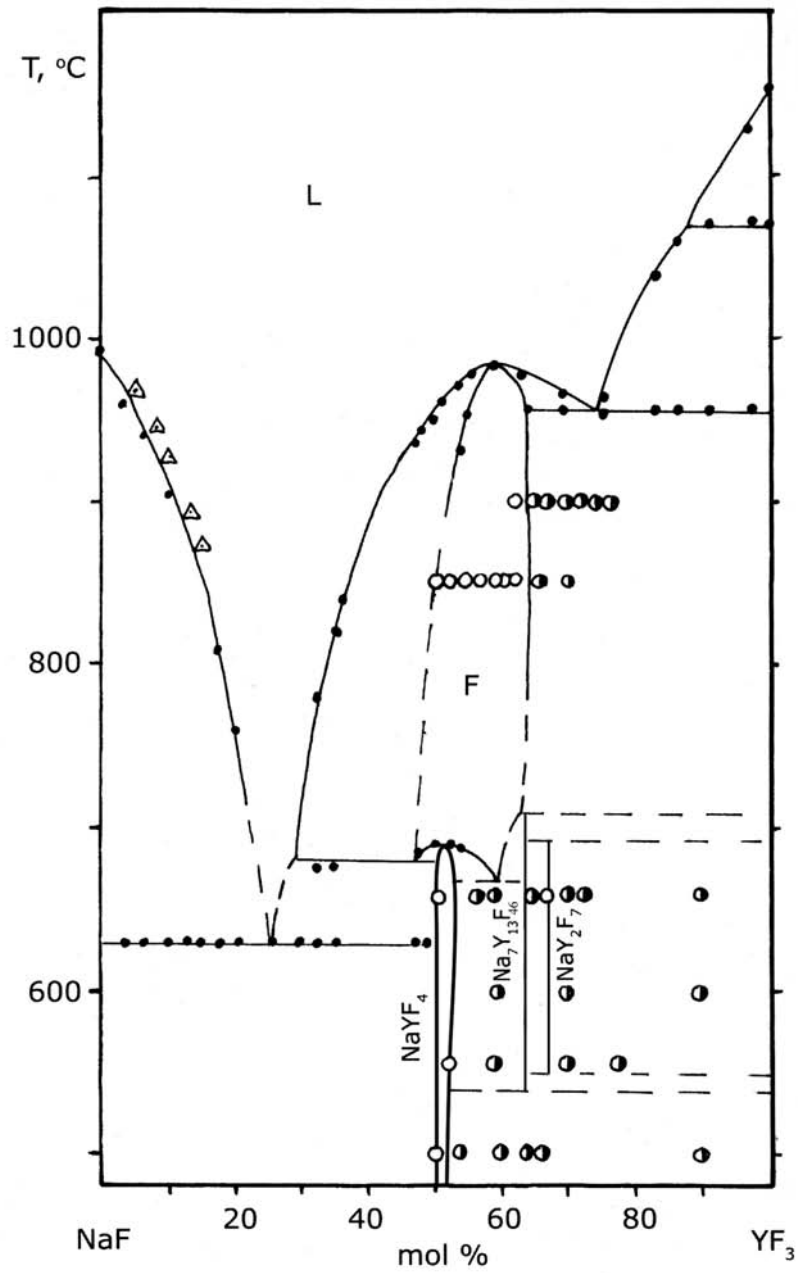


FIG. 1. NaF-YF<sub>3</sub> phase diagram [7, 8]: L — melt, F — cubic fluorite-type Na<sub>0.5-x</sub>Y<sub>0.5+x</sub>F<sub>2+2x</sub>,

- , Δ — differential thermal analysis (DTA) data,
- — single-phase samples,
- ◐ — two-phase samples (X-ray diffraction data)

doped NaYF<sub>4</sub> matrices is vast, but limited in its scope [4]. It should be noted that other researchers [1] focused their attention primarily on two compositions only, NaYF<sub>4</sub>:Yb(20 mol. %):Er(2 mol. %) and NaYF<sub>4</sub>:Yb(17 mol. %):Er(3 mol. 1%), without revealing the reasons for their choice. Also, various techniques were used to measure the quantum yields of their specimens as well as they prepared their samples by different methods [4]. As a result, the described optical materials possess different amounts of different impurities that seriously affect the obtained quantum yield data, and these circumstances make comparison of the existing literature data impossible.

Therefore, the aim of our study was a systematic research of the polycrystalline heat-resistant fluorite-type NaY<sub>1-x-y</sub>Yb<sub>x</sub>Er<sub>y</sub>F<sub>4</sub> solid solutions, prepared by the same method, in order to find dopant concentrations which yielded the highest up-conversion quantum yields.

## 2. Experimental

We used 99.99 wt. % pure Y(NO<sub>3</sub>)<sub>3</sub>·6H<sub>2</sub>O, Yb(NO<sub>3</sub>)<sub>3</sub>·6H<sub>2</sub>O, Er(NO<sub>3</sub>)<sub>3</sub>·5H<sub>2</sub>O (Lanhit, Moscow, Russia), NaF (99 wt. % pure) and double distilled water were used as starting materials. All experiments were carried out in a polypropylene reactor with polypropylene stirring bar and polypropylene solution dispensers at room temperature unless otherwise specified. Dropwise addition of the starting solutions was done under vigorous stirring. Phase compositions of the solid specimens were evaluated by X-ray diffraction (DRON-4M diffractometer; CuK $\alpha$  radiation; graphite monochromator). Calculations of the lattice parameters were done using Powder 2.0 software. We used NVision 40 workstation to record scanning electron microscopy (SEM) images of the formed nanoparticles.

Optical spectroscopy studies included the registration of up-conversion luminescence spectra at 400–900 nm and diffusely reflected excitation laser radiation, followed by calculation of the absolute quantum yields. We used our own assembly that included fiber optic LESA-01-BIOSPEC spectrometer (BIOSPEC, Russia) with a modified integrating sphere (Avantes, Netherlands) and Y-shaped fiber catheter (974 nm laser excitation wavelength; 1 W laser power output; UnoMomento processing software) [10]. The spectrometer was calibrated with LEDs of different wavelengths and known outputs as well as with LabMax®-TO power meter (Coherent, USA). Powder samples were placed between two cover slips, which were then fastened together and placed inside the integrating sphere. The scattered radiation was captured by the optical fibers connected to the spectrometer.

The quantum yield (QY) of the produced up-conversion luminescence was calculated [9] according to equation (1):

$$QY = \frac{P_{emitted}^{Sample}}{P_{974\_absorbed}^{Sample}} = \frac{P_{emitted}^{Sample}}{P_{974\_scattered}^{Reference} - P_{974\_scattered}^{Sample}}, \quad (1)$$

where:

- $P_{emitted}^{Sample}$  is power of radiation emitted by the sample and
- $P_{974\_absorbed}^{Sample}$  is the output power of 974 nm laser, absorbed by the sample. The latter is equal to the difference between:
  - $P_{974\_scattered}^{Reference}$  - the power of the scattered radiation of the reference specimen and
  - $P_{974\_scattered}^{Sample}$  - the power of the scattered radiation of the studied sample.

Reference samples were chosen among specimens containing no activator ions (e.g., intrinsic NaYF<sub>4</sub>) in order to enhance the accuracy of our measurements.

### 3. Sample preparation

Synthesis of fluoride nanopowders was done by co-precipitation from aqueous solution described in detail in [11, 12]. We used aqueous rare earth nitrates and sodium fluoride solutions of the same concentrations (0.35 M). Yttrium and dopant rare earth solutions were premixed before aqueous NaF was added to them under vigorous stirring. All experiments were carried out with 10-fold excess of NaF (calculated for  $\text{NaRF}_4$  stoichiometry). Precipitates were separated from their mother solutions by decanting. Collected precipitates were washed twice with double distilled water and dried at 35 °C under air. Calcination of the obtained samples was performed in an oven at 600 °C for 1 hour at a heating rate of 10 °C/min. In some cases, we used an Eppendorf 5804 centrifuge to separate precipitates from the mother liquors in order to reduce time of synthetic experiments.

### 4. Results and Discussion

Samples of  $\text{NaY}_{1-x-y}\text{Yb}_x\text{Er}_y\text{F}_4$  were synthesized with an Yb content ( $x$ ) which varied from 2 to 90 mol. %, and an Er content ( $y$ ) that varied from 0.5 to 20 mol. %. According to X-ray analysis, all samples contained only one fluorite-type phase (Table 1). A typical X-ray diffraction pattern of one of the synthesized samples (nominal composition  $\text{NaY}_{0.6}\text{Yb}_{0.3}\text{Er}_{0.1}\text{F}_4$ ) is shown in Fig. 2.

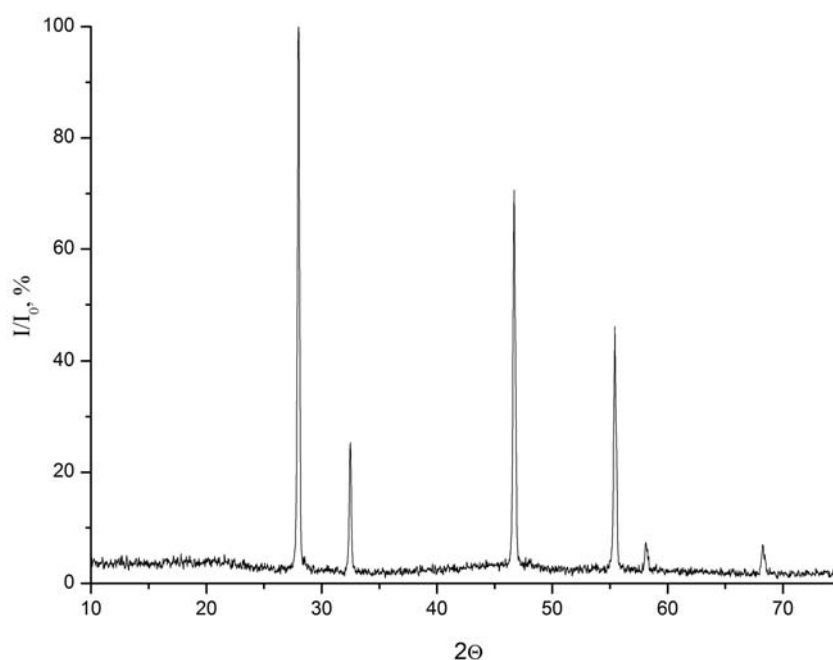


FIG. 2. Typical X-ray diffraction pattern of fluorite-type  $\text{NaY}_{0.6}\text{Yb}_{0.3}\text{Er}_{0.1}\text{F}_4$  sample

These single phase specimens contained 50–90 nm particles that formed 200–350 nm agglomerates (Fig. 3). The size of the latter is higher than the required particle size for photodynamic therapy (30–80 nm), but breaking up the agglomerates and dispersion of the individual particles were left outside of the scope of the present paper.

We evaluated  $\text{NaY}_{1-x-y}\text{Yb}_x\text{Er}_y\text{F}_4$  sample compositions with the use of correlation (2) between lattice parameter of  $\text{Na}_{0.5-x}\text{R}_{0.5+x}\text{F}_{2+2x}$  fluorite-type solid solutions and content of the rare earth ion [13]:

$$a = 5.398 + (6.7238 \times r^{cp} - 7.259) \times (x + 0.13), \quad (2)$$

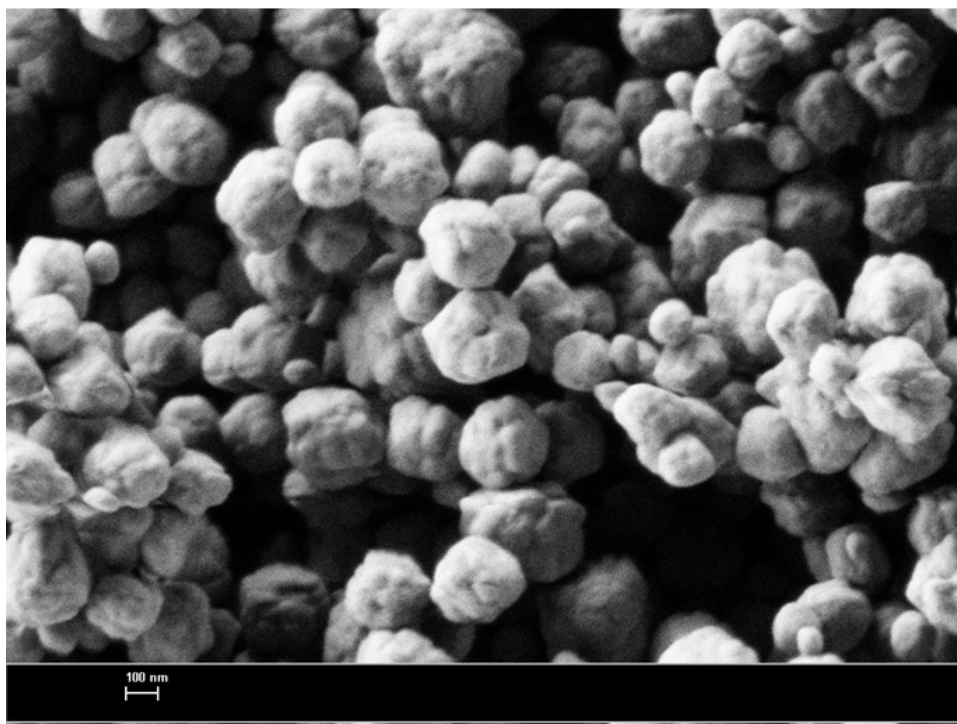


FIG. 3. Typical SEM image of the single phase sample with total  $\text{NaY}_{0.6}\text{Yb}_{0.3}\text{Er}_{0.1}\text{F}_4$  composition

where  $a$  is a cubic unit cell lattice parameter ( $\text{\AA}$ ) and  $r$  is the effective  $\text{RE}^{3+}$  ionic radius.

Because our samples were doped with ytterbium and erbium, we had to adjust the effective ionic radius of the rare-earth cation according to the following formula:

$$r_{cp} = X_Y * r_Y + X_{Yb} * r_{Yb} + X_{Er} * r_{Er}, \quad (3)$$

where  $r_Y = 1.159 \text{ \AA}$ ,  $r_{Yb} = 1.125 \text{ \AA}$ , and  $r_{Er} = 1.144 \text{ \AA}$  are ionic radii of the corresponding elements [13], and  $X_Y$ ,  $X_{Yb}$  and  $X_{Er}$  are their molar parts.

Estimated compositions of synthesized samples  $\text{Na}_{0.5-x}\text{R}_{0.5+x}\text{F}_{2+2x}$  are given in Table 1.

The quantum yield of up-conversion luminescence in the visible range of the spectrum (QY) was calculated by summarizing the integrated luminescence decay intensities corresponding to the following  $\text{Er}^{3+}$  transitions:  ${}^2\text{P}_{3/2} \rightarrow {}^4\text{I}_{11/2}$  at 480 nm;  ${}^2\text{H}_{11/2} \rightarrow {}^4\text{I}_{15/2}$  at 525 nm;  ${}^4\text{S}_{3/2} \rightarrow {}^4\text{I}_{15/2}$  at 545 nm; and  ${}^4\text{F}_{9/2} \rightarrow {}^4\text{I}_{15/2}$  at 665 nm ( $1 \text{ W/cm}^2$  the pump power density). The quantum yields of the other  $\text{Er}^{3+}$  transitions in the red region of the spectrum ( ${}^4\text{F}_{9/2} \rightarrow {}^4\text{I}_{15/2}$  at 665 nm) ( $\text{QY}_r$ ) as well as in the green region of the spectrum ( ${}^2\text{H}_{11/2} \rightarrow {}^4\text{I}_{15/2}$  at 525 nm and  ${}^4\text{S}_{3/2} \rightarrow {}^4\text{I}_{15/2}$  at 545 nm) ( $\text{QY}_g$ ) and  $f_{r/g}$  factor value, which characterizes the ratio of the intensities of the decay up-conversion luminescence in the red and green areas, were also accounted for.

The results of our studies for the up-conversion luminescence quantum yields as a function of ytterbium and erbium dopant concentrations are presented in Table 2 and Figs. 4(a,b).

The intensity of up-conversion luminescence was proportional to the amount of absorbed IR photons [14], but it exhibited a nonlinear dependency from the pump power density: quantum yields were lower at  $800 \text{ mW/cm}^2$  pump density than at  $1000 \text{ mW/cm}^2$  (Table 2).

TABLE 1. The lattice parameters of fluorite-type  $\text{NaY}_{1-x-y}\text{Yb}_x\text{Er}_y\text{F}_4$  samples, their estimated compositions and quantum yields

Samples	Sample nominal composition	Cubic lattice parameter $a$ , Å	Calculated composition, $\text{Na}_{0.5-x}\text{R}_{0.5+x}\text{F}_{2+2x}$	QY, %	QY <sub>r</sub> , %	QY <sub>g</sub> , %	$f_{r/g}$
F391	$\text{NaY}_{0.80}\text{Yb}_{0.17}\text{Er}_{0.03}\text{F}_4$	5.483(8)	$\text{Na}_{0.457}\text{R}_{0.543}\text{F}_{2.086}$	0.32	0.29	0.03	2.36
F393	$\text{NaYb}_{0.90}\text{Er}_{0.10}\text{F}_4$	5.448(1)	$\text{Na}_{0.466}\text{R}_{0.534}\text{F}_{2.068}$	0.02	0.02	< 0.01	4.11
F394	$\text{NaY}_{0.60}\text{Yb}_{0.30}\text{Er}_{0.10}\text{F}_4$	5.474(1)	$\text{Na}_{0.463}\text{R}_{0.537}\text{F}_{2.074}$	0.07	0.06	0.01	1.27
F398	$\text{NaY}_{0.20}\text{Yb}_{0.60}\text{Er}_{0.20}\text{F}_4$	5.454(1)	$\text{Na}_{0.476}\text{R}_{0.524}\text{F}_{2.048}$	0.01	0.01	< 0.01	2.28
F406	$\text{NaY}_{0.70}\text{Yb}_{0.10}\text{Er}_{0.2}\text{F}_4$	5.4861(6)	$\text{Na}_{0.477}\text{R}_{0.523}\text{F}_{2.046}$	0.05	0.05	< 0.01	2.25
F407	$\text{NaY}_{0.80}\text{Yb}_{0.10}\text{Er}_{0.10}\text{F}_4$	5.438(1)	$\text{Na}_{0.55}\text{R}_{0.45}\text{F}_{1.9}$	0.08	0.07	0.01	2.08
F442	$\text{NaY}_{0.63}\text{Yb}_{0.17}\text{Er}_{0.20}\text{F}_4$	5.474(2)	$\text{Na}_{0.459}\text{R}_{0.541}\text{F}_{2.082}$	0.22	0.19	0.03	1.49
F443	$\text{NaY}_{0.73}\text{Yb}_{0.17}\text{Er}_{0.10}\text{F}_4$	5.4840(4)	$\text{Na}_{0.451}\text{R}_{0.549}\text{F}_{2.098}$	0.04	0.04	< 0.01	2.10
F461	$\text{NaY}_{0.50}\text{Yb}_{0.30}\text{Er}_{0.20}\text{F}_4$	5.474(1)	$\text{Na}_{0.459}\text{R}_{0.518}\text{F}_{2.082}$	0.05	0.05	< 0.01	2.80
F462	$\text{NaY}_{0.67}\text{Yb}_{0.30}\text{Er}_{0.03}\text{F}_4$	5.464(3)	$\text{Na}_{0.487}\text{R}_{0.513}\text{F}_{2.026}$	0.22	0.21	0.01	3.89
F465	$\text{NaY}_{0.685}\text{Yb}_{0.30}\text{Er}_{0.015}\text{F}_4$	5.463(1)	$\text{Na}_{0.49}\text{R}_{0.51}\text{F}_{2.02}$	0.41	0.30	0.11	0.69
F471	$\text{NaY}_{0.37}\text{Yb}_{0.60}\text{Er}_{0.03}\text{F}_4$	5.4642(5)	$\text{Na}_{0.462}\text{R}_{0.538}\text{F}_{2.076}$	0.11	0.11	< 0.01	5.86
F472	$\text{NaY}_{0.385}\text{Yb}_{0.60}\text{Er}_{0.015}\text{F}_4$	5.4632(8)	$\text{Na}_{0.465}\text{R}_{0.535}\text{F}_{2.07}$	0.04	0.04	< 0.01	2.94
F473	$\text{NaY}_{0.07}\text{Yb}_{0.90}\text{Er}_{0.03}\text{F}_4$	5.446(1)	$\text{Na}_{0.482}\text{R}_{0.518}\text{F}_{2.036}$	0.07	0.07	< 0.01	5.06
F474	$\text{NaY}_{0.085}\text{Yb}_{0.90}\text{Er}_{0.015}\text{F}_4$	5.446(1)	$\text{Na}_{0.489}\text{R}_{0.511}\text{F}_{2.022}$	0.07	0.07	< 0.01	6.18
F647	$\text{NaY}_{0.95}\text{Yb}_{0.02}\text{Er}_{0.03}\text{F}_4$	5.493(7)	$\text{Na}_{0.541}\text{R}_{0.459}\text{F}_{1.918}$	0.31	0.16	0.15	0.28
F648	$\text{NaY}_{0.935}\text{Yb}_{0.05}\text{Er}_{0.015}\text{F}_4$	5.485(2)	$\text{Na}_{0.357}\text{R}_{0.643}\text{F}_{2.286}$	1.41	0.70	0.71	0.25
F685	$\text{NaY}_{0.77}\text{Yb}_{0.2}\text{Er}_{0.03}\text{F}_4$	5.476(2)	$\text{Na}_{0.47}\text{R}_{0.53}\text{F}_{2.06}$	1.53	1.11	0.42	0.67
F693	$\text{NaY}_{0.87}\text{Yb}_{0.10}\text{Er}_{0.03}\text{F}_4$	5.487(6)	$\text{Na}_{0.454}\text{R}_{0.546}\text{F}_{2.092}$	3.35	2.73	0.62	1.12
F702	$\text{NaY}_{0.885}\text{Yb}_{0.10}\text{Er}_{0.015}\text{F}_4$	5.481(2)	$\text{Na}_{0.466}\text{R}_{0.534}\text{F}_{2.068}$	3.62	2.48	1.14	0.55
F704	$\text{NaY}_{0.815}\text{Yb}_{0.17}\text{Er}_{0.015}\text{F}_4$	5.499(2)	$\text{Na}_{0.431}\text{R}_{0.569}\text{F}_{2.138}$	2.03	1.62	0.41	1.01
F740	$\text{NaY}_{0.895}\text{Yb}_{0.1}\text{Er}_{0.005}\text{F}_4$	5.4887(8)	$\text{Na}_{0.452}\text{R}_{0.548}\text{F}_{2.096}$	0.99	0.61	0.38	0.41
F741	$\text{NaY}_{0.825}\text{Yb}_{0.17}\text{Er}_{0.005}\text{F}_4$	5.4860(7)	$\text{Na}_{0.452}\text{R}_{0.548}\text{F}_{2.096}$	1.18	0.77	0.41	0.47
F743	$\text{NaY}_{0.695}\text{Yb}_{0.3}\text{Er}_{0.005}\text{F}_4$	5.4800(7)	$\text{Na}_{0.454}\text{R}_{0.546}\text{F}_{2.092}$	1.79	1.30	0.49	0.67
F744	$\text{NaY}_{0.395}\text{Yb}_{0.6}\text{Er}_{0.005}\text{F}_4$	5.464(1)	$\text{Na}_{0.463}\text{R}_{0.537}\text{F}_{2.074}$	0.56	0.51	0.05	2.55
F745	$\text{NaY}_{0.095}\text{Yb}_{0.9}\text{Er}_{0.005}\text{F}_4$	5.451(1)	$\text{Na}_{0.438}\text{R}_{0.562}\text{F}_{2.124}$	0.25	0.24	0.01	4.24

TABLE 2. Sample quantum yield at 800 mW/cm<sup>2</sup> and 1000 mW/cm<sup>2</sup> pump power

Samples	Sample nominal composition	Capacity, mW/cm <sup>2</sup>	QY, %	$f_{r/g}$	QY <sub>r</sub> , %	QY <sub>g</sub> , %
F693	$\text{NaY}_{0.87}\text{Yb}_{0.10}\text{Er}_{0.03}\text{F}_4$	800	1.10	1.38	0.93	0.17
		1000	3.35	1.12	2.73	0.62
F685	$\text{NaY}_{0.77}\text{Yb}_{0.2}\text{Er}_{0.03}\text{F}_4$	800	1.22	0.75	0.91	0.31
		1000	1.53	0.67	1.11	0.42
F702	$\text{NaY}_{0.885}\text{Yb}_{0.10}\text{Er}_{0.015}\text{F}_4$	800	2.21	0.55	1.51	0.70
		1000	3.64	0.55	2.48	1.14
F704	$\text{NaY}_{0.815}\text{Yb}_{0.17}\text{Er}_{0.015}\text{F}_4$	800	1.74	0.97	1.38	0.36
		1000	2.03	1.01	1.62	0.41

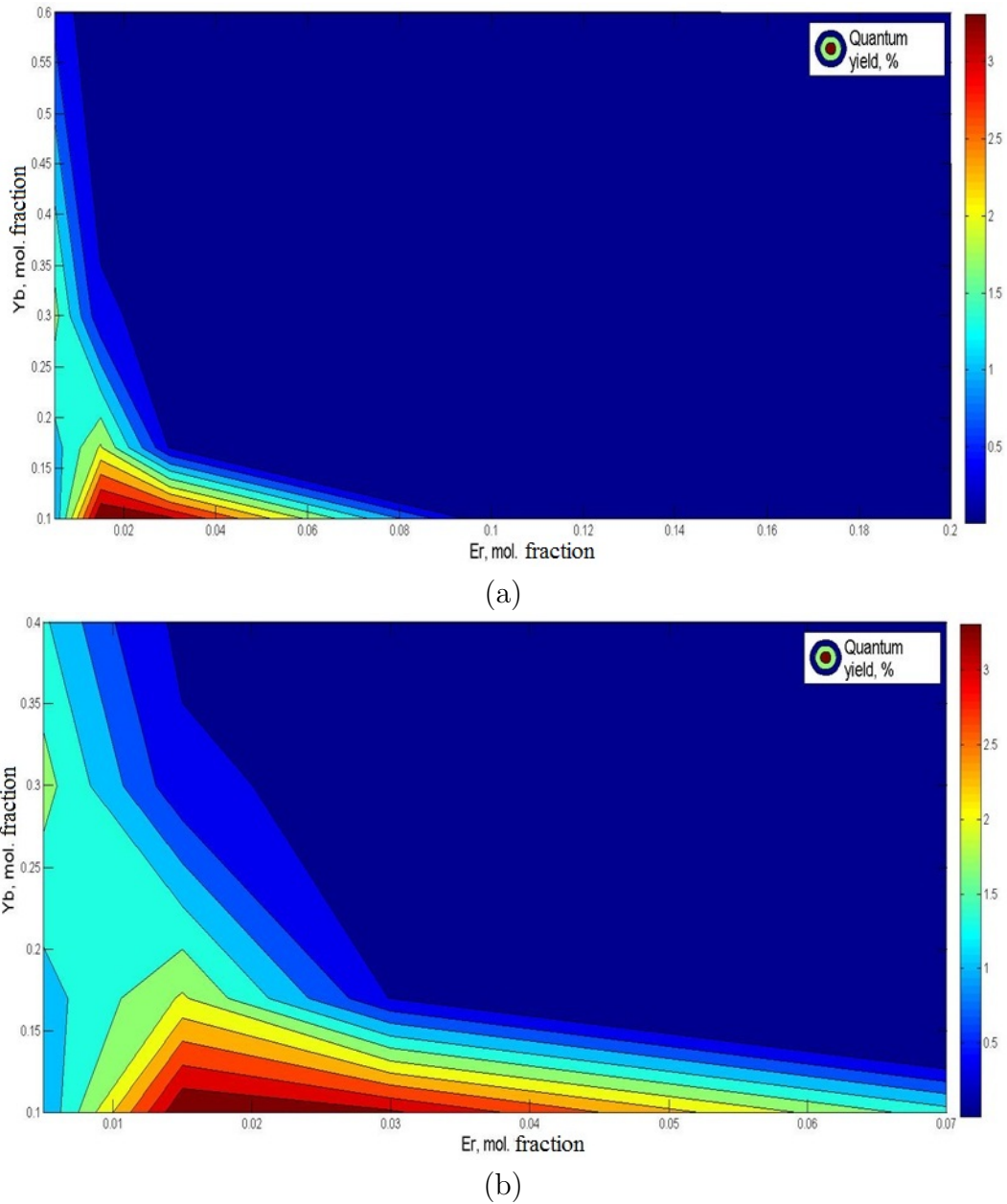


FIG. 4. The color-coded absolute quantum yields of the up-conversion luminescence  $\text{NaY}_{1-x-y}\text{Yb}_x\text{Er}_y\text{F}_4$  samples vs. doping Yb and Er concentrations: 0.1–0.6 mol. fraction Yb and 0–0.2 mol. fraction Er (a); 0.1–0.4 mol. fraction Yb and 0.005–0.07 mol. fraction Er (b)

Fig. 4 data clearly indicated the composition area with the highest quantum yields correspond to the samples containing 0.5–3 mol. % Er and 10–20 mol. % Yb as well as about 0.15 mol. % Er and about 10 mol. % Yb.  $\text{NaY}_{0.87}\text{Yb}_{0.10}\text{Er}_{0.03}\text{F}_4$  (3.35 %) and  $\text{NaY}_{0.885}\text{Yb}_{0.1}\text{Er}_{0.015}\text{F}_4$  (3.62 %) specimens demonstrated the highest quantum yields achieved during our experiments. Their composition was significantly different from the compositions of the samples described in the literature [1]. It is very hard to compare our results with previous data [1, 4], for, as we have already mentioned above, different researchers

utilized different synthetic methods (including different conditions of incongruent crystallization of the samples) and, therefore, impurity content and sample compositions were also different. However, it is worth noting that some authors [15, 16] reported a quantum yield decrease with decreased particle size for sub-micron crystals, whereas the quantum yields of their micron-sized agglomerates were the same as those obtained for bulk samples. All of their samples [15, 16] did not provide up-conversion quantum yields above 3.5% while still being unsuitable for photodynamic therapy because of their large size. In the present study, we achieved quantum yields above 3% using much smaller 50–90 nm particles. Further study of Yb/Er-doped NaYF<sub>4</sub> samples as prospective optical materials for use in photodynamic therapy are ongoing, and results will be reported soon.

## 5. Conclusions

NaY<sub>1-x-y</sub>Yb<sub>x</sub>Er<sub>y</sub>F<sub>4</sub> specimens were prepared by co-precipitation from aqueous solutions by dropwise addition of rare earth nitrate solutions to aqueous sodium fluoride. Study of the properties of polycrystalline fluorite-type NaY<sub>1-x-y</sub>Yb<sub>x</sub>Er<sub>y</sub>F<sub>4</sub> solid solutions demonstrated that NaY<sub>0.87</sub>Yb<sub>0.10</sub>Er<sub>0.03</sub>F<sub>4</sub> and NaY<sub>0.885</sub>Yb<sub>0.1</sub>Er<sub>0.015</sub>F<sub>4</sub> samples produced up-conversion luminescence with 3.35% and 3.62% quantum yields, which were higher than the quantum yields of the other NaY<sub>1-x-y</sub>Yb<sub>x</sub>Er<sub>y</sub>F<sub>4</sub> samples. The 50–90 nm particle size of the synthesized NaY<sub>1-x-y</sub>Yb<sub>x</sub>Er<sub>y</sub>F<sub>4</sub> specimens makes them useful for photodynamic therapy once a practical method for the dispersion of their 200–350 nm agglomerates is found.

## Acknowledgements

This work was supported by the grants of the Federal Program “Scientific and scientific-pedagogical personnel of innovative Russia” (State contract N 14.740.12.1343), RFBR (12-02-00851/a, N 12-02-12080-ofi-m, 13-02-12162 ofi-m) and a grant of the leading scientific schools (NSH-341.2012.2). Authors are very grateful to A. Baranchikov for his assistance in scanning electron microscopy studies and A. I. Popov and E. Chernova for their help in the manuscript preparation.

## References

- [1] P.P. Fedorov, A.A. Luginina, S.V. Kuznetsov, and V.V. Osiko. Nanofluorides. *J. Fluorine Chem.*, **132**, P. 1012–1039 (2011).
- [2] P. Zhang, W. Steelant, M. Kumar, M. Scholfield. Versatile photosensitizers for photodynamic therapy at infrared excitation. *J. Am. Chem. Soc.*, **129**, P. 4526–45257 (2007).
- [3] D.K. Chatterjee, L. Sh. Fong, and Y. Zhang. Nanoparticle photodynamic therapy PDT. *Advanced Drug Delivery Reviews.*, **60**, P. 1627–1637 (2008).
- [4] M. Haase and H. Schafer. Upconverting Nanoparticles. *Angew. Chem. Int. Ed.*, **50**, P. 5808–5829 (2011).
- [5] F. Auzel. Upconversion and anti-stokes processes with f and d ions in solids. *Chem Rev.*, **104**, P. 139–173 (2004).
- [6] V.V. Ovsyankin, P.P. Feofilov. Mechanism of summation of electronic excitations in activated crystals. *JETP Lett.*, **3**, P. 322–323 (1966).
- [7] P.P. Fedorov. Systems of alkali and rare-earth metal fluorides. *Russian J. Inorg. Chem.*, **44**, P. 1703–1727 (1999).
- [8] P.P. Fedorov, B.P. Sobolev, S.F. Belov. Fusibility diagram of the system NaF-YF<sub>3</sub>, and the cross-section Na<sub>0.4</sub>Y<sub>0.6</sub>F<sub>2.2</sub>-YOF. *Inorg. Mater.*, **15**(5), P. 640–643 (1979).
- [9] S.V. Kuznetsov, A.V. Ryabova, D.S. Los', P.P. Fedorov, V.V. Voronov, R.P. Ermakov, V.B. Loshchenov, V.V. Volkov, A.E. Baranchikov, V.V. Osiko. Synthesis and luminescent characteristics of submicron powders on the basis of sodium and yttrium fluorides doped with rare earth elements. *Nanotechnologies in Russia*, **7**, P. 615–628 (2012).

- [10] A.V. Ryabova, D.V. Pominova, V.A. Krut'ko, M.G. Komova, V.B. Loschenov. Spectroscopic research of upconversion nanomaterials based on complex oxide compounds doped with rare-earth ion pairs: benefit for cancer diagnostics by upconversion fluorescence and radio sensitive methods. *Photon Lasers Med* (2013). DOI 10.1515/plm-2013-0013.
- [11] P.P. Fedorov, S.V. Kuznetsov, V.V. Voronov, I.V. Yarotskaya, V.V. Arbenina. Soft chemical synthesis of NaYF<sub>4</sub> nanopowders. *Russian J. Inorg. Chem.*, **53**, P. 1681–1685 (2008).
- [12] D.S. Yasyrkina, S.V. Kuznetsov, P.P. Fedorov, V.V. Voronov, R.P. Ermakov, A.V. Ryabova, et al. Effect of the pH on the formation of NaYF<sub>4</sub>:Yb:Er nanopowders by co-crystallization in presence of polyethyleneimine. *J. Fluorine Chem.*, accepted for publication.
- [13] P.P. Fedorov, V.B. Alexandrov, O.S. Bondareva, I.I. Buchinskaya, M.D. Val'covskii, and B.P. Sobolev. Concentration dependences of the unit-cell parameters of nonstoichiometric fluorite-type phases Na<sub>0.5-x</sub>R<sub>0.5+x</sub>F<sub>2+2x</sub> (R = Rare-earth elements). *Crystallography Reports.*, **46**, P. 239–245 (2001).
- [14] M. Pollnau, D. R. Gamelin, S. R. Luthi, H. U. Gudel, M. P. Hehlen. Power dependence of upconversion luminescence in lanthanide and transition-metal-ion systems. *Phys. Rev. B*, **61**, P. 3337–3346 (2000).
- [15] D.O. Faulkner, S. Petrov, D.D. Perovic, N.P. Kherani, G.A. Ozin. Absolute quantum yields in NaYF<sub>4</sub>:Er,Yb upconverters – synthesis temperature and power dependence. *J. Mater. Chem.*, **22**, P. 24330–24334 (2012).
- [16] J-Ch. Boyer and Fr. van Veggel. Absolute quantum yield measurements of colloidal NaYF<sub>4</sub>: Er<sup>3+</sup>,Yb<sup>3+</sup> upconverting nanoparticles. *Nanoscale*, **2**, P. 1417–1419 (2010).

# ACCURATE ENERGY CONSERVATION IN MOLECULAR DYNAMICS SIMULATION

O. A. Zolotov, V. E. Zalizniak

Siberian Federal University, 79 Svobodny Prospect, Krasnoyarsk 660041, Russia  
ozolot\_@mail.ru, vzalizniak@sfu-kras.ru

**PACS 02.70.Ns, 45.20.dh, 45.50.Jf**

In molecular dynamics, Hamiltonian systems of differential equations are numerically integrated using some symplectic method. Symplectic integrators are simple algorithms that appear to be well-suited for large scale simulations. One feature of these simulations is that there is an unphysical drift in the energy of the system over long integration periods. A drift in the energy is more obvious when a relatively long time step is used. In this article, a special approach, based on symplectic discretization and momenta corrections, is presented. The proposed method conserves the total energy of the system over the interval of simulation for any acceptable time step. A new approach to perform a constant-temperature molecular dynamics simulation is also presented. Numerical experiments illustrating these approaches are described.

**Keywords:** Hamiltonian systems, symplectic numerical methods, energy conservation, molecular dynamics.

## 1. Introduction

In the field of molecular dynamics (MD), simulations of systems modeling materials or molecules at the microscopic scale are performed. There is a particular interest in large scale MD simulations, involving perhaps as many as several million atoms, over very long time scales. Such large simulations are of interest not only in standard macromolecular modeling but also in the modeling of various nanotechnology ideas. Molecular dynamics simulation first involves setting up the initial positions and velocities of the particles, and then the numerical integration of the classical equations of motion.

In a classical mechanics model, each atom is a particle with position  $\mathbf{r}_n$ , momentum  $\mathbf{p}_n$  and mass  $m_n$ . Positions and momenta are determined by the equations of motion:

$$\frac{d\mathbf{p}_n}{dt} = \mathbf{f}_n(t), \quad \frac{d\mathbf{r}_n}{dt} = \frac{\mathbf{p}_n}{m_n},$$

$$\mathbf{r}_n(0), \mathbf{p}_n(0) \text{ are given,}$$

$$n = 1, \dots, N,$$

where  $\mathbf{f}_n(t)$  is the force acting on the particle at time  $t$  and  $N$  is number of particles. Let us denote  $\mathbf{r} = (\mathbf{r}_1, \dots, \mathbf{r}_N)$  and  $\mathbf{p} = (\mathbf{p}_1, \dots, \mathbf{p}_N)$ . Forces are determined from the system potential energy  $U(\mathbf{r})$ :

$$\mathbf{f}_n(t) = -\frac{\partial U(\mathbf{r})}{\partial \mathbf{r}_n} = -\nabla_{\mathbf{r}_n} U(\mathbf{r}).$$

These equations are a special case of a Hamiltonian system of differential equations:

$$\frac{d\mathbf{p}_n}{dt} = -\frac{\partial H(\mathbf{r}, \mathbf{p})}{\partial \mathbf{r}_n}, \quad \frac{d\mathbf{r}_n}{dt} = \frac{\partial H(\mathbf{r}, \mathbf{p})}{\partial \mathbf{p}_n},$$

with Hamiltonian  $H = K + U$  where  $K$  is the kinetic energy:

$$H(\mathbf{r}, \mathbf{p}) = \sum_{n=1}^N \frac{\mathbf{p}_n^2}{2m_n} + U(\mathbf{r}). \quad (1)$$

Hamiltonian (1) is not explicitly time-dependent and its value is the total energy:  $H(\mathbf{r}, \mathbf{p}) = E$ . Classical dynamics is time reversible and the total energy of an isolated system is conserved. If the external forces on the individual particles sum to zero, the total momentum,

$$\mathbf{P} = \sum_{n=1}^N \mathbf{p}_n,$$

is conserved. If the external force acting on a system is zero, then the total angular momentum of the system,

$$\mathbf{L} = \sum_{n=1}^N \mathbf{r}_n \times \mathbf{p}_n,$$

is constant.

Numerical integration is the most computationally-intensive part of an MD simulation. The desirable qualities for a simulation algorithm might be as follows:

- (a) It should be fast, and require little memory. Numerical integration algorithms require a number of force evaluations in order to advance a trajectory by a given time step. The computational time is proportional to the number of force evaluations taken. Therefore, algorithms with one force evaluations per time step are preferable;
- (b) It should allow the use of a long time step;
- (c) It should reproduce the classical trajectory as closely as possible;
- (d) It should satisfy the known conservation laws for energy, total momentum and angular momentum, and be time-reversible.

Symplectic schemes have been found to be effective for MD simulations with classical dynamics, especially for long time integration (see, for example, [1–3] and references therein). The most commonly used symplectic algorithm is the Verlet algorithm [4] which appears in many different formulations. In what follows, we will use a second order method, first disclosed by Rowlands [5]:

$$\begin{aligned} \mathbf{r}_n^{k+1/2} &= \mathbf{r}_n^k + \tau_k \frac{\mathbf{p}_n^k}{2m_n}, \\ \mathbf{p}_n^{k+1} &= \mathbf{p}_n^k - \tau_k (\nabla_{\mathbf{r}_n} U(\mathbf{r})) \Big|_{\mathbf{r}_n = \mathbf{r}_n^{k+1/2}}, \\ \mathbf{r}_n^{k+1} &= \mathbf{r}_n^{k+1/2} + \tau_k \frac{\mathbf{p}_n^{k+1}}{2m_n}, \\ n &= 1, \dots, N; \quad k = 0, 1, \dots \end{aligned} \quad (2)$$

For symplectic algorithms, there exists a modified Hamiltonian  $H_m$ , which can be obtained from an asymptotic expansion of the original analytic Hamiltonian  $H$ . In the case of second order scheme, the general expression for the modified Hamiltonian is given in [6] and has the form:

$$H_m(\mathbf{r}, \mathbf{p}) = H(\mathbf{r}, \mathbf{p}) + \tau^2 g(\mathbf{r}, \mathbf{p}) + O(\tau^4).$$

Symplectic integrators do not in fact conserve the value of true Hamiltonian  $H$ ; instead, they reproduce more closely the value of modified Hamiltonian  $H_m$ . The accuracy of the energy conservation for the true Hamiltonian is dependent on the time step.

In numerical solutions of classical dynamics, all variables are discretized, and this could destroy the energy conservation. In MD simulations, interactions beyond a cutoff distance  $r_c$  are usually ignored. This means that the forces are not exactly correct. This also affects the energy conservation in MD simulations [7].

## 2. Constant energy simulation

Let us consider a system of  $N$  particles and  $U(\mathbf{r})$  is the potential energy of the system. Let  $E_0$  be the initial total energy of the system. Given coordinates and momenta at some time  $t_{k-1}$ ,  $(\mathbf{r}^{k-1}, \mathbf{p}^{k-1})$ , the one step given by equation (2) generates  $(\mathbf{r}^k, \mathbf{p}^k)$ . Then, the total energy of the system  $E(\mathbf{r}^k, \mathbf{p}^k) = K(\mathbf{p}^k) + U(\mathbf{r}^k) = E(t_k)$  and because the total energy is not conserved:  $E(t_k) \neq E_0$ . To achieve the energy conservation, we introduce corrections  $\Delta \mathbf{p}^k$  to momenta  $\mathbf{p}^k$  with the proviso that

$$\frac{1}{2} \sum_{n=1}^N \frac{(\Delta \mathbf{p}_n^k)^2}{m_n} = \min.$$

Using the method of Lagrange multipliers, we introduce functional

$$W(\Delta \mathbf{p}^k, \lambda) = \frac{1}{2} \sum_{n=1}^N \frac{(\Delta \mathbf{p}_n^k)^2}{m_n} + \lambda \left( \frac{1}{2} \sum_{n=1}^N \frac{(\mathbf{p}_n^k + \Delta \mathbf{p}_n^k)^2}{m_n} + U(\mathbf{r}^k) - E_0 \right).$$

When variation  $\delta W = 0$  for any arbitrary variations  $\delta(\Delta \mathbf{p}^k)$  and  $\delta \lambda$ , the functional  $W$  reaches its minimal value. Then, the condition  $\delta W = 0$  leads to the following system of equations:

$$\begin{aligned} \frac{1}{m_n} \Delta \mathbf{p}_n^k + \lambda \frac{1}{m_n} (\mathbf{p}_n^k + \Delta \mathbf{p}_n^k) &= 0, \\ \frac{1}{2} \sum_{n=1}^N \frac{(\mathbf{p}_n^k + \Delta \mathbf{p}_n^k)^2}{m_n} + U(\mathbf{r}^k) &= E_0. \end{aligned} \quad (3)$$

Solving the first of equations (3) we obtain:

$$\Delta \mathbf{p}_n^k = -\frac{\lambda}{1+\lambda} \mathbf{p}_n^k \quad \Rightarrow \quad \mathbf{p}_n^k + \Delta \mathbf{p}_n^k = \frac{1}{1+\lambda} \mathbf{p}_n^k = \alpha \mathbf{p}_n^k.$$

The second equation (3) gives us the value of coefficient  $\alpha$ :

$$\frac{1}{2} \sum_{n=1}^N \frac{(\mathbf{p}_n^k + \Delta \mathbf{p}_n^k)^2}{m_n} + U(\mathbf{r}^k) = \alpha^2 K(\mathbf{p}^k) + U(\mathbf{r}^k) = E_0 \quad \Rightarrow \quad \alpha = \sqrt{\frac{E_0 - U(\mathbf{r}^k)}{K(\mathbf{p}^k)}}.$$

In summary, the above results lead to the following algorithm (EC11 – energy conserving integrator 1):

$$\begin{aligned}
\mathbf{r}_n^{k+1/2} &= \mathbf{r}_n^k + \tau_k \frac{\mathbf{p}_n^k}{2m_n}, \\
\mathbf{p}_n^* &= \mathbf{p}_n^k - \tau_k (\nabla_{\mathbf{r}_n} U(\mathbf{r})) \Big|_{\mathbf{r}_n = \mathbf{r}_n^{k+1/2}}, \\
\mathbf{r}_n^{k+1} &= \mathbf{r}_n^{k+1/2} + \tau_k \frac{\mathbf{p}_n^*}{2m_n}, \\
\mathbf{p}_n^{k+1} &= \alpha_k \mathbf{p}_n^*, \quad \alpha_k = \sqrt{\frac{E_0 - U(\mathbf{r}^{k+1})}{K(\mathbf{p}^*)}}, \\
n &= 1, \dots, N; \quad k = 0, 1, \dots
\end{aligned} \tag{4}$$

In algorithm (4) the difference of two terms  $E_0 - U \approx K$ . In the case of a few body problems one can meet with the loss of numerical accuracy when kinetic energy  $K$  is small. Then we introduce corrections  $\Delta \mathbf{p}^k$  to momenta  $\mathbf{p}^k$  and corrections  $\Delta \mathbf{r}^k$  to positions  $\mathbf{r}^k$  with the proviso that

$$\frac{1}{2} \sum_{n=1}^N \frac{(\Delta \mathbf{p}_n^k)^2}{m_n} + \frac{k_s}{2} \sum_{n=1}^N (\Delta \mathbf{r}_n^k)^2 - \min.$$

It is assumed that every particle  $n$  is connected to position  $\mathbf{r}_n$  through the mediation of virtual spring with the stiffness  $k_s$ . A particle may not be easily displaced from the position  $\mathbf{r}_n$ , which means that one should choose:

$$k_s \sim \max_n \left| \frac{\partial^2 U}{\partial \mathbf{r}_n^2} \right|.$$

Using the method of Lagrange multipliers, we introduce functional

$$W = \frac{1}{2} \sum_{n=1}^N \frac{(\Delta \mathbf{p}_n^k)^2}{m_n} + \frac{k_s}{2} \sum_{n=1}^N (\Delta \mathbf{r}_n^k)^2 + \lambda \left( \frac{1}{2} \sum_{n=1}^N \frac{(\mathbf{p}_n^k + \Delta \mathbf{p}_n^k)^2}{m_n} + U(\mathbf{r}^k + \Delta \mathbf{r}^k) - E_0 \right).$$

The condition  $\delta W = 0$ , for any arbitrary variations  $\delta(\Delta \mathbf{p}^k)$ ,  $\delta(\Delta \mathbf{r}^k)$  and  $\delta \lambda$ , leads to the following system of equations:

$$\begin{aligned}
\frac{1}{m_n} \Delta \mathbf{p}_n^k + \lambda \frac{1}{m_n} (\mathbf{p}_n^k + \Delta \mathbf{p}_n^k) &= 0, \\
k_s \Delta \mathbf{r}_n^k + \lambda (\nabla_{\mathbf{r}_n} U(\mathbf{r})) \Big|_{\mathbf{r}_n = \mathbf{r}_n^k + \Delta \mathbf{r}_n^k} &= 0, \\
\frac{1}{2} \sum_{n=1}^N \frac{(\mathbf{p}_n^k + \Delta \mathbf{p}_n^k)^2}{m_n} + U(\mathbf{r}^k + \Delta \mathbf{r}^k) &= E_0.
\end{aligned} \tag{5}$$

Let us use the following approximations:

$$\begin{aligned}
(\nabla_{\mathbf{r}_n} U(\mathbf{r})) \Big|_{\mathbf{r}_n = \mathbf{r}_n^k + \Delta \mathbf{r}_n^k} &\approx (\nabla_{\mathbf{r}_n} U(\mathbf{r})) \Big|_{\mathbf{r}_n = \mathbf{r}_n^k}, \\
U(\mathbf{r}^k + \Delta \mathbf{r}^k) &\approx U(\mathbf{r}^k) + \sum_{n=1}^N (\nabla_{\mathbf{r}_n} U(\mathbf{r})) \Big|_{\mathbf{r}_n = \mathbf{r}_n^k} \cdot \Delta \mathbf{r}_n^k.
\end{aligned}$$

Then, the second and third equations in (5) give us the cubic equation in one unknown parameter  $\lambda$ :

$$\left(\frac{1}{1+\lambda}\right)^2 K(\mathbf{p}^k) - \frac{\lambda}{k_s} \sum_{n=1}^N \left[ (\nabla_{\mathbf{r}_n} U(\mathbf{r})) \Big|_{\mathbf{r}_n=\mathbf{r}_n^k} \right]^2 = E_0 - U(\mathbf{r}^k).$$

We are looking for approximate solution of this equation assuming that  $\lambda$  is close to zero because corrections should be relatively small. Then, we arrive at the following solution:

$$\lambda = \frac{U(\mathbf{r}^k) + K(\mathbf{p}^k) - E_0}{2K(\mathbf{p}^k) + \frac{1}{k_s} \sum_{n=1}^N \left[ (\nabla_{\mathbf{r}_n} U(\mathbf{r})) \Big|_{\mathbf{r}_n=\mathbf{r}_n^k} \right]^2}.$$

Taking into account first and second equations in (5), we arrive at the following algorithm (ECI2 – energy conserving integrator 2):

$$\begin{aligned} \mathbf{r}_n^{k+1/2} &= \mathbf{r}_n^k + \tau_k \frac{\mathbf{p}_n^k}{2m_n}, \\ \mathbf{p}_n^* &= \mathbf{p}_n^k - \tau_k (\nabla_{\mathbf{r}_n} U(\mathbf{r})) \Big|_{\mathbf{r}_n=\mathbf{r}_n^{k+1/2}}, \\ \mathbf{r}_n^* &= \mathbf{r}_n^{k+1/2} + \tau_k \frac{\mathbf{p}_n^*}{2m_n}, \\ \mathbf{r}_n^{k+1} &= \mathbf{r}_n^* - \beta_k (\nabla_{\mathbf{r}_n} U(\mathbf{r})) \Big|_{\mathbf{r}_n=\mathbf{r}_n^*}, \quad \beta_k = \frac{U(\mathbf{r}^*) + K(\mathbf{p}^*) - E_0}{2k_s K(\mathbf{p}^*) + \sum_{n=1}^N \left[ (\nabla_{\mathbf{r}_n} U(\mathbf{r})) \Big|_{\mathbf{r}_n=\mathbf{r}_n^*} \right]^2}, \\ \mathbf{p}_n^{k+1} &= \frac{1}{1 + k_s \beta_k} \mathbf{p}_n^*, \\ n &= 1, \dots, N; \quad k = 0, 1, \dots \end{aligned} \tag{6}$$

## 2.1. Harmonic oscillator

Consider the motion of a harmonic oscillator. The Hamiltonian equations in that case can be written as:

$$\begin{aligned} \frac{dp}{dt} &= -\omega^2 q, \quad \frac{dq}{dt} = p, \\ q(0), p(0) &\text{ are given,} \end{aligned} \tag{7}$$

where  $p$  is the momentum,  $q = mx$  is the canonical coordinate,  $\omega = (k/m)^{1/2}$ ,  $m$  is the mass and  $k$  is the stiffness. The total energy of the harmonic oscillator is  $E = K(p) + U(q) = 0.5(p^2 + q^2)/m$ . The exact solution of the problem (7) is:

$$\begin{bmatrix} q(t) \\ p(t) \end{bmatrix} = \begin{bmatrix} \cos(\omega t) & \omega^{-1} \sin(\omega t) \\ -\omega \sin(\omega t) & \cos(\omega t) \end{bmatrix} \begin{bmatrix} q(0) \\ p(0) \end{bmatrix}.$$

Application of symplectic method (2) to the harmonic oscillator problem gives the following scheme:

$$\begin{aligned} q^{k+1/2} &= q^k + 0.5\tau p^k, \quad p^{k+1} = p^k - \tau\omega^2 q^{k+1/2}, \\ q^{k+1} &= q^{k+1/2} + 0.5\tau p^{k+1}, \\ k &= 0, 1, \dots \end{aligned} \tag{8}$$

This scheme is stable if  $\tau\omega < 2$ .

Figures 1–3 show the phase trajectory and time dependence of the position of the harmonic oscillator, as calculated with the use of methods (4), (6) and (8). Initial conditions

are  $q(0) = 0$  and  $p(0) = 1$ . The oscillator parameters are  $m = 1$  and  $k = 1$ . A relatively long time step was chosen with  $\tau\omega = 0.25\pi$  (eight time steps per oscillation period). To estimate the energy conservation, we introduced the relative energy error as:

$$\langle \Delta E \rangle = \frac{1}{E(0)M} \sum_{k=1}^M |E(t_k) - E(0)|, \quad (9)$$

where  $E(0)$  is the initial total energy and  $M$  is the number of time steps. Fig. 1(a) indicates that the total energy is conserved, the relative energy error  $\langle \Delta E \rangle = 3.7 \cdot 10^{-17}$ , while Fig. 1(b) indicates that the position of harmonic oscillator slightly deviates from the exact solution.

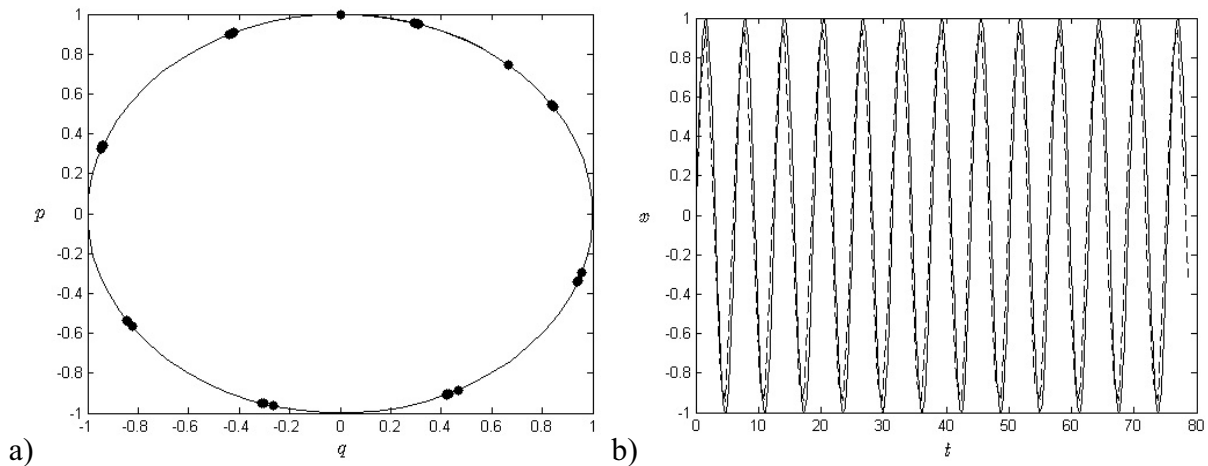


FIG. 1. Phase trajectory and time dependence of the position of harmonic oscillator, method (4); a) Phase trajectory in the phase space  $q-p$ , solid line is the exact trajectory, dots indicate approximate solution; b) position of harmonic oscillator versus time, solid line is the exact solution, dashed line indicates approximate solution.

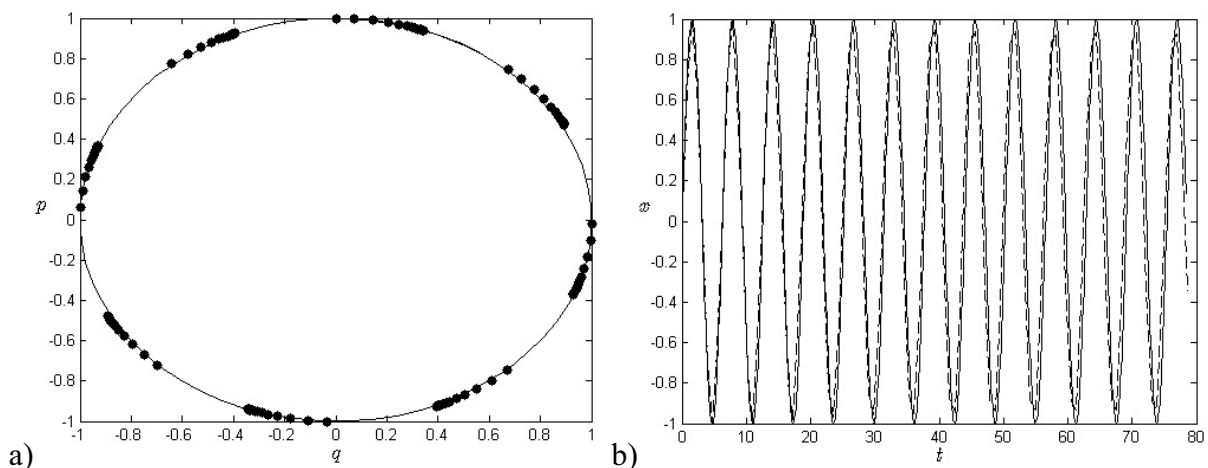


FIG. 2. Phase trajectory and time dependence of the position of harmonic oscillator, method (6) with  $k_s = 5$ ; a) Phase trajectory in the phase space  $q-p$ , solid line is the exact trajectory, dots indicate approximate solution; b) position of harmonic oscillator versus time, solid line is the exact solution, dashed line indicates approximate solution.

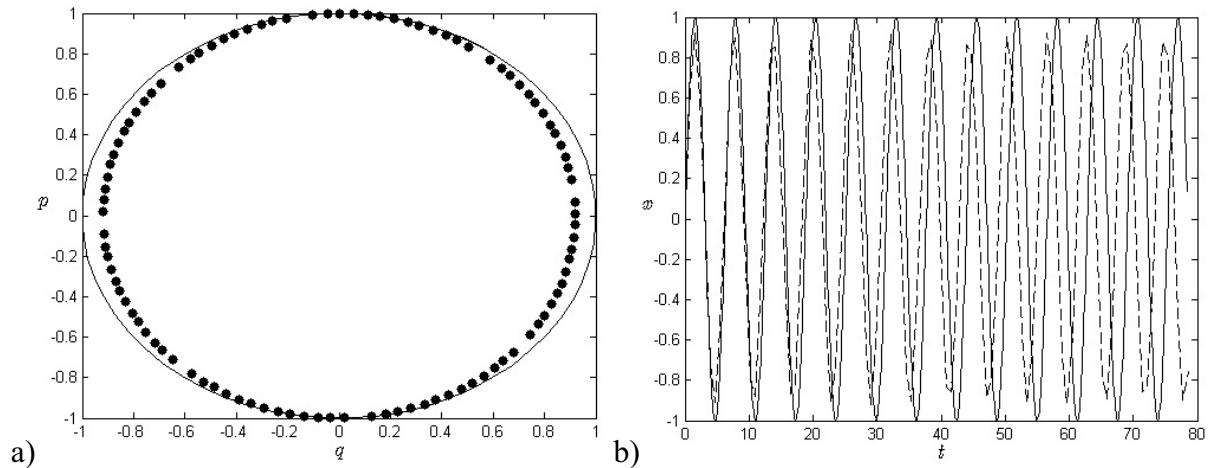


FIG. 3. Phase trajectory and time dependence of the position of harmonic oscillator, symplectic method (8); a) Phase trajectory in the phase space  $q - p$ , solid line is the exact trajectory, dots indicate approximate solution; b) position of harmonic oscillator versus time, solid line is the exact solution, dashed line indicates approximate solution.

As is seen from Fig. 2(a), the approximate phase trajectory slightly deviates from the exact one. Method (6) conserves the total energy much worse than method (4), the relative energy error being  $\langle \Delta E \rangle = 7.9 \cdot 10^{-3}$ , but provides similar results to method (4) for the time dependence of the harmonic oscillator's position, as shown in Fig. 2(b). Symplectic method (8) does not conserve the total energy, but rather the value of the modified Hamiltonian, as can be seen from Fig. 3(a). In this example, the relative energy error was  $\langle \Delta E \rangle = 7.7 \cdot 10^{-2}$ . The discrepancy between the calculated and exact position of the harmonic oscillator grows more quickly with time in comparison to methods (4) and (6).

The presented results demonstrated the accuracy and efficiency of the proposed method for a simple, analytically solvable, test case. However, actual MD simulations involve considerably more complicated dynamics, and it is therefore worthwhile to examine a more complex example.

## 2.2. MD simulation of the Lennard-Jones fluid

Let us analyze the time dependence of the energy for a fluid of  $N$  particles interacting via the well-known Lennard-Jones (LJ) pair potential:

$$\varphi(r) = 4\varepsilon \left[ \left( \frac{d}{r} \right)^{12} - \left( \frac{d}{r} \right)^6 \right],$$

where  $r$  is the distance between particles,  $\varepsilon$  and  $d$  are potential parameters. Particles are contained in a box with rigid walls and  $V$  is the volume of the box. The potential energy of the system is given by:

$$U(\mathbf{r}) = \frac{1}{2} \sum_{n=1}^N \sum_{\substack{m=1 \\ m \neq n}}^N \varphi(r_{nm}), \quad r_{nm} = |\mathbf{r}_n - \mathbf{r}_m|.$$

In order to choose the time step of the simulation, it is necessary to determine the highest oscillating frequency  $\omega_{\max}$  in the physical system and satisfy the condition for stability,  $\tau\omega_{\max} < 2$ . The second condition to be satisfied is that the integration of the trajectories for

most particles should be sufficiently accurate. Most particles will have an oscillation frequency  $\omega_a$  associated with the average separation  $r_a = (V/N)^{1/3}$ . The oscillation frequency estimate can be obtained with a simple one-dimensional argument considering the case when two neighboring particles move towards each other to a position of closest approach [8]. Then, we propose the following estimates that are sufficient for the choice of a reasonable time step:

$$\omega_{\max}^k = \left( \frac{1}{m_p} \frac{\partial^2 \varphi}{\partial r^2} (r_{\min}^k) \right), \quad \omega_a^k = \left( \frac{1}{m_p} \frac{\partial^2 \varphi}{\partial r^2} (r_a) \right),$$

where  $m_p$  is the minimal reduced mass and  $r_{\min}^k$  is the closest approach at some time  $t_k$ . They are:

$$m_p = \min_{i,j} \left( \frac{m_i m_j}{m_i + m_j} \right), \quad r_{\min}^k = \min_{i,j} (r_{ij}^k).$$

Another constraint on the time step arises from the requirement that a particle should not move more than the minimal distance between particles. Hence, the condition  $2\tau_k v_{\max}^k < r_{\min}^k$  should be satisfied, where  $v_{\max}^k$  is maximal particle velocity at some time  $t_k$  defined as:

$$v_{\max}^k = \max_n \left( \frac{1}{m_n} (\mathbf{p}_n^k \cdot \mathbf{p}_n^k)^{1/2} \right).$$

The condition on the time step may be summarized as follows:

$$\tau_k = \min \left( \frac{a_1}{\omega_{\max}^k}, \frac{a_2}{\omega_a^k}, \frac{a_3 r_{\min}^k}{v_{\max}^k} \right), \quad \tau = \frac{1}{M} \sum_{k=1}^M \tau_k.$$

Parameters  $a_1$ ,  $a_2$  and  $a_3$  define the accuracy of the integration of particle motion,  $\tau$  is the average time step and  $M$  is the number of time steps. Because the probability of small separations occurring between particles is small, it is not necessary to accurately integrate the motion of such particles. The trajectories for most particles should be integrated more accurately. Then, we have  $2 > a_1 > a_2$  and parameter  $a_3 \leq 0.1$ .

We considered a fictitious fluid with potential parameters  $\varepsilon = 0.015$  eV and  $d = 3$  Å. All particles have equal mass  $m = 20$  u. Then, an atomic time unit  $t_{au} = (\text{u} \cdot \text{Å}^2/\text{eV})^{1/2}$  corresponds to  $1.019 \cdot 10^{-14}$  s. We simulated  $N = 100$  LJ particles at reduced density  $\rho^* = 0.728$  and reduced temperature  $T^* = 1.376$ , a moderate-pressure liquid state. In MD simulations, interactions beyond a certain distance  $r_c$  are usually ignored. In what follows,  $r_c$  is taken to be equal to  $2.5d$ . To obtain initial conditions, we used symplectic method (2), with  $\tau \approx 0.001$ , and integrated the equations of motion for  $10^5$  time steps, saving the resulting coordinates and momenta. These coordinates and momenta were then used as initial conditions for all simulations. The resulting value of the total energy of the system was taken as the initial value of energy  $E(0)$  that must be conserved. The dynamics were simulated in double-precision arithmetic.

The parameters of three simulations are presented in Table 1.

TABLE 1. Parameters of simulations

	Method	$a_1$	$a_2$	$a_3$	$\tau$ , atomic units	$M$
1	Symplectic (2)	$0.025\pi$	$6.25 \cdot 10^{-3}\pi$	0.1	0.0081	$4 \cdot 10^5$
2	Symplectic (2)	$0.5\pi$	$0.125\pi$	0.1	0.161	$2 \cdot 10^4$
3	ECI1 (4)	$0.5\pi$	$0.125\pi$	0.1	0.162	$2 \cdot 10^4$

In all simulations, we considered the relative energy error (9) and some basic thermodynamic quantities, such as, temperature  $T$ , pressure  $P$  and constant-volume heat capacity  $C_V$ . These thermodynamic quantities can be calculated as averages in a microcanonical ensemble as follows [9]:

$$T = \frac{2}{3Nk_B} \langle K \rangle, \quad P = \frac{Nk_B T}{V} + \frac{1}{3V} \left\langle \sum_{n=1}^N \sum_{m>n}^N r_{nm} \frac{d\varphi}{dr}(r_{nm}) \right\rangle,$$

$$C_V = \frac{3}{2} Nk_B \left( 1 - \frac{3}{2} N \frac{\langle (\delta K)^2 \rangle}{\langle K \rangle^2} \right)^{-1},$$

where angle brackets  $\langle \cdot \rangle$  mean the time average,  $\delta K(t_k) = K(t_k) - \langle K \rangle$  is the fluctuation of kinetic energy at time  $t_k$  and  $k_B$  is the Boltzmann constant. Calculated thermodynamic quantities are presented in Table 2.

TABLE 2. Calculated properties for a LJ fluid

	$\langle \Delta E \rangle$	$T$ , K	$P$ , eV/Å <sup>3</sup>	$C_V$ , eV/K
1	$9.6 \cdot 10^{-3}$	240.3	$9.3 \cdot 10^{-4}$	0.0174
2	0.12	249.2	$10^{-3}$	0.0173
3	$1.1 \cdot 10^{-15}$	239.2	$9.5 \cdot 10^{-4}$	0.0175

The dependence of the energy of the system of LJ particles on time for three simulations presented in Table 1 is shown in Figs. 4-6. Symplectic methods do not conserve energy exactly along trajectories. However, although they do not conserve energy, symplectic methods have been observed to maintain system energy in a narrow band near the true energy for long periods of time (see Fig. 4). That is, the energy of the system fluctuates about some value with very little apparent long-term drift. However, over longer time periods there is a slow drift in the energy away from this range. If relatively long time step is used then a drift in the energy becomes even more apparent (see Fig. 5). We considered the system of particles contained in a box with rigid walls. In this case, the integration of the motion of the system with the use of symplectic method (2) resulted in an increase of the system's kinetic energy. The proposed method (4) conserved the total energy of the system over the interval of simulation (see Fig. 6); the relative energy error is close to round-off errors.

The average deviation  $\langle |1 - \alpha_k| \rangle$  is equal to  $4.8 \cdot 10^{-5}$  for simulation 3 ( $\alpha_k$  is momentum correction parameter from (4)), so very small correction of momenta is needed to conserve the total energy.

### 3. Constant temperature simulation

The definition of thermodynamic temperature can be obtained through the fundamental equation of state [10], from which we get:

$$\frac{1}{T} = \frac{dS}{dE},$$

where  $S$  is the entropy and  $T$  is the thermodynamic temperature recorded by a thermometer in thermal equilibrium with the system. The kinetic temperature of the system is related to system kinetic energy through the standard relationship:

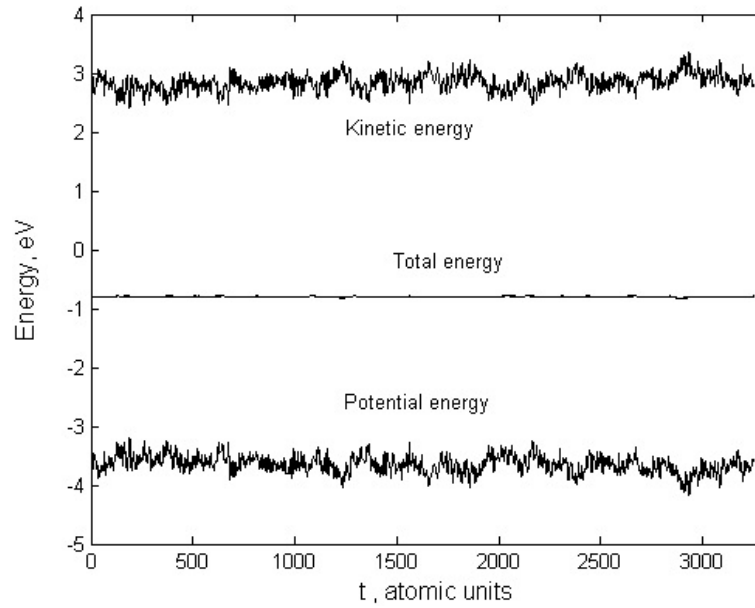


FIG. 4. The evolution of the energy for a LJ fluid, simulation 1.

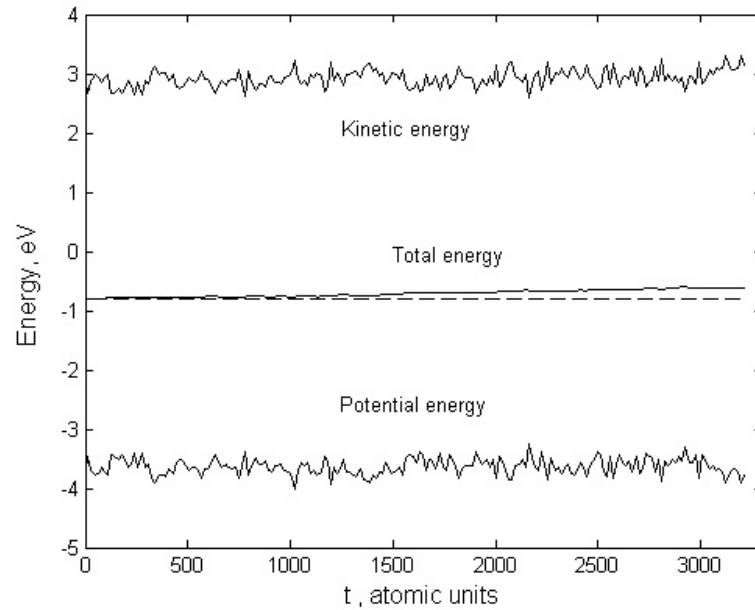


FIG. 5. The evolution of the energy for a LJ fluid, simulation 2. Dashed line indicates the initial total energy.

$$\frac{3}{2}Nk_B T_k = \langle K \rangle. \quad (10)$$

For a system in equilibrium, it is well known that the kinetic temperature is identical to the thermodynamic temperature, i.e.  $T = T_k$ . With the use of the maximum entropy formalism, it was found that even though a system is far enough from equilibrium for nonlinear effects,  $T_k/T - 1 < 0.01$  [11]. In what follows, we assume that  $T \simeq T_k$ .

Simulations at constant temperature are important for studying the behavior of systems at different temperatures. Several different methods of prescribing the temperature in a molecular

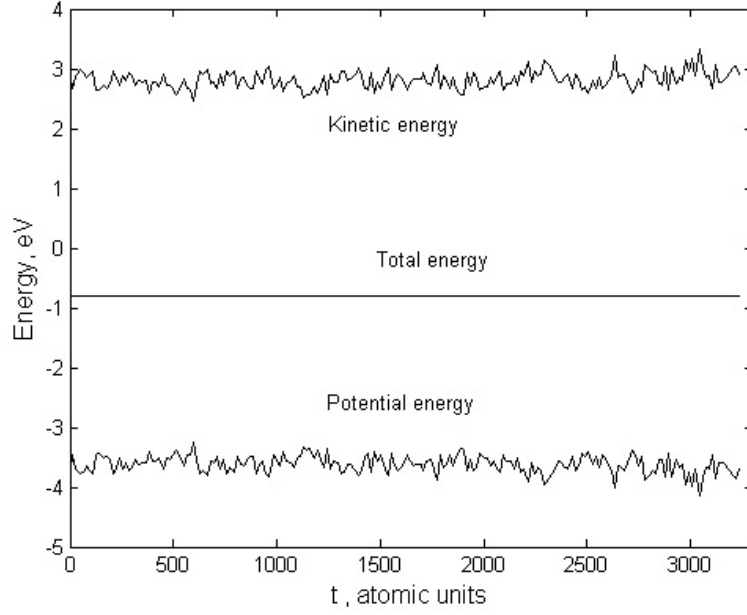


FIG. 6. The evolution of the energy for a LJ fluid, simulation 3.

dynamics simulation exist [9]. We propose a new approach to adapt MD so as to sample a constant-temperature ensemble.

Let us consider a system of  $N$  particles and  $T_0$  is the prescribed temperature that corresponds to the kinetic energy  $K_0$  through relation (10). Given coordinates and momenta at some time  $t_{k-1}$ ,  $(\mathbf{r}^{k-1}, \mathbf{p}^{k-1})$ , the one step given by equation (2) generates  $(\mathbf{r}^k, \mathbf{p}^k)$ . Then, the kinetic energy of the system  $K(\mathbf{p}^k)$  and particle kinetic energy  $K_n(\mathbf{p}_n^k)$  at time  $t_k$  are defined as:

$$K(\mathbf{p}^k) = \sum_{n=1}^N \frac{\mathbf{p}_n^k \cdot \mathbf{p}_n^k}{2m_n}, \quad K_n(\mathbf{p}_n^k) = \frac{\mathbf{p}_n^k \cdot \mathbf{p}_n^k}{2m_n}.$$

The kinetic energy (temperature) is not conserved:  $K(\mathbf{p}^k) \neq K_0$ . Let us introduce kinetic energy difference per particle as:

$$\Delta K(\mathbf{p}^k) = \frac{1}{N} (K_0 - K(\mathbf{p}^k)).$$

To achieve the conservation of kinetic energy, we introduce corrections  $\Delta \mathbf{p}^k$  to momenta  $\mathbf{p}^k$  with the proviso that  $K(\mathbf{p}^k + \Delta \mathbf{p}^k) = K_0$ . We assume that:

$$\mathbf{p}_n^k + \Delta \mathbf{p}_n^k = \mathbf{p}_n^k + \gamma_n^k \mathbf{p}_n^k = (1 + \gamma_n^k) \mathbf{p}_n^k.$$

Then, we have:

$$K_n(\mathbf{p}_n^k + \Delta \mathbf{p}_n^k) - K_n(\mathbf{p}_n^k) = \Delta K(\mathbf{p}^k) = (1 + \gamma_n^k)^2 K_n(\mathbf{p}_n^k) - K_n(\mathbf{p}_n^k).$$

Solving the last equation and assuming that  $\gamma$  is a real and positive parameter, we obtain:

$$1 + \gamma_n^k(\mathbf{p}_n^k) = \begin{cases} (1 + \Delta K(\mathbf{p}^k) / K_n(\mathbf{p}_n^k))^{1/2}, & \text{if } \Delta K(\mathbf{p}^k) / K_n(\mathbf{p}_n^k) > -1; \\ 1, & \text{otherwise.} \end{cases}$$

In summary, the above results lead to the following algorithm (KECI – kinetic energy conserving integrator):

$$\begin{aligned}
 \mathbf{r}_n^{k+1/2} &= \mathbf{r}_n^k + \tau_k \frac{\mathbf{p}_n^k}{2m_n}, \\
 \mathbf{p}_n^* &= \mathbf{p}_n^k - \tau_k (\nabla_{\mathbf{r}_n} U(\mathbf{r})) \Big|_{\mathbf{r}_n = \mathbf{r}_n^{k+1/2}}, \\
 \mathbf{r}_n^{k+1} &= \mathbf{r}_n^{k+1/2} + \tau_k \frac{\mathbf{p}_n^*}{2m_n}, \\
 \mathbf{p}_n^{k+1} &= (1 + \gamma_n^k(\mathbf{p}_n^*)) \mathbf{p}_n^*, \\
 n &= 1, \dots, N; \quad k = 0, 1, \dots
 \end{aligned} \tag{11}$$

Let us consider a system of  $N$  particles interacting via the Lennard-Jones pair potential defined in section 2.2. The target temperature  $T_0$  is set to 300 K. The system was integrated with the use of method (11) for  $2 \cdot 10^4$  time steps with the average time step  $\tau = 0.152$ . Fig. 7 shows the evolution of the instantaneous temperature deviation  $(T_0 - T)/T_0$  over the interval of the simulation. During the simulation, the speed distribution histogram was constructed. As can be seen from Fig. 8, the obtained speed distribution of the particles is close to the Maxwell distribution. Pearson's chi-squared test confirms this observation.

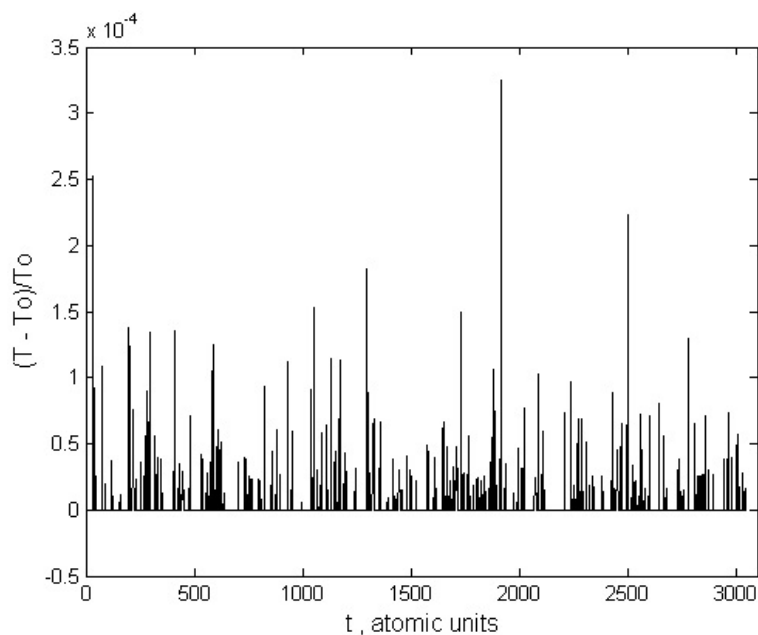


FIG. 7. The evolution of relative temperature deviation for a LJ fluid.

#### 4. Conclusions

Approximate solutions for the equations of motion in MD simulations are typically computed by some symplectic method, however any known symplectic numerical method does not conserve energy exactly along trajectories. This is because the various types of errors have an effect on the accuracy of the computation. Our investigation showed that the energy can be accurately conserved by introducing relatively small corrections to the particle momenta. These corrections bring the system back to a statistically-admissible state on the constant energy surface in a phase space.

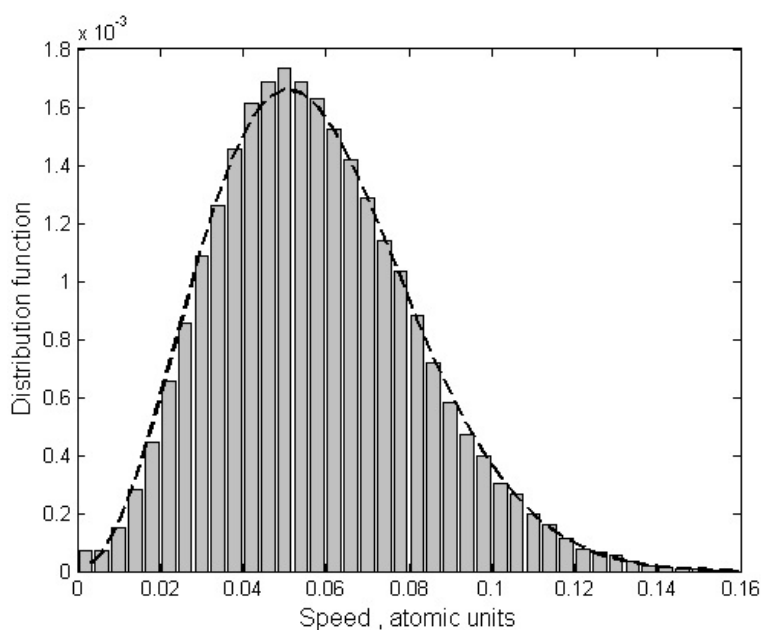


FIG. 8. Speed distribution. Histogram is obtained from simulation; dashed line corresponds to the Maxwell distribution.

The proposed kinetic energy conserving integrator is simple to implement and is very efficient for maintaining the desired temperature. It also does not depend upon any additional parameters. This method produces a statistical ensemble that is close to canonical ensemble.

## References

- [1] C.J. Budd, M.D. Piggott. Geometric integration and its applications. *Handbook of Numerical Analysis*, **XI**, North-Holland, Amsterdam, P. 35–139 (2003).
- [2] E. Hairer, C. Lubich, G. Wanner. *Geometric Numerical Integration*. Springer, Berlin, 2002, 644 p.
- [3] J.M. Sanz-Serna, M.P. Calvo. *Numerical Hamiltonian Problems*. Chapman and Hall, London, 1994, 207 p.
- [4] L. Verlet. Computer ‘experiments’ on classical fluids. I. Thermodynamical properties of Lennard-Jones molecules. *Phys. Rev.*, **159**, P. 98–103 (1967).
- [5] G. Rowlands. A numerical algorithm for Hamiltonian systems. *J. Comput. Phys.*, **97**, P. 235–239 (1991).
- [6] J. Gans, D. Shalloway. Shadow mass and the relationship between velocity and momentum in symplectic numerical integration. *Phys. Rev. E*, **61**, P. 4587–4592 (2000).
- [7] S. Toxvaerd, O.J. Heilmann, J.C. Dyre. Energy conservation in molecular dynamics simulations of classical systems. *J. Chem. Phys.*, **136**, P. 224106(8) (2012).
- [8] R.W. Hockney, J.W. Eastwood. *Computer Simulation Using Particles*. Adam Hilger, Bristol and New York, 1988, 523 p.
- [9] M.P. Allen, D.J. Tildesley. *Computer Simulation of Liquids*. Clarendon Press, Oxford, 1989, 385 p.
- [10] L.D. Landau, E.M. Lifshitz. *Statistical Physics, Part 1 (Course of Theoretical Physics, Volume 5)*, Third Edition, Elsevier Butterworth Heinemann, Oxford, 1980, 544 p.
- [11] R.E. Nettleton. On the relation between thermodynamic temperature and kinetic energy per particle. *Canadian Journal of Physics*, **72**(3–4), P. 106–112 (1994).

## MISCIBILITY STUDIES OF PC/PMMA BLENDS IN TETRAHYDROFURAN BY VISCOMETRY, FTIR AND SEM ANALYSIS

Ashok kumar Gupta, Gautam kumar sah

University Department of Chemistry (Physical Chemistry section),  
Lalit Narayan Mithila University Darbhanga India

ashokkumargupta80@gmail.com, gautamdar@gmail.com

### PACS 81.05.Lg

The coefficients of viscosity for polycarbonate/poly(methyl methacrylate) (PC/PMMA) blends in tetrahydrofuran at 303.15 K and 313.15 K have been measured. The measured parameters were used to estimate other related physical quantities, like Huggins constants and the interaction parameters  $\mu$  and  $\alpha$ , proposed by Chee and Sun et al. to identify the molecular interaction arising in solutions of the mentioned polymer blends. The peculiar deviation confirmed the structural changes in the solutions of the blends. FTIR and SEM studies confirm the formation of physical blends.

**Keywords:** Viscosity, polymer blends, Polycarbonate (PC), Poly(methyl methacrylate) (PMMA), molecular interaction, FTIR, SEM.

### 1. Introduction

In continuation of our work [1] on the miscibility study of poly(vinyl chloride)-poly(methyl methacrylate) PVC/PMMA blends by viscometry and other analytical methods, we have now studied the miscibility of PC/PMMA blends in THF by viscometry, FTIR and SEM analysis. Polymer blending is one of the most important contemporary methods for the development of new polymeric materials. Schurer et al. [2] studied the addition of monomeric and polymeric methyl methacrylate to improve the thermal and mechanical properties of poly(vinyl chloride) (PVC), who concluded that PVC was partially miscible with atactic and syndiotactic PMMA, but almost completely immiscible with isotactic PMMA. Polymers play an important role in all branches of industry today. The miscibility characteristics of methylcellulose (MC) and poly(vinyl alcohol) (PVA) have been investigated by viscometry, ultrasonic velocity, density and refractometric techniques at 30 °C and 40 °C. Methylcellulose/ poly(vinyl alcohol) blend films were prepared by the solution casting method and studied by scanning electron microscopy (SEM) [3]. PVC/ PMMA polymer blends were characterized at the molecular level by FTIR-ATR spectroscopy, providing important insight into the molecular interactions responsible for the enhancement of its mechanical properties. The changes in mechanical properties are reflected by the changes in the FTIR-ATR spectrum. The mechanical properties of such polymer blends revealed a substantial increase in the Young's modulus and ultimate tensile strength after an initial drop at 10% PMMA. A comparative study of the mechanical properties of PVC/ PMMA polymer blends with different weight percentages was carried out and their results were correlated with FTIR – ATR spectral studies, allowing important conclusions to be drawn about the possible molecular interactions between the constituent polymers [4]. The manifestation of superior properties depended upon the miscibility of the homo-polymers at the molecular scale. The miscibility resulted in different blend morphologies, ranging from a single phase system to a two- or multiphase systems. Polymer nanocomposites prepared by melt compounding using a

Twin screw extruder [5] exhibited superior mechanical, electrical, thermal, and morphological properties, as shown by DSC, TGA, FTIR and SEM analyses. The basis of polymer-polymer miscibility may arise from several different interactions, such as hydrogen bonding, dipole-dipole forces, and charge transfer complexes for homo-polymer mixtures. In the present case, FTIR study showed that PC/PMMA blends are physical blends, because there is no obvious interactions between the components. SEM studies supported the formation of physical blends of PC and PMMA.

## 2. Experimental

**Viscometry:**– PC (From Chennai Cipet India) and PMMA (grade LG 2 Sumitomo chemical Singapore), tetrahydrofuran from Fisher Scientific was used after purification by fractional distillation. A dilute polymer solution of 1% w/v was prepared for viscometric studies. Stock solutions of polymers and the blends of PC/PMMA of different compositions, 0/100, 20/80, 40/60, 60/40, 80/20 and 100/0 were prepared in tetrahydrofuran. Viscosity measurements at 303.15 K and 313.15 K were carried out using an Ostwald viscometer. The total weight of the two components in the solution was always maintained at 1 g/dL. Different temperatures were maintained in a thermostat-regulated bath, with a thermal stability of  $\pm 0.05$  K.

**FTIR and SEM analysis:**– The remaining stock solutions for viscometric experiments were mixed at room temperature and stirred for several hours. The solutions were then placed in a glass petri-dish separately and THF was slowly evaporated under ambient conditions. The resulting polymer and polymer blends were dried in a hot air oven for 24 hours. The film of component polymers and their blends were stored properly for FTIR scanning and SEM analysis. FTIR experiments were performed on thin films using an FTIR spectrophotometer (FTIR spectrometer spectrum Perkin elmer 400) from Punjab University Chandigarh (India). SEM experiments were carried out using thin films of polymers (PC and PMMA) and their blends (PC/PMMA) of different compositions by a scanning electron microscope (ZEOL JSM6610 LV) from IIT Roper (India).

## 3. Results and discussion

Viscometry is a simple and effective technique for monitoring the interactions in polymer blend solutions. From viscometric measurements, the relative and reduced viscosities of pure polymers and their blends were obtained. Figures 1 and 2 shows the Huggins plots for the PC/PMMA at 303.15 K and 313.15 K for different weight fractions of polymer 1 and polymer 2 ( $W_1 : W_2$ ), respectively. The  $K_H$  values were determined by extrapolation to infinite dilution of the Huggin's plots and the values of  $b$  are the slopes of the plots. This has been compared to the calculated results obtained from Huggins equation. The figure indicates a considerably higher slope variation for PC/PMMA blend compositions. This may be attributed to the mutual attraction of macromolecules in solution, because of the increase of hydrodynamic and thermodynamic interaction. Hence, the PC/PMMA blend was found to be miscible. Below this critical concentration, a sharp decrease in the slope was observed in the Huggin's plot because of phase separation. To quantify the miscibility of the polymer blends Chee (1990) [6] suggested that the general expression for the interaction parameter when polymers are mixed in weight fractions,  $W_1$  and  $W_2$  is as follows:

$$\Delta B = \frac{b - \bar{b}}{2W_1W_2},$$

where  $\bar{b} = W_1b_{11} + W_2b_{22}$  in which,  $b_{11}$  and  $b_{22}$  are the slopes of the viscosity curves for the pure components. The coefficient  $b$  is related to the Huggins's coefficient  $K_H$  as follows:

$$b = K_H[\eta]^2,$$

and for the ternary system, the coefficient  $b$  is also given by:

$$b = W_1^2 b_{11} + W_2^2 b_{22} + 2W_1 W_2 b_{12},$$

where  $b_{12}$  is the slope for the blend solution. Using these values, Chee (1990) defined a more effective parameter as follows:

$$\mu = \frac{\Delta B}{\{[\eta]_2 - [\eta]_1\}^2},$$

where  $[\eta]_1$  and  $[\eta]_2$  are the intrinsic viscosities for the pure component solutions. The blend is miscible when  $\mu \geq 0$  and immiscible when  $\mu < 0$ .

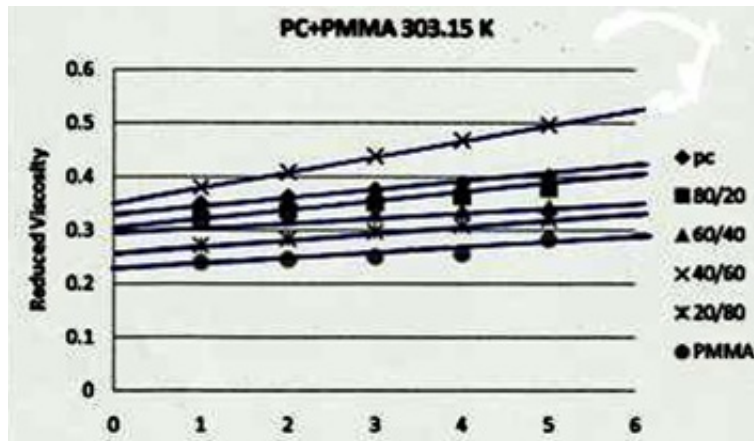


FIG. 1. Plot of  $\eta_{sp}/C$  vs. concentration for PC/PMMA/THF ternary systems at 303.15 K

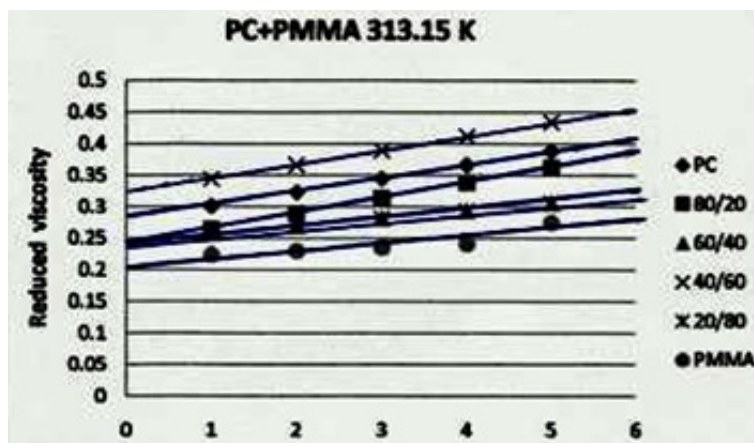


FIG. 2. Plot of  $\eta_{sp}/C$  vs. concentration for PC/PMMA/THF ternary systems at 313.15 K

The reduced viscosity data for PC/PMMA blends at different compositions at 303.15 K and 313.15 K have been recorded in Tables 1 and 2 respectively. Recently, Sun et al. (1992) have suggested a new formula for the determination of polymer miscibility as follows:

TABLE 1. The reduced viscosity data for PC/PMMA and their blends in tetrahydrofuran at 303.15 K at different concentrations

Concentration (g/dl)	PC/PMMA Composition of blends 303.15 K					
	100/0(PC)	80/20	60/40	40/60	20/80	0/100(PMMA)
0.2	0.34980	0.32361	0.31808	0.38129	0.27266	0.24045
0.4	0.36270	0.33702	0.32466	0.41059	0.28470	0.24592
0.6	0.37560	0.35044	0.33125	0.43988	0.29811	0.25133
0.8	0.38850	0.36385	0.33783	0.46918	0.30910	0.25681
1.0	0.40130	0.37727	0.34442	0.498481	0.32177	0.28308

TABLE 2. The reduced viscosity data for PC/PMMA and their blends in tetrahydrofuran at 313.15 K at different concentrations

Concentration (g/dl)	PC/PMMA Composition of blends 313.15 K					
	100/0(PC)	80/20	60/40	40/60	20/80	0/100 (PMMA)
0.2	0.30174	0.26455834	0.258320529	0.344648392	0.258359487	0.22441
0.4	0.32354	0.28913833	0.270324026	0.367186064	0.270326697	0.23009
0.6	0.34533	0.31371831	0.282327523	0.389723736	0.282293899	0.23577
0.8	0.36713	0.33829830	0.29433102	0.412261408	0.294261108	0.24145
1.0	0.38893	0.36287829	0.306334518	0.434799081	0.306228314	0.27543

$$\alpha = k_m - \frac{k_1[\eta]_1^2 W_1^2 + k_2[\eta]_2^2 W_2^2 + 2\sqrt{k_1 k_2}[\eta]_1[\eta]_2 W_1 W_2}{\{[\eta]_1 W_1 + [\eta]_2 W_2\}^2},$$

where  $k_1$ ,  $k_2$  and  $k_m$  are the Huggins's constants for individual components 1, 2 and the blend respectively. Long-range hydrodynamic interactions were considered while deriving this equation. Sun et al. (1992) have suggested that a blend will be miscible when  $\alpha \geq 0$  and immiscible when  $\alpha < 0$ .

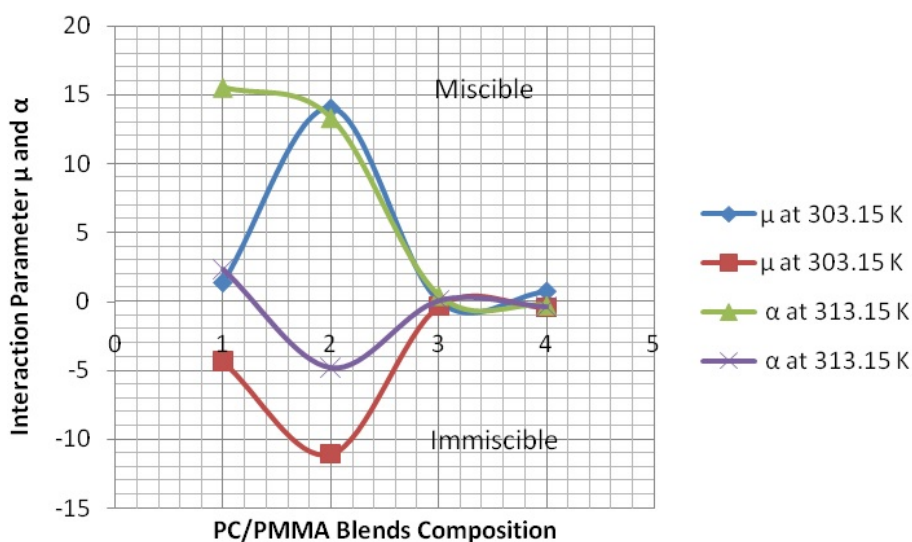
**FTIR analysis:**– The FTIR spectra of PC and PMMA are shown in Fig. 4 and 9. The IR spectrum of PMMA showed absorption bands at 2951 and 1736  $\text{cm}^{-1}$  due to  $-\text{CH}_3$  asymmetric stretching and C=O stretching respectively. The IR bands at 1481 and 1449  $\text{cm}^{-1}$  were due to  $\text{CH}_2$  scissoring and  $\text{CH}_3$  asymmetric stretching. The characteristic peak at 1386  $\text{cm}^{-1}$  appeared due to O- $\text{CH}_3$  deformation. C-O stretching resulted in the peak at 1271  $\text{cm}^{-1}$ . O- $\text{CH}_3$  stretching resulted in a peak at 1148  $\text{cm}^{-1}$ , while the peak at 752  $\text{cm}^{-1}$  was due to the  $\text{CH}_2$  rocking mode of vibration. Spectrum 1, was comparable to that of earlier reports [5,6]. The IR spectrum of PC showed absorption bands at 2968  $\text{cm}^{-1}$  attributed to  $-\text{CH}_3$  stretching vibration. Characteristic C=O stretching band was at 1773  $\text{cm}^{-1}$ . The ring (C-C) vibrational mode appeared at 1507  $\text{cm}^{-1}$ . Peaks at 1082 and 1013  $\text{cm}^{-1}$  were attributed to C-C-C (bending)

TABLE 3. Interaction parameters and Huggins's constants of PC/PMMA blends at 303.15 K

PC/PMMA 303.15 K	$[\eta]$	$K_H$	$\mu$	$\alpha$
100/0(PC)	0.33668	0.57181	–	–
80/20	0.31019	0.69711	1.38991	0.075999
60/40	0.311492	0.33934	-4.35556	-0.34108
40/60	0.35199	1.182301	15.55101	0.42952
20/80	0.26047	0.90384	2.35459	0.061105
0/100(PMMA)	0.22615	0.95694	–	–

TABLE 4. Interaction parameters and Huggins's constants of PC/PMMA Blends at 313.15 K

PC/PMMA 313.15 K	$[\eta]$	$K_H$	$\mu$	$\alpha$
100/0(PC)	0.27995	1.39054	–	–
80/20	0.23997	2.13406	14.06064	0.74914
60/40	0.24631	0.989210	-11.07531	-0.38944
40/60	0.32211	1.08609	13.34568	-0.28553
20/80	0.24639	0.985617	-4.81296	-0.378072
0/100(PMMA)	0.206702	1.35465	–	–

FIG. 3. Effect of temperature on the interaction parameter  $\mu$  and  $\alpha$  of PC/PMMA blend in at 303.15 K and 313.15 K

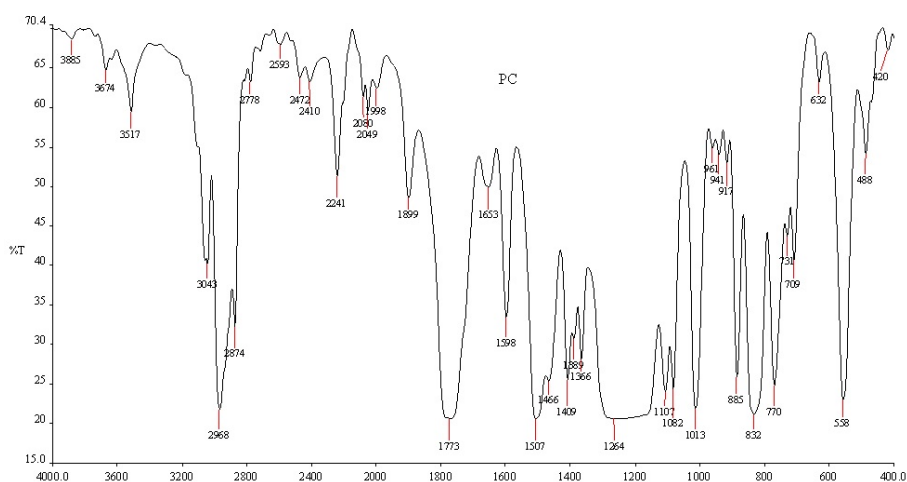


FIG. 4. PC

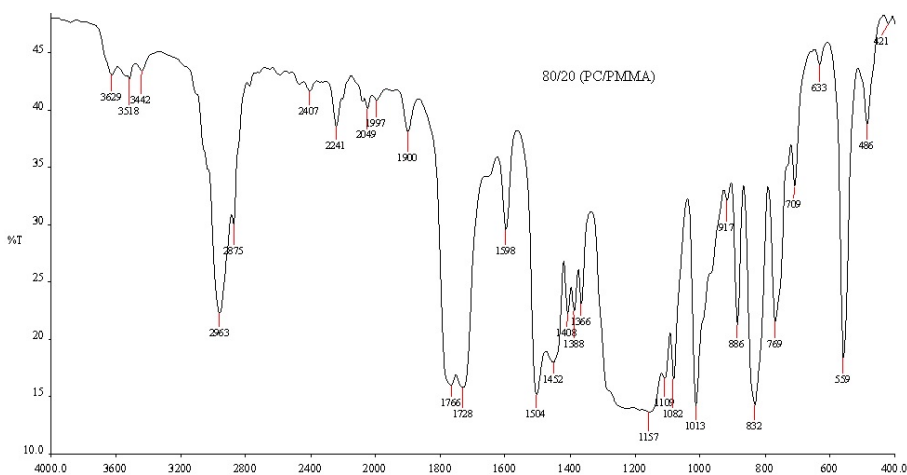


FIG. 5. PC/PMMA(80/20)

O–C–O stretching vibrational modes. These results were comparable to those given by Silverstein and Bassler [9] and Schnell [10]. Figures 5, 6, 7, 8 show the FTIR spectra of PC/PMMA blends with (80/20, 60/40, 40/60, and 20/80 %w/w) compositions respectively. These data showed that the blends did not indicate the existence of any chemical interaction between the components. A thorough analysis of the IR spectra for these blends showed a decrease in the transmittance of the carbonyl and methoxyl stretching of PMMA with an increase in the PMMA content and an increase in the transmittance of these peaks with an increase in the PC content. These data clearly indicate the formation of polymer blends, as there are no shifts in the peaks of any of these functional group in the PC/PMMA blend spectra, it may be concluded that there is no such chemical interaction between component polymers. Thus, these are certainly physical blends.

**SEM analysis:**– The scanning electron microscope (SEM) images the surface of a sample by scanning it with a high energy beam of electrons in a raster scan pattern. These electrons interact with surface atoms of sample, producing signals which reveal information about the surface topography of sample.

Figures 10 and 15 show the SEM images of PC and PMMA respectively. Fig. 11, 12, 13, and 14 exhibit SEM images of blends PC/PMMA of 80/20, 60/40, 40/60, and

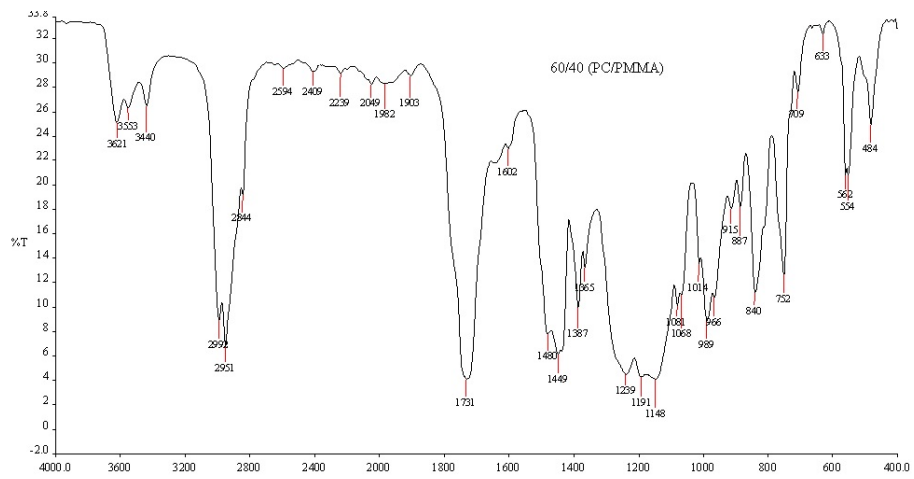


FIG. 6. PC/PMMA(60/40)

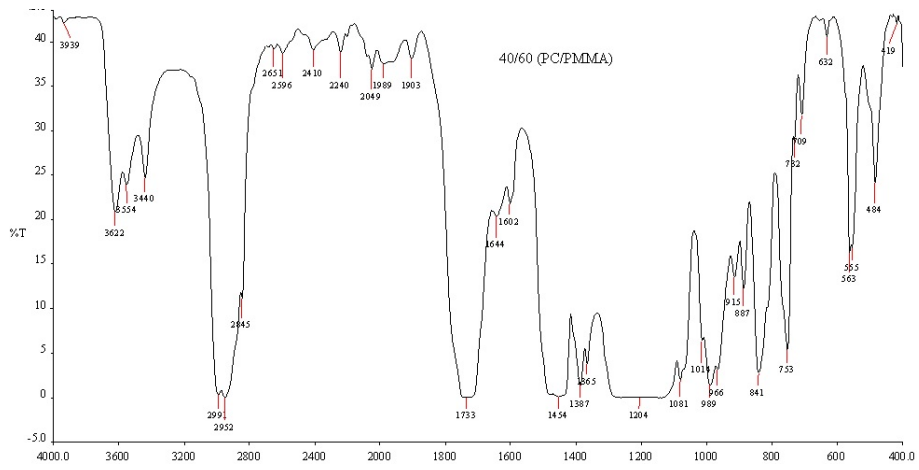


FIG. 7. PC/PMMA(40/60)

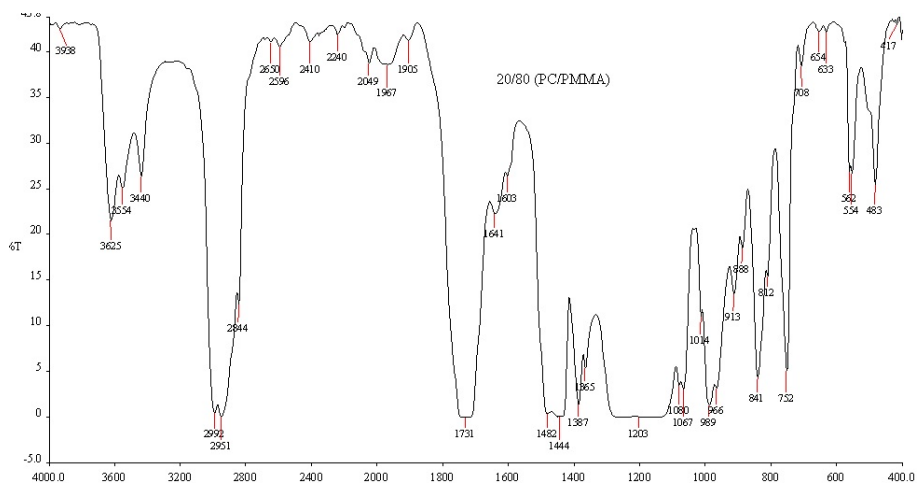


FIG. 8. PC/PMMA(20/80)

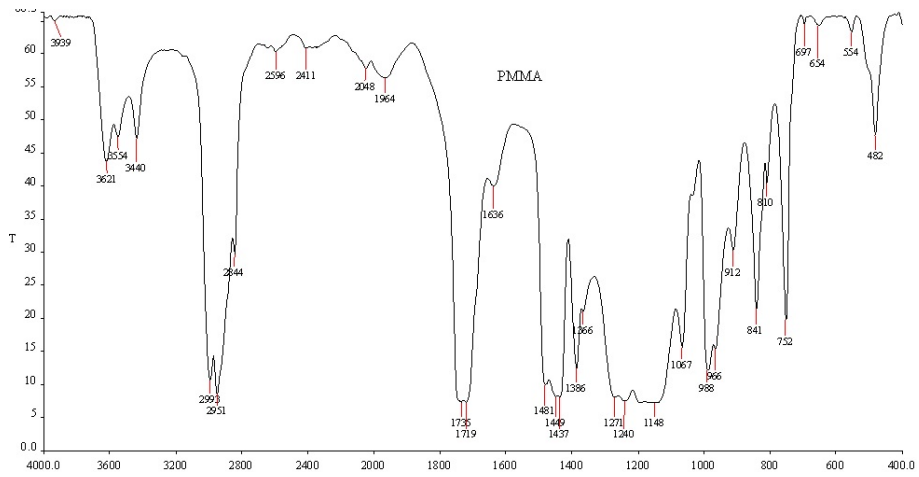


FIG. 9. PMMA

20/80 w/w % compositions respectively. The SEM images of each have been shown in three different magnifications. As can be seen from the images of blends, they show uniform morphological features without any phase separation. This shows the miscibility of blends to a large extent [9].

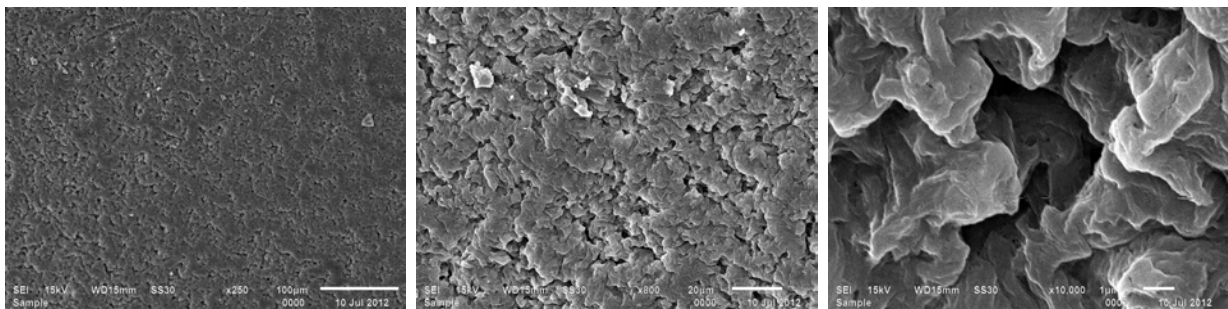


FIG. 10. PC

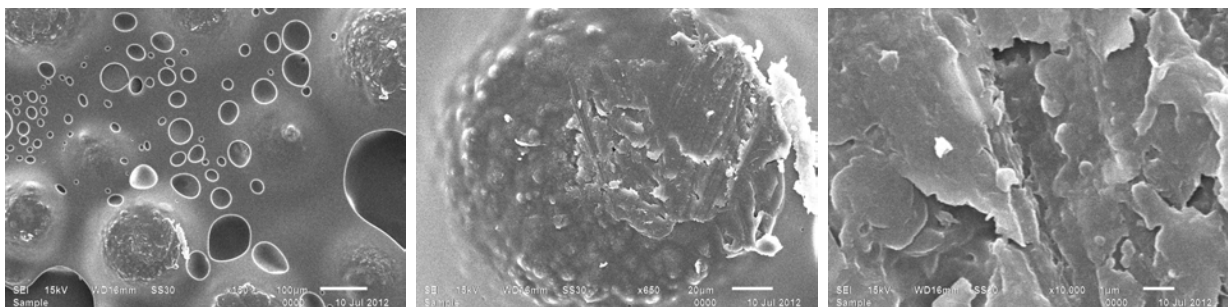


FIG. 11. 80/20(PMMA/PC)

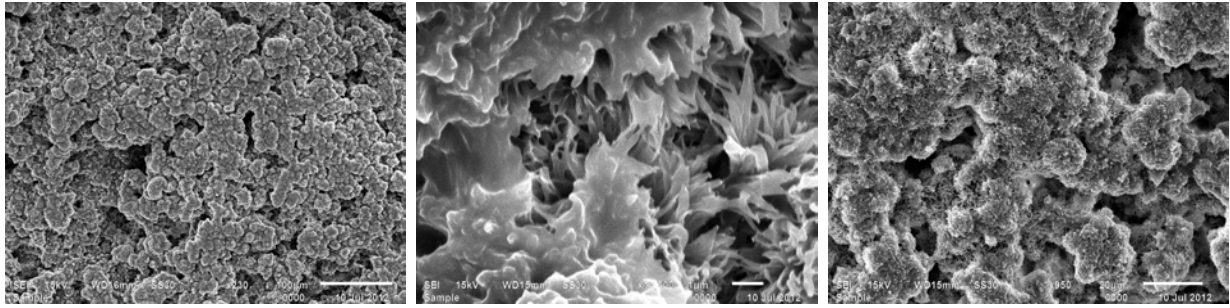


FIG. 12. 60/40(PMMA/PC)

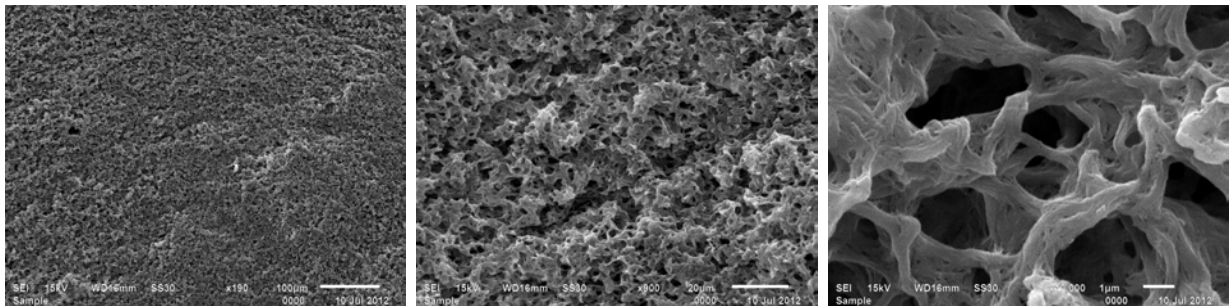


FIG. 13. 40/60(PMMA/PC)

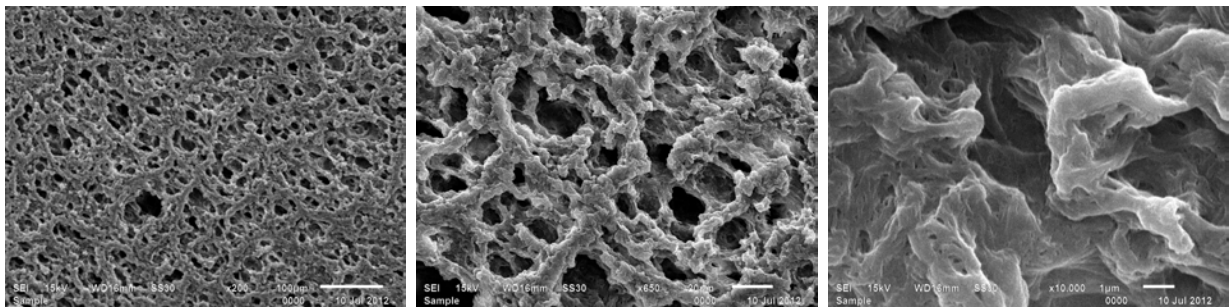


FIG. 14. 20/80(PMMA/PC)

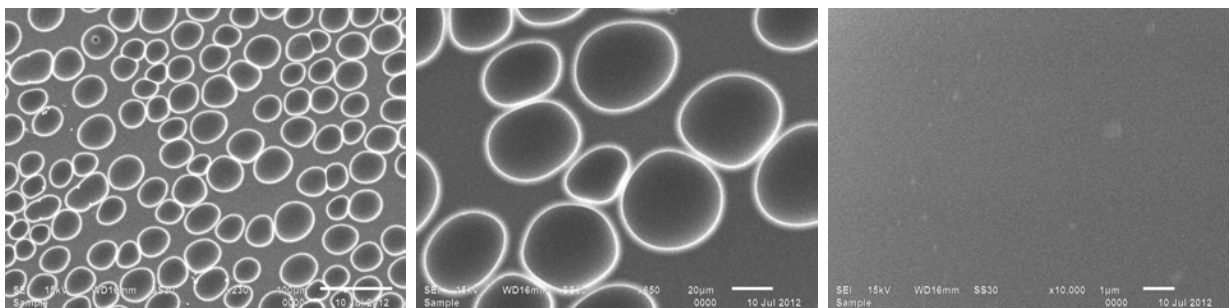


FIG. 15. PMMA

#### 4. Conclusion

Viscometric studies showed that most PC/PMMA blends displayed miscibility at both temperatures. However, at the higher temperature, the small negative values for the interaction parameters, not in a consistent manner for some compositions, indicated some degree of immiscibility. However, FTIR and SEM analyses showed the blends of PC/PMMA to be miscible in all compositions tested at ambient temperature. FTIR scanning of the blends showed no change in the wavenumbers of the functional groups, which support the formation of PC/PMMA physical blends.

#### References

- [1] Gautam kumar sah, Ashok kumar Gupta. Miscibility study of blends PVC/PMMA by viscometric etc. *Nanosystem: Physics, Chemistry, Mathematics*, **4** (2), P. 288–293 (2013).
- [2] J.W. Shurer, A. de Boer, G. Challa. Influence of tacticity of poly (methylmethacrylate) on the compatibility of poly (vinyl chloride). *Polymer*, **16**, P. 201 (1975).
- [3] G.S. Guru, P. Prasad, H.R. Shivakumar, S.K. Rai. Miscibility, Thermal and Mechanical Studies of Methylcellulose/Poly (vinyl alcohol) Blends. *IJRPC*, **2** (4), P. 957–968 2012.
- [4] Patel Gaurang, M. B. Sureshkumar, N.L. Singh. Spectroscopic Correlation of Mechanical Properties of PVC/PMMA Polymer Blend. *Journal of International Academy of Physical Sciences*, **14** (1), P. 91–100 (2010).
- [5] Gautam kumar Sah, S. Vijaykanth, Ashok kumar Gupta. Mechanical, Electrical, Thermal, and Morphological Properties of PP, PP-g-Mah and Mica silicate. *Nanoclay Nanocomposite: J. Environ. Nanotechnol.*, **1** (1), P. 13–19 (2012).
- [6] Sun Z., Wang W., Feng Z. Criterion of polymer-polymer miscibility determined by viscometry. *Eur. Polym. J.*, **28** (10), P. 1259–1261 (1992).
- [7] K. Kaniappan, S. Latha. Certain investigation on the formulation and characterization of PS/PMMA blends. *International journal chemtech research*, **3** (2), P. 708–711 (2011).
- [8] Mohammad Saleem Khan, Raina Aman Qazi, Mian Said Wahid. Miscibility studies of PVC/PMMA and PS/PMMA blends by dilute solution viscometry and FTIR. *African Journal of Pure and Applied Chemistry*, **2** (4), P. 041–045 (2008).
- [9] R. Silverstein, G. Bassler. *Spectrometric Identification of Organic Compounds*, Wiley: New York, 1963.
- [10] H. Schnell. *Chemistry and Physics of Polycarbonate*, Interscience: New York, 1964.
- [11] S.G. Adoor, L.S. Manjeshwar, et al. Solution and solid-state blend compatibility of poly (vinyl alcohol) and poly (methyl methacrylate). *J. appl. polymer sci.*, **100** (3), P. 2415–2421 (2006).

# NANOSCALE STRUCTURES BASED ON THE $\text{Zn}_{1-x}\text{Cd}_x\text{S}$

M. A. Jafarov, E. F. Nasirov

Baku State University, Baku 1045, Z.Khalilov st.23, Azerbaijan  
maarif.jafarov@mail.ru

**PACS 73.20.-e; 78.66.Hf; 68.55.-a**

In this work, the results of the investigation of the peculiarity near the solar spectrum region, of  $\text{Zn}_{1-x}\text{Cd}_x\text{S}$  nanoparticles, nanofilms, nanoscale p-n and heterojunction prepared on glass-ceramic and aluminium substrates by precipitation from aqueous solutions are presented. We investigated the preparation of ZnCdS nanoparticles in a micro-emulsion system stabilized with nonionic surface active materials, as well as the impact of drop volume and supersaturation the size of the formed ZnCdS particles. The temperature dependence of dark and light conductivity, spectrum and optical quenching of primary and impurity photoconductivity were investigated. Direct current-voltage characteristic structure of Al/p-CdS/n-CdS is almost identical to the current-voltage characteristics of p-n junctions. Volt-farad characteristics of the samples established the presence of conduction due to the presence of reverse bias p-n junctions. In the following order, CdTe/CdS/ $\text{Zn}_{1-x}\text{Cd}_x\text{S}$  structure have 75% or slightly higher quantum efficiency in the 400–850 nm wavelength region.

**Keywords:** chemical bath deposition, nanoparticle, nanoscale p-n junction, micro emulsion system.

## 1. Introduction

Among the many different methods available to deposit films of semiconductors, chemical bath deposition (CBD) must rank as the simplest conceptually [1–3]. CBD refers to depositions from solution (usually aqueous) where the required deposit is both chemically generated and deposited in the same bath [4–7]. Thus, deposition from a supersaturated solution or spin coating from a colloidal sol are not included under the aegis of CBD: in both cases, the layer material must be pre-prepared. Neither is sol-gel layer formation, although it could be reasonably argued that the cross-linking which occurs during the process constitutes a chemical reaction. Successive ion layer adsorption and reaction (SILAR) is a related technique, where a substrate is first dipped in an ionic solution of one component, rinsed, then dipped in a solution of the second component and rinsed; this ideally results in a single monolayer of the desired compound [8–10]. Liquid phase deposition (LPD) is a specific subset of CBD often used for acidic oxides. In spite of it being so simple, it is one of the least known. If scientists or engineers in general would be asked to name some semiconductor film deposition methods, evaporation, chemical vapor deposition, sputtering, perhaps even electrodeposition, would be the most obvious techniques that would come to mind: CBD would probably be lower on the list (with the obvious exception of those who work with the method). Part of the reason is the many different terms which are used to denote CBD: chemical solution deposition (previously more popular, but a consensus is beginning to favor the use of CBD), chemical deposition (when it is clear that chemical vapor deposition — a very different technique — is not meant) and liquid phase deposition [11–13].

In the last decade the interest in nano-objects with specific features is sharply increased. This interest is related to the unique properties of nanoparticles, which differ from

that of normal-size particles. The investigation nanoparticle properties is one of the main aims of the novel directions for physical chemistry. Developing of this direction is closely related with the methods of synthesis, which allow the preparation of nanoparticles having the required size and rather narrow size distribution. The reverse micro emulsion systems are thermodynamically sustainable double phase systems, which consist of polar phase micro drops, distributed in nonpolar ambient. Surface-active materials (SAM) are used to stabilize systems like this. This allows one to perform chemical reactions among materials in polar phase and forming sparingly-soluble compounds. The advantage of this nanoparticle preparation method is its relative simplicity and also the possibilities of simultaneous synthesis and stabilization of the prepared particles [14].

The obtained results show that when controlling ionic composition and heat treatment (HT) conditions, one can control the properties of  $Zn_{1-x}Cd_xS$  films. Furthermore, the above films are similar in their main photoelectric properties and parameters to such model crystals as CdS and ZnS, to allow for the effect of sticking centers, conditioned polycrystalline structure.  $Zn_{1-x}Cd_xS$  films can be used as photodetectors of the near IR region. The purposes of these investigations are to determine the general regularities and characteristic of recombination and electron-molecular processes, determinant high sensitivity in the IR region, versus the composition and HT conditions, the photoelectrical properties of  $Zn_{1-x}Cd_xS$  ( $0 \leq x \leq 0.6$ ) films deposited from the solution. Until recently, converters based on CdS were produced mainly as a heterostructure. Creation of a p-n junction is difficult because of the receipt of CdS with hole conductivity. The literature contains little data concerning the single-crystal film-p-n-junction. In this paper, we present the results for studies of nanoscale p-n junction based on solution-precipitated CdS. The samples were prepared by precipitation from solution onto an aluminum substrate. Before applying the lower aluminum electrode, the sample was kept in air at 300 °C, for 10 min. Based on the measurement of current-voltage (I-V), capacitance-voltage (C-U), and thermally stimulated conductivity (TSC) characteristics of the samples, it was established that conductivity exists due to the presence of p-n junctions.

In the solar cell of CdTe, the lattice mismatch between n-CdS and p-CdTe and the low bandgap of CdS window layer are known to have some drawback on cell performance. By using higher bandgap materials, like ZnS or  $Zn_{1-x}Cd_xS$  as a heterojunction partner to CdTe, one can improve the window bandgap, but the lattice mismatch of these materials is worse than that of CdS. Trading off the latter mismatch for the higher bandgap may not be the solution, for the loss in cell performance due to lattice mismatch outweighs the gain due to the increase in window bandgap. Therefore, to retain the compatibility of CdS and CdTe and still improve the short wavelength spectral response of CdTe solar cell, its traditional CdS/CdTe structure should be changed to  $Zn_{1-x}Cd_xS$ /CdTe. In other words, a  $Zn_{1-x}Cd_xS$ /CdS layer should replace the CdS-only window layer.

## 2. Experiment

In this paper we investigated the preparation of ZnCdS nanoparticles in a nonionic surfactant-stabilized micro emulsion as well as the impact of drop volume and supersaturation on the size of the formed ZnCdS particles. Hexamethylene was used as the non polar phase, while water, aqueous solutions of  $Cd(Ac)_2$ ,  $ZnCl_2$  and precrystallized  $Na_2S_2O_3$  were used as the polar phase.

All solutions were prepared in doubly-distilled water. Reverse micro emulsion systems were prepared by the solubilization of water, aqueous solutions according to salts in a reverse micellar system, in which the Tx-100 concentration was 0.3 M and SAM/n-SAM ratio was

4:1. The water or aqueous solutions of the corresponding salts were added to a defined volume of this solution with drops in such amount that the  $W=[\text{H}_2\text{O}]/[\text{SAM}]$  ratio was varied from 5–15. Equal volumes of the micro emulsion with similar content, containing ions of the reacting substances in aqueous phase were mixed for preparing cadmium sulfide.

The particle size of the prepared cadmium sulfide was determined by a spectrophotometric method. The dependence of optical density on the wavelength was measured by a spectrophotometer in a cuvette from 320–900 nm.

The  $\text{Zn}_{1-x}\text{Cd}_x\text{S}$  ( $0 \leq x \leq 0.6$ ) films of 0,03–2  $\mu\text{m}$  thickness were deposited on glass ceramic substrates from an aqueous solution by the method described previously [3]. The thicknesses of the p-CdS, CdTe and  $\text{Zn}_{1-x}\text{Cd}_x\text{S}$  ( $0 \leq x \leq 0.6$ ) films were obtained using a Dektak profilometer. Transmission measurements were performed using a spectrophotometer.

This was prepared by adding into the beaker containing the stirred deionized water at 85 °C,  $\text{Cd}(\text{OAc})_2$ ,  $\text{Zn}(\text{OAc})_2$ ,  $\text{NH}_4\text{OH}$ , and  $\text{Na}_2\text{S}_2\text{O}_3$ , from 0.05, 0.05, 12 and 0,2 M stock solutions, respectively, in that order.

Since the CBD-grown CdS layer has produced some of the best performing cells, the growth of the new  $\text{Zn}_{1-x}\text{Cd}_x\text{S}/\text{CdS}$  window layer by CBD should therefore be explored. Each experimental solution contained 300 ml of deionized water.

The nanofilm's composition ( $0 \leq x \leq 0.6$ ) was changed by the partial substitution of the thiourea and was controlled by chemical, spectral and X-ray phase analyses. XRD pattern of  $\text{Zn}_{1-x}\text{Cd}_x\text{S}$  thin films results are shown in Fig.1 a,b. The results for the spectral dependence of the optical transmittance of  $\text{Zn}_{1-x}\text{Cd}_x\text{S}$  films are shown in Fig. 2. Sections of the films were subjected to aerobic HT at temperatures of 400–500 °C for 0–30 min.

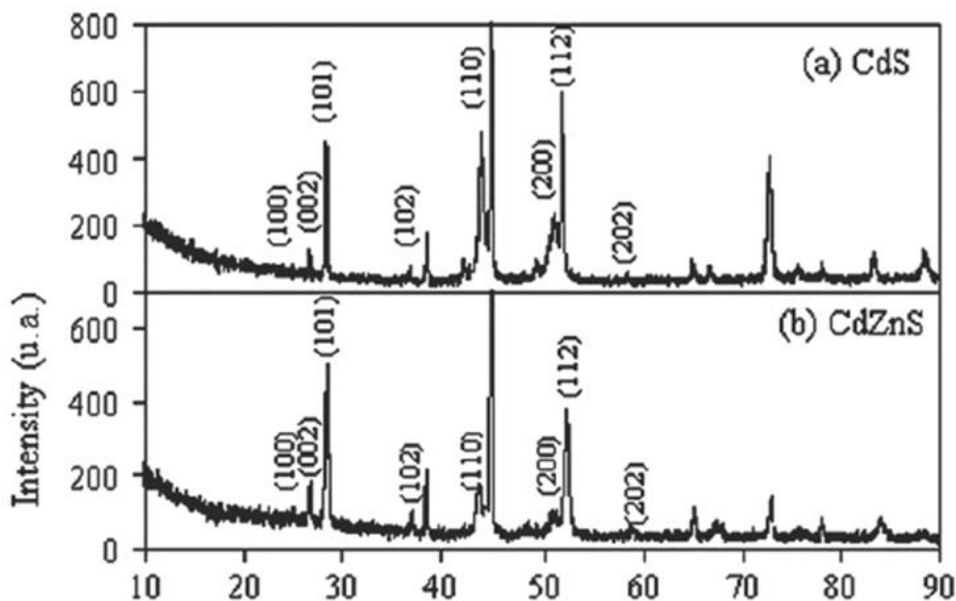


FIG. 1. XRD pattern of thin films: (a) CdS, (b) ZnCdS

The morphologies of the products were observed by SEM. These images clearly indicate that the products are spherical. It can also be seen that there is a uniform size distribution in all products. Figure 2 shows the scanning electron microscopy (SEM) micrographs for the films deposited and annealed at various temperatures. The SEM micrograph of the films deposited at a higher bath temperature, such as 80 °C, in the microemulsion system is shown in Fig. 2a. No pinholes can be observed for these films. The films show

more grain formation and well defined particle edges. However, there seems to be a slight decrease in the number of grains for the films annealed at 200, 300 and 500 °C. The surface of the substrate is not covered completely at these bath temperatures. The grain formation was observed as an irregular agglomeration with the grain sizes completely different from one another (2–5  $\mu\text{m}$ ). These observations suggest an incomplete nucleation step with an irregular grain growth rate. This is due to coating of inorganic core by the surfactant, which prevents the nanoparticle aggregation. It has been proven that the prevention of nanoparticle aggregation in the presence of a surfactant is more effective when the surfactant has a long and branched chain structure. Fig. 3. shows the distribution of nanoparticles ZnCdS.

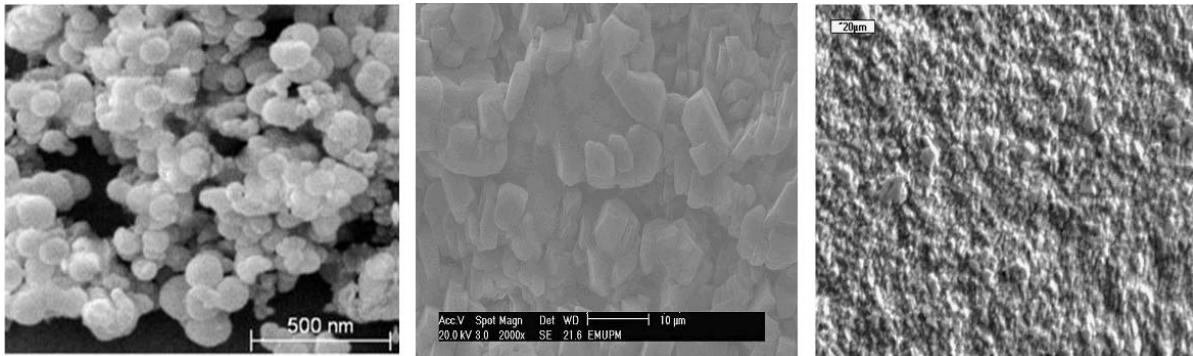


FIG. 2. SEM micrographs of  $Zn_{1-x}Cd_xS$  films deposited at higher bath temperature such as 80 °C in miroemulsion system (1) and annelaited at different temperatures, 2—300 °C, 3—500 °C

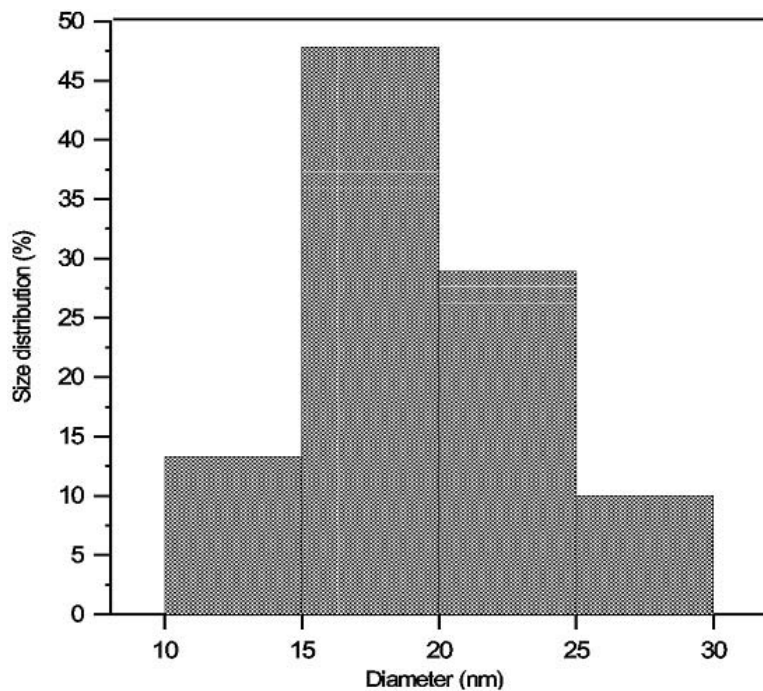


FIG. 3. Distribution nanoparticles Zn CdS

The temperature dependence of dark ( $\sigma_{dk}$ ) and light conductivity ( $\sigma_{ph}$ ), the spectrum and optical quenching of photoconductivity ( $\sigma_{oq}$ ), the current-illumination characteristics,

and the thermostimulated conductivity from 80–400 K were investigated. According to the thermopower measurements, the films were n-type. The dark conductivity of  $\text{Zn}_{1-x}\text{Cd}_x\text{S}$  films was found to vary with  $x$ , from  $10^{-4}$  to  $10^{-5}$  S/cm.

The ratio of photocurrent to the dark current reached  $10^2$  to  $10^3$ . The carrier concentration determined from Hall measurements was  $3\text{--}5 \times 10^{14}$   $\text{cm}^{-3}$  and  $10^{16}$   $\text{cm}^{-3}$  for the films with  $x=0$  and  $x=0.3$ , respectively. The spectral dependence of optical transmittance of  $\text{Zn}_{1-x}\text{Cd}_x\text{S}$  films is shown in Fig. 4.

Just after deposition, the above films were characterized by long-term relaxation photoeffects. Subsequent to heat-treatment, considerable changes in the photoelectric (PE) properties versus the composition, temperature and annealing time ( $\tau_a$ ) were observed. The dependence of conductivity as a function of time ( $\tau_0$ ) has a nonmonotonic character, i.e. with low  $\tau_a$ , the conductivity of films increases and achieves a maximum value exceeding the initial one by more than four orders of magnitude. Further increase of the annealing time up to 15 min leads to a sharp decrease in the conductivity.

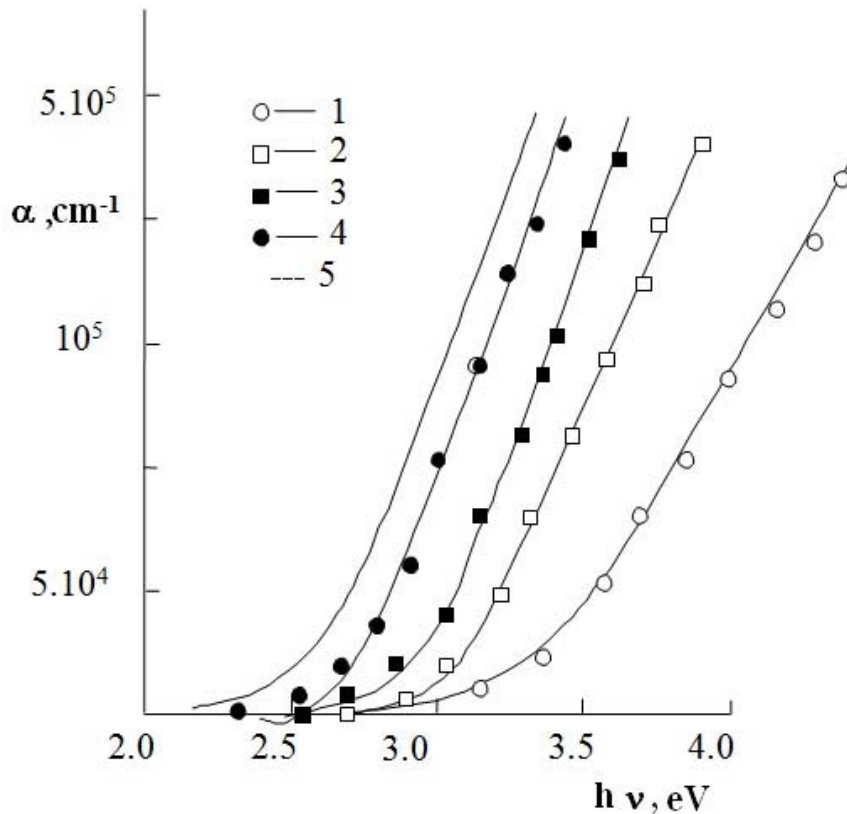


FIG. 4. The spectral dependence of optical transmittance of  $\text{Zn}_{1-x}\text{Cd}_x\text{S}$  films.  $x$ : 1—0.1, 2—0.3, 3—0.5, 4—0.7, 5—0.9

The  $\sigma_c(\tau_a)$  dependence has an extremum character, i.e. primarily it increases for annealing times up to 15 min, then ( $t \geq 15$  min), a slow decay is observed. With increased annealing temperatures and  $x$ , a shift of the above dependence extrema toward lower times takes place. A photoconductivity spectrum maximum of  $\text{Cd}_{1-x}\text{Zn}_x\text{S}$  ( $0 \leq x \leq 0.6$ ) films was observed at  $0.445\text{--}0.495$   $\mu\text{m}$  versus the composition. Subsequent to heat treatment, the photoconductivity spectrum considerably widened and the peaks at  $(0.58\text{--}0.70)$   $\mu\text{m}$  and  $(0.90\text{--}1.13)$   $\mu\text{m}$  appeared. With increased time, to  $4 \leq \tau_a \leq 15$  min, the intensities of additional maxima increased and the intensity of the principal maximum decreased. The  $\text{Cd}_{1-x}\text{Zn}_x\text{S}$

( $0 \leq x \leq 0.6$ ) films after the heat treatment at  $500^\circ\text{C}$  for 5–10 min exhibited high sensitivity ( $\sigma_{ph}/\sigma_{dk} = 10^7$  to  $10^8$ ) over a wide spectral range.

The research of I-U, C-U characteristics and thermally stimulated conductivity from 80–400 K was performed. The I-U was removed in a pulsed, static and dynamic mode and the C-U characteristics by the use of a RLC bridge, allowing simultaneous measurement of the barrier capacitance and the differential resistance of the barrier, as well as resistance in the neutral part of the semiconductor. Volt-ampere characteristic (VAC) nanoscale p-n transition p-CdS/n-CdS has rectifying properties by a factor of  $10^3$ – $10^4$  with a voltage of  $U = 1.5 \div 2$  B (Fig. 5). It is shown that the barrier width is 100 nm at zero bias and reaches 150 nm at a voltage of 2 V reverse mixing.

Below 250 K, the slope remains almost constant, which corresponds to the dominant role of tunneling processes, and above 250 K, with increased temperature the slope increases, indicating the growing role of thermal processes. Direct parts of the VAC (in logarithmic scale) consist of two parts, corresponding to different mechanisms of current flow.

We have demonstrated using chemical and thermal activated diffusion that  $Zn_{1-x}Cd_xS$  thin films can be synthesized from electrochemically-deposited ZnS/CdS multilayers. A more homogeneous  $Zn_{1-x}Cd_xS$  film is obtained at lower processing temperatures if the stacked layers are thin. It is of great importance that the grown structure is almost homogenized in the chemical bath at temperatures below  $90^\circ\text{C}$ . The homogenization of our structure was achieved by annealing at  $400^\circ\text{C}$ , the temperature generally used for processing solar cells. The low processing temperature developed here in the fabrication of  $Zn_{1-x}Cd_xS$  means that the proposed  $Zn_{1-x}Cd_xS$ /CdS solar cell window could be grown at temperatures that will not damage the glass or the underlying transparent conducting oxide generally used as a substrate in solar cells.

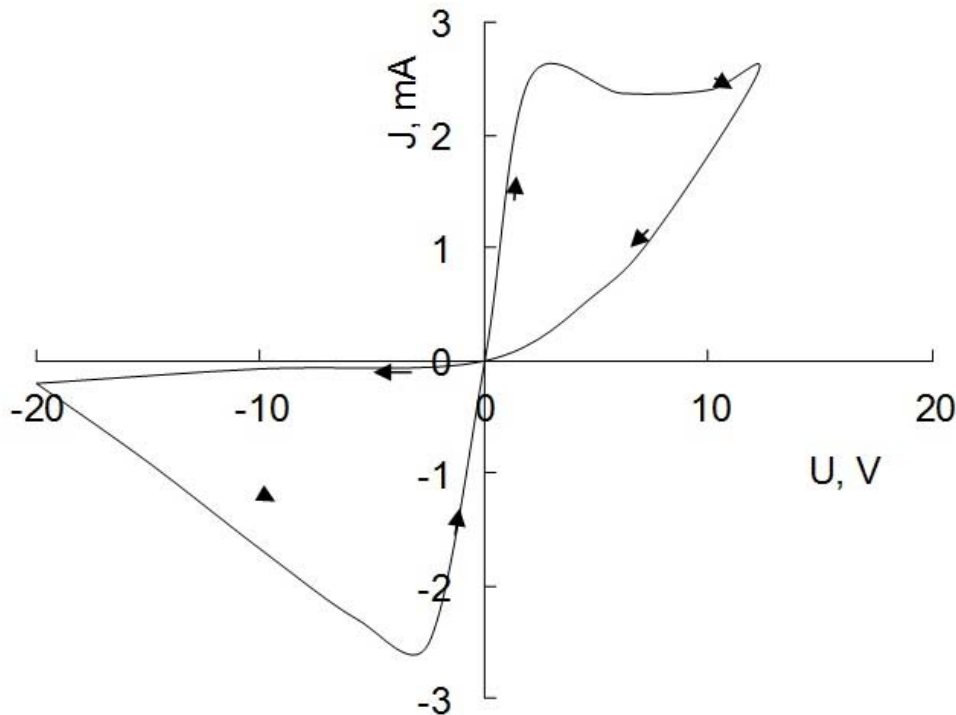


FIG. 5. VAX p-n junction based on CdS

To achieve the new  $Zn_{1-x}Cd_xS/CdS$  structure proposed for the CdTe window layer, what is required is simply an additional growth of CdS on top of the  $Cd_{1-x}Zn_xS$  layer obtained from a chemical deposition ZnS/CdS multilayer.

The structures are Al/p-CdTe/ $Zn_{1-x}Cd_xS$ /contact, type 1 Al/CdTe/CdS/ $Zn_{1-x}Cd_xS$  and type 2 Al/p-CdS/CdTe/ $Zn_{1-x}Cd_xS$  (Fig. 6).

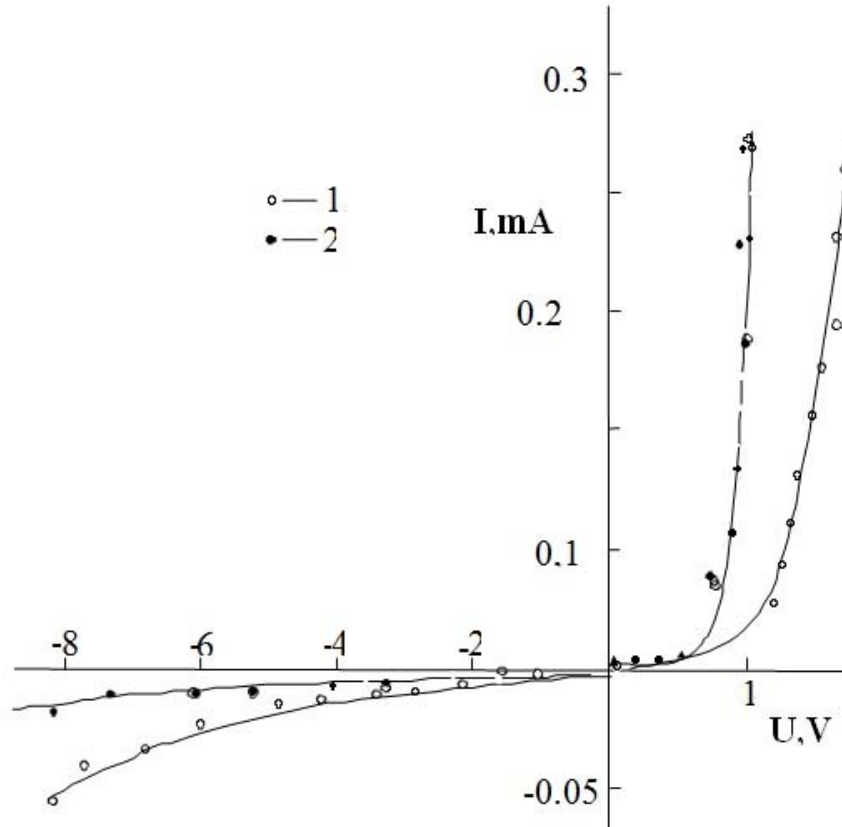


FIG. 6. VAX structures Al/CdTe/CdS/ $Zn_{1-x}Cd_xS$  (1) and Al/p-CdS/CdTe/ $Zn_{1-x}Cd_xS$  (2)

The sample was then annealed in  $CdCl_2/Ar$  ambient (75%  $CdCl_2 + 25%$  Ar) at  $400^\circ C$  for 15 min. The window fabrication was completed by the deposition of an additional  $0.35 \mu m$ -thick p-CdS film. In the following order, CdTe/p-CdS/ $Zn_{1-x}Cd_xS$  structure have 75% or slightly higher quantum efficiency in the 400–850 nm wavelength region (Fig. 7). We note that the structure with the  $Zn_{1-x}Cd_xS$  layer generally has a better short wavelength response, than the expected value.

### 3. Discussion of results

Interpretation of the experimental results becomes complicated due to the simultaneous occurrence of several processes (evaporation, generation and transformation of intrinsic defects) which arise in films during heat treatment. The kinetics of every process has a complicated character [5]. The dependence observed in photoelectric properties of films point out the changes of concentration of defects of donor and (or) acceptor character due to film annealing. Decreases of film photosensitivity at shorter annealing times ( $\tau_a$ ) indicated an increase in the concentration of fast-recombination centers (s-centers), i.e. the increase of

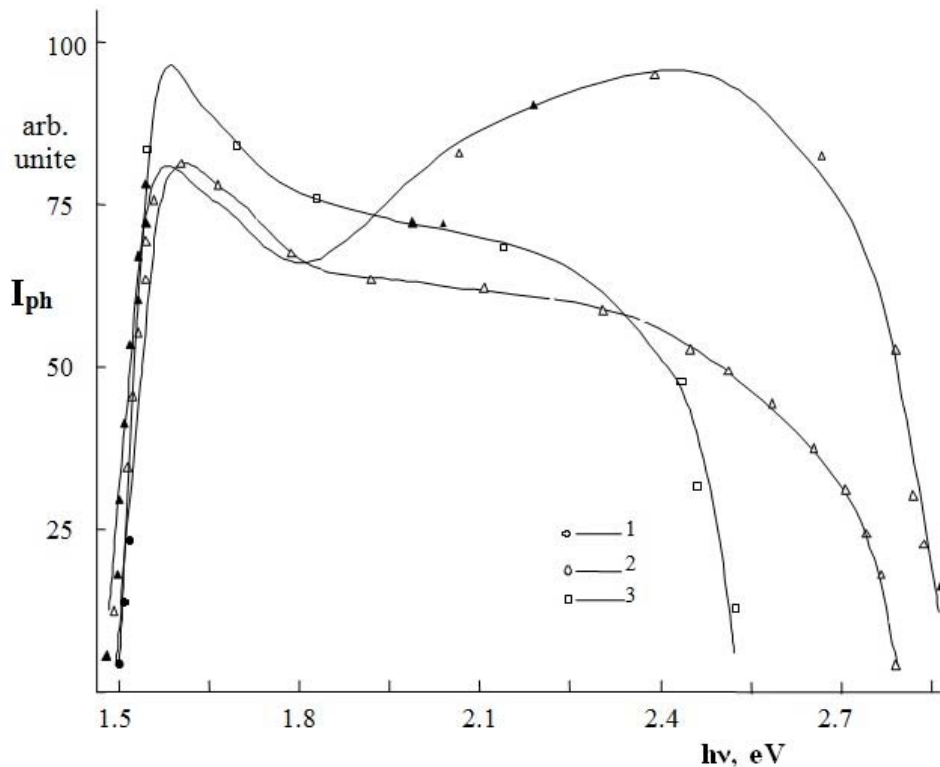


FIG. 7. Spectral response of the photocurrent through  $Zn_{1-x}Cd_xS$  ( $0 \leq x \leq 0.6$ ) films annealed in air at  $500^\circ C$  for (1) 0, (2) 5, (3) 15 min

the recombination flux ( $g_s$ ), and hence the decrease in the life of electrons takes place. Measurements of the current-illumination characteristics of the samples showed that at shorter annealing times the decrease in hole concentration on the slow recombination centers (r-centers) was observed. This fact can be attributed either to an increase of the compensating shallow donor concentration or a decrease of the r-center concentration. A simultaneous increase in the concentration of the shallow donor centers is responsible for the increased dark conductivity and the fast recombination centers, causing decreased photosensitivity, allowing us to assume that the s-centers are complexes consisting of shallow donors [9].

The change observed at  $\tau_a \geq 5$  min can be explained when the anion and the cation vacancies diffuse into the volume and are formed on their surfaces. Due to heavy evaporation of metal during initial stages of annealing, the near-surface region is mainly enriched by cadmium and sulfur vacancies playing the role of slow recombination centers. Their diffusion into the volume leads to an increased photosensitivity and to decreased dark conductivity. In this case, the complexes of cadmium, sulfur and selenium vacancies, i.e. the recombination r-centers, were formed.

The decreased photoconductivity for annealing times  $\tau_a > 15-20$  min is attributed to a single electron-molecular mechanism considering the initial state of the film surface as well as the local and collective phenomena during chemisorption. In the initial state of annealing, the increased surface potential barrier due to chemisorption leads to an increase of the film sensitivity due to slow recombination. When the recombination was controlled by r-centers, the increase in their occupancy by holes due to chemisorption resulted in a decrease of the photoholes' lifetime, i.e. the photoconductivity decreased. In this case, with increased sulfur concentration in films the effect of oxygen became lower.

The obtained results showed that when controlling the ionic composition and HT conditions, one can control the properties of  $\text{Zn}_{1-x}\text{Cd}_x\text{S}$  ( $0 \leq x \leq 0.6$ ) films, achieving the appropriate degree of compensation of recombination levels and traps attributed to the intrinsic defects or impurities. In this way, model crystals, such as CdS and ZnS, can explain the main photoelectrical properties and parameters of  $\text{Zn}_{1-x}\text{Cd}_x\text{S}$  ( $0 \leq x \leq 0.6$ ) films.

Hence, the space charge region in the investigated structures is only part of the film thickness and the space charge region in p-CdS is very narrow, due to the sharp asymmetry of the conductivity. In the beginning, the external voltage drops on the space charge region in CdS n-type. The presence of n-CdS with high resistivity excludes the presence of a strong field at the edge of the metal contact and forms p-n transition, parallel to the barrier, Al/p-CdS. The conductivity of the tunnel transparent dielectric  $\text{Al}_2\text{O}_3$  present on the surface of aluminum is much higher than the conductivity of an inversely biased p-n junction and most of the applied external voltage drops on the p-n junction. Direct current-voltage characteristic structure of Al/p-CdS/n-CdS is almost identical to the current-voltage characteristics of p-n junctions. In this case, the current through the structure increased exponentially with increased applied voltage. In the course of temperature dependence of the slopes of the lines  $\ln I \sim U$  can be divided into two temperature ranges.

The increase in the forward voltage observed at the beginning section of the VAC with a large slope corresponds to when one current flow mechanism is replaced by another. The reverse saturation current was two orders of magnitude smaller than the current through the tunnel-transparent oxide layer of  $\text{Al}_2\text{O}_3$  and  $10^{-10} \text{ cm}^{-2}$  for the high temperature region ( $T > 250 \text{ K}$ ). The activation energy of the saturation current in this case was 0.9 eV, which was less than the barrier and the current was not purely thermal emission, and thus the corresponding emission-recombination mechanism.

Film sandwich structures of CdS-Al in the presence of an intermediate  $\text{Al}_2\text{O}_3$  layer showed the effect of switching to a steady state conduction, which in some approximation can be regarded as the prebreakdown and breakdown after state. After the breakdown condition, studies showed that at  $T = 80 \text{ K}$ , there can be two types of conductivity — low and high. These states were also reproduced. The physical nature of the state can only be understood by studying the mechanisms of conduction film systems at different stages of change. The Ha basis for the measurement of volt-farad characteristics data of samples established the presence of conduction due to the presence of reverse bias p-n junctions. There was found to be high hole concentration ( $10^{21} \text{ cm}^{-3}$ ), characteristic of the conducting state.

In type 1  $\text{Zn}_{1-x}\text{Cd}_x\text{S}/\text{p-CdS}$  windows, a  $0.15 \mu\text{m}$ -thick ZnCdS film was first deposited on an Al substrate. This was then dipped in a  $\text{CdCl}_2$  methanol solution for about 30 s to improve the conductivity, then dried with an infrared lamp, and then rinsed in deionized water. This was followed by an additional deposition of  $0.05 \mu\text{m}$  CdS thin film to complete the window fabrication. In a type 2 p-CdS/ $\text{Zn}_{1-x}\text{Cd}_x\text{S}$  window, a  $0.15 \mu\text{m}$  thick p-CdS film, sandwiched between two  $0.4 \mu\text{m}$ -thick  $\text{Zn}_{1-x}\text{Cd}_x\text{S}$  films, was first deposited by CBD on an Al substrate.

#### 4. Conclusion

We investigated the preparation of ZnCdS nanoparticles in a micro emulsion system. The  $\text{Zn}_{1-x}\text{Cd}_x\text{S}$  ( $0 \leq x \leq 1$ ) films deposited from solution and the sensitivity conditions of these films have been determined. The obtained results showed that when controlling the ionic composition and HT conditions, one can control the properties of  $\text{Zn}_{1-x}\text{Cd}_x\text{S}$  ( $0 \leq x \leq 1$ ) films.

The chemical composition and the degree of crystallization are not the only determining factors for the difference in photoelectric properties, as this can also be attributed to the nature and the concentration distribution of recombination centers and trapping levels. The direct current-voltage characteristic structure of Al/p-CdS/n-CdS is almost identical to the current-voltage characteristics of p-n junctions. Volt-farad characteristics of samples established the presence of conduction due to the presence of reverse bias p-n junctions. In the following order, CdTe/CdS/ $Zn_{1-x}Cd_xS$  structures have 75% or slightly higher quantum efficiency in the 400–850 nm wavelength region.

## References

- [1] P.Babu, M.V. Reddy, N. K. Revathi, T.R. Reddy. Effect of pH on the physical properties of  $ZnIn_2Se_4$  thin films grown by chemical bath deposition. *Journal of Nano- and Electronic Physics*, **3**, P. 85–91 (2011).
- [2] E. Bacaksiz, S. Aksu, I. Polat, S. Yilmaz, M. Altunbas. The influence of substrate temperature on the morphology, optical and electrical properties of thermal evaporated ZnSe thin films. *Journal of Alloys and Compounds*, **487**, P. 280–285 (2009).
- [3] A.S. Abdinov, M.A. Jafarov, N.M. Mekhtiev. Photosensitivity of the CdSSe films near the JR region. *Proc. of SPIE*, **4340**, P. 107–111 (2000).
- [4] A. Dumbrava. Zinc sulfide fine particles obtained at low temperature. *Chalcogenide Letters*, **6**(9), P. 437–443 (2009).
- [5] J. Yang, G. Wang, H. Liu, X. Chen. Controlled synthesis and characterization of ZnSe nanostructures via a solvothermal approach in a mixed solution. *Mater. Chem. Phys.*, **115**, P. 204–208 (2009).
- [6] J.B. Chaudhari, N.G. Deshpande, Y.G. Gudage, A. Ghosh, V.B. Huse, R. Sharma. Studies on growth and characterization of ternary  $CdS_{1-x}Se_x$  alloy thin films deposited by chemical bath deposition technique. *Applied Surface Science*, **254**, P. 6810–6816 (2008).
- [7] A. Apolinar-Iribe, M.C. Acosta-Enriquez, M.A. Quevedo-Lopez, R. Ramirez-Bon, A. De-Leon, S.J. Castillo. Acetylacetone as complexing agent for CdS thin films grow chemical bath deposition. *Chalcogenide Letters*, **8**, P. 77–82(2011).
- [8] L.Y. Chen, D.L. Zhang, G.M. Zhai, J.B. Zhang. Comparative study of ZnSe thin films deposited from modified chemical bath solutions with ammonia-containing and ammonia free precursors. *Materials Chemistry and Physics*. **120**, P. 456–460 (2010).
- [9] V.E. Lashkarev, A.V. Lyubchenko, M.K. Sheynkman. *Nonequilibrium processes in photoconductors*. N. Dumka, Kiev, 264 p. (1991).
- [10] S.M. Nair, P.K. Nair, R.A. Zingaro. Chemical bath deposition of photosensitive CdS and CdSe thin films and their conversion to n-type for solar cell application. *Proc.SPIE*, **2531**, P. 254–264 (1995).
- [11] T.P. Kumar, P.D. Ramesh, B.J. Abaraj. Effect of ethylenediamine tetraacetic acid concentration on the photoluminescence behavior of CdZnS thin films. *Chalcogenide Letters*, **8**, P. 207–212 (2011).
- [12] Gopakumar, N.P. Anjana, P.P. Vidyadharan. Chemical bath deposition and characterization of CdSe thin films for optoelectronic applications. *J. Materials Sci.*, **45**, P. 6653–6656 (2010).
- [13] W.C. Song, J.H. Lee. Growth and characterization of  $Zn_xCd_{1-x}S$  films prepared by using chemical bath deposition for photovoltaic devices. *Journal of the Korean Physical Society*, **54**, P. 1660–1665 (2009).
- [14] D. Patidar, K.S. Rathore, N.S. Saxena, T.P. Sharma. Determination of optical and electrical properties of ZnSe thin films. *Journal of Modern Physics*, **55**, P. 3041–3047 (2008).

## SULFATED NANO-CERIA AS A CATALYST OF HEX-1-ENE OLIGOMERIZATION

S. A. Lermontov<sup>1\*</sup>, A. N. Malkova<sup>1</sup>, L. L. Yurkova<sup>1</sup>, A. Ye. Baranchikov<sup>2</sup>, V. K. Ivanov<sup>2,3</sup>

<sup>1</sup>Institute of Physiologically Active Compounds of the Russian Academy of Sciences, Chernogolovka, Moscow region, Russia

<sup>2</sup>Kurnakov Institute of General and Inorganic Chemistry of Russian Academy of Sciences, Moscow, Russia

<sup>3</sup>Materials Science Department, Moscow State University, Moscow, Russia

lermon@ipac.ac.ru, malkova@ipac.ac.ru, yurkova@ipac.ac.ru,  
a.baranchikov@yandex.ru, van@igic.ras.ru

**PACS 82.65.+r, 81.07.Bc, 81.16.Be**

Oligomerization of hex-1-ene over acid catalysts obtained by the impregnation of cerium dioxide by sulfate-containing compounds (sulfuric acid or its salts) was studied. Maximum conversion of hexene-1 over sulfated ceria catalysts was 7–12% at 60 °C.

**Keywords:** sulfated ceria, olefins oligomerization, hex-1-ene.

### 1. Introduction

Traditional acid-catalyzed industrial processes are often criticized because strong mineral acids are used as catalysts. The low cost of these catalysts does not compensate for the costs associated with the production of corrosion-resistant equipment, the transportation and disposal of liquid acid wastes. To solve this problem, sulfated metal oxides, possessing highly acidic properties were developed as an environmentally-safe alternative to mineral acids [1,2]. Superacidic catalysts based on fluorinated oxides are also known [3].

Solid acids including sulfated titania, zirconia, and stannia are among the most promising heterogeneous catalysts [4]. The acidity of sulfated oxides depends on many parameters, such as the nature of the metal, oxide preparation procedure, sulfation method, calcination temperature, particle size, and surface area [4]. Their acidity is much higher than that of concentrated H<sub>2</sub>SO<sub>4</sub>, with their surface sulfate groups promoting the formation of Lewis and Brønsted acid sites [5]. The Hammett acidity functions  $H_0$  for SO<sub>4</sub>/ZrO<sub>2</sub> and SO<sub>4</sub>/SnO<sub>2</sub> range from –16 to –18; while SO<sub>4</sub>/TiO<sub>2</sub> has a slightly lower value of –14.6 [6]. The SO<sub>4</sub>/ZrO<sub>2</sub> is the most comprehensively studied system, because its acidity is one of the highest among the sulfated oxides [5,7–12]. The main advantages of solid acid oxide catalysts include high stability at elevated temperatures, resistance to deactivation and easy regeneration.

Cerium dioxide (CeO<sub>2</sub>) is a multifunctional inorganic compound holding a great promise for a wide range of technological applications, including catalysis, ultraviolet shielding materials, sensors, electrochromic devices, anticorrosion coatings, abrasive materials, etc.

Cerium dioxide is widely used in redox catalysis and as an effective antioxidant [13]. Recently, cerium dioxide-based catalysts, wherein CeO<sub>2</sub> acts as a so-called oxygen buffer, has been widely used. The relative ease of Ce<sup>4+</sup> ↔ Ce<sup>3+</sup> transition in CeO<sub>2</sub> makes it possible to accumulate and release oxygen depending on the O<sub>2</sub> content in the environment —

cerium dioxide can accumulate oxygen from oxygen-enriched mixtures and, in the presence of reducing agent, release it forming nonstoichiometric  $\text{CeO}_{2-x}$  [14].

Despite the considerable information on  $\text{CeO}_2$  catalytic systems,  $\text{CeO}_2$  has not been studied yet as a solid acid. In this paper, we present the first use of sulfated cerium dioxide ( $\text{CeO}_2/\text{SO}_4$ ) as a solid acid for hex-1-ene oligomerization. Hex-1-ene was chosen as a model long-chain terminal olefin in the oligomerization reaction catalyzed by modified cerium dioxide. Previously, hex-1-ene oligomerization was used to probe the catalytic activity of both sulfated zirconia [15] and sulfated stannia [16].

## 2. Experimental

### 2.1. Catalysts synthesis

All starting materials used in the experiments were of analytical grade.

Ceria nanopowders were synthesized using a previously-described method [17]. A solution of  $\text{Ce}(\text{NO}_3)_3 \cdot 6\text{H}_2\text{O}$  ( $0.08 \text{ mol L}^{-1}$ ) in water/isopropanol mixture (1:1 v/v) was rapidly added under vigorous stirring to an aqueous ammonia ( $3 \text{ mol L}^{-1}$ ) solution taken in a five-fold molar excess. The resulting mixture was allowed to stir for 3 h at room temperature. Then, a yellow precipitate was separated by centrifugation, thoroughly washed by distilled water and then dried in air at  $50^\circ \text{C}$ .

To prepare each catalyst, 4 g of ceria nanopowder and 100 mL of aqueous 2M  $\text{NH}_4\text{F}$ , or 1M  $(\text{NH}_4)_2\text{SO}_4$ , or 0.3M  $\text{H}_2\text{SO}_4$ , or 3M  $\text{H}_2\text{SO}_4$  were stirred for 1 h in a glass flask at room temperature, filtered and dried at  $100^\circ \text{C}$ .

### 2.2. Methods

IR spectroscopy was performed on a Spectrum One (Perkin Elmer, USA) spectrometer from the  $4000\text{--}350 \text{ cm}^{-1}$  region (KBr pellets, 0.25–0.5 % mass sample content). Samples for IR analysis were prepared as follows: a catalyst sample ( $\sim 0.04 \text{ g}$ ) was calcined in a dry air flow tube reactor at  $475^\circ \text{C}$ . After that, the temperature was decreased to  $150^\circ \text{C}$ , a bubbler with 1 mL of pyridine was embedded into an air line and a resulting gas-pyridine mixture was passed over the catalyst sample until all pyridine was evaporated.

Low temperature nitrogen adsorption measurements were conducted using an ATX-6 analyzer (Katakon, Russia). Before measurement the samples were outgassed at  $200^\circ \text{C}$  for 30 min under dry helium flow. Surface area determination was carried out by the 8-point Brunauer-Emmett-Teller (BET) method.

Powder X-ray diffraction (XRD) analysis was carried out on a Rigaku D/Max 2500 diffractometer ( $\text{CuK}\alpha$  radiation) with a rotating copper anode ( $\text{CuK}\alpha$  irradiation,  $5\text{--}80^\circ$   $2\theta$  range,  $0.02^\circ$  step). Particle size was estimated using the Scherrer equation. Diffraction maxima were indexed using the PDF2 database.

Transmission electron microscopy images were taken using Leo 912 AB Omega electron microscope operating at 100 kV. Microstructure of the samples was also studied using a Carl Zeiss NVision 40 scanning electron microscope (micrographs were obtained at 1 kV acceleration voltage) equipped with Oxford Instruments X-MAX energy-dispersive X-ray (EDX) analyzer operating at 20 kV acceleration voltage. The samples were not specially prepared (*e.g.* coated with conducting material) for TEM and SEM measurements. Before EDX analysis the samples were coated with  $\sim 5 \text{ nm}$  Au/Pd.

NMR spectra were recorded using a Bruker DPX-200 spectrometer in  $\text{CDCl}_3$ . Tetramethylsilane (TMS) was used as an external standard.

### 2.3. Hex-1-ene oligomerization

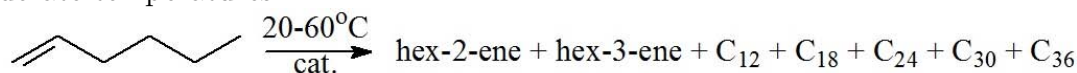
1 g of a catalyst sample was pre-conditioned in air at a chosen temperature (400, 475, or 500 °C) for 2 h in air and then cooled in a dry atmosphere.

A catalyst (1 g) and 0.1 mol of hex-1-ene were then placed into a water-jacketed glass flask and kept at constant temperature (20–60 °C) under vigorous stirring. Samples of the reaction mixture were periodically taken for <sup>1</sup>H-NMR and GC-MS analysis. A conversion degree was determined by monitoring the disappearance of vinyl group protons disappearance *via* <sup>1</sup>H-NMR.

## 3. Results and discussion

### 3.1. Hex-1-ene oligomerization

We found that sulfated ceria acts as an acid catalyst causing hex-1-ene oligomerization at moderate temperatures:



Catalytic activity of sulfated ceria samples depended strongly on the method of their preparation and the pre-conditioning temperature. The results of catalytic experiments are presented in Table 1.

TABLE 1. Hex-1-ene oligomerization

Entry	Reaction time, h	Reaction temperature, °C	Calcination temperature, °C	Catalyst	Conversion, %
1	24	rt	400	0.3M H <sub>2</sub> SO <sub>4</sub> /CeO <sub>2</sub>	0-2
2	2	rt			0-2
3	1	40			0-2
4	1	60			7
5	1	60	400	3M H <sub>2</sub> SO <sub>4</sub> /CeO <sub>2</sub>	2
6	1	60	500	0.3M H <sub>2</sub> SO <sub>4</sub> /CeO <sub>2</sub>	2
7	24	rt	475	1M (NH <sub>4</sub> ) <sub>2</sub> SO <sub>4</sub> /CeO <sub>2</sub>	0
8	1	40			2
9	1	60			12
10	24	rt-60	475	2M NH <sub>4</sub> F/CeO <sub>2</sub>	0-2
11	1	60	475	CeO <sub>2</sub>	0

Olefin isomerization and oligomerization are acid-catalyzed processes which were initiated by proton addition to a C=C bond (Fig. 1) to yield a secondary carbocation. This intermediate may then add to another molecule of hex-1-ene, yielding the dimeric carbocation shown, or, the initial intermediate may eliminate an H<sup>+</sup> to yield the isomerized internal alkene.

Highly acidic conditions are necessary for this process: ZrO<sub>2</sub> (−3.0 < H<sub>0</sub> < +1.5 [18]) and TiO<sub>2</sub> (H<sub>0</sub> ≤ −3.0 [19]) showed no catalytic effect in olefin oligomerization. Table 1 shows that sulfated ceria samples acquire acidic properties which are not inherent to unmodified CeO<sub>2</sub>. The 1M (NH<sub>4</sub>)<sub>2</sub>SO<sub>4</sub>/CeO<sub>2</sub> catalyst appeared to be slightly more active than the 0.3M H<sub>2</sub>SO<sub>4</sub>/CeO<sub>2</sub> and 3M H<sub>2</sub>SO<sub>4</sub>/CeO<sub>2</sub>. A sample calcined at 500 °C was relatively inactive.



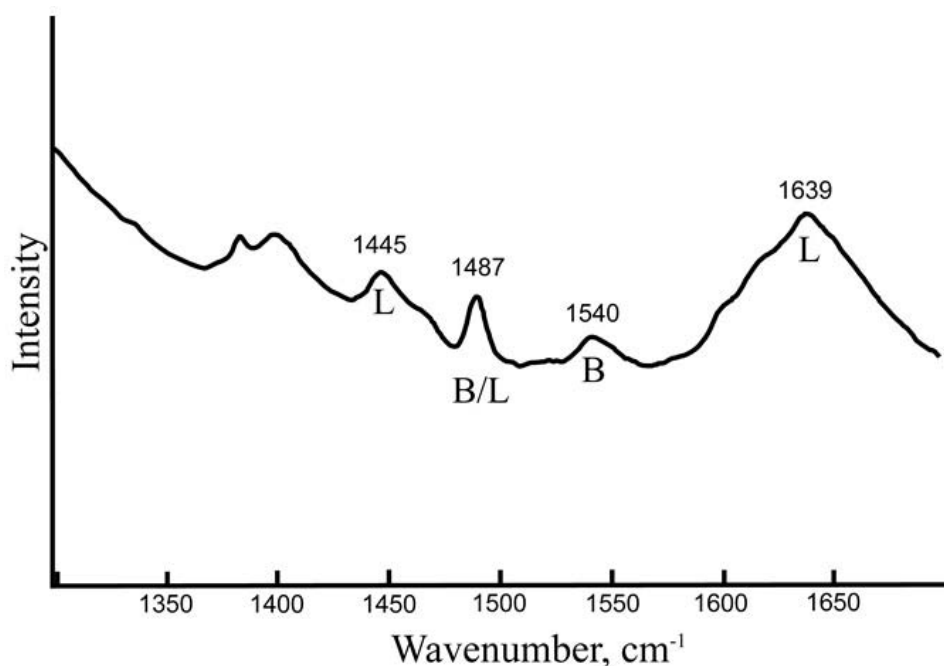


FIG. 2. IR spectroscopy data of pyridine adsorbed onto the surface of the 0.3M H<sub>2</sub>SO<sub>4</sub>/CeO<sub>2</sub> and 1M (NH<sub>4</sub>)<sub>2</sub>SO<sub>4</sub>/CeO<sub>2</sub> catalyst

## References

- [1] A. Corma. Inorganic solid acids and their use in acid-catalyzed hydrocarbon reactions. *Chem. Rev.*, **95**, P. 559–614 (1995).
- [2] A.S.C. Brown, J.S.J. Hargreaves Sulfated metal oxide catalysts. Superactivity through superacidity? *Green Chem.*, **1**, P. 17–20 (1999).
- [3] S.A. Lermontov, A.N. Malkova, L.L. Yurkova, V.K. Ivanov, A.Ye. Baranchikov, L.P. Vasilyeva. Fluorinated metal oxide-assisted oligomerization of olefins. *Mend. Comm.*, **23**, P. 110–112 (2013).
- [4] Y. Wu, S. Liao. Review of SO<sub>4</sub><sup>2-</sup>/M<sub>x</sub>O<sub>y</sub> solid super-acid catalysts. *Front. Chem. Eng. China*, **3**, P. 330–343 (2009).
- [5] J.R. Sohn. Recent advances in solid superacids. *J. Ind. Eng. Chem.*, **10**, P. 1–15 (2004).
- [6] K. Arata, H. Matsushita, M. Hino, H. Nakamura. Synthesis of solid superacids and their activities for reactions of alkanes. *Catal. Today*, **81**, P. 17–30 (2003).
- [7] M. Waqif, J. Bachelier, O. Saur. Lavalley J.-C. Acidic properties and stability of sulfate promoted metal oxides. *J. Mol. Catal.*, **72**, P. 127–138 (1992).
- [8] B.M. Reddy, M.K. Patil. Organic syntheses and transformations catalyzed by sulfated zirconia. *Chem. Rev.*, **109**, P. 2185–2208 (2009).
- [9] K. Arata. Organic syntheses catalyzed by superacidic metal oxides: sulfated zirconia and related compounds. *Green Chem.*, **11**, P. 1719–1728 (2009).
- [10] S.G. Ryu, B.C. Gates. n-Hexane conversion catalyzed by sulfated zirconia and by iron- and manganese-promoted sulfated zirconia: catalytic activities and reaction network. *Ind. Eng. Chem. Res.*, **37**, P. 1786–1792 (1998).
- [11] S. Rezgüi, R.E. Jentoft, B.C. Gates. n-pentane isomerization and disproportionation catalyzed by promoted and unpromoted sulfated zirconia. *Catal. Lett.*, **51**, P. 229–234 (1998).
- [12] T.K. Cheung, F.C. Lange, B.C. Gates. Propane conversion catalyzed by sulfated zirconia, iron- and manganese-promoted sulfated zirconia, and USY zeolite. *J. Catal.*, **159**, P. 99–106 (1996).
- [13] V.K. Ivanov, A.B. Shcherbakov, A.V. Usatenko. Structure-sensitive properties and biomedical applications of nanodispersed cerium dioxide. *Russ. Chem. Rev.*, **78**, P. 855–871 (2009).
- [14] *Catalysis by Ceria and Related Materials*. Imperial College Press, London, 528 pp (2002).

- [15] V. Ivanov, G. Kopitsa, S. Lermontov, L. Yurkova, N. Gubanova, O. Ivanova, A. Lermontov, M. Rummyantseva, L. Vasilyeva, M. Sharp, K. Pranzas, Yu. Tretyakov. pH control of the structure, composition, and catalytic activity of sulfated zirconia. *J. Solid State Chem.*, **198**, P. 496–505 (2013).
- [16] L.L. Yurkova, S.A. Lermontov, V.P. Kazachenko, V.K. Ivanov, A.S. Lermontov, A.E. Baranchikov, L.P. Vasil'eva. Sulfated SnO<sub>2</sub> as a high-performance catalyst for alkene oligomerization. *Inorganic Materials*, **48**, P. 1012–1019 (2012).
- [17] A.E. Baranchikov, O.S. Polezhaeva, V.K. Ivanov, Y.D. Tretyakov. Lattice expansion and oxygen non-stoichiometry of nanocrystalline ceria. *CrystEngComm*, **12**, P. 3531–3533 (2010).
- [18] J.R. Sohn, W.C. Park. New NiSO<sub>4</sub>/ZrO<sub>2</sub> catalyst for ethylene dimerization. *Bull. Korean Chem. Soc.*, **20**, P. 1261–1262 (1999).
- [19] J.R. Sohn, W.C. Park. New syntheses of active catalysts for ethylene dimerization. *Bull. Korean Chem. Soc.*, **21**, P. 1063–1064 (2000).
- [20] V.K. Ivanov, O.S. Polezhaeva, A.E. Baranchikov, A.B. Shcherbakov. Thermal stability of nanocrystalline CeO<sub>2</sub> prepared through freeze drying. *Inorg. Mater.*, **46**, P. 43–46 (2010).
- [21] A. Mantilla, F. Tzompantzi, G. Ferrat, A. Lopez-Ortega, E. Romero. Ortiz-Islas E., Gómez R., Torres M. Room temperature olefins oligomerization over sulfated titania. *Chem. Commun.*, P. 1498–1499 (2004).
- [22] R. Sakthivel, H.A. Prescott. Synthesis, characterization, and catalytic activity of SO<sub>4</sub>/Zr<sub>1-x</sub>Sn<sub>x</sub>O<sub>2</sub>. *Appl. Catal. A*, **253**, P. 237–247 (2003).

# INFLUENCE OF SYNTHESIS TEMPERATURE ON $\text{BiFeO}_3$ NANOPARTICLES FORMATION

N. A. Lomanova<sup>1</sup>, V. V. Gusarov<sup>1,2</sup>

<sup>1</sup>Ioffe Physical Technical Institute, 26 Polytekhnicheskaya Str.,  
St. Petersburg 194021, Russian Federation

<sup>2</sup>St. Petersburg State Technological Institute (Technical University),  
26 Moskovsky Ave., St. Petersburg, 190013, Russian Federation  
natus@hotbox.ru, victor.v.gusarov@gmail.com

## PACS 61.66.Fn

The mechanism of  $\text{BiFeO}_3$  nanoparticle formation from initial compositions obtained by bismuth and iron hydroxides co-precipitation has been studied. The activation temperature of the  $\text{BiFeO}_3$  nucleation and nanocrystal growth is shown to correlate with that of the nonautonomous phase's melting. The optimal temperature range during nanoparticle formation by the method in question was found to be between 460–520( $\pm 40$ ) °C.

**Keywords:** nanoparticles, multiferroics, bismuth ferrite, high-temperature X-ray diffractometry.

## 1. Introduction

Primarily,  $\text{BiFeO}_3$ -based materials are of interest as multiferroics used for the development of magnetoelectric materials and photovoltaics, including thin-film materials, nanostructures and compounds with  $\text{BiFeO}_3$  nanosized blocks [1–10].  $\text{BiFeO}_3$  nanoparticles may have other potential applications, for example in [11]  $\text{BiFeO}_3$  nanoparticles were used for  $\text{BiFeO}_3$ -graphene nanohybrids, which may find application due to their photocatalytic properties.

A wide range of investigations reviewed were devoted to the synthesis of  $\text{BiFeO}_3$  by applying different methods and determining the optimal conditions for producing this compound free from other impurity phases [12]. Nevertheless, obtaining a pure single-phase product has been problematic, so far. Various authors have suggested different reasons for this. Some works describing the synthesis of  $\text{BiFeO}_3$  synthesis mention its metastability as a reason for the inability to produce this compound uncontaminated by other components of the  $\text{Bi}_2\text{O}_3$ - $\text{Fe}_2\text{O}_3$  system (see, e.g., [13]). However, this is an equilibrium compound according to works on phase equilibria [14–17].

The difficulty of producing  $\text{BiFeO}_3$  free from other phases by means of a solid phase synthesis was explained by its nonstoichiometry and changes in the homogeneity region with increased temperature [18]. In the same work, the activation of  $\text{BiFeO}_3$  formation was shown to depend on the chemical background of the initial mixture. In this case, a number of subsequent transformations occur when  $\text{BiFeO}_3$  is synthesized from  $\text{Bi}_2\text{O}_3$  and  $\text{Fe}_2\text{O}_3$  by the solid state chemical reaction method. At the initial stage, the formation of  $\text{Bi}_{25}\text{FeO}_{39}$  takes place. Its maximum quantity was recorded at 500 °C. Then,  $\text{BiFeO}_3$  synthesis intensified sharply at about 600 °C, and the further increase in the reaction temperature leads to the formation of  $\text{Bi}_2\text{Fe}_4\text{O}_9$  along with  $\text{BiFeO}_3$  and  $\text{Bi}_{25}\text{FeO}_{39}$ .

The possibility of  $\text{Bi}_2\text{Fe}_4\text{O}_9$  and  $\text{Bi}_{25}\text{FeO}_{39}$  formation during  $\text{BiFeO}_3$  synthesis was shown to be dependent upon the quality of the initial reagents [19]. Insufficiently pure precursors resulted in the formation of the above-mentioned phases and to their stable existence as impurities during  $\text{BiFeO}_3$  formation. Some authors postulate that it is difficult to synthesize the

single-phase BiFeO<sub>3</sub> because Bi<sub>2</sub>Fe<sub>4</sub>O<sub>9</sub> and Bi<sub>25</sub>FeO<sub>39</sub> are thermodynamically more stable than BiFeO<sub>3</sub> [20,21].

According to data from [22], thermodynamic calculations have yielded a conclusion that synthesis for the production of single-phase BiFeO<sub>3</sub> should not be performed above 727 °C, that is, above the temperature of the  $\alpha \rightarrow \beta$  Bi<sub>2</sub>O<sub>3</sub> transition, as the high entropy of the disordered  $\beta$ -Bi<sub>2</sub>O<sub>3</sub> sharply decreases the Gibbs energy of bismuth ferrite formation. The suggested optimal synthesis temperature is around 720 °C.

A schematic description of BiFeO<sub>3</sub>, as well as Bi<sub>2</sub>Fe<sub>4</sub>O<sub>9</sub> and Bi<sub>25</sub>FeO<sub>39</sub> impurities formation has been given previously [23]. The diffusion of Bi<sup>3+</sup> ions through Fe<sub>2</sub>O<sub>3</sub> was shown to have a decisive role in BiFeO<sub>3</sub> synthesis. However, the diffusion of components into the reaction zone was hindered by the crystallization of the Bi<sub>2</sub>Fe<sub>4</sub>O<sub>9</sub> phase, which is more thermodynamically stable.

A detailed analysis of BiFeO<sub>3</sub> synthesis provided in [24] showed that when BiFeO<sub>3</sub> was synthesized from a xerogel, its crystallization started above 520 °C, which is more than 100 °C below the temperature of its synthesis from simple oxides by applying the solid state chemical reaction method with mechanochemical activation of components [25]. In this case, practically no formation of the intermediate phase Bi<sub>25</sub>FeO<sub>39</sub> was observed, and the yield of BiFeO<sub>3</sub> at 580 °C was 99.7 mass %, which was maintained over a wide temperature range.

Synthetic methods for obtaining BiFeO<sub>3</sub> nanoparticles have been considered in many publications. Several works describe the production of BiFeO<sub>3</sub> nanoparticles of various sizes and morphologies applying low temperature techniques, including the hydrothermal technique [25–32].

The details regarding the formation, structure and size of BiFeO<sub>3</sub> nanoparticles synthesized from different precursors were studied in [33,34]. It was demonstrated in [34] that BiFeO<sub>3</sub> crystallization begins around 400 °C, and, according to these publications, an increase in the reaction temperature of up to 500–600 °C may yield single-phase BiFeO<sub>3</sub>.

Various methods for synthesizing BiFeO<sub>3</sub> nanoparticles were described, which, however, did not yield monophasic nanopowders [35–39]. The published data analysis showed a lack of certainty in the interpretation of the reasons for the multiphase nature of the system during BiFeO<sub>3</sub> synthesis. This relates to the synthesis of both BiFeO<sub>3</sub> macroparticles and nanoparticles. Therefore, investigation of the mechanistic details of BiFeO<sub>3</sub> nanoparticle formation is topical.

## 2. Experimental

BiFeO<sub>3</sub> nanoparticles were synthesized by means of thermal treatment of hydroxides obtained by reverse co-precipitation from solutions of salts into a 25% solution of NH<sub>4</sub>OH. The purities of the starting materials, Bi(NO<sub>3</sub>)<sub>3</sub>·5H<sub>2</sub>O and Fe(NO<sub>3</sub>)<sub>3</sub>·9H<sub>2</sub>O, were 99.9% or higher. The concentration of bismuth and iron (III) nitrates was 0.1 M/l and dilute nitric acid was used as the solvent. Solutions of the salts were mixed in a ratio corresponding to BiFeO<sub>3</sub> stoichiometry. The coprecipitated mixture was washed with distilled water until the presence of ammonium ions was not detected. The precipitate was dried at about 70 °C for 2 hours.

The elemental composition of the studied samples was determined by the energy dispersive X-ray microanalysis (FEI Quanta 200 SEM with the EDAX attachment) prior to and after their thermal treatment. The changes induced in the samples by thermal treatment were studied by the simultaneous thermal analysis (STA) using STA 449 F3 Jupiter (NETZSCH), as well as by the high-temperature X-ray diffractometry (HT-XRD) employing XRD-7000 Shimadzu with HTK-1200N high-temperature attachment (Anton Paar).

The sample investigated by HT-XRD was heated in a stepwise manner from 480–630 °C and was subjected to isothermal exposure for 5–7 min before diffractogram recording. The

X-ray quantitative phase analysis (XQPA) employed the PDWin 4.0 code [40]. The material of the tray in which the sample was placed ( $\alpha$ -Al<sub>2</sub>O<sub>3</sub>) was used as the internal standard. The coherent scattering domain size was determined using the Scherrer equation. A correction for the X-ray line broadening (independent of the particle size) was made using the data on the  $\alpha$ -Al<sub>2</sub>O<sub>3</sub> line width.

### 3. Results and discussion

According to the elemental analysis data for the initial sample composed of coprecipitated bismuth and iron hydroxides and dried at  $\sim 70$  °C, the elemental ratio corresponded to BiFeO<sub>3</sub> stoichiometry; Fe:Bi =  $1.08 \pm 0.05$ . Elemental analysis data obtained after the HT-XRD for the sample heated in a stepwise manner up to 630 °C was shown to decrease in bismuth oxide content, which may be due to its evaporation (Fe:Bi =  $1.47 \pm 0.05$ ).

The HT-XRD of the initial sample (Fig. 1a) demonstrated the presence of only broad Bi(OH)<sub>3</sub> reflections in the diffractogram, which correspond to 30–35 nm crystallites. The absence of reflections for any other phases in the diffractogram obviously relates to the presence of an amorphous iron-containing component. It should be noted that according to [41], the amorphous state is characteristic of iron hydroxide precipitated in an alkaline medium.

A comparison of the HT-XRD (Fig. 1) and STA (Fig. 2) data makes it possible to present phase changes in the sample as a below-described series of transformations. Within the 40–160 °C range, dehydration of ferric oxyhydroxide yields an amorphous iron oxide. This dehydration temperature range corresponds to that published in [41]. This process is reflected in the TG and DSC curves as a loss in sample mass (1.8 %), and as a small and temperature-expanded endothermic effect (11 J/g). Mass-spectrometry of the evolving gases proved the process to be dehydration (Fig. 2).

Within the 160–300 °C range, the sample keeps losing mass due to Bi(OH)<sub>3</sub> dehydration and to decomposition of a small amount of carbonate, which is accompanied by the loss of 4 % of mass (Fig. 2). This process occurs simultaneously with the chemical reaction of iron oxide with the sillenite-structure bismuth, which is usually presented as the compound Bi<sub>25</sub>FeO<sub>39</sub> or Bi<sub>25</sub>FeO<sub>40</sub> [42]. The total endothermic effect with an enthalpy of 147 J/g corresponds to the mentioned processes.

Obviously, decomposition of the bismuth carbonate impurity accompanied by the loss of 2 % of mass and by the endothermic effect with enthalpy of 41 J/g were observed between 320–500 °C. Completion of this process was immediately followed by BiFeO<sub>3</sub> formation with the corresponding exothermic effect with an enthalpy of  $-30$  J/g.

Notable are the small differences between the data generated by HT-XRD and STA due to the idiosyncrasies of these techniques. Firstly, in HT-XRD, all processes are registered at lower temperatures than in STA. The reason is that the latter technique is dynamic, and therefore, it is more difficult to register the onset of a transformation with its help due to the final rate of temperature growth. On the other hand, the STA data make it possible to register the transformation of amorphous phases, while this is impossible with the HT-XRD data. Besides, HT-XRD requires a sufficiently long exposure of samples at each stage of the high-temperature measurements, which increases the possibility of shifts in the quantitative ratio of initial components due to the evaporation of the volatile bismuth oxide.

The results of XQPA (performed with due account of the mass balance, numerical data on the X-ray density of the crystal-forming phases and the data on the size of the crystallites in them) made it possible to determine volume fractions of the formed crystal phases, the volume of crystallites and their relative quantity (Fig. 3).

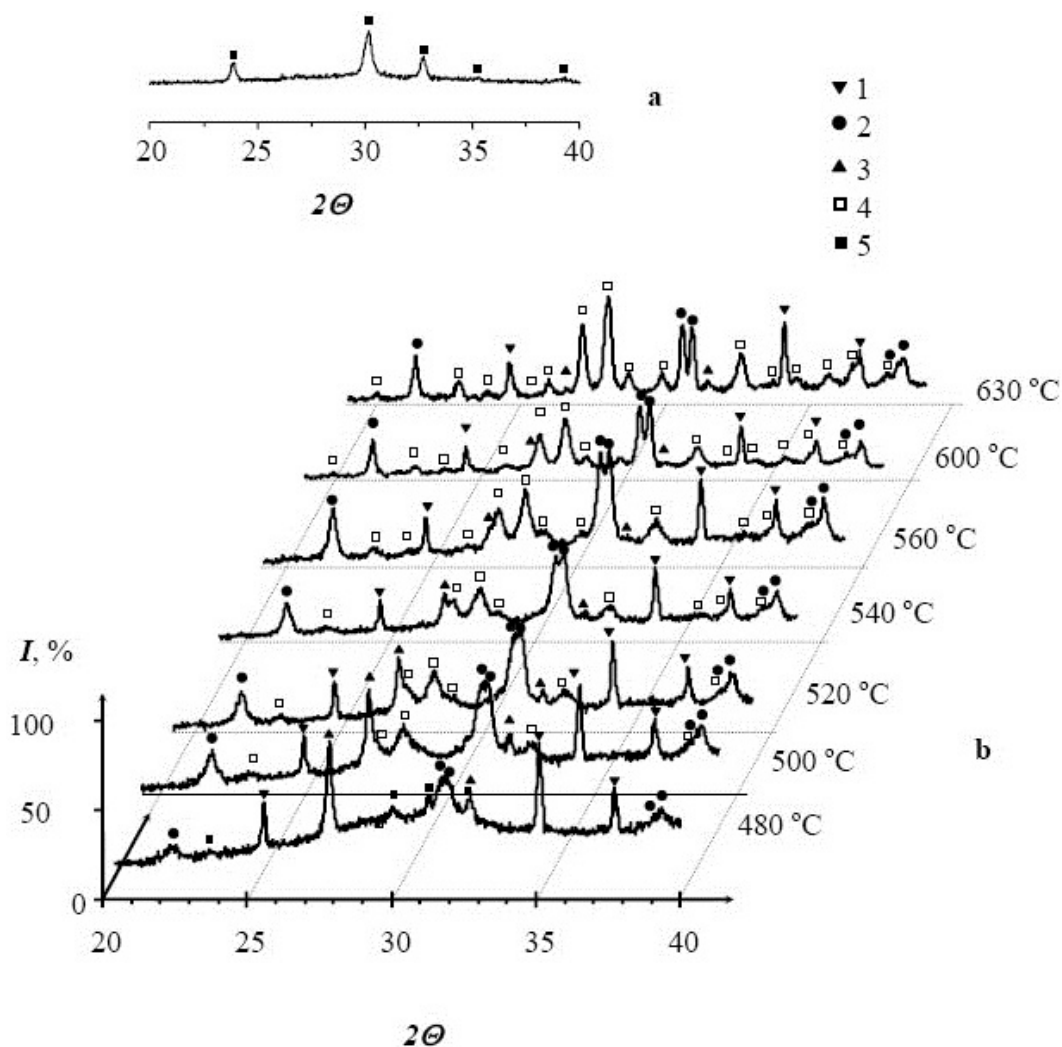


FIG. 1. X-ray diffractograms ( $\lambda = 1.54056 \text{ \AA}$ ): *a* – initial sample; *b* – sample after thermal treatment (1 –  $\text{Al}_2\text{O}_3$ , 2 –  $\text{BiFeO}_3$ , 3 –  $\text{Bi}_{25}\text{FeO}_{39}$ , 4 –  $\text{Bi}_2\text{Fe}_4\text{O}_9$ , 5 –  $\text{Bi}(\text{OH})_3$ )

Analysis of the data in Figs. 2, 3 suggests the below-described mechanism of phase formation in the mixture of coprecipitated bismuth and iron hydroxides. Obviously, the pH values of bismuth- and iron hydroxide precipitation under the applied conditions of coprecipitation differed so significantly that the precipitating components were segregated (Fig. 4). This was confirmed by the initially-obtained  $\text{Bi}(\text{OH})_3$  nanocrystallites (Fig. 1a). Segregation strengthens during thermal treatment due to the difference in dehydration temperatures for the components (Fig. 2).

Bismuth hydroxide dehydration in the presence of an amorphous iron oxide at temperatures around  $250 \text{ }^\circ\text{C}$  was accompanied by the active formation of sillenite-structure bismuth oxide nanoparticles with a chemical formula that can obviously be written in this case as  $\text{Bi}_{25}\text{FeO}_{39}$  (Fig. 3). As the temperature increased, the sillenite-structure bismuth oxide nanocrystals kept growing and reduced in number. This process is most prominent at  $480 \text{ }^\circ\text{C}$  or slightly below (Fig. 3). It should be noted that this temperature range correlates well with the temperature of particles surface transition into a liquid-like state [43,44], i.e., with the temperature of the

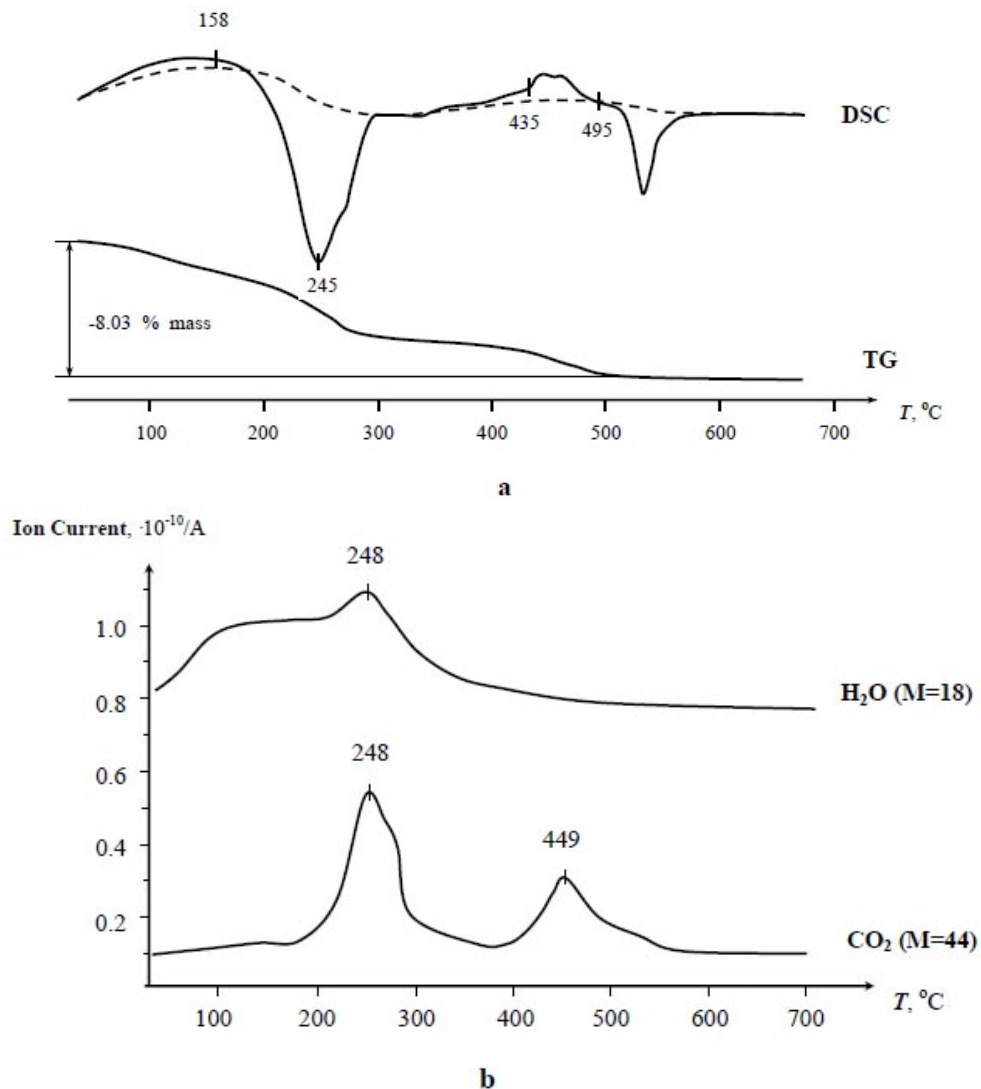


FIG. 2. Temperature-dependent a) mass change (TG), heat flow curve (DSC) and b) ion current mass numbers 18 ( $M=18$ ) and 44 ( $M=44$ ) of the sample.

bismuth oxide-based nonautonomous phase melting ( $460 \pm 40$  °C) [45], at which mass-transfer along grain boundaries is activated [46,47].

$\text{BiFeO}_3$  nanocrystals with  $12 \pm 2$  nm crystallites start forming in the same temperature range. Nanocrystal formation dominates over their growth until 520 °C. At 520–540 °C,  $\text{BiFeO}_3$  nanocrystal growth begins (Fig. 3), while their total number reduces (Fig. 3). These temperatures correlate with the calculated temperature of the  $\text{BiFeO}_3$ -based nonautonomous phase melting, which occurs at  $520 \pm 40$  °C [45]. Thus, it can be asserted that  $\text{BiFeO}_3$  crystallites grow in size and reduce in number in the system at temperatures of the  $\text{BiFeO}_3$ -based nonautonomous phase's melting and represent a consequence of mass transfer intensification along the boundaries of  $\text{BiFeO}_3$  grains.

It should also be noted that the maximum size of sillenite-structure bismuth oxide crystallites and stabilization of their numbers are observed at temperatures around 520 °C (Fig. 3). At higher temperatures, the sillenite-structure bismuth oxide fraction diminishes in the system, not at the expense of the reducing number of crystallites, but due to the decrease in their size resulting from the bismuth oxide/iron oxide interaction which yields  $\text{BiFeO}_3$  (Fig. 4).

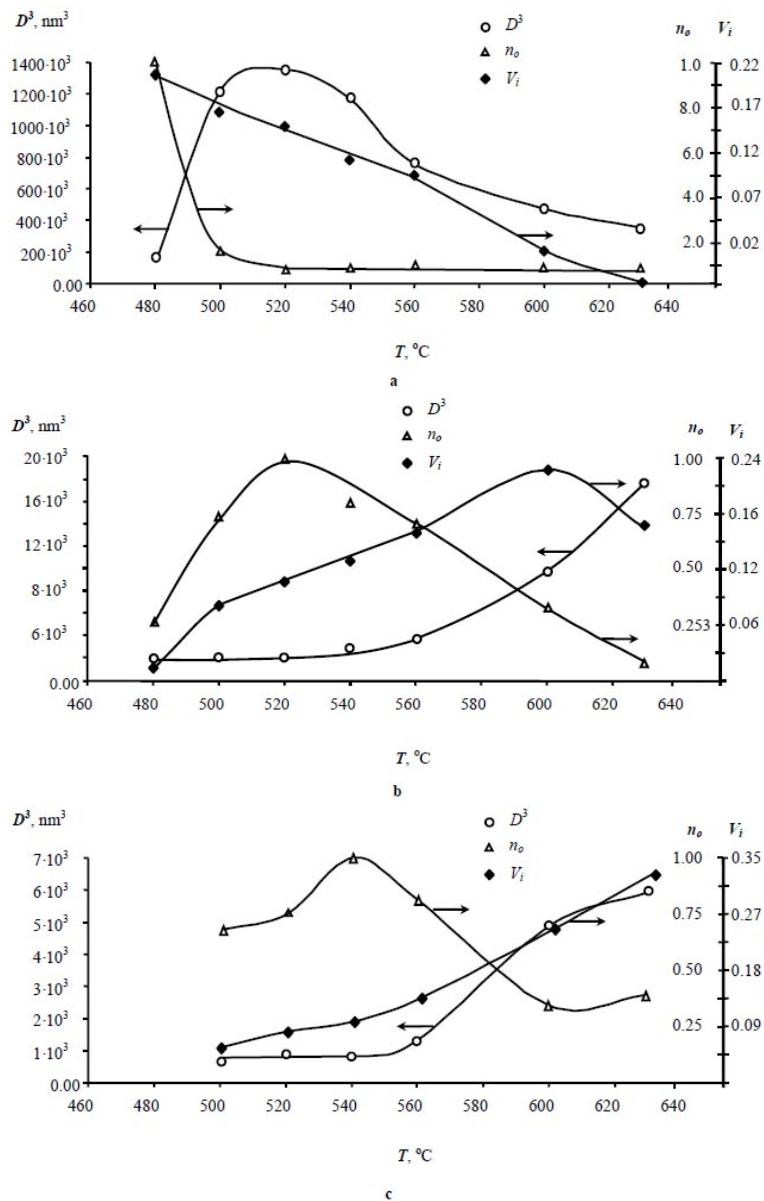


FIG. 3. Changes in crystallites volume ( $D^3$ ) relative to the crystallites number ( $n_0$ ) and volume fraction of the forming phases (a – Bi<sub>25</sub>FeO<sub>39</sub>, b – BiFeO<sub>3</sub>, c – Bi<sub>2</sub>Fe<sub>4</sub>O<sub>9</sub>) against the increasing temperature of isothermal exposure.

Formation of Bi<sub>2</sub>Fe<sub>4</sub>O<sub>9</sub> nanocrystals was observed only at temperatures around 500 °C and higher (Fig. 3). In this case, crystallites of the formed Bi<sub>2</sub>Fe<sub>4</sub>O<sub>9</sub> were about 6 nm in size, i.e., they were half the size of BiFeO<sub>3</sub> crystallites.

The size of crystallites, their number and the fraction of the Bi<sub>2</sub>Fe<sub>4</sub>O<sub>9</sub> phase changed little from 520–560 °C (Fig. 3). A sharp increase in the size of the Bi<sub>2</sub>Fe<sub>4</sub>O<sub>9</sub> crystallites, a decrease in their number and the simultaneous growth of the volume fraction of Bi<sub>2</sub>Fe<sub>4</sub>O<sub>9</sub> in the considered system occurred between 560–600 °C. It should be noted that this temperature range covers the values of the Bi<sub>2</sub>Fe<sub>4</sub>O<sub>9</sub>–based nonautonomous phase melting temperature (550±50 °C) calculated on the basis of the expression given in [45]. At temperatures above 600 °C, the BiFeO<sub>3</sub> fraction diminished, obviously due to bismuth oxide evaporation and the

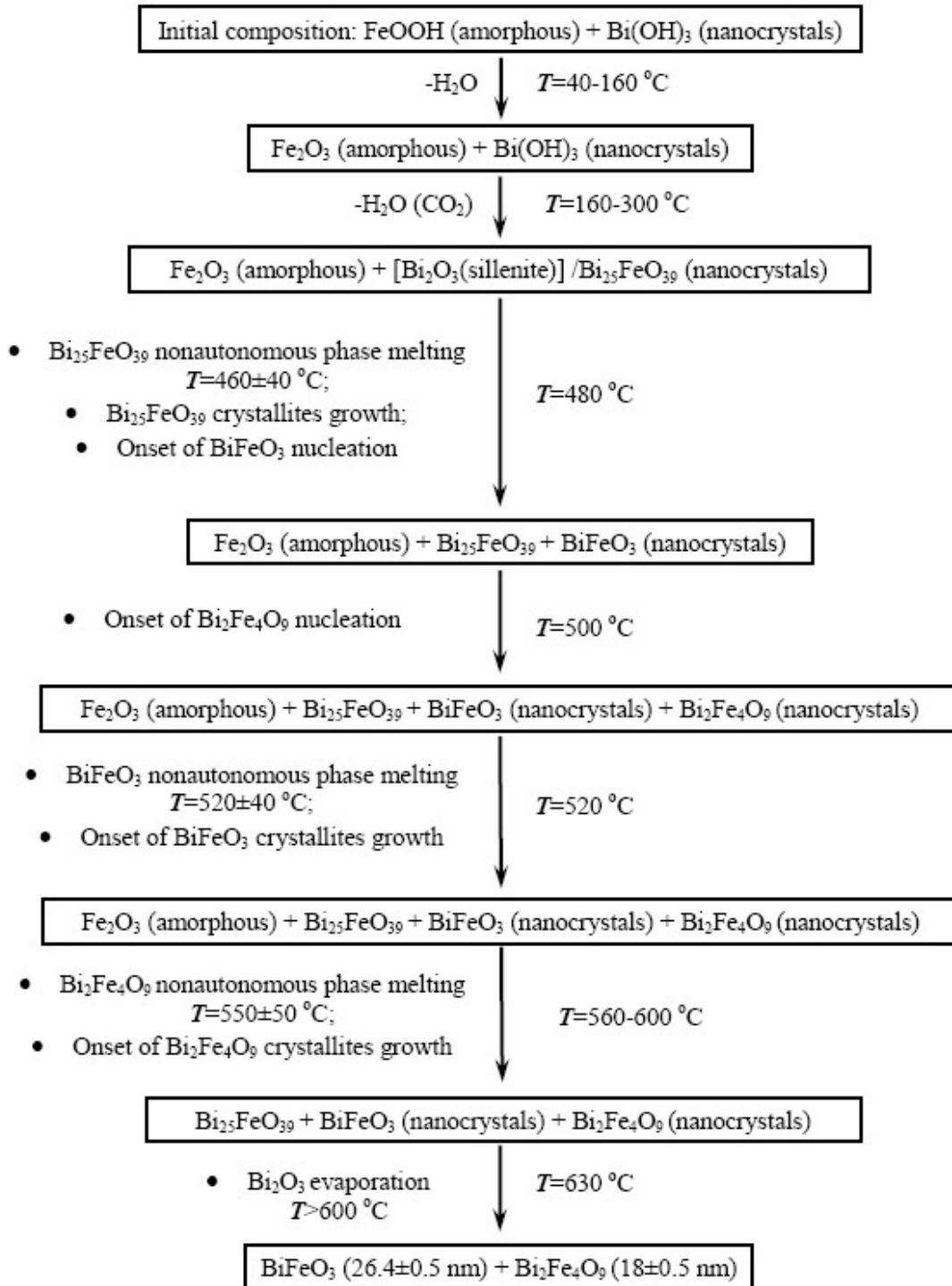


FIG. 4. Transformation in the reaction system. On the left of the arrows – descriptions of processes; on the right – temperature at which transformation was recorded.

respective growth of the Fe<sub>2</sub>O<sub>3</sub> fraction in the system (Fig. 3), which resulted in the active formation of Bi<sub>2</sub>Fe<sub>4</sub>O<sub>9</sub>.

Thus, the mechanism of BiFeO<sub>3</sub> formation from a mixture of coprecipitated bismuth and iron hydroxides may be described as a series of elementary transformations presented in Fig. 4. It follows from the analysis of the obtained results that in order to obtain nanocrystalline BiFeO<sub>3</sub>, the initial composition should be formed with the maximum possible degree of dispersion of reagents evenly spread within the reacting system, and that the temperature of bismuth and iron hydroxides' thermal treatment should be kept within a sufficiently narrow temperature range, 480–520 °C. All these conditions met, it may be expected that the produced nanocrystalline BiFeO<sub>3</sub> will contain the least amount of impurity phases.

#### 4. Conclusion

Analysis of the sintering temperature for co-precipitated bismuth and iron hydroxides on the formation of BiFeO<sub>3</sub> nanoparticles has shown that the transition of nonautonomous phases into a liquid-like state has a decisive influence on the processes of nucleation and crystal growth. The process of BiFeO<sub>3</sub> nucleation is activated in the temperature range that corresponds to the transition of the bismuth oxide-based nonautonomous phase into a liquid-like state. The reason is that the area of components contact broadens due to the increased mass transfer rate at the bismuth oxide surface. The growth of BiFeO<sub>3</sub> crystals is activated at the temperature of the BiFeO<sub>3</sub>-based nonautonomous phase melting, which is related to the increased mass transfer rate along grain boundaries at their transition into a liquid-like state.

Therefore, the optimal temperature range for the formation of BiFeO<sub>3</sub> nanoparticles from the coprecipitated hydroxides with nanosized particles of the starting materials is from 460–520(±40) °C. The temperature of BiFeO<sub>3</sub> nanoparticles synthesis can be reduced only when the initial composition features a much higher degree of spatial contact between components. When raising the temperature of synthesis above the mentioned upper value, it is necessary to decrease the sintering time significantly in order to keep the size of the formed BiFeO<sub>3</sub> crystals within the nanosize range.

#### Acknowledgment

The reported study was partially supported by RFBR, research project No. 12-08-31453 mol.a.

#### References

- [1] G.A. Smolenskii, V.A. Isupov, Ferroelectromagnets. *Physics-Uspekhi*, **137**, P. 415–435 (1982).
- [2] J. Wang, J. B. Neaton, et al. Epitaxial BiFeO<sub>3</sub> Multiferroic Thin Film Heterostructures. *Science*, **299**, P. 1719–1722 (2003).
- [3] Y.P. Wang, G.L. Yuan, et al. Electrical and magnetic properties of single-phased and highly resistive ferroelectromagnet BiFeO<sub>3</sub> ceramic. *J. Phys. D: Appl. Phys.*, **39**, P. 2019–2023 (2006).
- [4] T. Choi, S. Lee, et al. Switchable ferroelectric diode and photovoltaic effect in BiFeO<sub>3</sub>. *Science*, **324**, P. 63–68 (2009).
- [5] S.Y. Yang, L.W. Martin, et al. Photovoltaic effects in BiFeO<sub>3</sub>. *Appl. Phys. Lett.*, **95**, P. 062909 (2009).
- [6] H.T. Yi, T. Choi, et al. Mechanism of the switchable photovoltaic effect in ferroelectric BiFeO<sub>3</sub>. *Adv. Mater.*, **23**, P. 3403–3408 (2011).
- [7] A.P. Pyatakov, A. K. Zvezdin. Magnetolectric and multiferroic media. *Physics-Uspekhi*, **55**, P. 557–581 (2012).
- [8] S. Li, R. Nechache, C. Harnagea, L. Nikolova, F. Rosei. Single-crystalline BiFeO<sub>3</sub> nanowires and their ferroelectric behavior. *Appl. Phys Lett.*, **101**, P. 192903–192908 (2012).
- [9] H.W. Chang, F.T. Yuan, et al. Photovoltaic property of sputtered BiFeO<sub>3</sub> thin films. *J. All. Comp.*, **574**, P. 402–406 (2013).

- [10] N.A. Lomanova, V.V. Gusarov. On the limiting thickness of the Perovskite-like block in the Aurivillius phases in the  $\text{Bi}_2\text{O}_3\text{-Fe}_2\text{O}_3\text{-TiO}_2$  system. *Nanosystems: Physics, Chemistry, Mathematics*, **2**(3), P. 93–101 (2011).
- [11] Z. Li, Y. Shen, et al. Significant enhancement in the visible light photocatalytic properties of  $\text{BiFeO}_3$ -graphene nanohybrids. *J. Mater. Chem. A*, **1**, P. 823–829 (2013).
- [12] J. Silva, A. Reayes, et al.  $\text{BiFeO}_3$ : A Review on Synthesis, Doping and Crystal Structure. *Integrated Ferroelectrics*, **126**, P. 47–59 (2011).
- [13] J. Lu, L.J. Qiao, P.Z. Fu, Y.C. Wu. Phase equilibrium of  $\text{Bi}_2\text{O}_3\text{-Fe}_2\text{O}_3$  pseudo-binary system and growth of  $\text{BiFeO}_3$  single crystal. *J. Cryst. Grow*, **318**, P. 936–941 (2011).
- [14] A. Maitre, M. Francois, J.C. Gachon. Experimental study of the  $\text{Bi}_2\text{O}_3\text{-Fe}_2\text{O}_3$  pseudo-binary system. *J. Phase Equilibria and Diffusion*, **25**, P. 59–67 (2004).
- [15] R. Haumont, R. Saint-Martin, C. Byl. Centimeter-size  $\text{BiFeO}_3$  single crystals grown by flux method. *Phase Transitions*, **81**, P. 881–888 (2008).
- [16] R. Palai, R. S. Katiyar, et al.  $\beta$  phase and  $\beta$ - $\gamma$  metal-insulator transition in multiferroic  $\text{BiFeO}_3$ . *Phys. Rev. B*, **77**, P. 014110.1–014110.11 (2008).
- [17] E.I. Speranskaya, V.M. Skorikov, E.Ya. Rode, V.A. Terekhova. The phase diagram of the system  $\text{Bi}_2\text{O}_3\text{-Fe}_2\text{O}_3$ . *Izv. Bull. Acad. Sci. USSR, Div Chem. Sci.*, **5**, P. 905–906 (1965).
- [18] M.I. Morozov, N.A. Lomanova, V.V. Gusarov. Specific Features of  $\text{BiFeO}_3$  Formation in a mixture of bismuth(III) and iron(III) oxides. *Russ. J. Gen. Chem.*, **73**, P. 1676–1680 (2003).
- [19] M. Valant, A.-K. Axelsson, N. Alford. Peculiarities of a Solid-State Synthesis of Multiferroic Polycrystalline  $\text{BiFeO}_3$ . *Chem. Mater.*, **19**, P. 5431–5436 (2007).
- [20] S.M. Selbach, M.-A. Einarsrud, T. Grande. On the Thermodynamic Stability of  $\text{BiFeO}_3$ . *Chem. Mater.*, **21**, P. 169–173 (2009).
- [21] S. Phapale, R. Mishra, D. Das. Standard enthalpy of formation and heat capacity of compounds in the pseudo-binary  $\text{Bi}_2\text{O}_3\text{-Fe}_2\text{O}_3$  system. *J. Nuclear Mater.*, **373**, P. 137–141 (2008).
- [22] A.V. Mikhailov, A. R. Kaul, et al. Mass spectrometric investigation of vaporization in the  $\text{Bi}_2\text{O}_3\text{-Fe}_2\text{O}_3$  system. *Russ. J. Phys. Chem. A*, **85**, P. 26–30 (2011).
- [23] M.S. Bernardo, T. Jardiel, et al. Sintering and microstructural characterization of  $\text{W}^{6+}$ ,  $\text{Nb}^{5+}$  and  $\text{Ti}^{4+}$  iron-substituted  $\text{BiFeO}_3$ . *J. Eur. Cer. Soc.*, **31**, P. 3047–3053 (2011).
- [24] A.V. Egorisheva, T.B. Kuvshinova, et al. Synthesis of high nanocrystalline  $\text{BiFeO}_3$ . *Inorgan. Mater.*, **49**, P. 316–320 (2013).
- [25] A.V. Egorisheva, T.B. Kuvshinova, et al. Mechanochemical activation of the starting components for the solid phase synthesis of  $\text{BiFeO}_3$ . *Inorgan. Mater.*, **49**, P. 308–315 (2013).
- [26] S. Das, S. Basu. Solvothermal synthesis of nano-to-submicrometer sized  $\text{BiFeO}_3$  and Bi-Fe-oxides with various morphologies. *J. Nanosci. Nanotechnol.*, **9**, P. 5622–562 (2009).
- [27] J.-H. Xu, H. Ke, et al. Low-temperature synthesis of  $\text{BiFeO}_3$  nanopowders via a sol-gel method. *J. All. Comp.*, **472**, P. 473–477 (2009).
- [28] B. Liu, B. Hu, Z. Du. Hydrothermal synthesis and magnetic properties of single-crystalline  $\text{BiFeO}_3$  nanowires. *China Chem. Comm.*, **47**, P. 8166–8168 (2011).
- [29] J. Yang, X. Li, et al. Factors controlling pure-phase magnetic  $\text{BiFeO}_3$  powders synthesized by solution combustion synthesis. *J. All. Comp.*, **509**, P. 9271–9277 (2011).
- [30] D. Maurya, H. Thota, K. S. Nalwa, A. Garg.  $\text{BiFeO}_3$  ceramics synthesized by mechanical activation assisted versus conventional solid-state-reaction process: A comparative study. *J. All. Comp.*, **477**, P. 780–784 (2009).
- [31] M.M. Rashad. Effect of synthesis conditions on the preparation of  $\text{BiFeO}_3$  nanopowders using two different methods. *J. Mat. Sci.: Materials in Electronics*, **23**, P. 882–888 (2012).
- [32] A. Chaudhuri, S. Mitra, M. Mandal, K. Mandal. Nanostructured bismuth ferrites synthesized by solvothermal process. *J. All. Comp.*, **491**, P. 703–706 (2010).
- [33] M. Popa, D. Crespo, J.M. Calderon-Moreno, S.F. Preda. Synthesis and Structural Characterization of Single-Phase  $\text{BiFeO}_3$  Powders from a Polymeric Precursor. *J. Am. Cer. Soc.*, **90**, P. 2723–2727 (2007).
- [34] A. Hardy, S. Gielis, et al. Effects of precursor chemistry and thermal treatment conditions on obtaining phase pure bismuth ferrite from aqueous gel precursors. *J. Eur. Cer. Soc.*, **29**, P. 3007–3013 (2009).
- [35] Sh. Shetty, V. R. Palkar, R. Pinto. Size effect study in magnetoelectric  $\text{BiFeO}_3$  system. *J. Phys.*, **58**, P. 1027–1030 (2002).
- [36] J.-H. Xu, H. Ke, et al. Factors controlling pure-phase multiferroic  $\text{BiFeO}_3$  powders synthesized by chemical co-precipitation. *J. All. Comp.*, **472**, P. 473–477 (2009).
- [37] J. Prado-Gonjal, M.E. Villafuerte-Castrejorn, L. Fuentes, E. Morarn. Microwave-hydrothermal synthesis of the multiferroic  $\text{BiFeO}_3$ . *Mat. Res. Bull.*, **44**, P. 1734–1737 (2009).

- [38] V. Kothai, R. Rajeev. Synthesis of BiFeO<sub>3</sub> by carbonate precipitation. *Bull. Mat. Sci.*, **35**, P. 157–161 (2012).
- [39] B. Jurca, C. Paraschiv, A. Ianculescu, O. Carp. Thermal behaviour of the system Fe(NO<sub>3</sub>)<sub>3</sub>·9H<sub>2</sub>O–Bi<sub>5</sub>O(OH)<sub>9</sub>(NO<sub>3</sub>)<sub>4</sub>·9H<sub>2</sub>O–glycine/urea and of their generated oxides (BiFeO<sub>3</sub>). *J Therm. Anal. Calor.*, **97**, P. 91–98 (2009).
- [40] Quantitative analysis code. Registration certificate No. 2000611264 of 06.12.2000. PDWin-4.0. bundled software, “Burevestnik” Scientific and Production Association. St. Petersburg. 2004 24.
- [41] T. Misawa, K. Hashimoto, S. Shimodaira. The mechanism of formation of iron oxide and oxy-hydroxides in aqueous solutions at room temperature. *Corros. Sci.*, **14**, P. 131–135 (1974).
- [42] V.M. Denisov, N.V. Belousova, et al. Oxide compounds of Bi<sub>2</sub>O<sub>3</sub>–Fe<sub>2</sub>O<sub>3</sub> system I. The obtaining and phase equilibriums. *J. Siberian Federal University. Chemistry*, **5**, P. 146–167 (2012).
- [43] J.G. Dash. Surface melting. *Contemp. Phys.*, **30**, P. 89–100 (1989).
- [44] V.V. Gusarov, S.A. Suvorov. Melting-points of locally equilibrium surface phases in polycrystalline systems based on a single volume phase. *Journal of Applied Chemistry of the USSR*, **63**(8), P. 1560–1565 (1990).
- [45] V.V. Gusarov. The thermal effect of melting in polycrystalline systems. *Thermochimica Acta*. **256**, P. 467–472 (1995).
- [46] V.V. Gusarov, I.Yu. Popov. Flows in two-dimensional non-autonomous phases in polycrystalline systems. *Nuovo Cimento della Societa Italiana di Fisica. D*, **18**(7), P. 799–805 (1996).
- [47] V.V. Gusarov. Fast solid-phase chemical reactions. *Russian Journal of General Chemistry*, **67**(12), P. 1846–1851 (1997).

# SORPTION AND LIQUID CHROMATOGRAPHIC SEPARATION OF LIGHT FULLERENES C<sub>60</sub> AND C<sub>70</sub> WITH MULTIWALL CARBON NANOTUBES

V. N. Postnov<sup>2</sup>, A. Ya. Scaletckaya<sup>1</sup>, O. A. Krokhina<sup>2</sup>,  
V. A. Keskinov<sup>1</sup>, N. A. Charykov<sup>1</sup>, K. N. Semenov<sup>2</sup>

<sup>1</sup>Saint Petersburg State Technological Institute (Technical University),  
Saint Petersburg, Russia

<sup>2</sup>Saint Petersburg State University, Saint Petersburg, Russia  
keskinov@mail.ru

**PACS 61.48.+c**

Isotherms for the sorption of light fullerenes (C<sub>60</sub> and C<sub>70</sub>) from toluene solutions with the use of multiwall carbon nanotubes (MWCNTs) were investigated. Both isotherms are of the Langmuir-type. The successful liquid chromatographic separation of light fullerenes from toluene solutions was accomplished using the above-mentioned sorbent.

**Keywords:** light fullerenes, C<sub>60</sub>, C<sub>70</sub>, isotherms of sorption, toluene solutions, chromatographic separation.

## 1. Introduction

One of the main (if not unique) methods of industrial fullerenes separation and purification is now the method of liquid chromatography. In this method, one typically uses an aromatic solvent — mobile phase, where the solubility of the fullerenes is relatively high [1–4] (e.g. benzene, toluene, chlorobenzene, m-, p-, or often o-xylene or o-dichlorobenzene, etc), however, some non-aromatic solvents e.g. CS<sub>2</sub>, CCl<sub>4</sub>, etc. can be used as well. Sometimes, the addition of a non-aromatic solvent with comparatively low fullerenes solubility (e.g. n-hexane, n-octane, 1-hexanol, acetonitrile, etc.) [1–5] to an aromatic solvent is also done to increase the efficiency of the separation. As a stationary phase — one can use different sorbents with relatively high affinity for the fullerenes (e.g. different activated carbons, modified (carbonized silicates, silochroms, aerosols, etc) [5–8]. Literature searches yielded no information about the use of single-wall or multiwall carbon nanotubes (MWCNTs) for the chromatographic separation of the light fullerenes, C<sub>60</sub> and C<sub>70</sub> as the main components of standard fullerenes mixture, produced by the most popular current method — electric arc erosion of carbon rods in a He atmosphere. Meanwhile, such a stationary phase seems to be reasonable enough, because carbon nanotubes:

— are absolutely inert and insoluble in any nondestructive solutions used for fullerenes separation,

— have considerable specific surface (m<sup>2</sup>/gram),

— have high affinity for fullerenes (the main structural motif of carbon nanotubes and fullerenes is the same — carbon hexagons without any functional groups; carbon pentagons also are present in fullerenes and in the ends of carbon nanotubes),

— are relatively accessible, if we use MWCNTs, which are considerably cheaper than single wall ones and are produced in mass quantities.

So, the aim of preset work is:

- to investigate the isotherms for the sorption of light fullerenes ( $C_{60}$  and  $C_{70}$ ) from toluene solutions with the use of MWCNTs,
- to execute liquid chromatographic separation of light fullerenes with the use of the above-mentioned MWCNTs, produced by Bayer corporation (Germany).

## 2. Materials

1. MWCNTs used in this study were produced by Bayer corporation (Germany). Their physical properties are as follows: external diameter 50–60 nm, internal diameter 5–15 nm, specific surface area  $125 \pm 35 \text{ m}^2/\text{g}$  (BET – theory), bulk density  $\rho^b = 0.15 \pm 0.02 \text{ g/cm}^3$ , length 10–20  $\mu\text{m}$ , temperature of phase transition 3652–3697 °C. Typical electronic photo of MWCNTs, produced by Bayer corporation (Germany) is represented in Fig. 1.

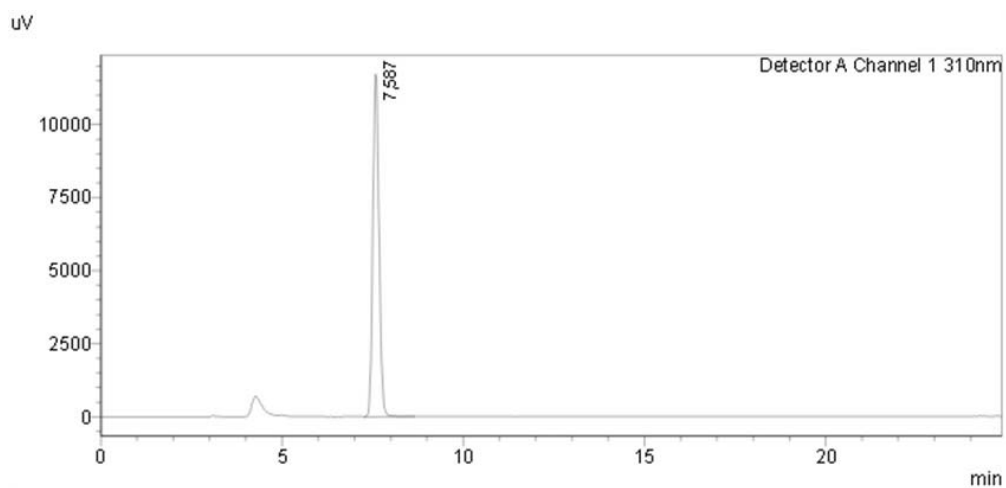
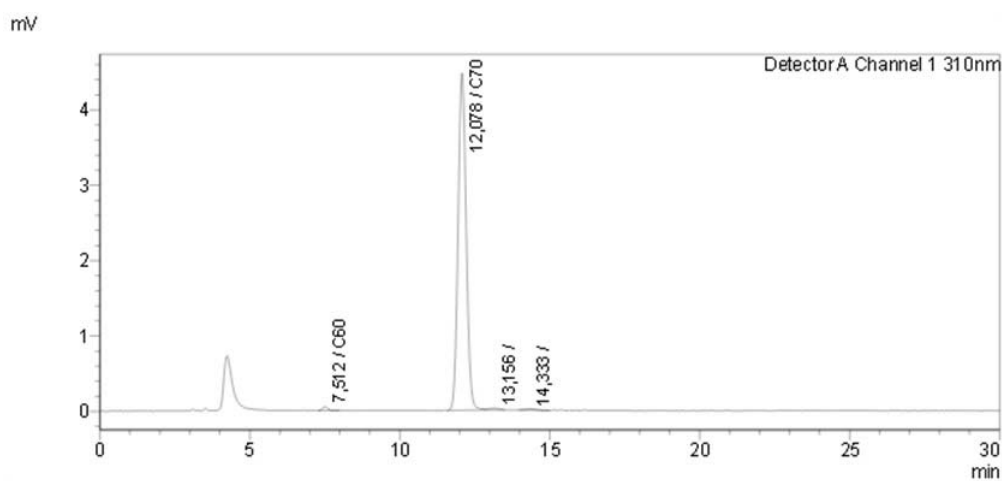
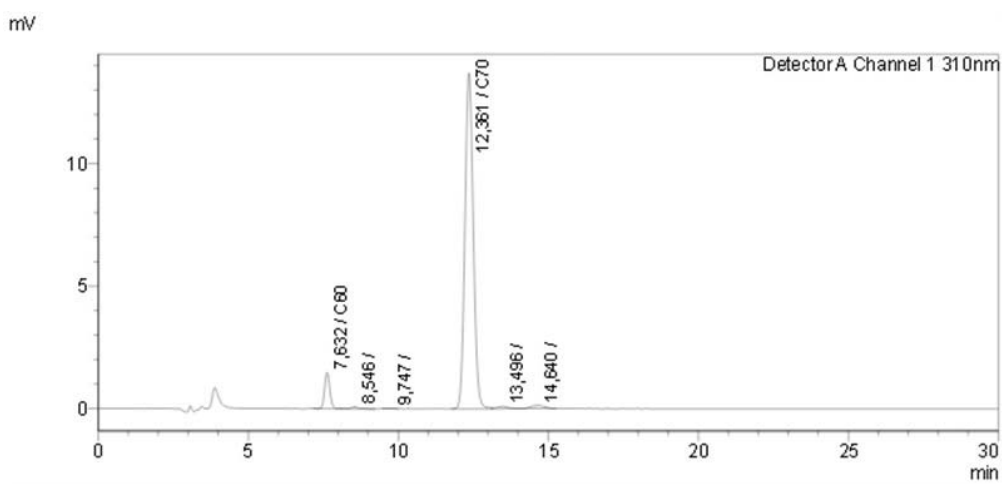
2.  $C_{60}$  and  $C_{70}$  fullerenes were produced by the “ILIP” corporation (Saint Petersburg) [6–8] with purities of 99.9 and 99.5 mass%, respectively. Liquid — phase chromatograms of these products are shown in Fig. 2 and 3. The condition of UHPLC-analysis hereinafter were the following: chromatograph – Shimadzu LC-20 Prominence, solvent – toluene, detector – light absorption at wavelength  $\lambda = 335 \text{ nm}$ , column Agilent HC-C18(2).

3. The  $C_{70}$ -enriched fullerene mixture  $C_{60} + C_{70}$  utilized in these separation studies was also produced by “ILIP” corporation [7–9]. This mixture had the following average composition:  $90 \pm 3 \text{ mass\% } C_{70}$ ,  $10 \pm 3 \text{ mass\% } C_{60}$ , high fullerenes  $C_{n>70} \leq 0.3 \text{ mass\%}$ . The fullerene mixture, enriched by the  $C_{60}$  fullerene was not investigated, because one can produce the pure individual light fullerene  $C_{60}$ , using the cheaper and more traditional sorbent with high exploitation characteristics, e.g. active carbon Norrit Azo [7, 8]. A typical liquid — phase chromatogram of such fullerene mixture is also represented in Fig. 4.

4. Toluene (“pure for analysis”, Rus. State Standard GOST — 5789-78) (boiling temperature (1 atm)  $T^b = 110.6 \text{ }^\circ\text{C}$ , refractive index  $n_D^{20} = 1.4969 \text{ rel.un.}$ ).



FIG. 1. Typical electronic photo of carbon multiwall nanotubes, produced by Bayer corporation (Germany) ( $\times 10^5$ )

FIG. 2. Liquid — phase chromatograms of  $C_{60}$ FIG. 3. Liquid — phase chromatograms of  $C_{70}$ FIG. 4. Liquid — phase chromatograms of mixture  $C_{60} + C_{70}$

### 3. Isotherms of sorption of light fullerenes

#### Experiment and discussion

The investigation of the isotherms for the sorption of individual light fullerenes —  $C_{60}$  and  $C_{70}$  separately, on Bayer MWCNTs, in toluene solutions was done using the static method. In preliminary experiments, it was established that 2–3 hours was long enough to realize sorption equilibrium — i.e. after this time, the concentration of fullerenes in the liquid solution ceased to change. So, the duration of the experiment was chosen as 4 h. The experiment was done at  $25.0 \pm 0.1$  °C in a shaker-thermostat by the method of constant volumes. A determined mass of the sorbent was added to an aliquot of the fullerene-toluene solution with a determined concentration (20 ml), and after shaking for 4 h with an equal mass of the sorbent (0.15 g), the concentration of fullerenes in liquid solution was determined. According to the changes of fullerenes concentrations in liquid solution the concentrations of the remaining fullerenes in the sorbent were calculated. In this manner, the sorbent capacity was determined.

To measure the fullerenes concentration, we used light absorption in the near-UV and visual spectral region. These measurements were done using a UV–1800 spectrophotometer (Shimadzu), quartz cuvette ( $l = 1$  cm), toluene as a solvent, spectral range ( $\lambda = 250 - 750$  nm). To calculate the concentration of  $C_{60}$  and  $C_{70}$ , we hereafter use the following system of equations, which are the decision of Burger-Lambert-Beer equations in the maxima of light absorption wavelengths for  $C_{60}$  and  $C_{70}$  — 335.7 and 472.0 nm, respectively:

$$C(C_{60}) = 13.10(D_{335.7} - 1.8051D_{472.0})$$

$$C(C_{70}) = 42.51(D_{472.0} - 0.00810D_{335.7})$$

Where:  $C(C_{60})$ ,  $C(C_{70})$  concentration of fullerenes  $C_{60}$  and  $C_{70}$  in mg/l,  $D_{335.7}$ ,  $D_{472.0}$  — optical density at  $l = 1$  cm and  $\lambda = 335.7$  nm and 472.0 nm, correspondingly [1–4]. Typical electronic spectrum of  $C_{60}$  and  $C_{70}$  are represented in Fig. 5.

Data obtained for the investigation of sorption isotherms in the  $C_{60}$  fullerene — Bayer MWCNTs — toluene and the  $C_{70}$  fullerene — Bayer MWCNTs — toluene systems are represented in Table 1 and in Fig. 6 and 7. Both isotherms are of the Langmuir-type. The graphics of the isotherms in Langmuir coordinates are also shown in Fig. 8 and 9.

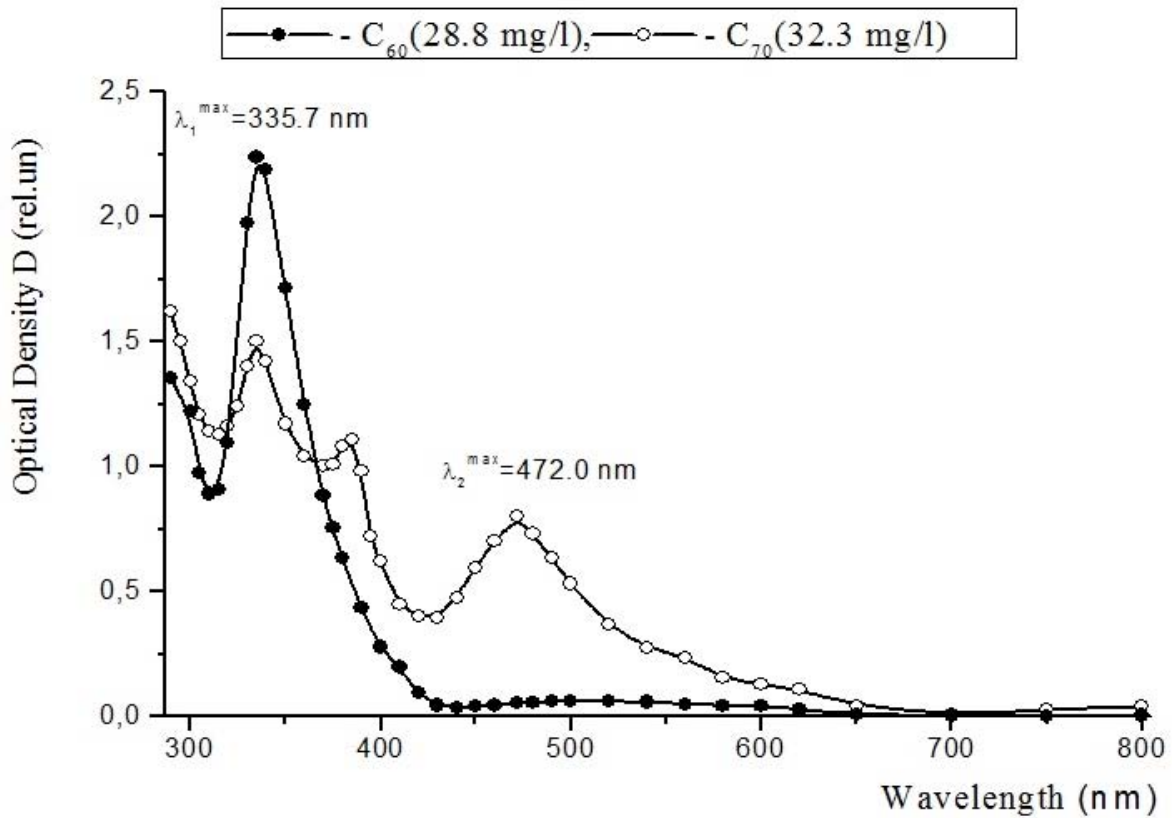
One can see, that the static capacities of the sorbent for both light fullerenes are very similar and rather high —  $C_{\max}^s \approx 21$  and 18 mg of  $C_{60}$  and  $C_{70}$  fullerenes per gram of sorbent, respectively. As a comparison, the capacity of traditional sorbent for  $C_{60}$  and  $C_{70}$  separation, carbon Norrit Azo, has capacities of  $C_{\max}^s \approx 14$  and 8 mg of  $C_{60}$  and  $C_{70}$  fullerenes per gram of sorbent, respectively.

### 4. Liquid chromatographic separation of light fullerenes

#### Experiment and discussion

As a typical example, the chromatographic separation of light fullerenes from toluene solutions was done with Bayer MWCNTs as the sorbent. The column volume was  $\approx 28$  ml, height  $\approx 56.5$  cm (so, we used “thick” preparative column). The composition of the initial fullerene solution was as follows:  $C_{60} \approx 1450$  mg/l,  $C_{70} \approx 178$  mg/l ( $C_{60} \approx 11$  mass%,  $C_{70} \approx 89$  mass%), the volume of fullerene toluene solution was  $\approx 33$  ml. The mass of the sorbent was  $m \approx 4.254$  g. So, we used dynamical capacity of the sorbent  $C_{dyn}^s \approx 12.6$  mg of total light fullerenes per gram of sorbent or approximately 2/3 of its average static capacity. The results of the separation are represented in Fig. 10.

One can see the following:

FIG. 5. Electronic spectrum of  $C_{60}$  and  $C_{70}$ TABLE 1. Sorption isotherms for the  $C_{60}$  fullerene – Bayer MWCNTs – toluene and the  $C_{70}$  fullerene – Bayer MWCNTs – toluene systems at 25 °C

System	Concentration in liquid phase $C^l(g/l)$	Concentration in solid phase $C^s(mg/g \text{ sorbent})$	Degree of sorbent filling $\theta = C^s/C_{max}^s$ (rel.un.)
$C_{60}$ fullerene – Bayer MWCNTs – toluene	0.00	0.0	0.00
- “-	0.12	10.7	0.52
- “-	0.26	18.7	0.91
- “-	0.47	20.0	0.97
- “-	0,65	20.4	0.99
$C_{70}$ fullerene $C_{70}$ – Bayer MWCNTs – toluene	0.00	0.0	0.00
- “-	0.13	9.3	0.51
- “-	0.30	13.3	0.73
- “-	0.48	16.0	0.88
- “-	0.67	17.3	0.95
- “-	0.86	18.0	0.99

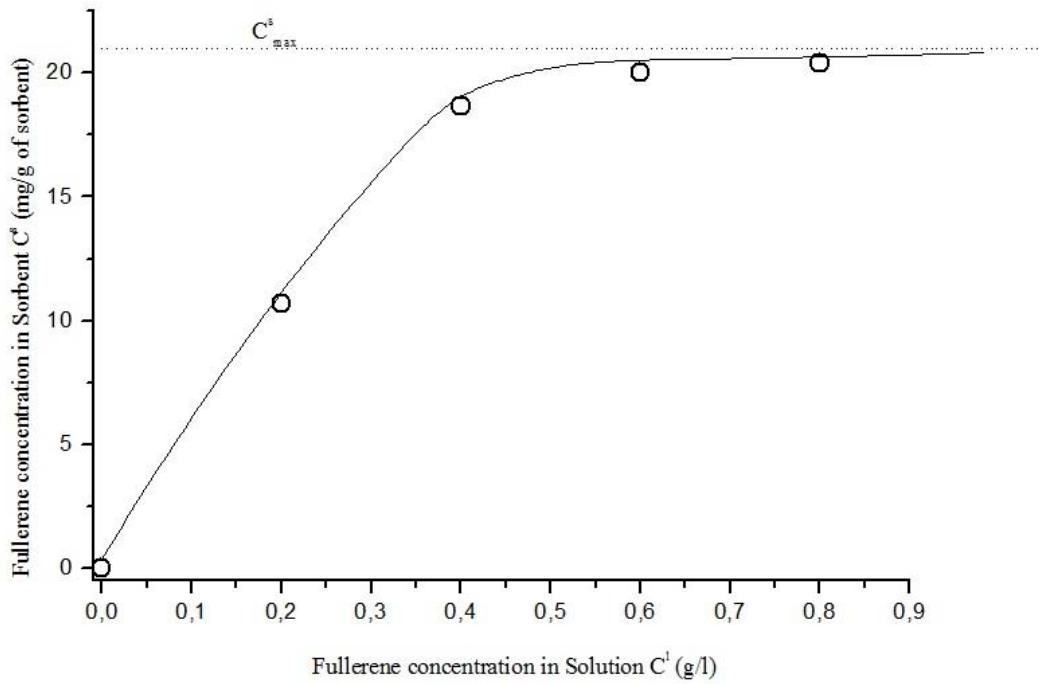


FIG. 6. Sorption isotherms in the  $C_{60}$  fullerene – Bayer MWCNTs – toluene system in normal coordinates

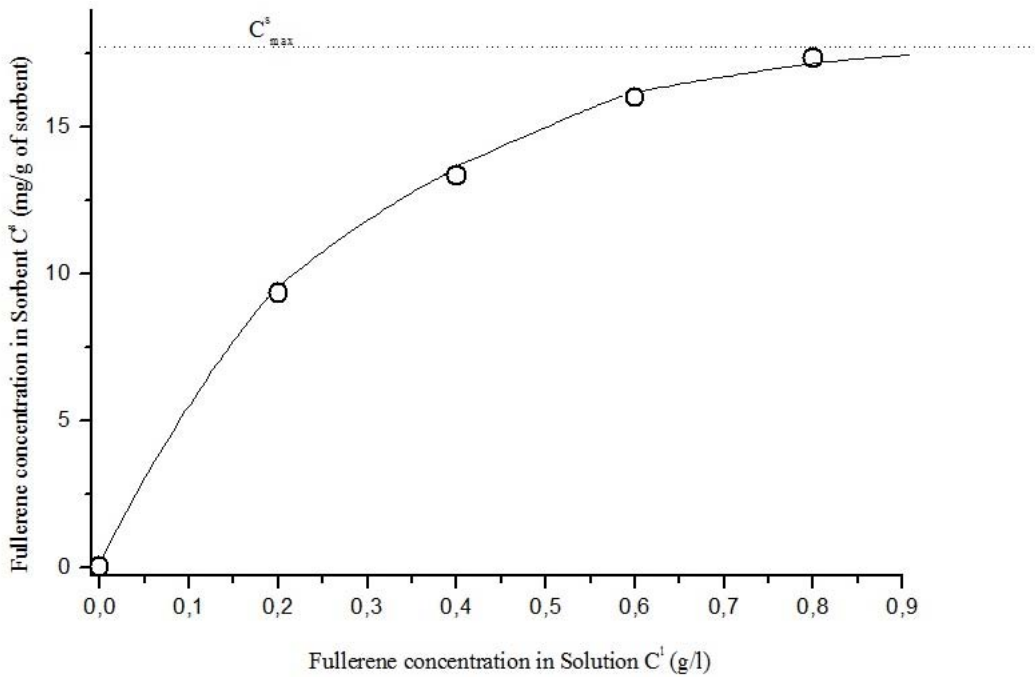


FIG. 7. Sorption isotherms in the  $C_{70}$  fullerene – Bayer MWCNTs – toluene system in normal coordinates

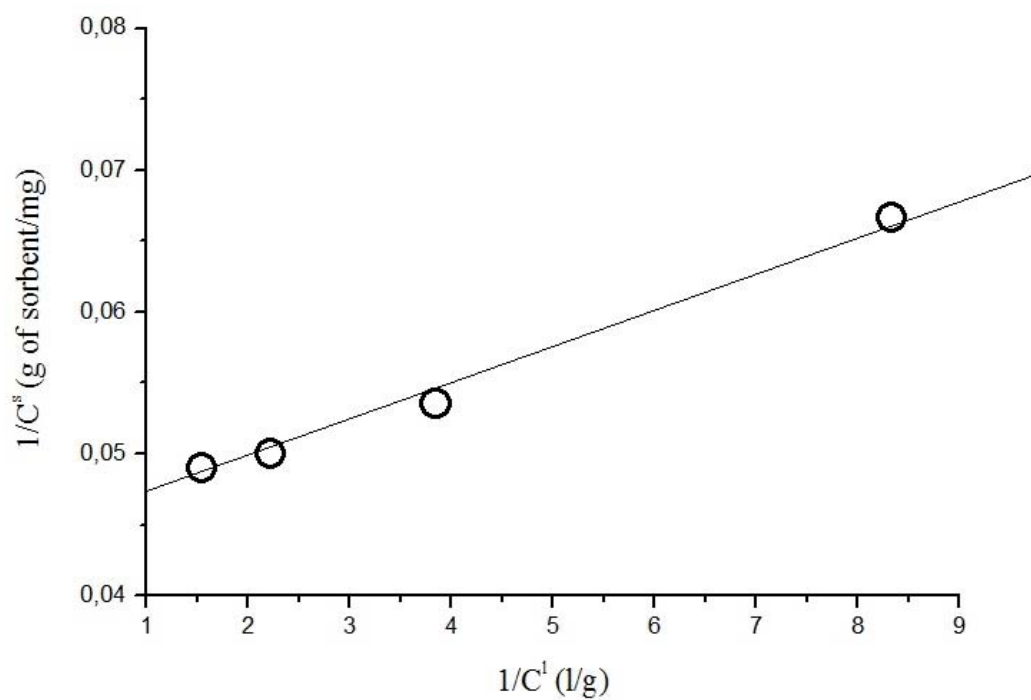


FIG. 8. Sorption isotherms in the  $C_{60}$  fullerene – Bayer MWCNTs – toluene system in Langmuir coordinates

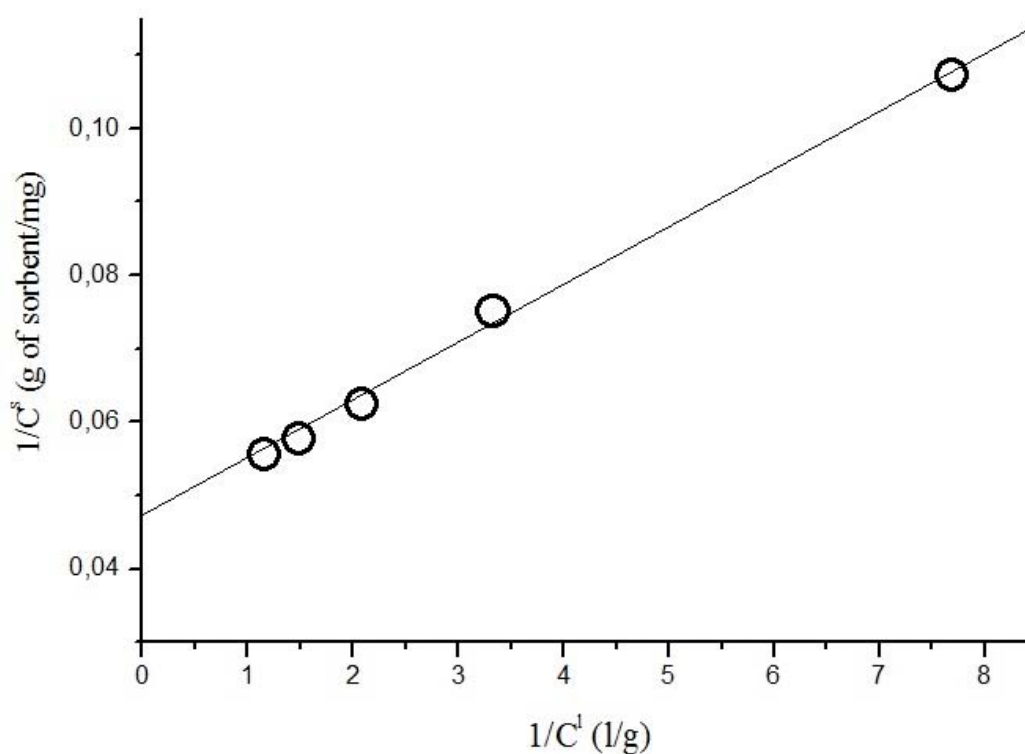


FIG. 9. Sorption isotherms in the  $C_{70}$  fullerene – Bayer MWCNTs – toluene system in Langmuir coordinates

- We produced more than 85 mass% of  $C_{70}$  fullerene (in relation to the entered  $C_{70}$  — dotted line in Fig. 10, nearly 3 column volumes),
  - Thus, the average concentration of produced  $C_{70}$  (3 → 8 column volumes) was more than 99 mass%,
  - The losses of both fullerenes  $C_{60}$  and  $C_{70}$  were negligible (< 3 mass%).
- So, the chromatographic separation was thus deemed successful.

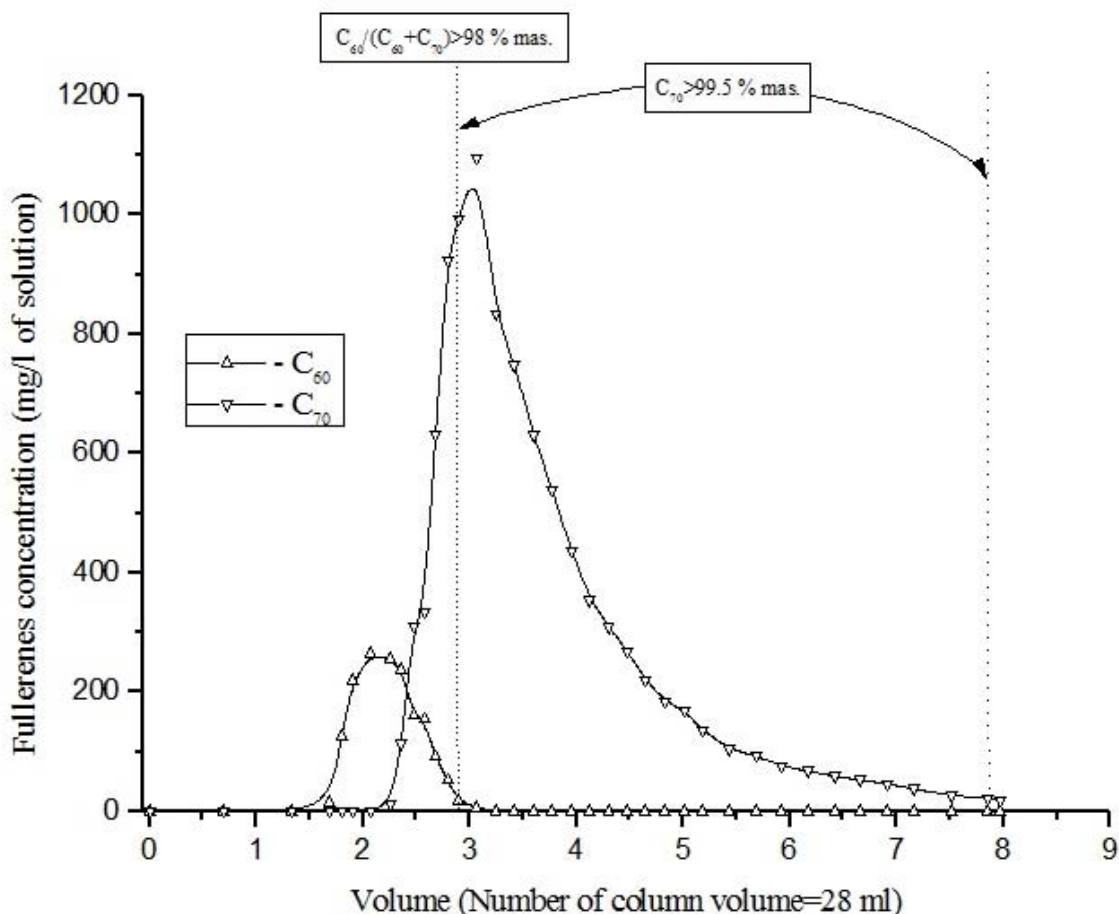


FIG. 10. Chromatographic separation of light fullerenes  $C_{60}$  and  $C_{70}$  with the help of the sorbent Bayer Multiwall Carbon Nanotubes from toluene solutions

A similar experiment was performed using mixed sorbent Bayer MWCNTs/granules of fluorine plastic (IV) in equal volume (1/1 v/v). We used a “thick” laboratory little column and a dynamical capacity of the mixed sorbent  $C_{dyn}^s \approx 12.6$  mg of total light fullerenes per gram of Bayer MWCNTs without taking into account the fluorine plastic (which was used to allow free flow of the solution through the sorbent in the column, and simultaneously, for the consolidation of the sorbent). The initial mixed fullerene solution was the same. The results of the separation are also represented in Fig. 11. In this case, chromatographic separation was also successful and very close to the above-mentioned results, however this separation was realized more quickly (4 → 6.5 column volumes) and the concentration of the separated fullerenes were lower.

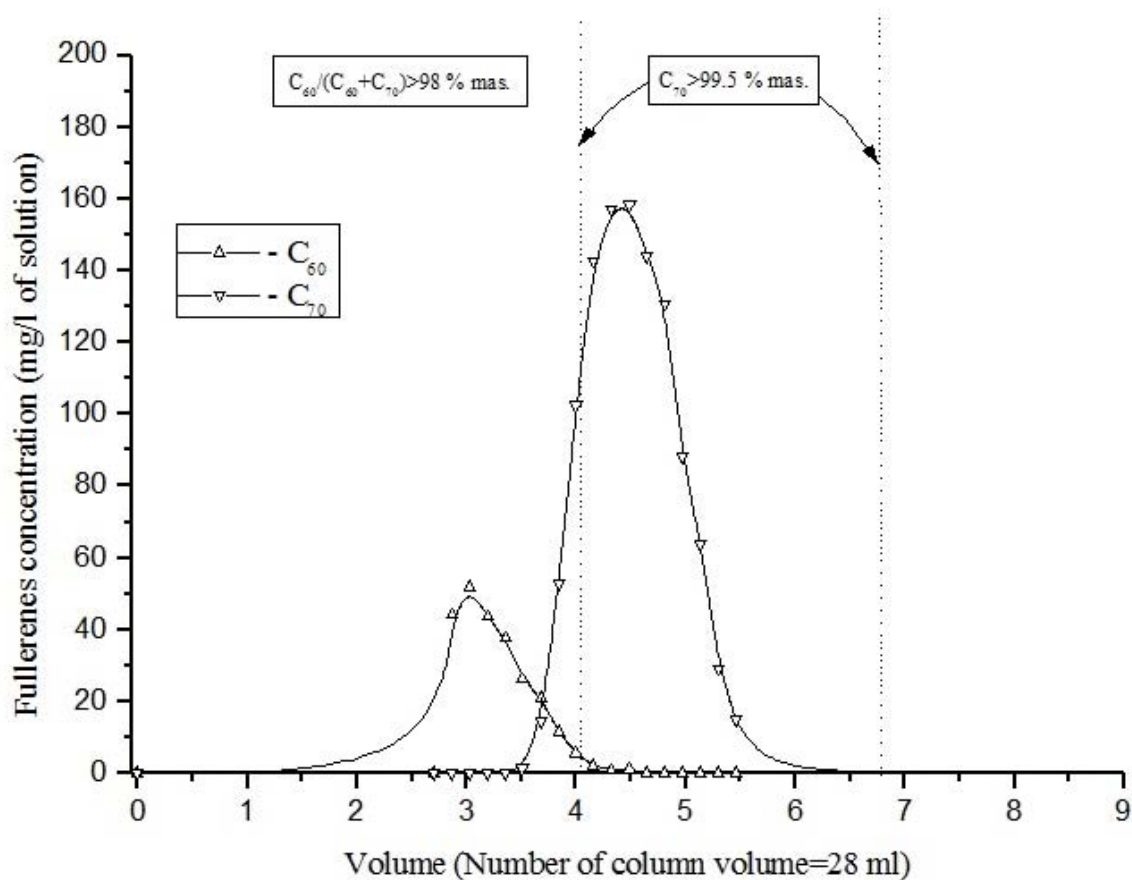


FIG. 11. Chromatographic separation of light fullerenes  $C_{60}$  and  $C_{70}$  with the help of the mixed sorbent Bayer MWCNTs/granules of fluorine plastic from toluene solutions

## 5. Conclusions

Isotherms for the sorption of light fullerenes ( $C_{60}$  and  $C_{70}$ ) from toluene solutions with the use of MWCNTs were investigated. Both isotherms were of the Langmuir-type. The static capacities of the sorbent, for both light fullerenes, are very similar and rather high. Successful liquid chromatographic separation of light fullerenes has been achieved using the above-mentioned sorbent from toluene solutions. The results showed that Bayer MWCNTs are a reasonable and effective material for the separation and purification of light fullerenes.

## Acknowledgements

Authors are grateful to the Russian Found of Fundamental Researches for the support (Project N 09-03-00350-a).

## References

- [1] K. Semenov, N. Charykov. *Solubility of Light Fullerenes and Derivatives*. LAP LAMBERT Academic Publishing GmbH & Co. KG, Saarbrücken, Germany, 238 pp. (2011).
- [2] Semenov K. N., Charykov N.A. Phase Equilibria in the Fullerene-Containing Systems. *Handbook on Fullerene: Synthesis, Properties and Applications*. P. 1-91 (2012).
- [3] Semenov K.N., Charykov N.A. Solubility of Light Fullerenes and Fullerenol in Biocompatible with Human Beings Solvents. Chapter in Handbook: *Grapes: Cultivation, Varieties and Nutritional Uses*, Nova Sciences Publishers, Inc., P. 1-48 (2011).

- [4] K.N. Semenov, N.A. Charykov, V.A. Keskinov, et al. Solubility of Light Fullerenes in Organic Solvents. *J. Chem. Eng. Data*, **55**, P. 13–36 (2010).
- [5] L.N. Sidorov, M.A. Yurovskaya, et al. *Fullerenes*. Ekzamen, Moscow, 688 pp. (2005).
- [6] A.A. Blokhin, V.A. Keskinov, Yu.V. Murashkin, et al. Method for chromatographic separation of fullerenes. Patent RF 2302372, C01B 31/02 (2007).
- [7] N.N. Ermilov, N.A. Charykov, et al. Nanotechnology — from theory to practical application. *Journal of Innovations (rus.)*, **12**, P.79–83 (2007).
- [8] N.A. Charykov, V.V. Zuev, E.A. Kuznetsova. High-efficiency complex for fullerenes production. *Petersburg Electronics Journal*, **4**, P. 16–31 (2007).
- [9] V.A. Keskinov, N.A. Charykov, M.V. Keskinova, et al. Pre-chromatography crude separation of light fullerenes by poly-thermal re(crystallization) method. *Nanosystems: Physics, Chemistry, Mathematics*, **4**(3), P. 344–351 (2013).

# CORRECTION TO THE PAPER ”SILVER-NANOPARTICLE-BASED ETCH MASK CONTROL FOR SUBWAVELENGTH STRUCTURE DEVELOPMENT”

Nazme Moushumi<sup>1</sup>, Kamal Alameh<sup>1,2</sup>, V. Rajendran<sup>3</sup>, Yong Tak Lee<sup>2</sup>

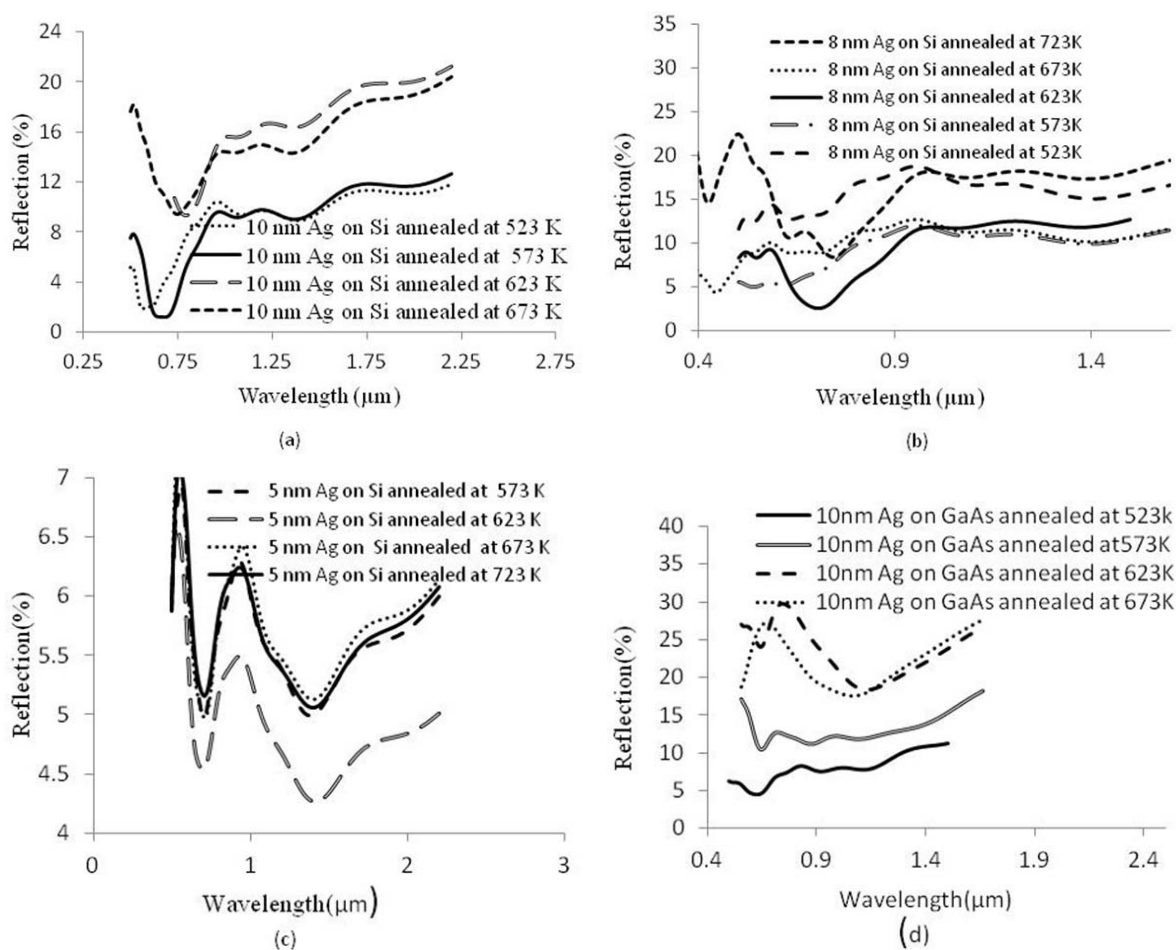
<sup>1</sup>Electron Science Research Institute, Edith Cowan University, 270 Joondalup Dr,  
Joondalup, WA 6027, Australia

<sup>2</sup>Department of Nanobio Materials and Electronics, Gwangju Institute of Science and  
Technology, World-Class University (WCU), Gwangju Institute of Science & Technology  
(GIST), Gwangju 500–712, South Korea

<sup>3</sup>Centre for Nano Science and Technology, K S R College of Technology, K S R Kalvi  
Nagar, Tiruchengode — 637 215, Namakkal (Dt.), Tamil Nadu, India

PACS 61.46.df

In the text published in Nanosystems: Physics, Chemistry, Mathematics, 4(3) (2013),  
P. 387–394, figure 6 should be replaced by the following more precise figure



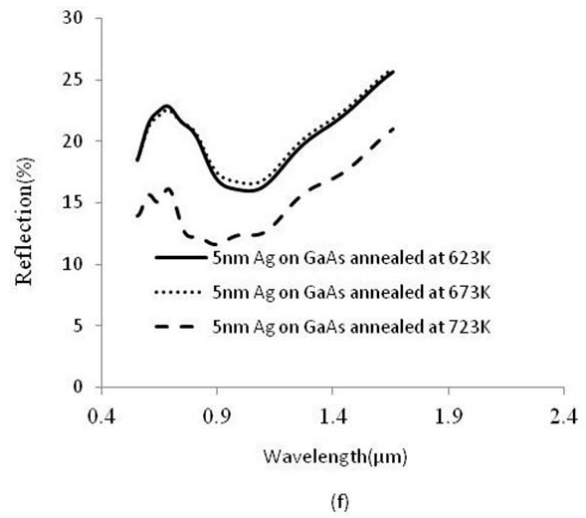
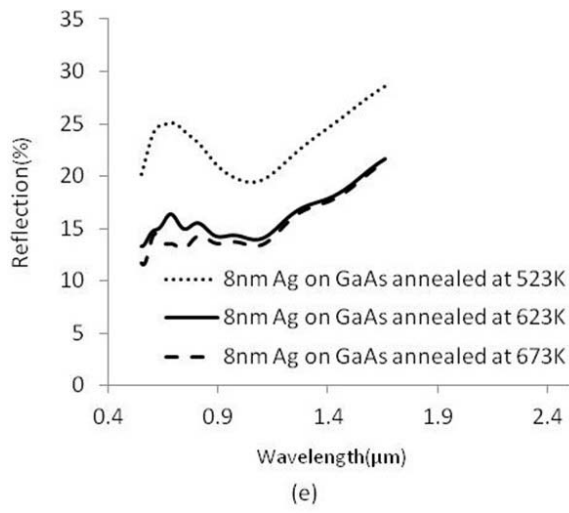


Fig.6. Reflection spectra for various SWG structures developed using 10 nm, 8 nm and 5 nm thick Ag films on Si and GaAs substrates, annealed at different temperatures



# **NANOSYSTEMS:**

## **PHYSICS, CHEMISTRY, MATHEMATICS**

### **INFORMATION FOR AUTHORS**

The journal publishes research articles and reviews, and also short scientific papers (letters) which are unpublished and have not been accepted for publication in other magazines. Articles should be submitted in English. All articles are reviewed, then if necessary come back to the author to completion.

The journal is indexed in Chemical Abstract Service of the American Chemical Society and in Russian Scientific Citation Index.

#### **Author should submit the following materials:**

1. Article file in English, containing article title, the initials and the surname of the authors, Institute (University), postal address, the electronic address, the summary, keywords, MSC or PACS index, article text, the list of references.
2. Files with illustrations, files with tables.
3. The covering letter in English containing the article information (article name, MSC or PACS index, keywords, the summary, the literature) and about all authors (the surname, names, the full name of places of work, the mailing address with the postal code, contact phone number with a city code, the electronic address).
4. The expert judgement on possibility of publication of the article in open press (for authors from Russia).

Authors can submit a paper and the corresponding files to the following addresses: nanojournal.ifmo@gmail.com, popov1955@gmail.com.

#### **Text requirements**

Articles should be prepared with using of text editors MS Word or LaTeX (preferable). It is necessary to submit a pdf copy. In the name of files the English alphabet is used. The recommended size of short communications (letters) is 4-6 pages, research articles – 6-15 pages, reviews – 30 pages.

##### Recommendations for text in MS Word:

Formulas should be written using Math Type. Figures and tables with captions should be inserted in the text. Additionally, authors present separate files for all figures and Word files of tables.

### Recommendations for text in LaTeX:

Please, use standard LaTeX without macros and additional style files. The list of references should be included in the main LaTeX file. Single LaTeX file of the paper with the corresponding pdf file should be submitted.

References in the article text are given in square brackets. The list of references should be prepared in accordance with the following samples:

- [1] N. Surname. *Book Title*. Nauka Publishing House, Saint Petersburg, 281 pp. (2000).
- [2] N. Surname, N. Surname. Paper title. *Journal Name*, **1**(5), P. 17-23 (2000).
- [3] N. Surname, N. Surname. Lecture title. In: Abstracts/Proceedings of the Conference, Place and Date, P. 17-23 (2000).
- [4] N. Surname, N. Surname. Paper title (2010). URL: <http://books.ifmo.ru/ntv>.
- [5] N. Surname, N. Surname. Patent Name. Patent No. 11111, Bul. No. 33, 5 pp. (2010).
- [6] N. Surname, N. Surname. Thesis Title. Thesis for full doctor degree in math. and physics, Saint Petersburg, 105 pp. (2000).

### **Requirements to illustrations**

Illustrations should be submitted as separate black-and-white files. Formats of files – jpeg, eps, tiff.



# **NANOSYSTEMS:**

**PHYSICS, CHEMISTRY, MATHEMATICS**

**Журнал зарегистрирован**

Федеральной службой по надзору в сфере связи, информационных технологий и массовых коммуникаций

(свидетельство ПИ № ФС 77 - 49048 от 22.03.2012 г.)

ISSN 2220-8054

**Учредитель:** федеральное государственное бюджетное образовательное учреждение высшего профессионального образования «Санкт-Петербургский национальный исследовательский университет информационных технологий, механики и оптики»

**Издатель:** федеральное государственное бюджетное образовательное учреждение высшего профессионального образования «Санкт-Петербургский национальный исследовательский университет информационных технологий, механики и оптики»

**Отпечатано** в типографии «Фалкон Принт»

Адрес: 197101, г. Санкт-Петербург, ул. Большая Пушкарская, 54

**Подписка на журнал НФХМ**

На 2014 год подписка осуществляется через ОАО Агентство «Роспечать»

Подписной индекс 57385 в каталоге «Издания органов научно-технической информации»